



HAL
open science

**The Pierre Auger Observatory: Contributions to the
36th International Cosmic Ray Conference (ICRC 2019)
The Pierre Auger Collaboration**

A Aab, P Abreu, M Aglietta, I F M Albuquerque, J M Albury, I Allekotte, A
Almela, J Alvarez Castillo, J Alvarez-Muñiz, G A Anastasi, et al.

► **To cite this version:**

A Aab, P Abreu, M Aglietta, I F M Albuquerque, J M Albury, et al.. The Pierre Auger Observatory: Contributions to the 36th International Cosmic Ray Conference (ICRC 2019) The Pierre Auger Collaboration. 36th International Cosmic Ray Conference (ICRC 2019), Jul 2019, Madison, United States. hal-03389637

HAL Id: hal-03389637

<https://hal.science/hal-03389637>

Submitted on 21 Oct 2021

HAL is a multi-disciplinary open access archive for the deposit and dissemination of scientific research documents, whether they are published or not. The documents may come from teaching and research institutions in France or abroad, or from public or private research centers.

L'archive ouverte pluridisciplinaire **HAL**, est destinée au dépôt et à la diffusion de documents scientifiques de niveau recherche, publiés ou non, émanant des établissements d'enseignement et de recherche français ou étrangers, des laboratoires publics ou privés.



The Pierre Auger Observatory: Contributions to the 36th International Cosmic Ray Conference (ICRC 2019)

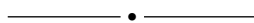
The Pierre Auger Collaboration



PIERRE
AUGER
OBSERVATORY

A. Aab⁷⁵, P. Abreu⁶⁷, M. Aglietta^{50,49}, I.F.M. Albuquerque¹⁹, J.M. Albury¹², I. Allekotte¹, A. Almela^{8,11}, J. Alvarez Castillo⁶³, J. Alvarez-Muñiz⁷⁴, G.A. Anastasi^{42,43}, L. Anchordoqui⁸², B. Andrada⁸, S. Andringa⁶⁷, C. Aramo⁴⁷, H. Asorey^{1,28}, P. Assis⁶⁷, G. Avila^{9,10}, A.M. Badescu⁷⁰, A. Bakalova³⁰, A. Balaceanu⁶⁸, F. Barbato^{56,47}, R.J. Barreira Luz⁶⁷, S. Baur³⁷, K.H. Becker³⁵, J.A. Bellido¹², C. Berat³⁴, M.E. Bertaina^{58,49}, X. Bertou¹, P.L. Biermann^b, T. Bister³⁹, J. Biteau³², A. Blanco⁶⁷, J. Blazek³⁰, C. Bleve^{52,45}, M. Boháčová³⁰, D. Boncioli^{42,43}, C. Bonifazi²⁴, N. Borodai⁶⁴, A.M. Botti^{8,37}, J. Brack^e, T. Bretz³⁹, F.L. Briechele³⁹, P. Buchholz⁴¹, A. Bueno⁷³, S. Buitink¹⁴, M. Buscemi^{54,44}, K.S. Caballero-Mora⁶², L. Caccianiga⁵⁵, L. Calcagni⁴, A. Cancio^{11,8}, F. Canfora^{75,77}, I. Caracas³⁵, J.M. Carceller⁷³, R. Caruso^{54,44}, A. Castellina^{50,49}, F. Catalani¹⁷, G. Cataldi⁴⁵, L. Cazon⁶⁷, M. Cerda⁹, J.A. Chinellato²⁰, K. Choi¹³, J. Chudoba³⁰, L. Chytka³¹, R.W. Clay¹², A.C. Cobos Cerutti⁷, R. Colalillo^{56,47}, A. Coleman⁸⁸, M.R. Coluccia^{52,45}, R. Conceição⁶⁷, A. Condorelli^{42,43}, G. Consolati^{46,51}, F. Contreras^{9,10}, F. Convenga^{52,45}, M.J. Cooper¹², S. Coutu⁸⁶, C.E. Covault^{80,h}, B. Daniel²⁰, S. Dasso^{5,3}, K. Daumiller³⁷, B.R. Dawson¹², J.A. Day¹², R.M. de Almeida²⁶, S.J. de Jong^{75,77}, G. De Mauro^{75,77}, J.R.T. de Mello Neto^{24,25}, I. De Mitri^{42,43}, J. de Oliveira²⁶, V. de Souza¹⁸, J. Debatin³⁶, M. del Río¹⁰, O. Deligny³², N. Dhital⁶⁴, A. Di Matteo⁴⁹, M.L. Díaz Castro²⁰, C. Dobrigkeit²⁰, J.C. D'Olivo⁶³, Q. Dorosti⁴¹, R.C. dos Anjos²³, M.T. Dova⁴, A. Dundovic⁴⁰, J. Ebr³⁰, R. Engel^{36,37}, M. Erdmann³⁹, C.O. Escobar^c, A. Etchegoyen^{8,11}, H. Falcke^{75,78,77}, J. Farmer⁸⁷, G. Farrar⁸⁵, A.C. Fauth²⁰, N. Fazzini^c, F. Feldbusch³⁸, F. Fenu^{58,49}, L.P. Ferreyro⁸, J.M. Figueira⁸, A. Filipčić^{72,71}, M.M. Freire⁶, T. Fujii^{87,f}, A. Fuster^{8,11}, B. García⁷, H. Gemmeke³⁸, F. Gesualdi⁸, A. Gherghel-Lascu⁶⁸, P.L. Ghia³², U. Giaccari¹⁵, M. Giammarchi⁴⁶, M. Giller⁶⁵, D. Glas⁶⁶, J. Glombitza³⁹, F. Gobbi⁹, G. Golup¹, M. Gómez Berisso¹, P.F. Gómez Vitale^{9,10}, J.P. Gongora⁹, N. González⁸, I. Goos^{1,37}, D. Góra⁶⁴, A. Gorgi^{50,49}, M. Gottowik³⁵, T.D. Grubb¹², F. Guarino^{56,47}, G.P. Guedes²¹, E. Guido^{49,58}, S. Hahn³⁷, R. Halliday⁸⁰, M.R. Hampel⁸, P. Hansen⁴, D. Harari¹, T.A. Harrison¹², V.M. Harvey¹², A. Haungs³⁷, T. Hebbeker³⁹, D. Heck³⁷, G.C. Hill¹², C. Hojvat^c, E.M. Holt^{36,8}, J.R. Hörandel^{75,77}, P. Horvath³¹, M. Hrabovský³¹, T. Huege^{37,14}, J. Hulsman^{8,37}, A. Insolia^{54,44}, P.G. Isar⁶⁹, J.A. Johnsen⁸¹, J. Jurysek³⁰, A. Kääpä³⁵, K.H. Kampert³⁵, B. Keilhauer³⁷, N. Kemmerich¹⁹, J. Kemp³⁹, H.O. Klages³⁷, M. Kleifges³⁸, J. Kleinfeller⁹, G. Kukec Mezek⁷¹, A. Kuotb Awad³⁶, B.L. Lago¹⁶, D. LaHurd⁸⁰, R.G. Lang¹⁸, R. Legumina⁶⁵, M.A. Leigui de Oliveira²², V. Lenok³⁷, A. Letessier-Selvon³³, I. Lhenry-Yvon³², O.C. Lippmann¹⁵, D. Lo Presti^{54,44}, L. Lopes⁶⁷, R. López⁵⁹, A. López Casado⁷⁴, R. Lorek⁸⁰, Q. Luce³⁶, A. Lucero⁸, M. Malacari⁸⁷, G. Mancarella^{52,45}, D. Mandat³⁰, B.C. Manning¹², J. Manshanden⁴⁰, P. Mantsch^c, A.G. Mariazzi⁴, I.C. Mariş¹³, G. Marsella^{52,45}, D. Martello^{52,45}, H. Martinez¹⁸, O. Martínez Bravo⁵⁹, M. Mastrodicasa^{53,43}, H.J. Mathes³⁷, S. Mathys³⁵, J. Matthews⁸³, G. Matthiae^{57,48}, E. Mayotte³⁵, P.O. Mazur^c, G. Medina-Tanco⁶³,

D. Melo⁸, A. Menshikov³⁸, K.-D. Merenda⁸¹, S. Michal³¹, M.I. Micheletti⁶, L. Miramonti^{55,46}, D. Mockler¹³, S. Mollerach¹, F. Montanet³⁴, C. Morello^{50,49}, G. Morlino^{42,43}, M. Mostafá⁸⁶, A.L. Müller^{8,37}, M.A. Muller^{20,d}, S. Müller³⁶, R. Mussa⁴⁹, W.M. Namasaka³⁵, L. Nellen⁶³, M. Niculescu-Oglinza⁶⁸, M. Niechciol⁴¹, D. Nitz^{84,8}, D. Nosek²⁹, V. Novotny²⁹, L. Nožka³¹, A. Nucita^{52,45}, L.A. Núñez²⁸, A. Olinto⁸⁷, M. Palatka³⁰, J. Pallotta², M.P. Panetta^{52,45}, P. Papenbreer³⁵, G. Parente⁷⁴, A. Parra⁵⁹, M. Pech³⁰, F. Pedreira⁷⁴, J. Peřkala⁶⁴, R. Pelayo⁶¹, J. Peña-Rodríguez²⁸, L.A.S. Pereira²⁰, M. Perlin⁸, L. Perrone^{52,45}, C. Peters³⁹, S. Petrera^{42,43}, J. Phuntsok⁸⁶, T. Pierog³⁷, M. Pimenta⁶⁷, V. Pirronello^{54,44}, M. Platino⁸, J. Poh⁸⁷, B. Pont⁷⁵, M. Pothast^{77,75}, R.R. Prado¹⁸, P. Privitera⁸⁷, M. Prouza³⁰, A. Puyleart⁸⁴, S. Querchfeld³⁵, R. Ramos-Pollán²⁸, J. Rautenberg³⁵, D. Ravnani⁸, M. Reininghaus³⁷, J. Ridky³⁰, F. Riehn⁶⁷, M. Risse⁴¹, P. Ristori², V. Rizi^{53,43}, W. Rodrigues de Carvalho¹⁹, J. Rodríguez Rojo⁹, M.J. Roncoroni⁸, M. Roth³⁷, E. Roulet¹, A.C. Rovero⁵, P. Ruehl⁴¹, S.J. Saffi¹², A. Saftoiu⁶⁸, F. Salamida^{53,43}, H. Salazar⁵⁹, G. Salina⁴⁸, J.D. Sanabria Gomez²⁸, F. Sánchez⁸, E.M. Santos¹⁹, E. Santos³⁰, F. Sarazin⁸¹, R. Sarmento⁶⁷, C. Sarmiento-Cano⁸, R. Sato⁹, P. Savina^{52,45}, M. Schauer³⁵, V. Scherini⁴⁵, H. Schieler³⁷, M. Schimassek³⁶, M. Schimp³⁵, F. Schlüter³⁷, D. Schmidt³⁶, O. Scholten^{76,14}, P. Schovánek³⁰, F.G. Schröder^{88,37}, S. Schröder³⁵, J. Schumacher³⁹, S.J. Sciutto⁴, M. Scornavacche⁸, R.C. Shellard¹⁵, G. Sigi⁴⁰, G. Silli^{8,37}, O. Sima^{68,h}, R. Šmída⁸⁷, G.R. Snow⁸⁹, P. Sommers⁸⁶, J.F. Soriano⁸², J. Souchard³⁴, R. Squartini⁹, M. Stadelmaier³⁷, D. Stanca⁶⁸, S. Stanić⁷¹, J. Stasielak⁶⁴, P. Stassi³⁴, M. Stolpovskiy³⁴, A. Streich³⁶, M. Suárez-Durán²⁸, T. Sudholz¹², T. Suomijärvi³², A.D. Supanitsky⁸, J. Šupík³¹, Z. Szadkowski⁶⁶, A. Taboada³⁶, O.A. Taborda¹, A. Tapia²⁷, C. Timmermans^{77,75}, P. Tobiska³⁰, C.J. Todero Peixoto¹⁷, B. Tomé⁶⁷, G. Torralba Elipe⁷⁴, A. Travaini⁹, P. Travnicek³⁰, M. Trini⁷¹, M. Tueros⁴, R. Ulrich³⁷, M. Unger³⁷, M. Urban³⁹, J.F. Valdés Galicia⁶³, I. Valiño^{42,43}, L. Valore^{56,47}, A.M. van den Berg⁷⁶, A. van Vliet⁷⁵, E. Varela⁵⁹, B. Vargas Cárdenas⁶³, A. Vásquez-Ramírez²⁸, D. Veberic³⁷, C. Ventura²⁵, I.D. Vergara Quispe⁴, V. Verzi⁴⁸, J. Vicha³⁰, L. Villaseñor⁵⁹, J. Vink⁷⁹, S. Vorobiov⁷¹, H. Wahlberg⁴, A.A. Watson^a, M. Weber³⁸, A. Weindl³⁷, M. Wiedeński⁶⁶, L. Wiencke⁸¹, H. Wilczyński⁶⁴, T. Winchen¹⁴, M. Wirtz³⁹, D. Wittkowski³⁵, B. Wundheiler⁸, L. Yang⁷¹, A. Yushkov³⁰, E. Zas⁷⁴, D. Zavrtnik^{71,72}, M. Zavrtnik^{72,71}, L. Zehrer⁷¹, A. Zepeda⁶⁰, B. Zimmermann³⁷, M. Ziolkowski⁴¹, F. Zuccarello^{54,44}



- ¹ Centro Atómico Bariloche and Instituto Balseiro (CNEA-UNCuyo-CONICET), San Carlos de Bariloche, Argentina
- ² Centro de Investigaciones en Láseres y Aplicaciones, CITEDEF and CONICET, Villa Martelli, Argentina
- ³ Departamento de Física and Departamento de Ciencias de la Atmósfera y los Océanos, FCEyN, Universidad de Buenos Aires and CONICET, Buenos Aires, Argentina
- ⁴ IFLP, Universidad Nacional de La Plata and CONICET, La Plata, Argentina
- ⁵ Instituto de Astronomía y Física del Espacio (IAFE, CONICET-UBA), Buenos Aires, Argentina
- ⁶ Instituto de Física de Rosario (IFIR) – CONICET/U.N.R. and Facultad de Ciencias Bioquímicas y Farmacéuticas U.N.R., Rosario, Argentina
- ⁷ Instituto de Tecnologías en Detección y Astropartículas (CNEA, CONICET, UNSAM), and Universidad Tecnológica Nacional – Facultad Regional Mendoza (CONICET/CNEA), Mendoza, Argentina
- ⁸ Instituto de Tecnologías en Detección y Astropartículas (CNEA, CONICET, UNSAM), Buenos Aires, Argentina
- ⁹ Observatorio Pierre Auger, Malargüe, Argentina
- ¹⁰ Observatorio Pierre Auger and Comisión Nacional de Energía Atómica, Malargüe, Argentina
- ¹¹ Universidad Tecnológica Nacional – Facultad Regional Buenos Aires, Buenos Aires, Argentina
- ¹² University of Adelaide, Adelaide, S.A., Australia
- ¹³ Université Libre de Bruxelles (ULB), Brussels, Belgium
- ¹⁴ Vrije Universiteit Brussels, Brussels, Belgium
- ¹⁵ Centro Brasileiro de Pesquisas Físicas, Rio de Janeiro, RJ, Brazil

- 16 Centro Federal de Educação Tecnológica Celso Suckow da Fonseca, Nova Friburgo, Brazil
- 17 Universidade de São Paulo, Escola de Engenharia de Lorena, Lorena, SP, Brazil
- 18 Universidade de São Paulo, Instituto de Física de São Carlos, São Carlos, SP, Brazil
- 19 Universidade de São Paulo, Instituto de Física, São Paulo, SP, Brazil
- 20 Universidade Estadual de Campinas, IFGW, Campinas, SP, Brazil
- 21 Universidade Estadual de Feira de Santana, Feira de Santana, Brazil
- 22 Universidade Federal do ABC, Santo André, SP, Brazil
- 23 Universidade Federal do Paraná, Setor Palotina, Palotina, Brazil
- 24 Universidade Federal do Rio de Janeiro, Instituto de Física, Rio de Janeiro, RJ, Brazil
- 25 Universidade Federal do Rio de Janeiro (UFRJ), Observatório do Valongo, Rio de Janeiro, RJ, Brazil
- 26 Universidade Federal Fluminense, EEIMVR, Volta Redonda, RJ, Brazil
- 27 Universidad de Medellín, Medellín, Colombia
- 28 Universidad Industrial de Santander, Bucaramanga, Colombia
- 29 Charles University, Faculty of Mathematics and Physics, Institute of Particle and Nuclear Physics, Prague, Czech Republic
- 30 Institute of Physics of the Czech Academy of Sciences, Prague, Czech Republic
- 31 Palacky University, RCPTM, Olomouc, Czech Republic
- 32 Institut de Physique Nucléaire d'Orsay (IPNO), Université Paris-Sud, Univ. Paris/Saclay, CNRS-IN2P3, Orsay, France
- 33 Laboratoire de Physique Nucléaire et de Hautes Energies (LPNHE), Universités Paris 6 et Paris 7, CNRS-IN2P3, Paris, France
- 34 Univ. Grenoble Alpes, CNRS, Grenoble Institute of Engineering Univ. Grenoble Alpes, LPSC-IN2P3, 38000 Grenoble, France, France
- 35 Bergische Universität Wuppertal, Department of Physics, Wuppertal, Germany
- 36 Karlsruhe Institute of Technology, Institute for Experimental Particle Physics (ETP), Karlsruhe, Germany
- 37 Karlsruhe Institute of Technology, Institut für Kernphysik, Karlsruhe, Germany
- 38 Karlsruhe Institute of Technology, Institut für Prozessdatenverarbeitung und Elektronik, Karlsruhe, Germany
- 39 RWTH Aachen University, III. Physikalisches Institut A, Aachen, Germany
- 40 Universität Hamburg, II. Institut für Theoretische Physik, Hamburg, Germany
- 41 Universität Siegen, Fachbereich 7 Physik – Experimentelle Teilchenphysik, Siegen, Germany
- 42 Gran Sasso Science Institute, L'Aquila, Italy
- 43 INFN Laboratori Nazionali del Gran Sasso, Assergi (L'Aquila), Italy
- 44 INFN, Sezione di Catania, Catania, Italy
- 45 INFN, Sezione di Lecce, Lecce, Italy
- 46 INFN, Sezione di Milano, Milano, Italy
- 47 INFN, Sezione di Napoli, Napoli, Italy
- 48 INFN, Sezione di Roma "Tor Vergata", Roma, Italy
- 49 INFN, Sezione di Torino, Torino, Italy
- 50 Osservatorio Astrofisico di Torino (INAF), Torino, Italy
- 51 Politecnico di Milano, Dipartimento di Scienze e Tecnologie Aerospaziali, Milano, Italy
- 52 Università del Salento, Dipartimento di Matematica e Fisica "E. De Giorgi", Lecce, Italy
- 53 Università dell'Aquila, Dipartimento di Scienze Fisiche e Chimiche, L'Aquila, Italy
- 54 Università di Catania, Dipartimento di Fisica e Astronomia, Catania, Italy
- 55 Università di Milano, Dipartimento di Fisica, Milano, Italy
- 56 Università di Napoli "Federico II", Dipartimento di Fisica "Ettore Pancini", Napoli, Italy
- 57 Università di Roma "Tor Vergata", Dipartimento di Fisica, Roma, Italy
- 58 Università Torino, Dipartimento di Fisica, Torino, Italy
- 59 Benemérita Universidad Autónoma de Puebla, Puebla, México
- 60 Centro de Investigación y de Estudios Avanzados del IPN (CINVESTAV), México, D.F., México
- 61 Unidad Profesional Interdisciplinaria en Ingeniería y Tecnologías Avanzadas del Instituto Politécnico Nacional (UPIITA-IPN), México, D.F., México

- 62 Universidad Autónoma de Chiapas, Tuxtla Gutiérrez, Chiapas, México
- 63 Universidad Nacional Autónoma de México, México, D.F., México
- 64 Institute of Nuclear Physics PAN, Krakow, Poland
- 65 University of Łódź, Faculty of Astrophysics, Łódź, Poland
- 66 University of Łódź, Faculty of High-Energy Astrophysics, Łódź, Poland
- 67 Laboratório de Instrumentação e Física Experimental de Partículas – LIP and Instituto Superior Técnico – IST, Universidade de Lisboa – UL, Lisboa, Portugal
- 68 “Horia Hulubei” National Institute for Physics and Nuclear Engineering, Bucharest-Magurele, Romania
- 69 Institute of Space Science, Bucharest-Magurele, Romania
- 70 University Politehnica of Bucharest, Bucharest, Romania
- 71 Center for Astrophysics and Cosmology (CAC), University of Nova Gorica, Nova Gorica, Slovenia
- 72 Experimental Particle Physics Department, J. Stefan Institute, Ljubljana, Slovenia
- 73 Universidad de Granada and C.A.F.P.E., Granada, Spain
- 74 Instituto Galego de Física de Altas Enerxías (I.G.F.A.E.), Universidad de Santiago de Compostela, Santiago de Compostela, Spain
- 75 IMAPP, Radboud University Nijmegen, Nijmegen, The Netherlands
- 76 KVI – Center for Advanced Radiation Technology, University of Groningen, Groningen, The Netherlands
- 77 Nationaal Instituut voor Kernfysica en Hoge Energie Fysica (NIKHEF), Science Park, Amsterdam, The Netherlands
- 78 Stichting Astronomisch Onderzoek in Nederland (ASTRON), Dwingeloo, The Netherlands
- 79 Universiteit van Amsterdam, Faculty of Science, Amsterdam, The Netherlands
- 80 Case Western Reserve University, Cleveland, OH, USA
- 81 Colorado School of Mines, Golden, CO, USA
- 82 Department of Physics and Astronomy, Lehman College, City University of New York, Bronx, NY, USA
- 83 Louisiana State University, Baton Rouge, LA, USA
- 84 Michigan Technological University, Houghton, MI, USA
- 85 New York University, New York, NY, USA
- 86 Pennsylvania State University, University Park, PA, USA
- 87 University of Chicago, Enrico Fermi Institute, Chicago, IL, USA
- 88 University of Delaware, Department of Physics and Astronomy, Bartol Research Institute, Newark, DE, USA
- 89 University of Nebraska, Lincoln, NE, USA

^a School of Physics and Astronomy, University of Leeds, Leeds, United Kingdom

^b Max-Planck-Institut für Radioastronomie, Bonn, Germany

^c Fermi National Accelerator Laboratory, USA

^d also at Universidade Federal de Alfenas, Poços de Caldas, Brazil

^e Colorado State University, Fort Collins, CO, USA

^f now at Hakubi Center for Advanced Research and Graduate School of Science, Kyoto University, Kyoto, Japan

^g also at Karlsruhe Institute of Technology, Karlsruhe, Germany

^h also at Radboud University Nijmegen, Nijmegen, The Netherlands

Acknowledgments

The successful installation, commissioning, and operation of the Pierre Auger Observatory would not have been possible without the strong commitment and effort from the technical and administrative staff in Malargüe. We are very grateful to the following agencies and organizations for financial support:

Argentina – Comisión Nacional de Energía Atómica; Agencia Nacional de Promoción Científica y Tecnológica (ANPCyT); Consejo Nacional de Investigaciones Científicas y Técnicas (CONICET); Gobierno de la Provincia de Mendoza; Municipalidad de Malargüe; NDM Holdings and Valle Las Leñas; in gratitude for their continuing cooperation over land access; Australia – the Australian Research Council; Brazil – Conselho Nacional de Desenvolvimento Científico e Tecnológico (CNPq); Financiadora de Estudos e Projetos (FINEP); Fundação de Amparo à Pesquisa do Estado de Rio de Janeiro (FAPERJ); São Paulo Research Foundation (FAPESP) Grants No. 2010/07359-6 and No. 1999/05404-3; Ministério da Ciência, Tecnologia, Inovações e Comunicações (MCTIC); Czech Republic – Grant No. MSMT CR LTT18004, LO1305, LM2015038 and CZ.02.1.01/0.0/0.0/16_013/0001402; France – Centre de Calcul IN2P3/CNRS; Centre National de la Recherche Scientifique (CNRS); Conseil Régional Ile-de-France; Département Physique Nucléaire et Corpusculaire (PNC-IN2P3/CNRS); Département Sciences de l’Univers (SDU-INSU/CNRS); Institut Lagrange de Paris (ILP) Grant No. LABEX ANR-10-LABX-63 within the Investissements d’Avenir Programme Grant No. ANR-11-IDEX-0004-02; Germany – Bundesministerium für Bildung und Forschung (BMBF); Deutsche Forschungsgemeinschaft (DFG); Finanzministerium Baden-Württemberg; Helmholtz Alliance for Astroparticle Physics (HAP); Helmholtz-Gemeinschaft Deutscher Forschungszentren (HGF); Ministerium für Innovation, Wissenschaft und Forschung des Landes Nordrhein-Westfalen; Ministerium für Wissenschaft, Forschung und Kunst des Landes Baden-Württemberg; Italy – Istituto Nazionale di Fisica Nucleare (INFN); Istituto Nazionale di Astrofisica (INAF); Ministero dell’Istruzione, dell’Università e della Ricerca (MIUR); CETEMPS Center of Excellence; Ministero degli Affari Esteri (MAE); México – Consejo Nacional de Ciencia y Tecnología (CONACYT) No. 167733; Universidad Nacional Autónoma de México (UNAM); PAPIIT DGAPA-UNAM; The Netherlands – Ministry of Education, Culture and Science; Netherlands Organisation for Scientific Research (NWO); Dutch national e-infrastructure with the support of SURF Cooperative; Poland -Ministry of Science and Higher Education, grant No. DIR/WK/2018/11; National Science Centre, Grants No. 2013/08/M/ST9/00322, No. 2016/23/B/ST9/01635 and No. HARMONIA 5-2013/10/M/ST9/00062, UMO-2016/22/M/ST9/00198; Portugal – Portuguese national funds and FEDER funds within Programa Operacional Factores de Competitividade through Fundação para a Ciência e a Tecnologia (COMPETE); Romania – Romanian Ministry of Research and Innovation CNCS/CCCDI-UESFISCDI, projects PN-III-P1-1.2-PCCDI-2017-0839/19PCCDI/2018 and PN18090102 within PNCDI III; Slovenia – Slovenian Research Agency, grants P1-0031, P1-0385, I0-0033, N1-0111; Spain – Ministerio de Economía, Industria y Competitividad (FPA2017-85114-P and FPA2017-85197-P), Xunta de Galicia (ED431C 2017/07), Junta de Andalucía (SOMM17/6104/UGR), Feder Funds, RENATA Red Nacional Temática de Astropartículas (FPA2015-68783-REDT) and María de Maeztu Unit of Excellence (MDM-2016-0692); USA – Department of Energy, Contracts No. DE-AC02-07CH11359, No. DE-FR02-04ER41300, No. DE-FG02-99ER41107 and No. DE-SC0011689; National Science Foundation, Grant No. 0450696; The Grainger Foundation; Marie Curie-IRSES/EPLANET; European Particle Physics Latin American Network; and UNESCO.

Contributions

1	Energy Spectrum	8
1.1	Valerio Verzi: <i>Measurement of the energy spectrum of ultra-high energy cosmic rays using the Pierre Auger Observatory</i>	9
1.2	Alan Coleman: <i>Measurement of the cosmic ray flux near the second knee with the Pierre Auger Observatory</i>	17
1.3	Vladimír Novotný: <i>Measurement of the spectrum of cosmic rays above $10^{16.5}$ eV with Cherenkov-dominated events at the Pierre Auger Observatory</i>	25
1.4	Jonas Glombitza: <i>Air-Shower Reconstruction at the Pierre Auger Observatory based on Deep Learning</i>	33
1.5	Bruce R. Dawson: <i>The Energy Scale of the Pierre Auger Observatory</i>	41
1.6	Daniela Mockler: <i>Reconstruction of Vertical Events Recorded by the Surface Detector of the Pierre Auger Observatory</i>	49
2	Arrival Directions and Anisotropies	57
2.1	Marcus Wirtz: <i>Search for magnetically-induced signatures in the arrival directions of ultra-high energy cosmic rays measured by the Pierre Auger Observatory</i>	58
2.2	Esteban Roulet: <i>Large-scale anisotropies above 0.03 EeV measured by the Pierre Auger Observatory</i>	66
2.3	Lorenzo Caccianiga: <i>Anisotropies of the highest energy cosmic-ray events recorded by the Pierre Auger Observatory in 15 years of operation</i>	74
3	Nuclear mass composition, photons, and neutrinos	82
3.1	Alexey Yushkov: <i>Mass composition of cosmic rays with energies above $10^{17.2}$ eV from the hybrid data of the Pierre Auger Observatory</i>	83
3.2	Carlos José Todero Peixoto: <i>Estimating the Depth of Shower Maximum using the Surface Detectors of the Pierre Auger Observatory</i>	91
3.3	Michael Schimp: <i>Follow-up searches for ultra-high energy neutrinos from transient astrophysical sources with the Pierre Auger Observatory</i>	99
3.4	Francisco Pedreira: <i>Bounds on diffuse and point source fluxes of ultra-high energy neutrinos with the Pierre Auger Observatory</i>	107
3.5	Julian Rautenberg: <i>Limits on ultra-high energy photons with the Pierre Auger Observatory</i>	115
4	Hadronic Interactions and Shower Physics	123

4.1	Federico Sánchez: <i>The muon component of extensive air showers above $10^{17.5}$ eV measured with the Pierre Auger Observatory</i>	124
4.2	Felix Riehn: <i>Measurement of the fluctuations in the number of muons in inclined air showers with the Pierre Auger Observatory</i>	132
5	Cosmology and Geophysics	140
5.1	Rodrigo Guedes Lang: <i>Testing Lorentz Invariance Violation at the Pierre Auger Observatory</i>	141
5.2	Roberto Mussa: <i>ELVES reconstruction and characterization at the Pierre Auger Observatory</i>	149
5.3	Martin Schimassek: <i>Analysis of Data from the Low-energy Modes of the Surface Detector of the Pierre Auger Observatory</i>	157
6	Detectors and AugerPrime Upgrade	165
6.1	Violet M. Harvey: <i>Real-time Measurements with Atmospheric Instruments at the Pierre Auger Observatory</i>	166
6.2	Koun Choi: <i>Long Term Performance of the Pierre Auger Observatory</i>	174
6.3	Álvaro Taboada: <i>Analysis of Data from Surface Detector Stations of the AugerPrime Upgrade</i>	182
6.4	Marvin Gottowik: <i>Measurements of Inclined Air Showers with the Auger Engineering Radio Array at the Pierre Auger Observatory</i>	190
6.5	Ana Martina Botti: <i>The AMIGA underground muon detector of the Pierre Auger Observatory – performance and event reconstruction</i>	198
6.6	Bjarni Pont: <i>A Large Radio Detector at the Pierre Auger Observatory – Measuring the Properties of Cosmic Rays up to the Highest Energies</i>	206
6.7	Dave Nitz: <i>New Electronics for the Surface Detectors of the Pierre Auger Observatory</i> . . .	214
6.8	Martina Boháčová: <i>Test benches for the upgrade of the Pierre Auger Observatory electronics</i>	222
6.9	Jan Peřkala: <i>Production and Quality Control of the Scintillator Surface Detector for the AugerPrime Upgrade of the Pierre Auger Observatory</i>	230
7	Outreach	238
7.1	Beatriz García: <i>Social Impact of Outreach at the Pierre Auger Observatory</i>	239

1

Energy Spectrum





Measurement of the energy spectrum of ultra-high energy cosmic rays using the Pierre Auger Observatory

Valerio Verzi^{*a} for the Pierre Auger Collaboration^{b†}

^a*Sezione INFN Roma "Tor Vergata", via della Ricerca Scientifica 1, 00133 Roma, Italy*

^b*Observatorio Pierre Auger, Av. San Martín Norte 304, 5613 Malargüe, Argentina*

E-mail: auger_spokespersons@fnal.gov

Full author list: http://www.auger.org/archive/authors_icrc_2019.html

The energy spectrum of ultra-high energy cosmic rays measured using the Pierre Auger Observatory is presented. The measurements benefit from the huge exposure of approximately 80000 km² sr yr achieved in 14 years of data taking with a surface-detector array that extends over 3000 km² having 1600 detectors on a 1500 m spacing, and from the almost-calorimetric estimation of the energy scale provided by the fluorescence detector. In this contribution, we address recent improvements in the measured spectrum at energies above 3 EeV using events with zenith angles less than 60°. These improvements concern the estimation of the shower energy and its resolution. Further, we report on updates of the energy spectra derived from other independent and complementary data sets, namely from showers with larger zenith angles, those detected by a smaller and denser array with 750 m spacing, and those detected by the fluorescence detector, together with the recent extension of the flux measurements to lower energies using atmospheric Cherenkov radiation.

36th International Cosmic Ray Conference — ICRC2019

24 July – 1 August, 2019

Madison, Wisconsin, USA

^{*}Speaker.

[†]for collaboration list see PoS(ICRC2019)1177

1. Introduction

The Pierre Auger Observatory [1] is located in a region called *Pampa Amarilla*, near the small town of Malargüe in the province of Mendoza (Argentina) at a latitude of about 35.2° S and an altitude of 1400 m above sea level. The Observatory, completed in 2008, is a hybrid system, a combination of a large surface detector (SD) and a fluorescence detector (FD).

The SD comprises 1660 water-Cherenkov detectors (WCD) laid out on a 1500 m triangular grid, covering an area of about 3000 km^2 , and an additional 61 detectors covering 23.5 km^2 on a 750 m grid. The FD consists of 4×6 telescopes placed in four locations on the perimeter of the site (also called *eyes*) that detect the fluorescence light emitted during the shower development. Each telescope has a field of view of $30^\circ \times 30^\circ$ with a minimum elevation of 1.5° above the horizon. Three additional telescopes, the High Elevation Auger Telescopes (HEAT), cover an elevation up to 60° to detect low-energy showers in coincidence with the 750 m array. The FD may operate only in clear moonless nights and therefore with an on-time of about 13%.

The main advantage of a hybrid system is that the energy scale of the Observatory can be set with the FD measurements that provide an almost calorimetric estimate of the shower energy. This allows us to measure the energy spectrum with the high efficiency of the SD and with an energy estimation which is largely independent of air shower simulations and of assumptions on hadronic interaction models.

In this contribution we present the energy spectrum measured at the Pierre Auger Observatory using an exposure of about $80000 \text{ km}^2 \text{ sr yr}$. First we describe the recent improvements in the spectrum measured with the 1500 m array using events with zenith angles (θ) less than 60° . We then report on updates of the energy spectra derived from other independent and complementary data sets. In comparison to our previous publication [2], the energy threshold above which we measure the spectrum is lowered by one decade down to $10^{16.5} \text{ eV}$. We will present the spectral features in the full energy range, from $10^{16.5} \text{ eV}$ up to the suppression of the flux at the highest energies.

2. The energy spectrum from the 1500 m array using events with $\theta < 60^\circ$

The reconstruction of events detected by the 1500 m array with zenith angles less than 60° is described in [3]. The shower size and core position are estimated by fitting to the data a modified Nishimura-Kamata-Greisen lateral distribution function (LDF) with slope parameters determined from data which are a function of the shower size and zenith angle. The shower size is the signal at 1000 m from the core in the plane of the shower front ($S(1000)$). $S(1000)$ is the optimal energy estimator for a grid spacing of 1500 m because it minimises the uncertainties of the signal due to limited knowledge of the LDF in individual events [4]. $S(1000)$ is measured in units of vertical equivalent muon (VEM). 1 VEM corresponds to the signal released by a muon traversing the tank vertically and it is measured for each WCD every 60 s [1].

For a given energy, the value of $S(1000)$ decreases with the zenith angle because of the increasing atmospheric depth crossed by the shower. Given the highly isotropic flux, the shape of the attenuation curve can be inferred from data using the Constant Intensity Cut (CIC) method [5]. The curve is parameterised with a third degree polynomial in terms of the variable $x = \cos^2 \theta - \cos^2 38^\circ$,

where $S(1000) = S_{38}(1 + ax + bx^2 + cx^3)$. S_{38} is the zenith-angle independent energy estimator and can be thought of as the signal, $S(1000)$, that the shower would have produced at a zenith angle of 38° . In our previous publication [2] the coefficients a , b and c were calculated at a fixed intensity threshold (number of events per steradian above a given $S(1000)$ threshold). In figure 1 we show how the shape of the attenuation curves are slightly different for different intensity thresholds. Thus, to obtain a more precise energy estimator, for the measurements presented in this paper, the CIC is calculated at different thresholds. In practice, the energy dependence of the CIC curve is accounted for by expressing the coefficients a , b and c with a second degree polynomial in the variable $k = \log_{10}(S_{38}/40 \text{ VEM})$, i.e. $y = \sum_l^{[0,2]} y_l k^l$. The value of the coefficients (y_0, y_1, y_2) are: $(0.952, 0.0587, -0.370)$ for a , $(-1.636, -0.425, 0.087)$ for b and $(-0.978, -0.041, 1.335)$ for c . The parameterisation is valid for S_{38} between 15 VEM and 120 VEM. Outside this range, we use the coefficients calculated on the boundaries of the validity range.

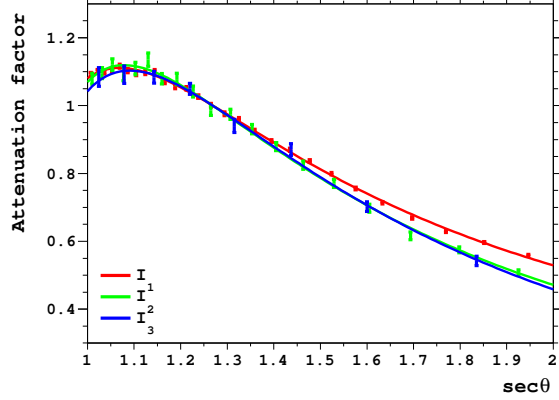


Figure 1: Attenuation curves as a function of $\sec \theta$ normalised to 1 for $\theta = 38^\circ$ for the three different intensity thresholds that correspond approximatively to the energies 3 EeV (I_1), 8 EeV (I_2) and 20 EeV (I_3).

The calibration of S_{38} against the calorimetric energy E_{FD} is obtained by analysing the so called *hybrid* events, that are a subset of SD events where the FD was triggered independently. The reconstruction of the FD events is described in [1] and provides an estimation of the calorimetric energy of the showers (E_{cal}). The total shower energy (E_{FD}) is obtained by adding to E_{cal} an *invisible energy* correction that accounts for the energy carried into the ground by high-energy muons and neutrinos. This correction is estimated by exploiting the sensitivity of the WCDs to muons with an analysis that minimises the uncertainties arising from the hadronic interaction models and the primary mass composition [6]. The *hybrid* events are selected to guarantee a precise estimation of the FD energies and to minimise biases from the mass distribution of the cosmic rays introduced by the field of view of the FD telescopes [6]. The calibration is performed by selecting events with $E_{FD} > 3 \times 10^{18}$ eV to guarantee a nearly 100% trigger efficiency of the SD array [7]. The correlation between the FD energies and S_{38} of 3338 events selected from the data collected between 1 January 2004 to 31 December 2017 is shown in figure 2. The correlation is well described by a simple power-law relationship $E = A S_{38}^B$ where the two parameters A and B are fitted to the data. For the fit we use a maximum-likelihood method where the probability density function is given by a bootstrap estimate of the energy distribution of the selected events and where the uncertainties in S_{38} and FD energy [8] are evaluated on an event-by-event basis. The uncertainties in S_{38} are defined by considering the error from the $S(1000)$ fit [3] and shower-to-shower fluctuations (they amount to about 13% – 7%, lower at higher energies). The latter are estimated by subtracting from the total SD energy resolution (which will be presented later) the errors from the $S(1000)$ fit. The best fit parameters are

$A = (0.186 \pm 0.003)$ EeV and $B = 1.031 \pm 0.004$ and the correlation coefficient between them is $\rho = -0.98$. The resulting calibration curve is shown as the red line in figure 2. The highest-energy event is detected by all four FD *eyes*. Its energy is $(8.5 \pm 0.4) \times 10^{19}$ eV, obtained from a weighted average of the four calorimetric energies and using the resulting energy to evaluate the invisible energy correction [6]. The corresponding SD energy obtained from S_{38} using the calibration parameters is $(7.9 \pm 0.6) \times 10^{19}$ eV, in good agreement with the FD energy.

The parameters A and B define the energy scale of the 1500 m array and are used to estimate the energy for the bulk of SD events. The systematic uncertainty in the energy scale is 14% [9]. It is approximately constant with energy, being dominated by the uncertainty in the absolute calibration of the FD telescopes, and benefits from the high precision measurement

of the fluorescence yield made by the AIRFLY experiment [10]. After the major revision of the energy scale that was presented in 2013 [9], the Auger Collaboration has made several checks and improvements in the estimation of the FD energies. The results of these activities are reported in [8] and no effect has been discovered that contradicts the estimation of the systematic uncertainties addressed in [9].

The estimation of the differential energy spectrum is done by counting the number of SD events N_i in differential bins centered at energy E_i with equal-size width in decimal logarithm $\Delta \log E_i = 0.1$:

$$J = f(E_i) J_{\text{raw}} = f(E_i) \frac{N_i}{\mathcal{E} \Delta E_i} \quad (2.1)$$

where \mathcal{E} is the exposure, $f(E_i)$ accounts for resolution effects responsible for a bin-to-bin event migration and J_{raw} is the estimation of the spectrum neglecting the resolution effects. The spectrum J is estimated by selecting events in which the WCD with the highest signal is enclosed in a hexagon of six active stations and requiring that the events have an energy larger than $10^{18.4}$ eV and zenith angle less than 60° . In this way the trigger efficiency is larger than 97% and the calculation of the exposure reduces to a geometrical calculation plus knowledge of the live-time of the array [7]. For the analysis presented in this paper, we use 215030 events among those collected from 1 January 2004 to 31 August 2018 with an accumulated exposure of $\mathcal{E} = (60400 \pm 1800)$ km² sr yr, 17% higher than the one used for our previous publication [2].

The estimation of the correction factor, $f(E_i)$, needs knowledge of the resolution in SD energies. Moreover, to account for the migration of the events with energy below the threshold for the saturation of the trigger efficiency, one has to know the trigger efficiency as a function of energy and zenith angle as well as the bias affecting E_{SD} . In fact, when the array is not fully efficient, we

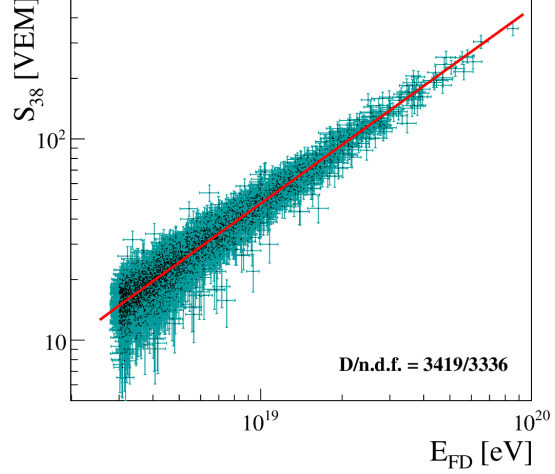


Figure 2: Correlation between the FD energies and S_{38} . Each event is shown with a point together with its individual uncertainties. The line is the best fit calibration curve.

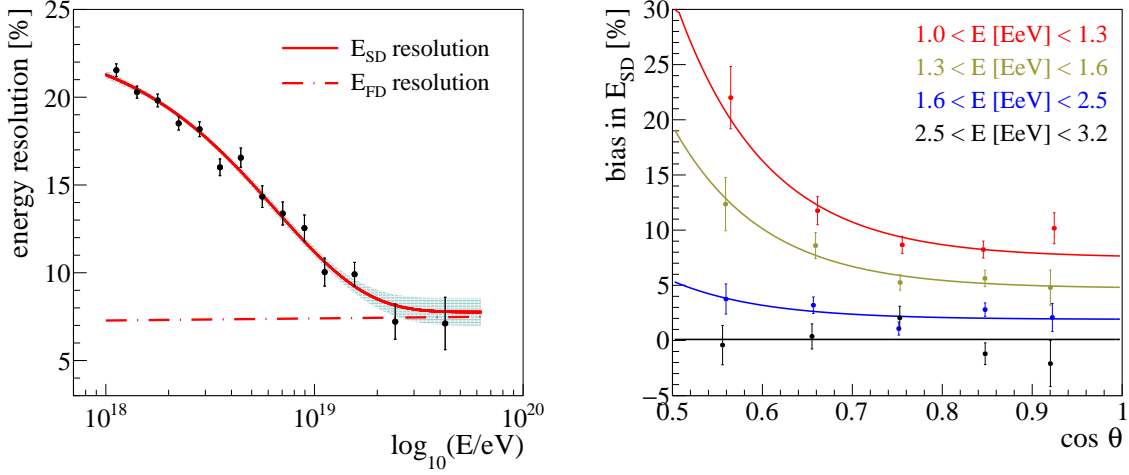


Figure 3: Energy resolution and bias for SD events estimated from hybrid data.

preferably trigger on events with upward fluctuations of muons that lead to higher values of S_{38} and thus to an overestimation of the shower energy. For the measurement presented in this paper all the ingredients needed to calculate $f(E_i)$ are inferred from an analysis of the hybrid data with energy $E_{FD} > 10^{18}$ eV. The trigger efficiency is estimated following the approach described in [11]. It is parametrised with the error function $1/2 \{1 + \text{erf}[(\log_{10} E - p_0)/p_1]\}$ where $p_1 = 0.373$ and p_0 is a third degree polynomial in terms of $k = \cos^2 \theta$ ($p_0 = \sum_l^{[0,3]} y_l k^l$) with coefficients $(y_0, y_1, y_2, y_3) = (18.63, -3.18, 4.38, -1.87)$. The resolution and bias are estimated by studying the distributions of E_{SD}/E_{FD} in different energy and zenith angle bins. The distributions are fitted to a Gaussian ratio distribution leaving as free parameters the resolution and bias in E_{SD} and fixing the resolution in E_{FD} to about 7.4% [8]. The results of the analysis are presented in figure 3. The resolution in SD energies is approximately zenith-angle independent and it is parametrised with the functional form $0.078 + 0.16 \exp(-0.15 E/\text{EeV})$. It is estimated with a relative systematic uncertainty ranging from 5% to 15% (larger at higher energies). The energy bias below $E_b = 2.5 \times 10^{18}$ eV is parametrised with the function $\{0.20 + 0.59 \exp[-10 (\cos \theta - 0.5)]\} \log_{10}(E_b/E)$. Above E_b the bias is 0.

The correction factor, $f(E_i)$, is estimated with a "forward folding" technique: we make a fit of J_{raw} assuming an empirical functional shape for the spectrum defined by a set of free parameters and calculating the bin-to-bin migration matrix due to resolution effects. At the end of the fit $f(E_i)$ is given by the ratio of the input spectrum to the convoluted one. The optimal functional shape can be inferred by looking at the raw energy spectrum. The latter multiplied by E_i^3 is shown in the left panel of figure 4. J_{raw} shows a dip centered at about 5×10^{18} eV (a feature called the *ankle*) and an abrupt suppression at the highest energies. A better description of the shape of the spectrum can be obtained by considering the following two functional forms:

$$J_{12\Delta} \propto E^{-\gamma} \frac{1 + (E/E_{12})^{\gamma_1}}{1 + (E/E_{12})^{\gamma_2}} \frac{1}{1 + (E/E_{2\Delta})^{\Delta\gamma}} \quad (2.2)$$

$$J_{1234} \propto E^{-\gamma} \frac{1 + (E/E_{12})^{\gamma_1}}{1 + (E/E_{12})^{\gamma_2}} \frac{1 + (E/E_{23})^{\gamma_2}}{1 + (E/E_{23})^{\gamma_3}} \frac{1 + (E/E_{34})^{\gamma_3}}{1 + (E/E_{34})^{\gamma_4}} \quad (2.3)$$

where the first terms common to the two functions define a smooth transition between the two power laws around the *ankle*. The other terms define the transition at the highest energies: a smooth suppression with fixed curvature with $J_{12\Delta}$ [2] and two additional transitions between power laws with J_{1234} . Thanks to the high quality of the data and the huge statistics of events collected at the Observatory, one can qualitatively appreciate that the data are better described by J_{1234} . Therefore we use this function to perform the "forward folding". The raw spectrum and the one corrected for resolution effects are shown in the right panel of figure 4. They are very similar with a difference that is about 9% close to 3×10^{18} eV, decreasing to below 2% at 10^{19} eV and slightly increasing up to 5% at the highest energies. The corrections for resolution effects are small and do not change significantly the shape of the spectrum that is captured by J_{1234} . The same outcome is attained if the "forward folding" is done with $J_{12\Delta}$. Finally, we have verified that the small energy-dependent systematic uncertainties affecting $S(1000)$ [3] do not impact the conclusion that the shape of the spectrum is better described by the J_{1234} function rather than by $J_{12\Delta}$.

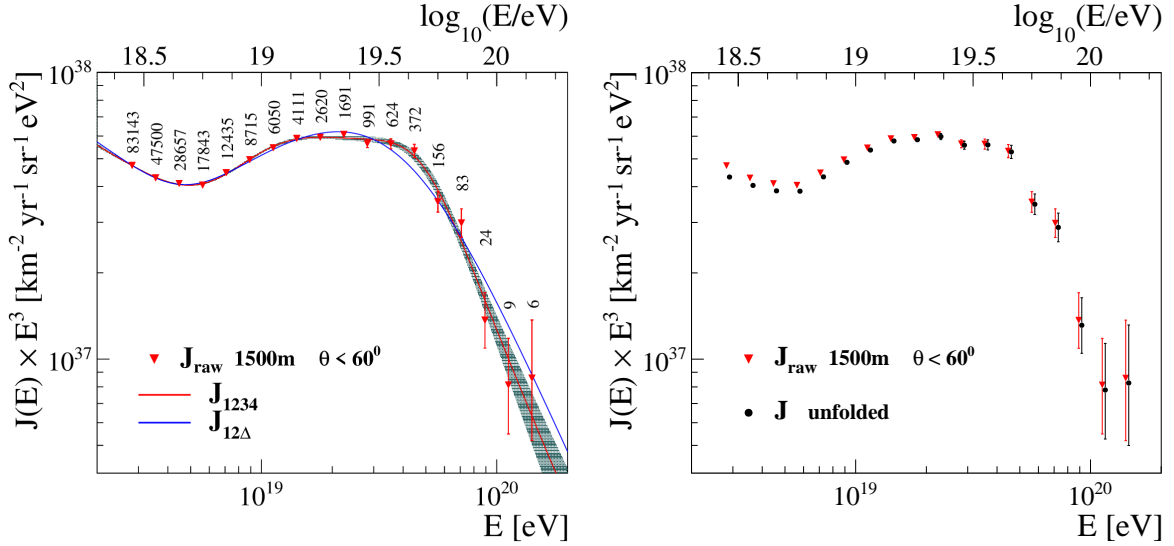


Figure 4: Left panel: raw energy spectrum together with the results of the fit using the two functional forms addressed in the text. Right panel: raw spectrum and the one corrected for resolution effects.

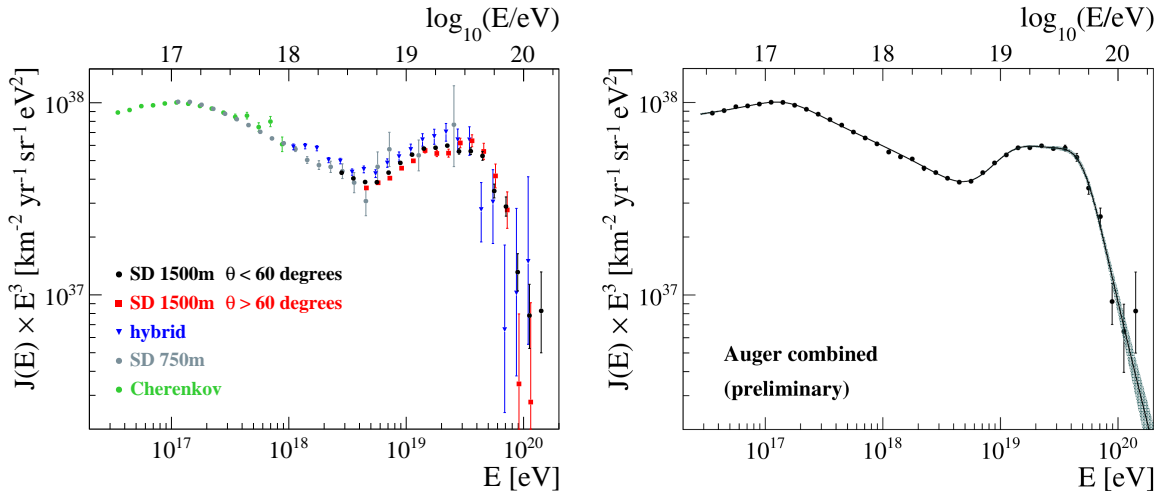
The huge accumulated exposure allows us to measure the spectrum precisely in different declination bands. The results of the studies are reported in [13] and show that the spectrum does not have any significant declination dependence.

3. Other measurements of the energy spectrum

The energy spectrum is measured at the Observatory using several independent and complementary data sets. At the highest energies, we increase the SD exposure for events with $\theta < 60^\circ$ by about 30% by analysing the events detected at larger zenith angles ($60^\circ < \theta < 80^\circ$). In these events, the signals detected by the WCDs are dominated by muons and the energy estimator is given by a normalisation factor of simulated muon density maps that is fitted to the data and calibrated against the FD energies. The spectrum is measured in the energy region where the array is fully efficient ($E_{SD} > 4 \times 10^{18}$ eV) and using a data-driven approach similar to the one applied to the events with

Table 1: Relevant parameters of the data samples used to measure the energy spectrum.

	1500 m $\theta < 60^\circ$	1500 m $\theta > 60^\circ$	750 m	Hybrid	Cherenkov
data taking period	01/2004-08/2018	01/2004-08/2018	01/2014-08/2018	01/2007-12/2017	06/2012-12/2015
exposure [km ² sr yr]	60426	17447	105.4	2248 at 10 ¹⁹ eV	2.86 at 10 ¹⁷ eV
number of events	215030	24209	569285	13655	69793
zenith angle range [°]	0 - 60	60 - 80	0 - 40	0 - 60	0 - 85
energy threshold [eV]	10 ^{18.4}	10 ^{18.6}	10 ¹⁷	10 ¹⁸	10 ^{16.5}
energy resolution [%] (from low to high E)	18 - 8	22 - 10	22 - 8	7.4	18
calibration parameters					
number of events	3338	393	1179		
A [EeV]	0.186 ± 0.003	5.51 ± 0.07	0.0132 ± 0.0004		
B	1.031 ± 0.004	1.04 ± 0.02	1.006 ± 0.009		

**Figure 5:** Energy spectra measured using the Pierre Auger Observatory (left) and spectrum obtained combining the different measurements (right).

$\theta < 60^\circ$ (see also [11]). Another measurement of the spectrum is obtained by analysing the hybrid events detected by the FD simultaneously with at least one WCD. The measurement benefits from the high precision in the FD energy estimation and is made selecting events with energy $> 10^{18}$ eV. The exposure is calculated using a full time-dependent simulation of the hybrid events and detector response [12].

The spectrum measurements are extended to lower energies using the 750 m array. Thanks to the implementation of a new trigger algorithm at the WCD level, in comparison to our previous publication [2], we have been able to lower the energy threshold by half a decade down to 10¹⁷ eV [14]. This measurement is unique of its kind, similar to the one performed with the 1500 m array, because it is done with an array in the regime of full trigger efficiency and using a fully data-driven approach. Finally, as pioneered by the Telescope Array [15], for the first time we show the spectrum derived using the events detected by HEAT in which the observed light is dominated by Cherenkov radiation. This allows us to lower the energy threshold to 10^{16.5} eV [16] and, together with the 750 m spectrum, to precisely study the spectral features around 10¹⁷ eV.

The parameters used to define the various spectra are detailed in table 1 and the measured spectra multiplied by E_i^3 are shown in the left panel of figure 5. The spectrum obtained by com-

binning the five measurements is shown in the right panel of figure 5. The combined spectrum is obtained through shifting by +5% and −9% the normalisations of the 1500 m $\theta > 60^\circ$ and the hybrid spectra, respectively, and by −1% those both the 750 m and Cherenkov spectra, while the shift for the 1500 m $\theta < 60^\circ$ spectrum is negligible. A fit to the data is performed using an extension of the function (2.3) that includes the smooth change of the spectral index around 10^{17} eV

$$J_{01234} \propto E^{-\gamma_0} \frac{1 + (E/E_{01})^{\gamma_0}}{1 + (E/E_{01})^{\gamma_1}} \frac{1 + (E/E_{12})^{\gamma_1}}{1 + (E/E_{12})^{\gamma_2}} \frac{1 + (E/E_{23})^{\gamma_2}}{1 + (E/E_{23})^{\gamma_3}} \frac{1 + (E/E_{34})^{\gamma_3}}{1 + (E/E_{34})^{\gamma_4}}. \quad (3.1)$$

The fitted functional form is shown with a black line superimposed to the data. The fitted parameters are: $E_{01} = (0.15 \pm 0.02) \times 10^{18}$ eV, $E_{12} = (6.2 \pm 0.9) \times 10^{18}$ eV, $E_{23} = (12 \pm 2) \times 10^{18}$ eV, $E_{34} = (50 \pm 7) \times 10^{18}$ eV, $\gamma_0 = 2.92 \pm 0.05$, $\gamma_1 = 3.27 \pm 0.05$, $\gamma_2 = 2.2 \pm 0.2$, $\gamma_3 = 3.2 \pm 0.1$ and $\gamma_4 = 5.4 \pm 0.6$, where the errors include the statistical and systematic uncertainties. The data show with high significance two inflection points commonly called the *second-knee* and the *ankle*, an indication of a further point of inflection as already addressed in section 2, and the abrupt suppression at the highest energies.

References

- [1] The Pierre Auger Collaboration, Nucl. Instrum. Meth. A **798** (2015) 172.
- [2] F. Fenu, for the Pierre Auger Collaboration, Proc. of 35th Int. Cosmic Ray Conf., Bexco, Busan, Korea, PoS(ICRC2017)486.
- [3] D. Mockler, for the Pierre Auger Collaboration, these proceedings, PoS(ICRC2019)353.
- [4] D. Newton, J. Knapp and A. A. Watson, Astropart. Phys. **26** (2007) 414.
- [5] J. Hersil *et al.*, Phys. Rev. Lett. **6** (1961) 22.
- [6] The Pierre Auger Collaboration, submitted to PRD (2019).
- [7] The Pierre Auger Collaboration, Nucl. Instrum. Meth. A **613** (2010) 29.
- [8] B. Dawson, for the Pierre Auger Collaboration, these proceedings, PoS(ICRC2019)231.
- [9] V. Verzi, for the Pierre Auger Collaboration, Proc. of 33rd Int. Cosmic Ray Conf., Rio de Janeiro, Brazil (2013) [arXiv:1307.5059].
- [10] M. Ave *et al.*, Astropart. Phys. **42** (2013) 90.
- [11] The Pierre Auger Collaboration, JCAP **08** (2015) 049.
- [12] The Pierre Auger Collaboration, Astropart. Phys. **34** (2011) 368.
- [13] O. Deligny, for the Pierre Auger and Telescope Array Collaborations, these proceedings, PoS(ICRC2019)234.
- [14] A. Coleman, for the Pierre Auger Collaboration, these proceedings, PoS(ICRC2019)225.
- [15] R. U. Abbasi *et al.*, Astrophys. J. **865** (2018) no.1, 74.
- [16] V. Novotny, for the Pierre Auger Collaboration, these proceedings, PoS(ICRC2019)374.



Measurement of the cosmic ray flux near the second knee with the Pierre Auger Observatory

Alan Coleman^{*a} for the Pierre Auger Collaboration^{b†}

^a*Bartol Research Institute, Dept. of Phys. & Astro., University of Delaware, Newark, DE, USA*

^b*Observatorio Pierre Auger, Av. San Martín Norte 304, 5613 Malargüe, Argentina*

E-mail: auger_spokespersons@fnal.gov

Full author list: *Pierre Auger Collaboration and additional author(s):*

http://www.auger.org/archive/authors_icrc_2019_b.html

We present the first measurement of the energy spectrum of cosmic rays down to 100 PeV from the Pierre Auger Observatory using the part of the surface-detector array with 750 m spacing. This analysis is made possible by a set of additional particle triggers, installed in 2013, which lowers the threshold above which the array is fully efficient by half an order of magnitude. The measurement thus covers a critical energy range around 10^{17} eV where previous observations have shown a change in the spectral index, the so-called second or iron knee. The work relies on a geometrical exposure, a nearly 100% duty cycle, and an almost model-independent analysis, with the energy estimation provided by the fluorescence detector. We discuss the spectrum and the associated uncertainties and compare the results to other studies in the same energy range.

36th International Cosmic Ray Conference — ICRC2019

24 July – 1 August, 2019

Madison, Wisconsin, USA

^{*}Speaker.

[†]for collaboration list see PoS(ICRC2019)1177

1. Introduction

The cosmic ray flux spectrum is one of the cornerstone measurements within the field of astroparticle physics. The small irregularities in its shape indicate regions of transition over which the types of particles, classes of sources, propagational effects, etc. are likely changing. Thus, an understanding of the environments in which the highest energy particles in the universe are being accelerated can be directly enhanced by precise measurements of the shape of the energy spectrum.

While the three most notable features of the energy spectrum above TeV energies are the so-called *knee* (at $\sim 10^{15.5}$ eV), *ankle* (at $\sim 10^{18.7}$ eV), and suppression (at $> 10^{20}$ eV), other inflection points have been identified through recent high-statistics measurements. Of most interest to this work is the *second-knee* at roughly 10^{17} eV. The second knee corresponds to an observed hardening/softening for light/heavy elements [1–3] and an overall steepening of the all-particle flux [4–9]. This work focuses on the first measurement of the softening of the all-particle spectrum by the Pierre Auger Observatory [10] via an extension to lower energies than previously possible.

2. Improvements to Cosmic Ray Detection at Auger

Covering over 3000 km^2 , Auger is the world’s largest cosmic ray detector located in the Mendoza province of Argentina. The observatory’s design consists of a hybrid detection scheme which includes both a fluorescence detector (FD) and a surface detector (SD). The FD telescopes are situated on hills at the edge of the observatory and directly image the nitrogen fluorescence light emitted by air molecules which become excited by the developing shower front. In this way, the FD can make nearly calorimetric measurements of the electromagnetic component of air showers and thus set the energy scale for the observatory [11]. On the ground, the secondary particles are observed by the SD which is comprised of around 1600 water-Cherenkov detectors (WCDs), arranged in a hexagonal grid with 1500 m spacing. Nested within this array is a low-energy extension to the SD which is comprised of identical detectors but with half the grid-spacing, 750 m. The measurements of air showers by the the 750 m array from January 2014 to August 2018 are the focus of this work.

The acquisition system for the SD [10] relies on a 5-level trigger hierarchy. At the station-level (i.e. for individual WCDs), the T1 and T2 triggers are used to determine when the measured signal in a station is likely the result of air shower particles. Similarly, at the array-level, the triggers (T3, T4, and T5) are used to classify when configurations of T1/T2-triggered stations are consistent with an air shower footprint. A complete description of the triggers can be found in [10].

In 2014, after a decade of SD observations, two new station-level triggers, called Time Over Threshold Deconvolved (TOTd) and Multiplicity of Positive Steps (MoPS), were added to the existing T2 triggers. TOTd and MoPS were designed to be mostly sensitive to the low-energy electromagnetic component of air showers and insensitive to the muons which make up the dominant background for individual WCDs. In practice this is done by identifying the low-amplitude, long-duration waveforms which result from electromagnetic particles entering the water and rejecting the short spikes caused by single muons. The inclusion of these triggers into the hierarchy directly increases the SD’s sensitivity to the low-energy component of air showers, far from the central axis. The distribution of deposited charge in individual WCDs is shown in the left plot of figure

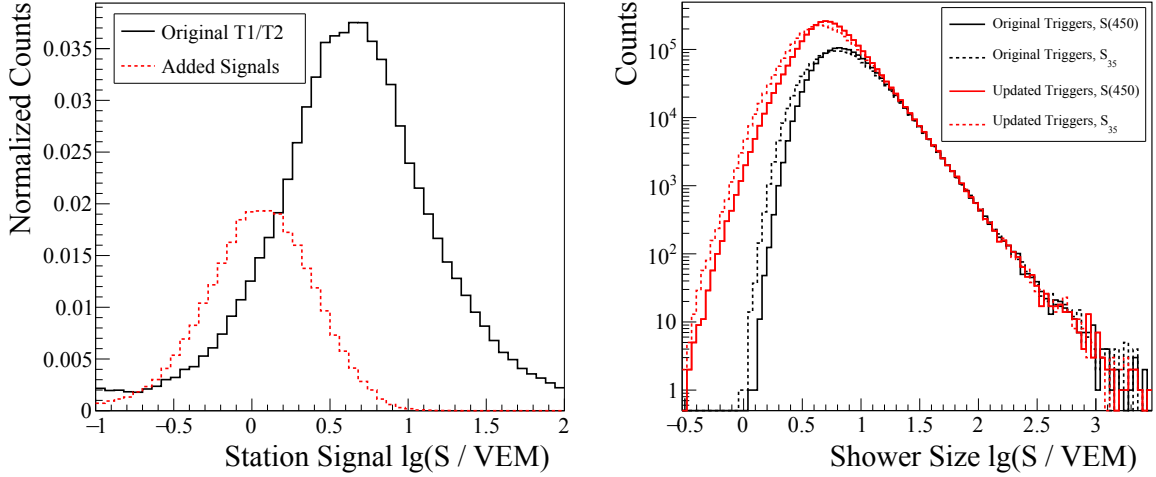


Figure 1: Left: Measured distribution of deposited charge in stations which pass the original T1/T2 algorithms (solid black) and those that pass the new algorithms (red dashed). Right: The observed shower sizes using the full T1/T2 trigger set (red) versus using only the original (black) is shown. Both the raw shower sizes (solid lines) and bias-corrected (dashed lines) are included, see text.

1 in units of Vertical Equivalent Muons¹ (VEM). The signal sizes that can be measured with only the original T1/T2 trigger set is shown in solid black. The dashed red line shows the added signal sizes that are now accessible via the TOTd and MoPS triggers.

The philosophy of the SD reconstruction using the updated trigger set is unchanged with respect to previous SD analyses. First an event cleaning is performed to remove stations which are likely to have been triggered by coincident, background particles. Next, the shower direction is determined using the start times of the signals in the stations. The final step is a fit of the lateral distribution of signals using an empirically chosen lateral distribution function, in this case, a log-log parabola. From this fit, a first-order energy estimator, sometimes referred to as a *shower size*, is chosen to be the signal that would be expected to be measured at a reference distance² of 450 m from the shower axis, $S(450)$. For a more detailed description of the reconstruction process, see [13].

Following the reconstruction, two corrections are applied to the $S(450)$ values. The first is an atmospheric correction which accounts for the changing weather conditions at the Observatory. The changes in local air pressure and density affect the measurements of the shower sizes on the ground. Thus, the $S(450)$ values are scaled to what one would expect to observe had the showers developed in an atmosphere with the average pressure and density measured at Auger, see [14].

A second correction is applied to the $S(450)$ values using a constant intensity cut (CIC) [15]. This corrects for the increased attenuation, and thus smaller observed $S(450)$ values, of showers that arrive at higher inclinations. The CIC rescales the energy estimator to that which would have been measured had the shower arrived at a zenith angle of 35° , S_{35} . See [17] for more information.

The increase in sensitivity of the array to lower energy showers can be seen in the right plot of

¹One VEM is defined to be the average amount of signal that would be measured in a station by a muon traversing vertically through the water volume, see [12].

²The reference distance was chosen to minimize the impact of the unknown lateral distribution of particles on the energy estimator.

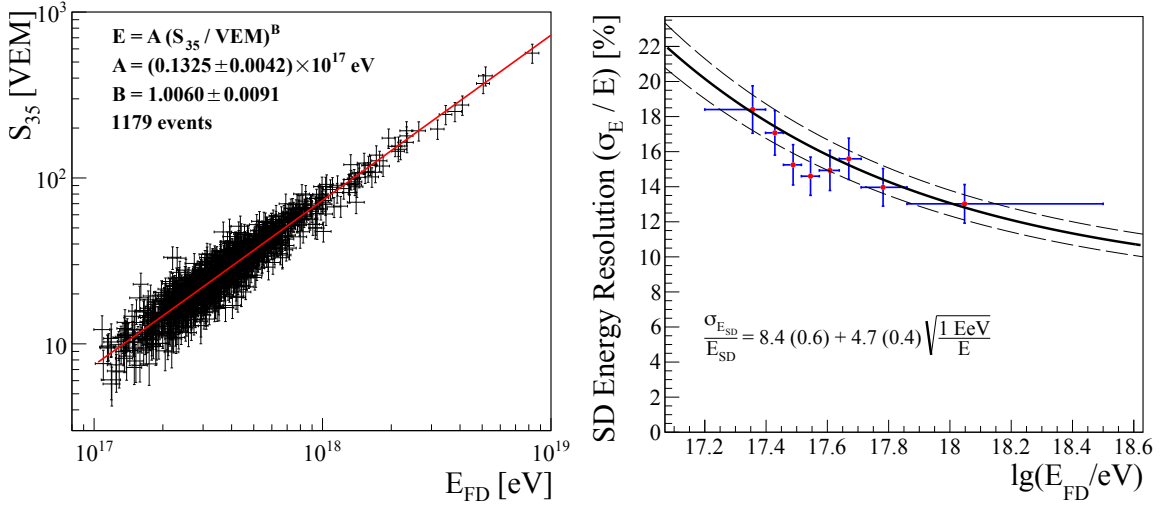


Figure 2: Left: Events used in the energy calibration (black points) are shown along with a power law fit (red line). Right: The SD energy resolution as a function of energy (black line) is plotted with the 1σ errors (dashed lines). The resolution in energy bins (red points) are also shown.

figure 1 which shows the distribution of observed shower sizes, $S(450)$ (solid lines) and S_{35} (dashed lines). The shower sizes observed by the 750 m array when only using the original trigger set is shown in black whereas the sizes now observable after including the TOTd and MoPS algorithms are shown in red. The two distributions agree well for higher energy showers and a clear increase is seen in the number of observed low energy showers now detectable via the new trigger algorithms.

3. Energy Calibration and Resolution

To estimate the energy of showers observed by the SD, the S_{35} values are calibrated using the energy measurements from the FD. This is performed using a set of high-quality, *golden hybrid*, events which were independently reconstructed by both the SD and FD. The relationship between FD energies, E_{FD} , and S_{35} is well described by a power law, $E_{FD} = A(S_{35}/\text{VEM})^B$, with fit parameters A and B , see [17] for more. The calibration was performed using 1179 golden hybrid events from January 2014 to August 2018. The left plot of figure 2 shows the fitted curve (red line) and the observed shower energies/estimators (black points). The best fit values for the calibration are $A = 0.1325 \pm 0.0042 \times 10^{17} \text{ eV}$ and $B = 1.0060 \pm 0.0091$, a nearly linear relationship.

The same set of golden hybrid events was also used to characterize the energy resolution of the SD. The resolution of the surface array is comprised of two components. The first is a result of the statistical uncertainties in the reconstruction, including contributions from the atmospheric/CIC corrections, which can be estimated on an event-by-event basis. The second component of the SD resolution is the shower-to-shower fluctuations, a result of the stochastic processes that govern the development of particle cascades. Since any two cosmic rays, with identical initial conditions, do not necessarily have the same first interaction depth, the two resultant air showers will arrive at the SD after a differing amount of attenuation, and will not be assigned the same value of $S(450)$. This uncertainty in the shower size cannot be estimated on an event-by-event basis by the SD.

However, using the events observed by both the SD and FD, the combination of these two effects can be estimated. Using the independent energy assignments by the two detectors, the

distribution of the quantity $z = E_{SD}/E_{FD}$ can be calculated for each event, where $\langle z \rangle \equiv 1$, by construction. Thus, z is the ratio of two random variables with a probability distribution, $\text{PDF}(z)$, which depends on the resolution of both the SD, $\sigma_{E,SD}$, and FD, $\sigma_{E,FD}$, and the energy bias between the two detectors. Note that, $\sigma_{E,FD}$ can be estimated on an event-by-event basis and is typically $8\% > \frac{\sigma_{E,FD}}{E_{FD}} > 6.7\%$ for energies above 10^{17} eV [11]. The distribution of z measurements was fit using $\text{PDF}(z)$ with an energy dependent parameterization of the SD resolution, $\frac{\sigma_{E,SD}}{E_{SD}}(E_{FD}) = \alpha + \beta \sqrt{1 \text{ EeV}/E_{FD}}$, where α and β are free parameters. Figure 2 shows the measured resolution for various energy bins (red circles), and the SD's resolution (solid) with 1 sigma error bars (dashed). Above $10^{17.0}$ eV, the SD resolution is 8-24%.

4. Measurement of the Spectrum

The event set used to measure the energy spectrum was restricted to the phase space where the array has a $>98\%$ efficiency to detect an air shower that lands inside the array. This phase space was determined using CORSIKA simulations of air showers for proton and iron primaries using both QGSJetII-04 and EPOS-LHC as hadronic models. For each model-primary combination, 150k events were simulated, 600k events in total, with energies ranging from $10^{16} \text{ eV} < E_{MC} < 10^{18} \text{ eV}$ and zenith angles $0^\circ < \theta < 55^\circ$.

A full detector simulation of the 750 m array was performed on each event which was then tested against the triggering algorithms. As a function of zenith angle, the triggering efficiency improved slightly at 55° (the zenith angle cut used in previous 750 m array analyses). However, a much larger improvement was found if restricting the angular acceptance to 40° . Figure 3 shows the triggering efficiency at 40° for all four model-primary combinations as well as for only using the original station triggers, for reference. Note that in this plot, the energy scale is the same as that of the FD, calculated via a cross-calibration to the Monte Carlo energies. For such a zenith angle cut, the array is $>98\%$ efficient for showers with energies greater than 10^{17} eV, regardless of hadronic model or mass.

Two energy spectra were created using data collected from January 2014 to August 2018 by the 750 m array. The first data set uses a zenith angle and energy cut of $\theta < 40^\circ$ and $E > 10^{17}$ eV, while the second uses the same zenith angle cut as previous 750 m analyses [16] but a slightly improved energy threshold, $\theta < 55^\circ$ and $E > 10^{17.3}$ eV, as a cross-check. Over this period the

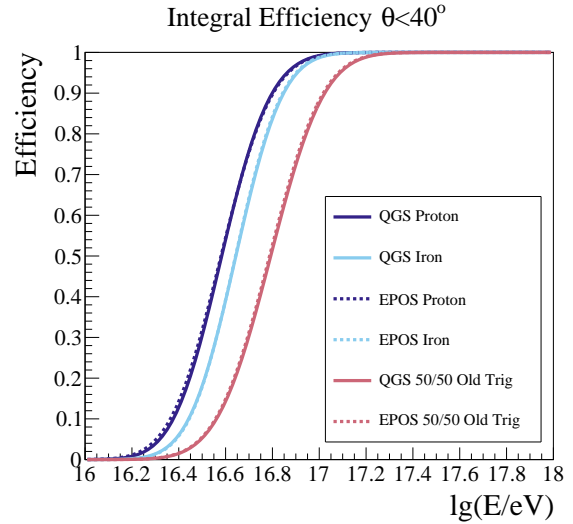


Figure 3: The integral trigger efficiency is shown for showers with zenith angles less than 40° . This quantity is shown for proton (solid lines) and iron (dashed lines) when including the new T1/T2 triggers as well as for a 50-50 mix of proton and iron for only the original trigger set, as a reference.

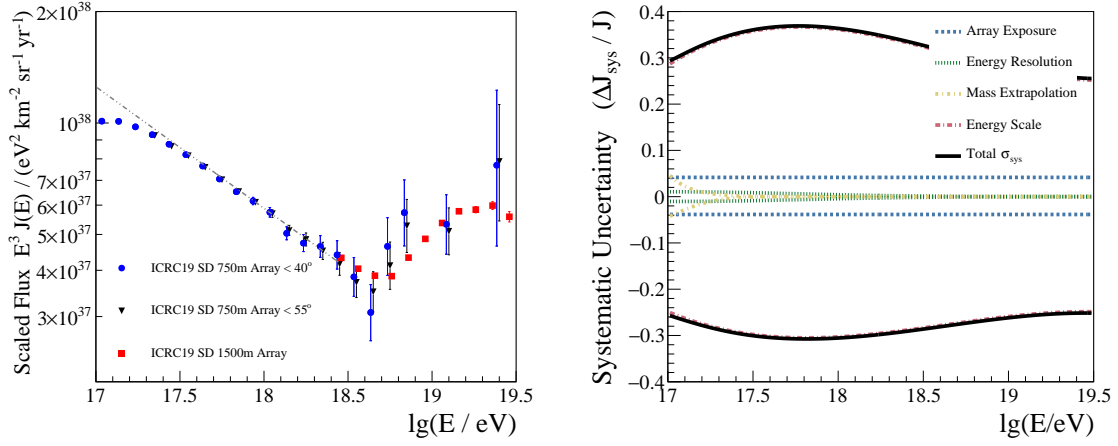


Figure 4: Left: The spectral measurements are shown for the 750 m array for zenith angle cuts of $\theta < 40^\circ$ (blue circles) and $\theta < 55^\circ$ (black triangles) as well as the 1500 m array (red squares). Right: The systematic uncertainty on the flux is shown as a function of energy.

accumulated exposure was $105.4 \text{ km}^2 \text{ sr yr}$, $\sim 570\text{k}$ events, in the first data set and $171.1 \text{ km}^2 \text{ sr yr}$, $\sim 190\text{k}$ events, in the second data set.

A correction was applied to the flux measurements to account for various detector effects that cause events to migrate, asymmetrically, between energy bins. The scaling was calculated using a forward folding method [16, 17] which included the previously described measurement of $\sigma_{E,SD}$ and triggering efficiency as well as the energy bias below 10^{17} eV which was determined via Monte Carlo. The resultant spectra for the 40° (blue circles) and 55° (black triangles) data sets are shown in the left plot of figure 4 along with the one observed by the 1500 m array (red squares). All three spectra agree within statistical uncertainties. A more detailed comparison between the 750 m spectra and those measured by the 1500 m array and the FD can be found in [17]

This measurement includes a systematic uncertainty that is dominated by the energy scale, $\sigma_{E_{FD}}/E_{FD} = 14\%$ which translates to a $\simeq 35\%$ uncertainty in the flux. The subdominant uncertainties include the array exposure (4%) and the energy resolution ($< 1.5\%$). This measurement includes an uncertainty from having to extrapolate the primary-mass composition down to energies below where they have been measured by the FD ($E < 10^{17.2} \text{ eV}$) [18]. However, due to the zenith angle and energy restrictions, the impact on the flux is small ($< 5\%$). These contributions and the total systematic uncertainty on the flux is shown in the right plot of figure 4.

The flux of cosmic rays in the energy region around $10^{17.0} \text{ eV}$ has been probed by many experiments as shown in figure 5. Many of them have observed a softening near this energy which has been called the second knee, including a new Cherenkov measurement using the FD. For Auger, previous measurements by the SD of the all particle spectrum, restricted to $E > 10^{17.5} \text{ eV}$, have been consistent with a simple power law below the ankle. However, with the extension of the flux measurement down to $E > 10^{17} \text{ eV}$, a single power law no longer describes the data well.

To understand the significance of the change in spectral index, γ , a power law fit, $J(E) \propto E^{-\gamma}$, with $\gamma = 3.33$, was extended down to 10^{17} eV (see the dash-dotted gray line in the left plot of figure 4). The residuals with respect to this power law are shown in the left plot of figure 6 (blue circles). The deviation from the power law fit, is as large as 15% which is well excluded by the statistical

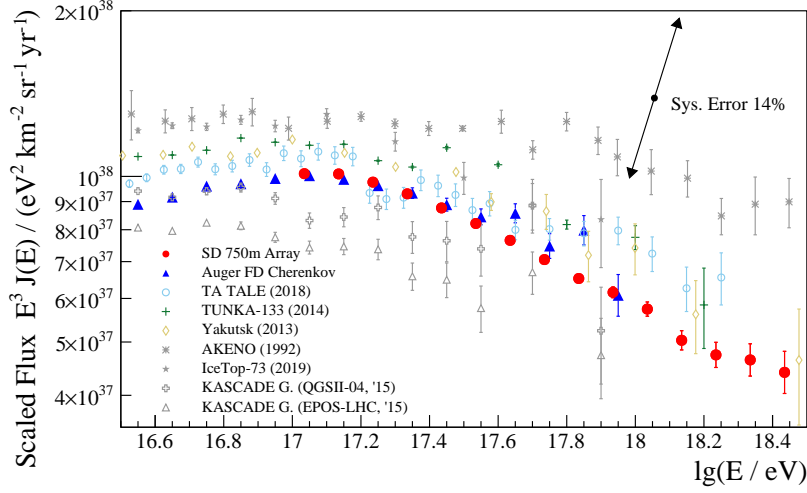


Figure 5: The cosmic ray spectra which observe a softening in the $\sim 10^{17}$ eV energy region are shown including Auger (both this work and via Cherenkov measurements by the FD [19]), AKENO [4], IceTop [6], KASCADE-Grande [2, 3], TALE [9], TUNKA [8], and Yakutsk [5]. Spectra with energy scales set via calorimetric measurements are shown in color, otherwise, shown in gray.

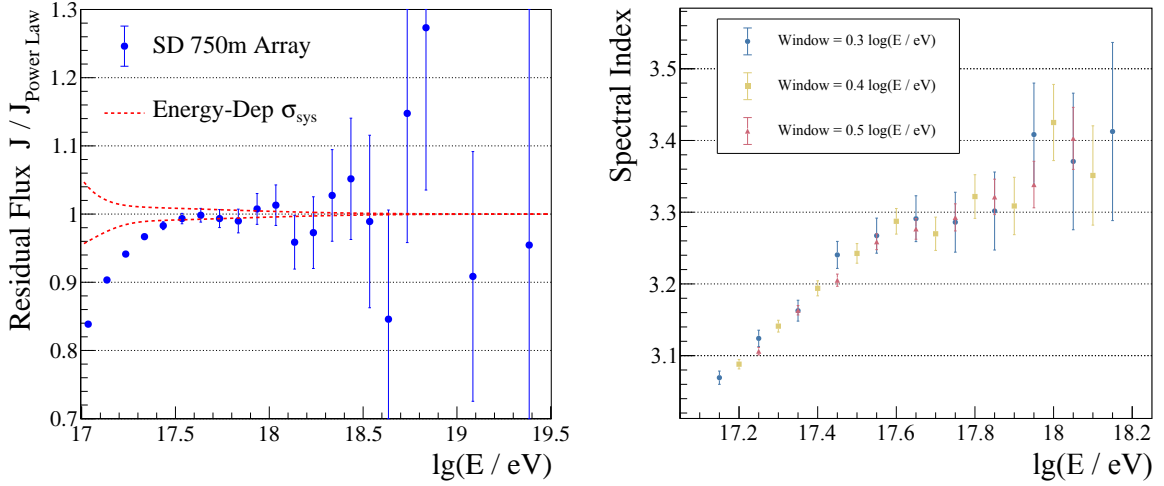


Figure 6: Left: The ratio of the 750 m array spectrum and a power law (blue points) is shown along with the energy-dependent systematic uncertainties of the flux. Right: Power law fits to the 750 m spectrum were performed over limited windows in energy. The spectral indexes are shown for windows of 0.3 (blue circles), 0.4 (gold squares), and 0.5 (red triangles) $\log(E/eV)$.

uncertainties of the measurement. Further, we can rule out such a deviation being a result of a systematic shift by comparing the residuals to the energy-dependent systematic flux uncertainties (red line). The disagreement with respect to a single power law fit below the ankle is at the level of $4.1 \sigma_{\text{sys}}$.

As a method of estimating the change in spectral index as a function of energy, the spectrum was fit using a series of power laws over limited windows in energy (0.3, 0.4, and 0.5 $\log(E/eV)$). The spectral indices corresponding to each fit are shown in the right plot of figure 6. A fairly constant increase in γ up to about $10^{17.6}$ eV is observed with a rate of change of about $\frac{d\gamma}{d\log E} \simeq 0.5$.

Such a change in spectral index is incompatible with a single power law.

5. Conclusion

In this work we presented a new measurement of the all-particle cosmic ray spectrum using the 750 m array at Auger. This work is a significant improvement on previously possible measurements of the flux by the SD in its extension to lower energies, $E > 10^{17}$ eV. Such an extension was made possible by an additional set of particle triggers for the WCDs.

Because of the 750 m array's size, this is the highest precision measurement in an energy region where most other measurements begin to be dominated by statistical uncertainties, including $\sim 570k$ events above 10^{17} eV. Further, this work is unique in this energy region in that it includes an energy scale set by the FD rather than Monte Carlo simulations and a data-driven approach to estimate the energy resolution. Thus, the result is nearly-model independent. We have shown that there is a significant softening between 10^{17} eV and the ankle where the spectral index increases from ≤ 3.1 to 3.3. This softening is larger than can be explained by either the statistical or systematic uncertainties of the measurement.

References

- [1] [KASCADE Collaboration], *Astropart. Phys.* **24.1-2** (2005) 1 [[astro-ph/0505413](#)].
- [2] [KASCADE-Grande Collaboration], *Phys. Rev. Lett.* **107.17** (2011) 171104 [[astro-ph/1107.5885](#)].
- [3] [KASCADE-Grande Collaboration], *Phys. Rev. D* **87.8** (2013) 081101 [[astro-ph/1304.7114](#)].
- [4] M.Nagano, et al., *J. Phys. G Nucl. Partic.* **18.2** (1992) 423.
- [5] S.P.Knurenko, et al., *EPJ Web Conf.* **53** (2013) 04004 [[astro-ph/1112.2430](#)].
- [6] [IceCube Collaboration] *Cosmic Ray Spectrum and Composition from PeV to EeV Using 3 Years of Data From IceTop and IceCube*, [astro-ph/1906.04317](#), [PoS \(ICRC2019\) 172](#) (2019).
- [7] M.E.Bertaina [KASCADE-Grande Collaboration], in proceedings of *The 34th Int. Cosmic Ray Conf.*, [PoS \(ICRC2015\) 359](#) (2015).
- [8] V.V.Prosin, et al., *EPJ Web Conf.* **121** (2016) 03004.
- [9] R.U.Abbasi, et al., *Astrophys. J.* **865.1** (2018) 74 [[astro-ph/1803.01288](#)].
- [10] A.Aab [Pierre Auger Collaboration], *Nucl. Instrum. Meth. A* **798** (2015) 172 [[astro-ph/1502.01323](#)].
- [11] B.Dawson [Pierre Auger Collaboration], in proceedings of *The 36th Int. Cosmic Ray Conf.*, [PoS \(ICRC2019\) 231](#) (2019).
- [12] X.Bertou, et al., *Nucl. Instrum. Meth. A* **568.2** (2006) 839.
- [13] D.Mockler [Pierre Auger Collaboration], in proceedings of *The 36th Int. Cosmic Ray Conf.*, [PoS \(ICRC2019\) 353](#) (2019).
- [14] A.Aab [Pierre Auger Collaboration], *JINST* **12** (2017) P02006
- [15] J.Hersil, et al., *Phys. Rev. Lett.* **6** (1961) 22.
- [16] F.Fenu [Pierre Auger Collaboration], in proceedings of *The 35th Int. Cosmic Ray Conf.*, [PoS \(ICRC2017\) 486](#) (2017).
- [17] V.Verzi [Pierre Auger Collaboration], in proceedings of *The 36th Int. Cosmic Ray Conf.*, [PoS \(ICRC2019\) 450](#) (2019).
- [18] J.Bellido [Pierre Auger Collaboration], in proceedings of *The 35th Int. Cosmic Ray Conf.*, [PoS \(ICRC2017\) 506](#) (2017)
- [19] V.Novotny [Pierre Auger Collaboration], in proceedings of *The 36th Int. Cosmic Ray Conf.*, [PoS \(ICRC2019\) 374](#) (2019).



Measurement of the spectrum of cosmic rays above $10^{16.5}$ eV with Cherenkov-dominated events at the Pierre Auger Observatory

Vladimír Novotný^{*†} for the Pierre Auger Collaboration^{†b}

^a*Institute of Particle and Nuclear Physics, Faculty of Mathematics and Physics,
Charles University, Prague, Czech Republic*

^b*Observatorio Pierre Auger, Av. San Martín Norte 304, 5613 Malargüe, Argentina*
E-mail: auger_spokespersons@fnal.gov

Full author list: http://www.auger.org/archive/authors_icrc_2019.html

We present a profile constrained geometry fit (PCGF) method for shower geometry reconstruction implemented in the Pierre Auger Observatory analysis chain. It is used to reconstruct low-energy extensive air showers (3×10^{15} eV $< E < 10^{18}$ eV) detected by the high elevation Auger telescopes (HEAT). The method is proven to be particularly important for events with signal dominated by Cherenkov light. The precision of the reconstruction is evaluated using full Monte Carlo simulations of the showers and telescopes. Simulations are compared to the data, and the results are discussed. A preliminary measurement of the energy spectrum in the second knee region is presented.

*36th International Cosmic Ray Conference — ICRC2019
24 July – 1 August, 2019
Madison, Wisconsin, USA*

*Speaker.

†for collaboration list see PoS(ICRC2019)1177

1. Introduction

The Pierre Auger Observatory [1] is primarily designed to measure the highest energy cosmic rays at energies above 10^{18} eV. This is achieved with an array of water-Cherenkov surface detectors (SD) with a 1500 m spacing and 24 telescopes of the fluorescence detector (FD) looking at an elevation of 1.51° above the horizon with a field of view of $30^\circ \times 30^\circ$. The FD is situated at four sites called Los Leones, Los Morados, Loma Amarilla and Coihueco.

Besides the instruments dedicated to the highest energies, two low-energy extensions are present at the Observatory, i.e. the SD array with 750 m spacing, and three high elevation Auger telescopes (HEAT). HEAT covers an elevation range up to 60° and is able to work in hybrid mode together with the 750 m array down to energies around 10^{17} eV. The 750 m array itself also delivers results down to 10^{17} eV [2].

The standard hybrid detection, commonly used by the Pierre Auger Observatory, is not suitable to address lower energies. This is caused by the weakness of the fluorescence light produced by air showers of lower energy. In this contribution, we utilize the showers approaching FD telescopes along their telescope axes. Such events have a lower detection threshold caused by the air-Cherenkov light emission from the charged particles in the shower. To solidly reconstruct Cherenkov-dominated events, we utilize the profile constrained geometry fit (PCGF). It was invented at the HiRes experiment [3] for fluorescence-dominated events and is currently used by TALE [4] for Cherenkov-dominated data.

2. Method

The PCGF is a method of shower geometry reconstruction that works for a monocular view of an extensive air shower. It is favoured over the simple monocular time fit because the time fit suffers from correlations between shower axis parameters described below. If the shower is assumed to propagate with a velocity equal to the speed of light c , then the shower axis is determined by R_p , t_0 and χ_0 inside the shower-detector plane (SDP), see [5] for parameter definitions. The parameters are connected by the formula

$$t_i = t_0 + \frac{R_p}{c} \tan\left(\frac{\chi_0 - \chi_i}{2}\right), \quad (2.1)$$

where t_i is the time when the light from the shower is detected at a viewing angle χ_i inside the SDP. Because the field of view of the FD telescope is limited, the range of χ_i available for the fit is also limited. For events with a short angular track length, we see a correlation between two of the three parameters.

Within the PCGF approach, the above mentioned correlation is removed by an additional requirement on the energy deposit profile in the atmosphere. We require that the energy deposit profile calculated for a given geometry is compatible with the Gaisser-Hillas (GH) function [6],

$$\frac{dE}{dX}(X) = \left(\frac{dE}{dX}\right)_{\max} \left(\frac{X - X_0}{X_{\max} - X_0}\right)^{\frac{X_{\max} - X_0}{\lambda}} \exp\left(\frac{X_{\max} - X}{\lambda}\right), \quad (2.2)$$

where X_0 and λ are GH shape parameters, X_{\max} is the depth of the shower maximum, and $\left(\frac{dE}{dX}\right)_{\max}$ is the maximum of energy deposit.

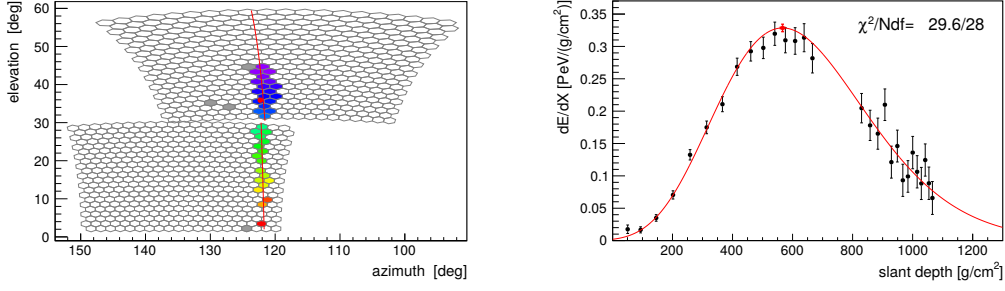


Figure 1: Reconstruction of event 6/1990/13000. The camera view (left panel) together with the reconstructed energy deposit profile (right panel) are shown. The reconstructed calorimetric energy is 2.1×10^{17} eV. The gap in the profile corresponds to the crossing between two telescopes.

Technically, a scan in χ_0 is performed, and for each fixed χ_0 the two remaining parameters, R_p and t_0 , are calculated by linear regression of Eq. (2.1). For the geometry fixed in this way, a fit of the GH function Eq. (2.2) to the energy deposit profile is done as follows. The X_0 , X_{\max} , λ and $\left(\frac{dE}{dX}\right)_{\max}$ are varied, and for each of the combinations, the light flux that would be measured in the FD telescopes is predicted and compared to the measured flux. In the end, the likelihood that is used to quantify the level of agreement between the particular χ_0 -defined geometry and our assumptions is then composed of parts corresponding to the time fit Eq. (2.1), constraints on GH parameters, and the observed light flux in the telescopes. Finally, the most likely geometry is selected, and for this geometry the resulting energy deposit profile is fine-tuned in later reconstruction steps.

Besides the implementation of the basic method described above, the PCGF reconstruction module is able to deal with telescopes placed at different positions. It allows us to use the HEAT telescopes together with Coihueco site telescopes¹, effectively working in a partial stereo observation regime for showers seen by both detectors. An example of a shower detected simultaneously by HEAT and Coihueco telescopes that was reconstructed by a PCGF is shown in Fig. 1.

3. Accuracy and precision of reconstruction

To evaluate the accuracy and precision of the PCGF reconstruction, a set of Monte Carlo (MC) simulations was produced. The air showers were generated with the CONEX program [7], and the light simulation together with the full FD response were calculated within the Offline framework [8]. Sibyll 2.3c [9] was used as the high-energy interaction model. The range of simulated energies was 10^{15} – $10^{18.2}$ eV for both protons and iron nuclei as primary particles.

Although the PCGF also works in principle for fluorescence-dominated events, our interest is restricted to the Cherenkov-dominated data only. The first reason is due to a better accuracy of the geometry reconstruction which is connected to the strong collimation of the Cherenkov beam produced by showers. It improves the sensitivity of the reconstruction to small changes in the mutual telescope-shower axis position. The second reason is the fact that low-energy showers are detectable thanks to the Cherenkov radiation, and fluorescence is mostly absent. In this contribu-

¹ Coihueco and HEAT sites are placed ca. 170 m apart.

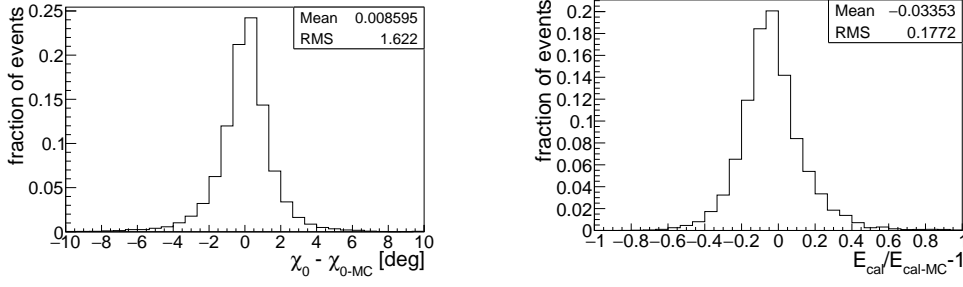


Figure 2: Resolution of the χ_0 shower axis parameter (left panel) and the calorimetric energy (right panel) reconstructed by the PCGF at calorimetric energies between $10^{15.5} - 10^{18}$ eV. The energy spectrum in simulations was re-weighted to $E^{-2.8}$.

tion, we are interested in the low-energy part of the cosmic-ray spectrum and the high-energy part is better analysed by hybrid measurements.

To reduce the number of badly reconstructed events, quality cuts were applied. In line with the preceding paragraph, only events with a total Cherenkov light fraction above 50% were used. Due to the limited FD electronics readout, the fast Cherenkov-dominated events are in general poorly sampled in time. Because of that, we applied a cut on the minimum number of points in the detected light flux to be at least 5, which corresponds to 250 ns and 500 ns durations in HEAT and Coihueco telescopes, respectively, due to different electronics. This cut² allows reasonable fits of the GH function to the energy deposit profile, see Fig. 1.

The overall precision of the reconstruction of the shower geometry can be quantified by the resolution and bias of the χ_0 parameter. The distribution of differences between the reconstructed and simulated χ_0 is shown in the left panel of Fig. 2. It corresponds to a simulated range of $10^{15.5} - 10^{18}$ eV in calorimetric energy (E_{cal}), and simulations were re-weighted according to the energy spectrum of $E^{-2.8}$, which also holds for all further plots. An almost unbiased estimation of χ_0 is achieved together with a resolution of about 1.6° .

The most critical observable for studies of cosmic rays is the energy of the incident air shower. Utilizing the full MC simulations, an energy response was calculated and is depicted in the right panel of Fig. 2. The obtained reconstruction resolution of calorimetric energy is 18%, and on average the energies are slightly underestimated. This result takes into account all the machinery of the shower reconstruction, i.e. the bias is not solely due to the discrepancy in the reconstructed shower axis³. The effects that are related to uncorrelated systematic uncertainties are not included in the reported energy resolution and will be evaluated in the future.

It is worth noting that the energy that is estimated is the calorimetric energy. The Cherenkov radiation reflects the integrated track length of charged particles above the Cherenkov energy threshold, which may not follow the energy deposit profile exactly. Such effects are taken into account in our simulations, and in the reconstruction, an average energy deposit per charged particle is used [10]. The fluctuations of energy deposit per charged particle at the CONEX level are still present, and the Cherenkov energy threshold is controlled by the model of light emission as described in

²We also use a reduced $\chi^2 < 3$ cut on the energy deposit profile.

³Actually, an energy bias of a similar value is also found for a MC-fixed shower axis. Nevertheless, in that case, the resolution is much better.

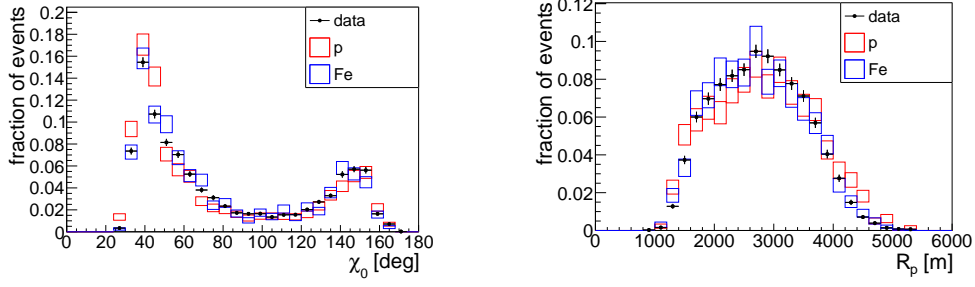


Figure 3: Distributions of reconstructed χ_0 (left panel) and R_p (right panel) in the energy bin of $10^{16.9} - 10^{17.1}$ eV for the data (black). Simulations of protons and iron nuclei are shown by red and blue boxes, respectively.

[11].

Besides the precision of the PCGF reconstruction itself, it is necessary to check the agreement between the simulated MC sample and the data. For this purpose, we present the distributions of shower axis parameters χ_0 and R_p in the calorimetric energy range of $10^{16.9} - 10^{17.1}$ eV. The distributions are shown in Fig. 3 for χ_0 and R_p in the left and right panel, respectively; the data are depicted by black points. Colored boxes correspond to simulations, and their length represents the statistical uncertainty of the MC.

4. Towards an energy spectrum

Data processed by the PCGF give rise to the possibility of an energy spectrum measurement at energies below the hybrid detection limit. However, the new measurement technique is complicated by several sources of systematic uncertainty. Besides the invisible energy correction and composition systematics described below, we also investigated other uncertainties related to the determination of the energy spectrum. The energy scale systematics of the FD [12], common to all Auger measurements, is the most important source of systematic uncertainty. It also affects the exposure through its dependence on the number of detected photoelectrons; the effect is ca. 15% on the flux at 10^{17} eV. The systematic uncertainty in energy due to the Cherenkov emission model used [13] is estimated to be 5%, and the uncertainty in the energy reconstruction procedure is below 6%.

4.1 Invisible energy

To estimate the total energy (E_{tot}) of an air shower, a correction for the energy that was not deposited in the atmosphere, called the invisible energy (E_{inv}), has to be applied. For the purpose of the Cherenkov-dominated measurement, we estimate the invisible energy from IceTop data [14] with the use of the equation

$$E_{\text{inv}} = \varepsilon_C^\pi N_\mu, \quad (4.1)$$

which comes from the extended Heitler model [15]. In this equation, N_μ is the number of muons in the extensive air shower reaching ground level, and ε_C^π is the pion critical energy. Justification of Eq. (4.1) is based on detailed MC simulations provided in [16].

polynomial	a	b	c
P	4.213	-0.463	0.013
P_{low}	3.838	-0.420	0.012
P_{up}	4.623	-0.509	0.015

Table 1: Parameters of the invisible energy model below 10^{17} eV. Above 10^{17} eV, the values reported in [16] are used.

A recalculation of muon densities at ground level reported by IceTop was done in [17], where the z quantity is defined by

$$z = \frac{\ln(N_{\mu}^{\text{det}}) - \ln(N_{\mu,p}^{\text{det}})}{\ln(N_{\mu,\text{Fe}}^{\text{det}}) - \ln(N_{\mu,p}^{\text{det}})}. \quad (4.2)$$

N_{μ}^{det} is the muon density estimate as seen in the detector, while $N_{\mu,\text{Fe}}^{\text{det}}$ and $N_{\mu,p}^{\text{det}}$ are the simulated muon density estimates for p and Fe induced showers after a full detector simulation. However, the simulated number of muons is dependent on the particular model of high-energy interactions. For the purpose of the invisible energy calculation, the QGSJetII-04 model [18] was chosen.

Utilizing Eqs. (4.1) and (4.2), the formula for the invisible energy is

$$E_{\text{inv}} = E_{\text{inv,p}} \left(\frac{E_{\text{inv,Fe}}}{E_{\text{inv,p}}} \right)^z, \quad (4.3)$$

where $E_{\text{inv,p}}$ and $E_{\text{inv,Fe}}$ are the invisible energies estimated by the chosen high-energy interaction model for protons and iron nuclei, respectively. Values of $E_{\text{inv,p}}$ and $E_{\text{inv,Fe}}$ are parametrized using CONEX simulations, and z is taken directly from [17]. The invisible energy is evaluated according to Eq. (4.3) and shown in Fig. 4 by green and orange points for 600 m and 800 m core distances, respectively.

To combine our estimates with those at higher energies [16], we performed a fit of the 2nd order polynomial P

$$E_{\text{inv}}/E_{\text{tot}} = a + b \log_{10} E_{\text{cal}}/\text{eV} + c (\log_{10} E_{\text{cal}}/\text{eV})^2, \quad (4.4)$$

to the data derived from IceTop in the energy range of $10^{15} - 10^{17}$ eV. The upper energy point at 10^{17} eV was fixed to the value reported in [16]. Systematic uncertainties were estimated combining the uncertainty reported in [16] and the one obtained by fitting the polynomials P_{low} and P_{up} to the IceTop lower and upper uncertainty bounds, respectively; for coefficients see Tab. 1.

4.2 Exposure

The exposure of HEAT and Coihueco telescopes to the Cherenkov-dominated events was estimated from detailed MC simulations introduced in Section 3. Protons and iron nuclei were used as primary particles to estimate the composition systematics. In the left panel of Fig. 5, the exposure in the time period of 06/2012–12/2015 is visualized under the condition that the invisible energy follows the model depicted in Fig. 4. In this way, only the systematic effects connected to the limited field of view of telescopes and different slant depth evolution of showers induced by

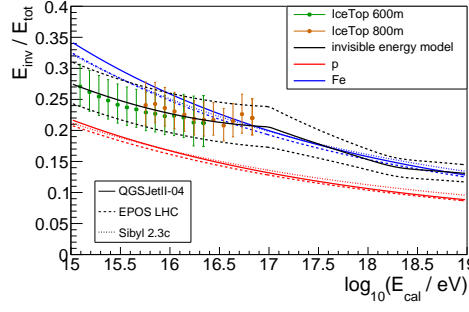


Figure 4: Invisible energy model (black line) estimated with the use of IceTop data [14] (points). The high-energy part above 10^{17} eV is fixed to the values reported in [16]. Dashed black lines show the systematic uncertainty. Red and blue lines correspond to the MC predictions for protons and iron nuclei, respectively.

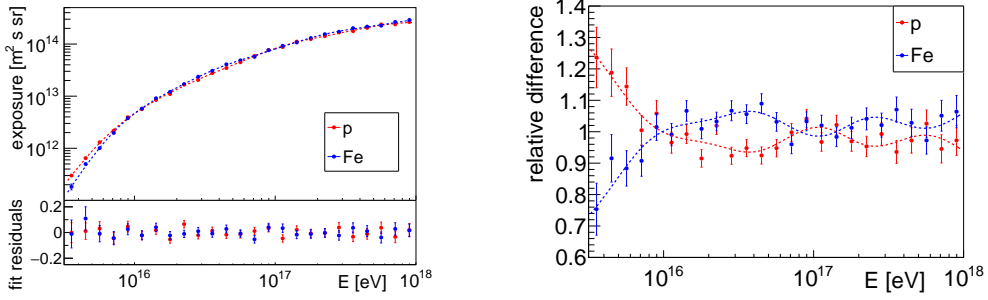


Figure 5: Left panel: Exposure to the Cherenkov-dominated events over the time period of 06/2012-12/2015 (top panel). Protons (red) and iron nuclei (blue) were used as primary particles. Residuals to the fitted functions (dashed lines) are shown in the bottom panel. Right panel: Relative difference between exposures inferred from pure primary beams and the 50% + 50% mix. Points depict the difference derived from the MC simulations directly, dashed lines correspond to the difference calculated with the use of exposure fits.

different primaries are estimated. The difference in the exposure to protons and iron nuclei with respect to the 50% + 50% mix is shown in the right panel of Fig. 5. The systematic uncertainty of the exposure connected to the uncertain composition is below 10% above 10^{16} eV.

Knowing the exposure, we calculate a preliminary energy spectrum. It is shown in Fig. 6 and restricted to energies above $10^{16.5}$ eV. Unfolding of the resolution and bias of the energy reconstruction is applied. Points correspond to the used composition assumption [19]. Magenta boxes show the acceptance systematics due to uncertain composition, and grey regions show the systematic uncertainties corresponding to other investigated effects.

5. Conclusions

The PCGF method of shower axis geometry reconstruction was successfully implemented in the Offline software used at the Pierre Auger Observatory. The resolution of the χ_0 reconstruction is 1.6° , and the calorimetric energy is reconstructed with a resolution of 18%. Correspondence between the measured data and full simulations of air showers and the FD is at a reasonable level.

A preliminary energy spectrum of cosmic rays in the energy region of $10^{16.5} - 10^{18}$ eV was estimated. Dominant systematic uncertainties are in the FD energy scale (14% in energy) and MC

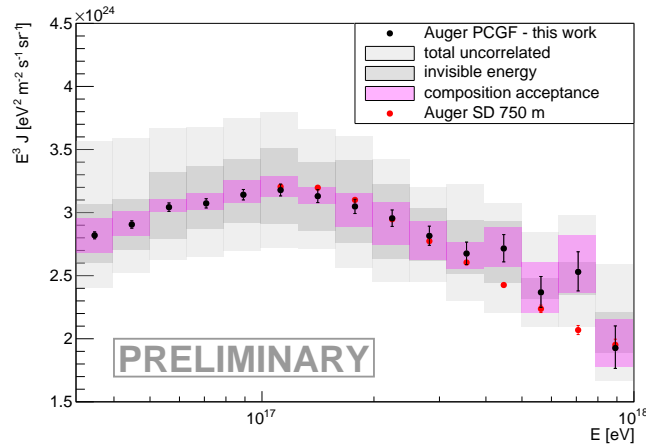


Figure 6: Preliminary energy spectrum derived from Cherenkov-dominated events detected by the HEAT and Coihueco telescopes (black). Light grey region corresponds to the total uncertainty uncorrelated with the Auger SD 750 m [2] measurement (red). It consists of uncertainties in the Cherenkov emission model, exposure and in the reconstruction procedure. Dark grey and magenta regions show the uncertainty due to the invisible energy model and different detector acceptance for different primaries, respectively.

simulations of the FD (15% in exposure). The reconstruction procedure and Cherenkov emission model contribute to the uncertainty in the Cherenkov energy scale by ca. 5% each. A presence of the second knee is robust against changes in the invisible energy even to the MC predictions for pure beams.

References

- [1] The Pierre Auger Collaboration, Nucl. Instrum. Meth. A **798** (2015) 172.
- [2] Coleman, A. et. al., PoS ICRC2019 (2019) 225
- [3] HiRes Collaboration, Phys. Rev. Lett. **100** (2008) 101101.
- [4] Abbasi, R.U. et. al., Astrophys. J. **865** (2018) no.1, 74.
- [5] Kuempel, D., Kampert, K.-H., and Risse, M., Astropart. Phys. **30** (2008) 167–174
- [6] Gaisser, T.K. and Hillas, A.M., Proc. of 15th Int. Cosmic Ray Conf., **8** (1977) 353
- [7] Bergmann, T. et. al., Astropart. Phys. **26** (2007) 420–432
- [8] Argiro, S. et. al., Nucl. Instrum. Meth. A **580** (2007) 1485–1496
- [9] Riehn, F., Dembinski, H.P., Engel, R., Fedynitch, A., Gaisser, T.K., Stanev, T., PoS ICRC2017 (2018) 301
- [10] Novotny, V. and Nosek, D., PoS ICRC2017 (2018) 338
- [11] Unger, M., Dawson, B.R., Engel, R., Schussler, F., Ulrich, R., Nucl. Instrum. Meth. A **588** (2008) 433-441
- [12] Dawson, B. et. al., PoS ICRC2019 (2019) 231
- [13] Nerling, F., Bluemer J., Engel, R., Risse, M., Astropart. Phys. **24** (2006) 421–437
- [14] Gonzalez, J., *Measuring the Muon Content of Air Showers with IceTop*, ISVHECRI 2018
- [15] Matthews, J., Astropart. Phys. **22** (2005) 387–397
- [16] The Pierre Auger Collaboration, arXiv:1901.08040, Submitted to Phys. Rev. D (2019)
- [17] Dembinski, H.P. et. al., *Report on Tests and Meas. of Hadronic Int. Prop. with Air Showers*, UHECR 2018
- [18] Ostapchenko, S., EPJ Web Conf. **52** (2013) 02001
- [19] Dembinski, H.P., Engel, R., Fedynitch, A., Gaisser, T., Riehn, F., Stanev, T., PoS ICRC2017 (2018) 533



Air-Shower Reconstruction at the Pierre Auger Observatory based on Deep Learning

Jonas Glombitza^{*a} for the Pierre Auger Collaboration^{†b}

^a*RWTH Aachen University, Aachen, Germany*

^b*Observatorio Pierre Auger, Av. San Martín Norte 304, 5613 Malargüe, Argentina*

E-mail: auger_spokespersons@fnal.gov

Full author list: http://www.auger.org/archive/authors_icrc_2019.html

The surface detector array of the Pierre Auger Observatory measures the footprint of air showers induced by ultra-high energy cosmic rays. The reconstruction of event-by-event information sensitive to the cosmic-ray mass, is a challenging task and so far mainly based on fluorescence detector observations with their duty cycle of $\approx 15\%$. Recently, great progress has been made in multiple fields of machine learning using deep neural networks and associated techniques. Applying these new techniques to air-shower physics opens up possibilities for improved reconstruction, including an estimation of the cosmic-ray composition. In this contribution, we show that deep convolutional neural networks can be used for air-shower reconstruction, using surface-detector data. The focus of the machine-learning algorithm is to reconstruct depths of shower maximum. In contrast to traditional reconstruction methods, the algorithm learns to extract the essential information from the signal and arrival-time distributions of the secondary particles. We present the neural-network architecture, describe the training, and assess the performance using simulated air showers.

36th International Cosmic Ray Conference — ICRC2019

24 July – 1 August, 2019

Madison, Wisconsin, USA

^{*}Speaker.

[†]for collaboration list see PoS(ICRC2019)1177

1. Introduction

The search for the origin of ultra-high energy cosmic rays (UHECRs) is one of the greatest challenges of astroparticle physics. Studying the mass of these particles helps to localize possible source candidates and to understand the acceleration mechanisms at the sources. UHECRs exceed primary energies of 10^{18} eV leading to extensive air showers when impacting the Earth's atmosphere. To allow for accurate measurements of UHECRs, the Pierre Auger Observatory [1] was completed in 2008 featuring a hybrid design. The baseline of the Observatory is the surface detector [2] (SD) formed by 1660 water-Cherenkov stations placed in a hexagonal grid, which measure the footprint of extensive air showers induced by UHECRs. The stations are separated by a distance of 1500 m covering an area of ≈ 3000 km². This surface detector grid is overlooked by 27 fluorescence telescopes which measure the light emission of nitrogen excited by the particles of the extensive cascade.

The air-shower development is especially dependent on the energy and the mass of the primary cosmic ray, causing greater depth of shower maximum for lighter masses and higher energies. Hence, the atmospheric depth of the shower maximum X_{\max} enables an estimation of the cosmic-ray composition [3]. The observable X_{\max} can be directly measured with the fluorescence detector (FD). However, measurements of the FD are only possible on moonless nights, which reduces the duty cycle to $\approx 15\%$. Alternatively, measuring the shower maximum using the SD is a challenging task, since it has to be inferred indirectly from the secondary particles recorded on the ground.

Recently, great progress has been made in machine learning using deep neural networks and associated techniques (deep learning) [4, 5]. The basic elements of deep learning are neural networks holding adaptive weights, which can be adjusted to the task at hand by exploring a data set. The use of graphics processing units (GPUs), large amounts of data and the latest developments have recently made it possible to train deep networks which hold several million parameters. Especially in computer vision [6], pattern [7] and speech [8] recognition, using deep networks paved the way for results of previously unreachable precision [4, 9].

The symmetric placement of sensors in a regular grid is ideally suited for the use of deep-learning techniques. Besides using pattern recognition for analyzing the spatial characteristic of the footprint, the arrival-time distribution of the secondary particles is encoded in the time evolution of the measured signal (signal trace) in each water-Cherenkov station. Recognizing single muons and particles of the electromagnetic component to infer the longitudinal shower development further encourages the use of techniques of speech recognition or natural language processing.

Apart from the total signal and the signal start time as used in the standard reconstruction [10], the machine-learning approach relies on the time-dependent distributions of particles traversing the water-Cherenkov stations. In contrast to shower-universality analyses [11, 12] where humans parametrize the signal and arrival-time distributions of secondary particles using analytic models, the deep-learning algorithm discovers the best parametrization itself.

In this contribution we show that using deep networks enables the reconstruction of several air-shower properties by combining spatial and time information of the detected air shower. First, we introduce the deep-convolutional network architecture and discuss the training. Subsequently, we show that the network is capable of reconstructing the basic shower geometry and providing a reconstruction of the primary particle energy. Finally, we show that the deep-convolutional neural

network provides promising results in the reconstruction of the depth of the shower maximum X_{\max} on an event-by-event level.

2. Surface detector data

The air-shower footprint triggers several water-Cherenkov stations, thus inducing a characteristic signal pattern on the hexagonal SD grid. Each of the triggered stations provides a signal trace which encodes a time-dependent density of particles traversing the station. The resulting data are illustrated in Figure 1.

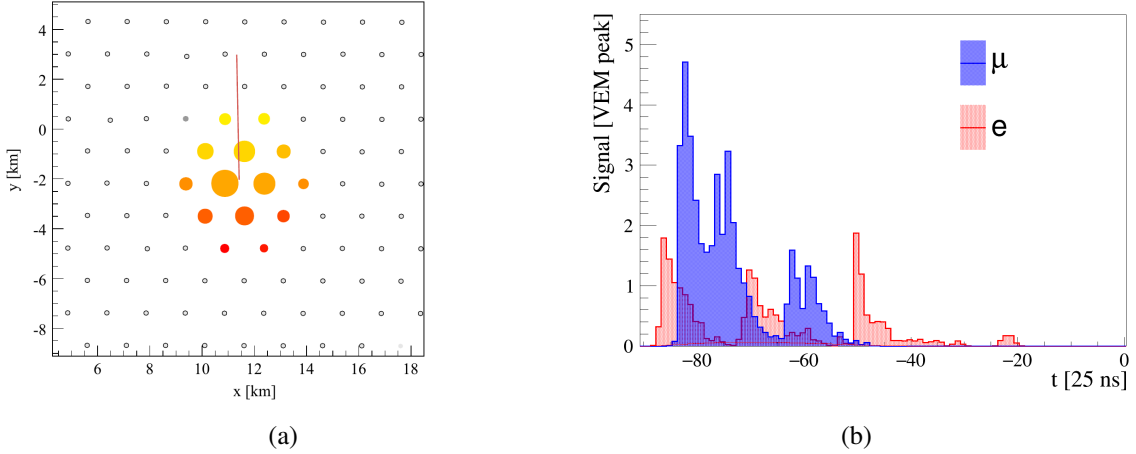


Figure 1: (a) Measured surface-detector signal pattern, induced by a simulated air shower. (b) Simulated time traces measured at one surface-detector station.

2.1 Preprocessing

In order to stabilize the training of the deep network, we used data preprocessing. By normalizing the input variables to $[1, -1]$, we observed better training stability and faster convergence. To further enforce all mappings in the neural network to act on the same scale, we adopted a standard normalization ($\sigma = 1$, $\mu = 0$) of our label distributions.

2.1.1 Signal patterns and coordinates

Due to the hexagonal grid of the surface detector, we cannot make direct use of convolutions which rely on Cartesian representations. In order to use convolutions, we transform our signal patterns using an axial representation, by padding with zeros and shifting each second row until alignment is achieved [13]. As a measured footprint usually has a size of several tens of square kilometers, the pattern is cropped to a window of 13×13 stations to reduce memory consumption. The station with the largest signal is used as the center of this frame and defines the origin of the local coordinate system.

As the placement of the stations shows slight deviations from a perfect grid, we use the coordinates of each station as additional inputs. We first transform the x and y coordinate of each event, into the respective local coordinate system and calculate the deviation with respect to a perfect

grid. Additionally, we normalize the deviation by dividing by σ_C , which is the spread of the distribution of grid deviations. For the altitude z of the respective station we use standard normalization ($\sigma_z = 1$, $\mu_z = 0$), otherwise the relative height would be calibrated out, which would cause shifts of the observed atmospheric depth. In order to use the same representations, the position of the shower core is transformed in the same way.

2.1.2 Signal traces

As the number of particles measured in each detector is approximately exponentially distributed, we use a logarithmic re-scaling of the trace:

$$\tilde{S}_i(t) = \frac{\log_{10}[S_i(t) + 1]}{\log_{10}[S_{sat} + 1]}. \quad (2.1)$$

To allow for positive values only we use $S_i(t) + 1$. The signal amplitude $S_i(t)$ is linearly re-scaled into the range $[0; 1]$ using the minimum and maximum signal level S_{sat} that can be digitized by the simulated data-acquisition system.

2.1.3 Arrival time

The arrival direction of the primary particle can be reconstructed using the arrival times $t_{0,i}$ of the shower front at the stations. For each station, the arrival time is normalized with respect to the arrival time τ_{center} measured at the central station and $\sigma_{t, \text{data set}}$, the standard deviation of the arrival time distribution:

$$\tilde{t}_{0,i} = \frac{t_{0,i} - \tau_{center}}{\sigma_{t, \text{train data set}}}. \quad (2.2)$$

2.1.4 Station states

Due to aging effects, bad calibrations or broken PMTs, some of the water-Cherenkov stations may not be ready to measure real data. In order to let the network correct for this, we add a feature map encoding the station states (1 = ready to measure, 0 = broken) as additional input. During the training, we further imitate broken stations by randomly masking stations and propagating this information to the feature map of stations states.

3. Deep network for air shower reconstruction

The network design for reconstructing cosmic-ray induced air showers features three stages and is based on [13]. The first stage is used for the characterization of the time trace, hence learning features which include information about the shower development. The following part allows forming spatial features. In the final stage, several sub-parts for each reconstruction task are used.

3.1 Time trace characterization

The first part relies on characterizing the measured signal trace. Investigating the time-dependent signals allows for measuring the content of the muon and electromagnetic components of the air shower which each induce different signal shapes. The separation of the components yields information about the shower age, energy and the primary mass. To let the network exploit local

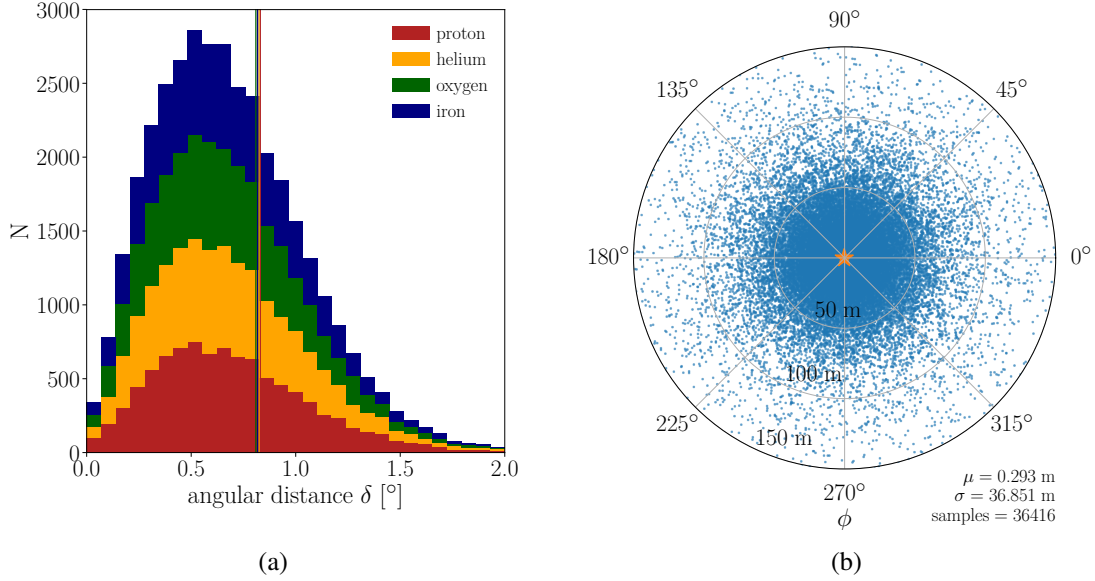


Figure 2: (a) Angular distance between the reconstructed and the true shower axes. Different colors indicate different primaries. (b) Azimuth dependence of the shower-core reconstruction. The network provides on average an unbiased estimate of the core position (yellow marker).

features in the signal traces, e.g., sharp edges or spikes, we apply convolutions. We use rectified linear units [5] as activation functions and three convolutional layers with varying kernel sizes. To stabilize the training and to increase generalization performance, we use weight sharing along the spatial dimensions. Hence, the convolutional operation works on the time dimension only and reduces the time trace with a length of 251 time steps, to 10 features. In each station the same type of features are extracted which allows the concatenation of station-dependent inputs in the following part.

3.2 Spatial representation

After the characterization of the signal traces, the extracted features are used as input for the second part and concatenated with the additional feature maps holding the arrival times, station coordinates and the station states. The following network structure is based on densely connected [14] and separable convolutions [15]. This stabilizes the training process and provides important physics parameters like the arrival time in each layer. We observed that using batch normalization adds too much disturbance in the training. Hence, as activation functions we used scaled exponential linear units [16] to normalize the data between the layers.

3.3 Task-related part

The final part of the neural-network architecture consists of individual network parts for each reconstruction task. This last stage is based on residual units [6] and pooling operations. In total, we used two residual blocks covering three residual units each. Each of the residual units contains two layers using a rectified linear unit in between. As the last layer we used global average pooling.

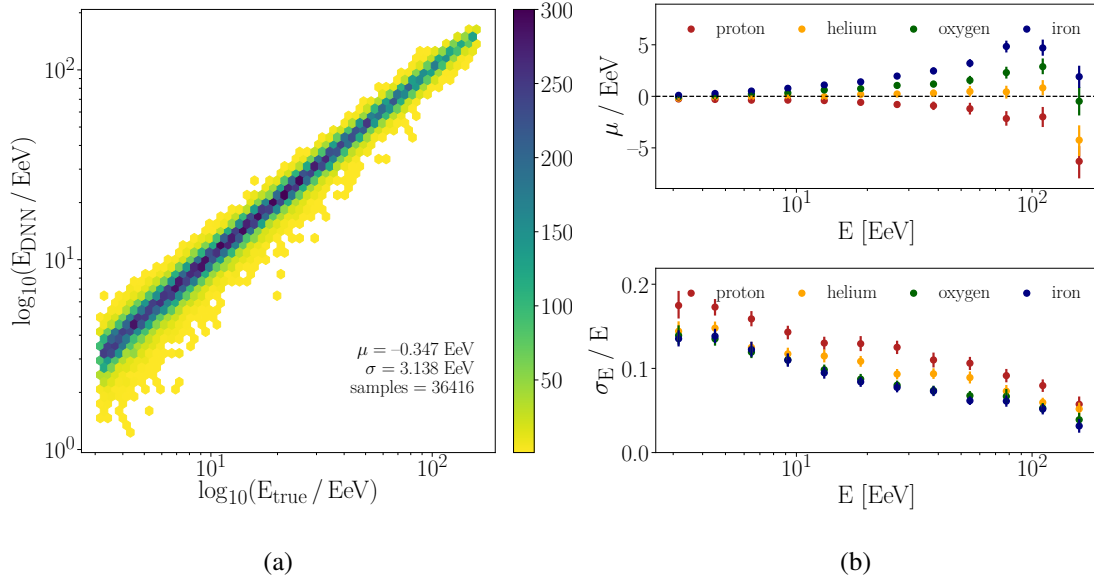


Figure 3: (a) Correlation between reconstructed and true energies. (b) Energy-dependent bias and resolution of the reconstruction shown for different primaries.

4. Performance in simulations

We used in total $\approx 400,000$ air showers simulated with CORSIKA [17] using the hadronic interaction model EPOS-LHC [18]. The data is simulated in an energy range of 1 – 160 EeV following a spectrum of E^{-1} . As primary particles, protons, helium, oxygen and iron nuclei are used covering a full azimuth range and a zenith range of $\theta \in [0^\circ, 65^\circ]$. We used 360,000 showers for training the network, 4,000 for the validation and around 37,000 for the final evaluation.

4.1 Training

We trained the model for 27 epochs on a Nvidia GeForce GTX 1080 graphics card which took ≈ 7 h with a batch size of 32. For training the network, we used Keras [19] with the TensorFlow [20] backend. As optimizer Adam [21] was used with its default settings. We further smoothly decayed the learning rate and dropped the learning rate by a factor of 1.33 when the validation loss did not decrease after three epochs. As loss for all tasks, we used the mean squared error and re-weighted the losses to the same order of magnitude.

4.2 Geometry reconstruction

Before investigating the reconstruction of complex shower variables like the shower maximum, the network needs to be capable of providing a reconstruction of the basic air-shower properties. For the validation of the deep-learning based reconstruction, we first investigated the quality of the reconstructed shower geometry. In Figure 2a, the angular distance between the reconstructed and the true shower axis is illustrated, showing a good angular resolution (68% quantile) of $q_{68} = 0.8^\circ$. The colors represent different primary particles. Figure 2b shows the reconstruction

of the shower core. The absolute resolution amounts to $\sigma \approx 37$ m. Further, no azimuth-dependent bias is visible which implies that the network is able to correct for shower asymmetry effects.

4.3 Reconstruction of the energy

After validating the basic reconstruction of the shower geometry, the reconstruction of the primary cosmic-ray energy can be studied. Figure 3a shows the reconstruction of the energy. The overall reconstruction shows no bias. In Figure 3b the different resolutions and biases are plotted for different primaries. The composition bias depends on the energy and increases for higher energies. The relative energy resolution improves for higher energies due to decreasing fluctuations and achieves a relative resolution of $\sigma_E/E \leq 10\%$ at around 100 EeV.

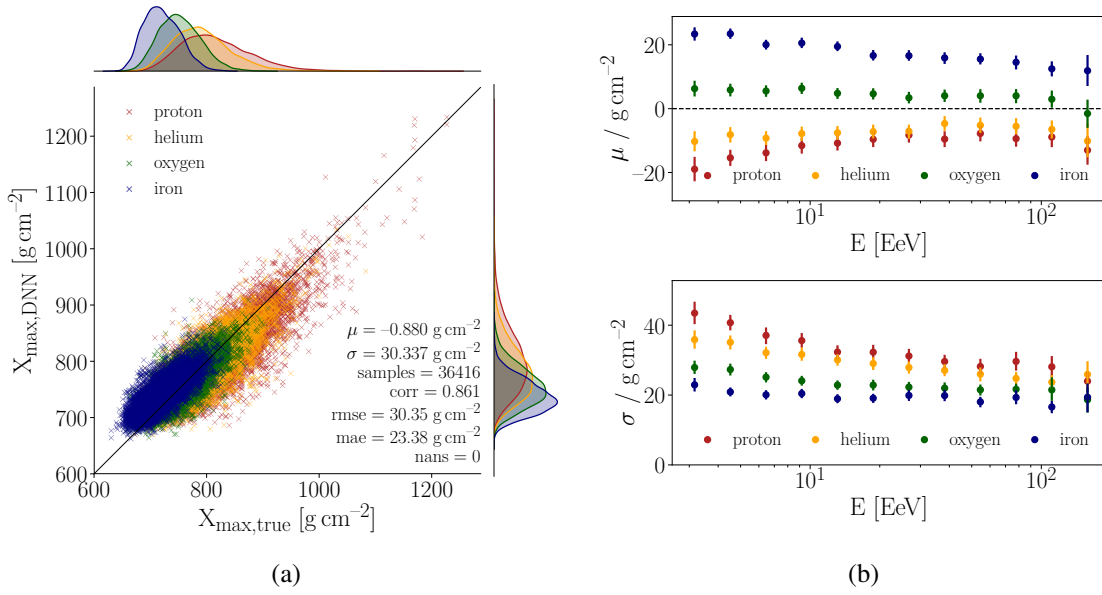


Figure 4: (a) Correlation between reconstructed and true depths of shower maximum X_{\max} . (b) Energy-dependent resolution and bias of the X_{\max} reconstruction.

4.4 Reconstruction of the shower maximum

With the precision described previously, the network is able to reconstruct the air-shower geometry and estimate the primary cosmic-ray energy. In the following the reconstruction of the shower maximum X_{\max} is investigated. In Figure 4a, the reconstructed shower maxima are shown for proton, helium, oxygen and iron. The correlation between the true X_{\max} and the reconstruction amounts to 0.8. It can be seen that the elements show separation in the reconstructed shower maxima, and hence the algorithm can be used for an estimation of the cosmic-ray mass. The overall resolution of the reconstruction is $\approx 30 \text{ g/cm}^2$. The energy dependence of the resolution and bias is shown in Figure 4b for different primaries. The bias decreases from $\approx 40 \text{ g/cm}^2$ at 3 EeV to $\leq 25 \text{ g/cm}^2$ at 150 EeV. Due to the decreased shower-to-shower fluctuations, the reconstruction of heavier elements shows an improved resolution of $\sigma_{X_{\max}} \approx 25 \text{ g/cm}^2$ at the highest energies.

5. Conclusion

Extensive air showers induce time-dependent signal patterns at the surface detector of the Pierre Auger Observatory. To reconstruct the properties of the primary cosmic ray we used a deep neural network. The presented algorithm relies on convolutions exploring huge amounts of data. We have discussed the intrinsic structure of our model, which learns time-dependent representations in a first stage. In the second stage the network allows for the extraction and combination of features in space and time. We have demonstrated that deep learning can be used to reconstruct the geometry and energy of the air shower using simulated surface-detector data. In addition, the reconstruction of the shower maximum X_{\max} showed very promising results. Further validating the performance with fluorescence detector measurements, and investigating different hadronic interaction models, would allow for a mass-composition estimation with the full SD event statistics.

References

- [1] A. Aab et al. [Pierre Auger Collaboration], The Pierre Auger Cosmic Ray Observatory, *Nucl. Instrum. Meth. A* **798** (2015) 172.
- [2] A. Aab et al. [Pierre Auger Collaboration], The Surface Detector System of the Pierre Auger Observatory, *Nucl. Instrum. Meth. A* **586** (2008) 409.
- [3] A. Aab et al. [Pierre Auger Collaboration], Depth of Maximum of Air-Shower Profiles at the Pierre Auger Observatory: Composition Implications, *Phys. Rev. D.*, **12** (2014) 1.
- [4] I. Goodfellow, Y. Bengio, A. Courville, Deep Learning, MIT Press, Cambridge, MA, US (2016).
- [5] Y. LeCun, Y. Bengio, G. Hinton, Deep Learning, *Nature* **521** (2015) 436.
- [6] K. He et al., Deep residual learning for image recognition, [arXiv/1512.03385](https://arxiv.org/abs/1512.03385).
- [7] O. Ronneberger, P. Fischer, T. Brox, U-Net: Convolutional Networks for Biomedical Image Segmentation, [arXiv/1505.04597](https://arxiv.org/abs/1505.04597).
- [8] D. Yu, L. Deng, Automatic Speech Recognition: A Deep Learning Approach, Springer, London, UK (2014).
- [9] O. Russakovsky et al., Imagenet large scale visual recognition challenge, *IJCV* **115** (2015) 211.
- [10] S. Argiro et al., The Offline software framework of the Pierre Auger Observatory, *Nucl. Instrum. Meth. A* **580** (2007) 1485.
- [11] A. M. Hillas, Angular and energy distributions of charged particles in the electron photon cascades in air, *J. Phys. G.* **8** (1982) 1461.
- [12] M. Ave, M. Roth, A. Schulz, A generalized description of the time dependent signals in extensive air shower detectors and its applications, *Astropart. Phys.*, **88** (2017) 46.
- [13] M. Erdmann, J. Glombitza, D. Walz, A Deep Learning-based Reconstruction of Cosmic Ray-induced Air Showers. *Astropart. Phys.* **97** (2018) 46.
- [14] G. Huang et al., Densely Connected Convolutional Networks, [arXiv/1608.06993](https://arxiv.org/abs/1608.06993).
- [15] F. Chollet, Xception: Deep Learning with Depthwise Separable Convolutions, [arXiv/1610.02357](https://arxiv.org/abs/1610.02357).
- [16] G. Klambauer, T. Unterthiner, A. Mayr, S. Hochreiter, Self-Normalizing Neural Networks, [arXiv/1706.02515](https://arxiv.org/abs/1706.02515).
- [17] D. Heck et al., CORSIKA: A Monte Carlo code to simulate extensive air showers, Forschungszentrum Karlsruhe Report FZKA (1998) 6019.
- [18] T. Pierog et al., EPOS LHC : test of collective hadronization with LHC data, [arXiv/1306.0121](https://arxiv.org/abs/1306.0121).
- [19] F. Chollet, Keras: Deep Learning for Python (2015), github.com/fchollet/keras.
- [20] M. Abadi et al., TensorFlow: Large-scale machine learning on heterogeneous systems (2015), [tensorflow.org](https://www.tensorflow.org).
- [21] D. P. Kingma, J. Ba, Adam: A Method for Stochastic Optimization, Proc. 3rd Int. Conf. on Learning Representations (ICLR), San Diego (2015), [arXiv/1412.6980](https://arxiv.org/abs/1412.6980).



The Energy Scale of the Pierre Auger Observatory

Bruce R. Dawson^{*a} for the Pierre Auger Collaboration^{†b}

^a*Department of Physics, The University of Adelaide, Adelaide 5005, Australia*

^b*Observatorio Pierre Auger, Av. San Martín Norte 304, 5613 Malargüe, Argentina*

E-mail: auger_spokespersons@fnal.gov

Full author list: http://www.auger.org/archive/authors_icrc_2019.html

The measurement of energy is one of the most important and challenging tasks of an astroparticle observatory, especially given that the energy must be accompanied by reliable statistical and systematic uncertainties. The energy scale of the Pierre Auger Observatory is based on observations made by its fluorescence detector, taking advantage of the near-calorimetric measurements afforded by this technique. This fluorescence energy calibration is transferred to the surface detector measurements via coincident fluorescence and surface detector observations of air showers at the hybrid observatory. In this contribution, we present the current status of our energy scale. We demonstrate our confidence in the cosmic ray energy assignments by discussing our methods and their systematic and statistical uncertainties. We describe the impact of recent improvements in the estimation of invisible energy, and discuss uncertainties associated with the fluorescence yield, the atmosphere, detector calibration, and the event reconstruction process.

36th International Cosmic Ray Conference — ICRC2019

24 July – 1 August, 2019

Madison, Wisconsin, USA

^{*}Speaker.

[†]for collaboration list see PoS(ICRC2019)1177

1. Introduction

The Pierre Auger Observatory [1] consists of a surface detector (SD) of 1660 water-Cherenkov detector stations spanning an area of 3000 km² overlooked by 27 large telescopes forming the fluorescence detector (FD). This combination of the SD and the FD provides the advantages of a so-called hybrid observatory. The SD consists of robust detectors that operate 24 hours per day, measuring characteristics of the extensive air shower (EAS) at ground level, including the water-Cherenkov detector signal 1000 m from the shower core, $S(1000)$, the primary energy estimator from the SD. On clear, dark nights the FD observes showers also detected by the SD, providing a near-calorimetric measurement of the primary cosmic ray energy, since the quantity of fluorescence light produced is directly proportional to the total energy deposited by the EAS in the atmosphere. Thus, these hybrid observations calibrate the SD measurement of $S(1000)$ (or more precisely a zenith-angle corrected version of this signal), providing the “energy scale” of the observatory 24 hours per day [2]. While conceptually simple, the definition of the energy scale from the FD observations requires careful measurements and the understanding of many detector and reconstruction effects. Of particular importance are real-time measurements of atmospheric characteristics, including aerosols and clouds [3].

In 2013 we described a comprehensive study of the Auger FD energy scale [4], including a systematic error budget and an estimate of the FD energy resolution. The plan for this contribution is not to update the table of systematic uncertainties, though we plan to publish minor adjustments in the near future. Rather, we will describe the ongoing work in several areas dedicated to cross-checks of assumptions, reduction of model-dependence, incremental improvements to the energy scale, and checks on systematic uncertainties. These activities span both detector and reconstruction effects. We have not discovered any effect that contradicts the 2013 systematic uncertainties in energy, which total 14%.

We have recently completed a review of the FD energy resolution, reported here for the first time. With this quantity and its energy dependence, we can estimate the resolution in the SD energy estimators, important when correcting our SD-based energy spectra for resolution effects [2].

2. Determining primary cosmic ray energy with the fluorescence technique

We briefly describe the method for determining the EAS energy using the FD technique, with reference to the energy systematic uncertainties listed in Table 1. These systematics are estimated for energies above 3×10^{18} eV, the full efficiency threshold energy of the 1500 m-spaced SD array. However, the total systematic of 14% is expected to be approximately valid at lower energies, for example down to an energy of 10^{17} eV relevant for measurements with the 750 m SD array [5].

The air shower deposits energy into the atmosphere via ionisation energy losses, and a known fraction of that energy appears as fluorescence light. We use the AIRFLY laboratory measurements [6] of fluorescence yield, including its precise measurement of the emission spectrum, and the fluorescence quenching dependence on atmospheric pressure, temperature, and humidity. The total energy systematic associated with the fluorescence yield is 3.6%.

The isotropically emitted light traverses the atmosphere to reach the FD, typically through larger distances for the rarer, higher energy showers. Energy systematics from the atmosphere include those associated with scattering of light by molecules and aerosols, and those connected to

the quenching of fluorescence light at the source. The total systematic ranges between 3.4% and 6.2% (smaller uncertainty at lower energies), dominated by the uncertainty in aerosol optical depth.

The photometric calibration of the FD telescopes contributes 9.9% to the energy systematic uncertainty. This includes uncertainties in the absolute calibration at 375 nm using the end-to-end “drum” method performed from time to time, and the nightly relative calibration done with fixed telescope-based light sources [1]. Uncertainty in the wavelength-dependence of the telescope efficiency (including filter, lens, mirror and camera) is also included, one of the systematics checked recently, and reported on below.

Given the measured light as a function of time at the FD, the “shower profile”, or energy deposit as a function of atmospheric depth, $\frac{dE}{dX}(X)$, is reconstructed. Several reconstruction uncertainties contribute to an energy systematic of 6.5% – 5.6%, slightly larger at lower energies. The main contributor is an uncertainty in light collection, given that the image spot is a convolution of the optical point spread function and the finite width of the shower image. Also included are a small systematic associated with the model for multiple-scattered light, and a contribution to account for systematics from the constraints placed on parameters of the Gaisser-Hillas function (see below), mainly important for close-by showers where a smaller range of atmospheric depths is viewed by the FD.

The FD technique actually measures the *calorimetric* energy of the EAS, that portion of the primary cosmic ray energy visible via fluorescence light. A small ($\sim 15\%$) correction is applied to the calorimetric energy to get the total energy, accounting for the *invisible energy*, E_{inv} , associated with high energy muons and neutrinos which deposit most of their energy in the ground. A systematic uncertainty in this correction leads to a systematic in the primary energy of 3% – 1.5%. Our data-driven approach to estimating E_{inv} has recently been updated, and is discussed below.

The FD energy scale must be transferred to the SD. Each SD event has an energy estimator $S(1000)$, the detector signal 1000 m from the shower core [7]. To remove the zenith angle dependence, we convert $S(1000)$ to S_{38} , the value it would have if the shower had arrived with the median zenith angle of $\theta = 38^\circ$. Then, hybrid events are used to fit a relationship between S_{38} and the FD-measured energy, E_{FD} , of the form $E_{FD} = AS_{38}^B$. In 2013, the statistical error in this fit led to a small contribution to the systematic in the SD energy scale, but given the current event statistics, this contribution is now negligible. However, a related systematic contribution of 5% is part of Table 1 to account for stability of the energy scale over time. This was estimated by checking the stability of the SD energy, $E_{SD} = AS_{38}^B$, for a given S_{38} over a 9-year period.

3. Examples of checks and improvements to the FD energy scale

3.1 Calibration

Absolute calibrations of the FD telescopes are performed periodically at 375 nm, with nightly

Systematic uncert. in energy scale	
Fluorescence yield	3.6%
Atmosphere	3.4% – 6.2%
FD calibration	9.9%
FD profile recon.	6.5% – 5.6%
Invisible energy	3% – 1.5%
Energy scale stability	5%
TOTAL	14%

Table 1: Current energy scale systematic uncertainties [4]. A range refers to the change in systematic from 3×10^{18} eV to the highest energies.

relative calibrations done at 470 nm [1]. At the time of the 2013 energy scale definition, the relative spectral response of the telescopes (relative efficiency vs. wavelength) was based on a measurement at a single telescope at 5 wavelengths (320 nm to 420 nm) using a filtered xenon light source in the drum calibration apparatus. The wavelength range of the spectral efficiency is mostly defined by the band pass of the UV-transmitting optical filters. The efficiency also depends on the transmission of the ring of Schmidt corrector lenses at the aperture, the mirror reflectivity, and the PMT quantum efficiency. We have since improved the measurements of the spectral efficiency, using a drum-mounted monochromator and xenon light source, with measurements over a range from 280 nm to 440 nm in 5 nm steps [8]. Half of the observatory's telescopes are constructed with aluminized glass mirrors, and half with polished aluminium mirrors. The corrector lenses are made of either Borofloat-33 or BK7 glass. Thus, we have measured the relative spectral efficiency for two telescopes each of the four possible combinations of mirror and corrector material. We conclude that the use of these telescope-wise spectral efficiencies, rather than the original five-point calibration, results in cosmic ray energy increases of about 1% averaged over all telescopes, with one telescope type increasing by 2.5%. These shifts are well within the systematic uncertainty of 3.5% assigned to the efficiency, as part of the 9.9% calibration systematic, in the 2013 energy scale study [4]. We note that in [8] we have also established that the relative spectral efficiency is stable with time.

In recent years we have implemented multiple relative calibrations of each telescope during a night, a so-called running calibration. Each camera is illuminated with LED flashes every 30 minutes (with the shutters on the telescope aperture open) as well as at the beginning and end of the nightly run (with shutters closed). This has enabled us to study the nightly variation in calibration associated with the PMT exposure to night sky background light. We conclude that the variations in the relative gain of PMTs during a night are small (up to 2%) and consistent with the systematic assigned to this in the 2013 study.

Cross-checks of the absolute photometric calibration of the FD telescopes have been achieved using bright U-band stars [9, 10]. The apparent absolute brightness of a star is measured as a function of the air-mass traversed by the light, allowing for the effect of the atmosphere to be accounted for with this standard astronomical technique. Comparing the estimated star brightness above the atmosphere with the true value yields a check of the calibration. We have confirmed the standard calibration of the FD to a level of approximately 8%, the systematic uncertainty associated with the star technique for a star like Sirius, with a well-known spectrum and apparent magnitude.

3.2 Atmosphere

As mentioned, the dominant energy systematic related to the atmosphere is in the determination of the aerosol content. We derive the vertical aerosol optical depth as a function of height, $VAOD(h)$, from FD observations of the two central laser facilities, the CLF and XLF [11]. Several small improvements have been made to the analysis in recent years, including accounting for the fact that multiple-scattered laser light reaches the FD, and that the quantity of light scattered out of the laser beam is affected by the aerosol content, even though the dominant process is molecular scattering. These improvements, implemented in 2017, led to increases in assigned cosmic ray energies from 1.5% at $10^{17.5}$ eV to 3% at $10^{19.5}$ eV [12]. More recently, a complete overhaul of the VAOD analysis software (and an integration of it within the observatory's Offline analysis frame-

work [13]) has allowed us to review all the analysis steps, as well as the statistical and systematic error estimates [3]. The systematics reported in 2013 are still valid.

3.3 Reconstruction

In reconstruction of the shower development profile, $\frac{dE}{dX}(X)$, our normal practice is to fit the Gaisser-Hillas (GH) function [1, 14] to the measurements. This takes account of energy losses outside the field of view of the FD, since the calorimetric energy estimate, E_{cal} , is the integral of the GH function over all X . The GH function has four fitted parameters, namely two shape parameters X_0 and λ , the depth of shower maximum X_{max} , and the energy deposit at maximum, $(dE/dX)_{max}$. In the past, we have fitted these parameters with a procedure that loosely constrains X_0 and λ (tuned using data), and the shower “width”, $k = E_{cal}/(dE/dX)_{max}$ (tuned using simulations) [15, 16]. These constraints have little effect on showers with measurements over a large range of depth X , but they help minimise systematics for shorter track-length events. However, a long-standing problem, intrinsic to the GH function, is that fitted values of X_0 and λ are strongly correlated.

In 2019 we have implemented a new function for the shower profile, based on the GH function, but with new shape parameters R and L [17, 18], namely

$$f(X) = (dE/dX)_{max} \left(1 + \frac{R}{L}(X - X_{max}) \right)^{1/R^2} \exp\left(-\frac{X - X_{max}}{RL}\right). \quad (3.1)$$

Here L is a measure of the shower profile width, and R is an asymmetry parameter. These two parameters are not correlated, despite them being related to the two parameters X_0 and λ that they replace (see [18]). In our new procedure, we fit the four parameters of the function, with loose constraints on R (0.257 ± 0.055) and L ($(227.3 + 7.44 \log(E_{cal}/EeV)) \pm 11.5 \text{ g/cm}^2$). The central values come from fits to well-measured showers, while the (1σ) ranges are determined, from simulations, to be large enough to account for shower-shower fluctuations, and different primary masses. The new procedure reduces reconstructed energies by less than 0.5% on average, but it has the benefit of fewer constraints and better behaved fits.

3.4 Invisible Energy

As mentioned earlier, a portion of the cosmic ray energy is not visible through the fluorescence technique, since that energy is carried by neutrinos and high energy muons that deposit their energy into the ground. Since 2013, we have used data from the observatory to estimate this invisible energy, E_{inv} , rather than using estimates from air shower simulations [19]. In 2019 we have implemented new E_{inv} estimates, after a detailed study of two alternative methods both using Auger data, one using “vertical” events ($\theta < 60^\circ$) and the other using inclined events ($60^\circ < \theta < 80^\circ$) [20]. The methods give consistent results within uncertainties, and are consistent with the 2013 estimates. We now use E_{inv} from the inclined shower analysis, since it is the most direct of the two methods, given that inclined showers are muon-dominated at ground level. The advantages of using a data-driven estimation of E_{inv} are that simulations are known to be deficient in their estimation of the muon content of air showers [21] (critical to the invisible energy), and that the estimation naturally takes into account the evolving mass composition of the cosmic rays with energy.

Our 2019 E_{inv} parameterisation covers primary energies E_0 from 10^{17} eV to 10^{20} eV, with values of E_{inv}/E_0 ranging from 20% to 12%, and with systematic uncertainties less than 2% [20].

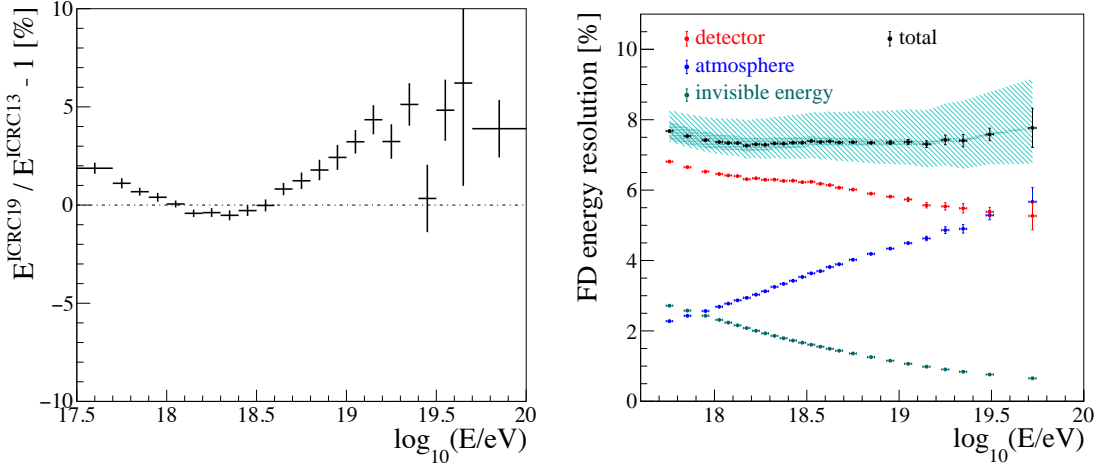


Figure 1: (a): A summary of the FD energy changes for a representative sample of showers, comparing the 2013 and the present FD energy scale. (b): The 2019 FD energy resolution, showing the contributions from the detector (including reconstruction), the atmosphere, and the invisible energy correction. The shaded blue area represents the total systematic uncertainty on the resolution, dominated by the detector/atmosphere, but including the contribution from E_{inv} (darker shading).

This more extensive study has confirmed the 2013 analysis, and the systematic uncertainties are compatible with the 2013 energy scale error budget in Table 1.

3.5 Summary of FD energy shifts since 2013

In Figure 1(a) we show a summary of the small shifts in FD energy assignment that have occurred since 2013, including those from improvements described above. This figure has been derived using a sample of showers already available in 2013, which have been analysed with the reconstruction code used for ICRC 2013 and ICRC 2019.

4. The FD energy resolution

We have recently reviewed the assignment of statistical uncertainties to FD-measured energies, and report results here for the first time. We use this FD energy resolution to scale the statistical errors of the SD-measured energies (by requiring a good χ^2 for the $E_{FD} = AS_{38}^B$ calibration fit), and the deduced SD resolution is used to correct the measured SD energy spectra for resolution effects [2]. The sources of finite FD energy resolution can be divided into three areas - the atmosphere, the detector (including reconstruction), and the invisible energy correction. The study was performed using a large sample of hybrid events with at least three triggered SD stations from the main array, defining an energy range from $10^{17.7}$ eV to $10^{19.8}$ eV. (A similar study using the 750 m array, not discussed here, has extended the energy range down to approximately 10^{17} eV). We show the results in Table 2 and Figure 1(b), and we now explain the contributions.

The atmosphere: We use 3-hourly atmospheric density profiles from the GDAS assimilation model [22]. Fluctuations of pressure, temperature and humidity around the GDAS profiles have been estimated using locally-launched radiosonde balloons, resulting in a 1% (energy-independent) contribution to the energy resolution. Statistical uncertainties in the aerosol optical depth result from uncertainties in the laser energy and FD photometric calibration, and from the variation in

FD energy resolution	
Aerosol optical depth	1.2% – 3.8%
Horiz. uniform. of aerosols	1.6% – 5%
Molecular atmosphere	1%
Nightly relative calib.	1.3%
Time drift of FD energies	2.5%
Mismatch between telescopes	3.5%
Stat. error from geom. and GH fit	4.6% – 2.8%
Extrapolation of profile	2.2%
E_{inv} shower-to-shower fluc.	1.1% – 0.6%
E_{inv} mass uncertainty	2.4% – 0.3%
TOTAL	7.6% – 8.6%

Table 2: New results on the fluorescence detector energy resolution. The table is separated into three sections, referring to contributions from the atmosphere, from the detector and reconstruction, and from invisible energy. A range refers to the change in resolution from $10^{17.7}$ eV to $10^{19.8}$ eV.

aerosol optical depth across the four quarter-hour measurements in a given hour. These aerosol uncertainties have been reviewed as part of the software overhaul described above, and contribute 1.2% to 3.8% to the FD energy resolution, larger at higher energies. Finally, comparing reconstructed energies, and their uncertainties, for “stereo” events (showers seen from two FD sites) has allowed us to estimate an uncertainty that we attribute to non-uniformity of aerosols across the observatory. (Our aerosol measurements, using central laser facilities, probe aerosol content along a limited number of paths.) We estimate this contribution to be from 1.6% to 5%, again energy-dependent. The experimental uncertainty of this stereo study (and whether the effect seen is wholly attributable to non-uniformity of aerosols) leads to the dominant contribution to the systematic uncertainty on the total resolution, shown with the blue band in Figure 1(b).

The detector and reconstruction: Detector calibration plays a major role here. Uncertainties include a new estimate of the contribution of the nightly relative calibration (from the new running calibration described above) of 1.3%, and a contribution of 3.5% that takes into account the small systematic differences in telescope gains across the observatory, determined by studying the ratio E_{FD}/E_{SD} for showers seen by different telescopes. Long-term monitoring of the stability of the telescope gains introduces an uncertainty of 2.5% to any FD measurement. In the area of reconstruction, formal statistical uncertainties in the shower geometry and the profile function fit (Eq. 3.1) result in a contribution to energy resolution of between 4.6% and 2.8%. We include an additional 2.2%, derived from simulations, to take into account the uncertainty of the extrapolation of the GH function beyond the viewed profile, something not included in the formal fit error.

The invisible energy correction: This data-driven correction is a fixed function of primary energy, so natural shower-to-shower fluctuations in development, and primary mass variations from the mean mass at a given energy, result in statistical uncertainties in the E_{inv} correction. We estimate the contribution to energy resolution from shower-to-shower fluctuations to be about 1%,

with a contribution from mass composition uncertainty ranging from 2.4% to 0.3%, reflecting the reduction in the spread in mass with energy inferred from X_{\max} measurements [23]. Systematic uncertainties in these estimates lead to the darker-shaded band in Figure 1(b), derived from the uncertainty in the spread of mass, and from assuming either pure proton or pure iron primaries in the estimate of shower-to-shower fluctuations.

The overall FD energy resolution shown in Figure 1(b) takes into account the advantage of “stereo” views of showers at the highest energies. In these cases, the energy used in analyses is the mean of the reconstructed energies (weighted by uncertainties) from the two (or more) stereo views, with the resulting improvement in the statistical error.

5. Conclusion

We have reviewed the main systematic uncertainties associated with measuring cosmic ray energy with the Pierre Auger Observatory fluorescence detector. A series of studies have confirmed the total systematic uncertainty of 14% established in 2013 [4]. A new study of the FD energy resolution has also been described, an important ingredient in evaluating SD energy resolution, and in the correction of energy spectra for resolution effects. The new FD resolution is also consistent with that reported in 2013, but it results from a thorough review where several components have changed in their contributions.

References

- [1] A. Aab et al. [Pierre Auger Collaboration], Nucl. Instrum. Meth. A **798** (2015) 172.
- [2] V. Verzi et al. [Pierre Auger Collaboration], PoS (ICRC2019) 450.
- [3] V.M. Harvey et al. [Pierre Auger Collaboration], PoS (ICRC2019) 283.
- [4] V. Verzi et al. [Pierre Auger Collaboration], Proc. 33th ICRC 2013, Rio de Janeiro, Brazil [arXiv:1307.5059].
- [5] A. Coleman et al. [Pierre Auger Collaboration], PoS (ICRC2019) 225.
- [6] M. Ave et al. [AIRFLY Collaboration], Astropart. Phys. **42** (2013) 90.
- [7] D. Mockler et al. [Pierre Auger Collaboration], PoS (ICRC2019) 353.
- [8] A. Aab et al. [Pierre Auger Collaboration], Astropart. Phys. **95** (2017) 44.
- [9] A. Segreto et al. [Pierre Auger Collaboration], Proc. CR Intl. Seminar 2018, Nucl. Part. Phys. P. (submitted).
- [10] P.H. Nguyen, Ph.D. thesis, The University of Adelaide, <http://hdl.handle.net/2440/113385> (2018).
- [11] P. Abreu et al. [Pierre Auger Collaboration], JINST **8** (2013) P04009.
- [12] M. Malacari et al. [Pierre Auger Collaboration], PoS (ICRC2017) 398.
- [13] S. Argirò et al., Nucl. Instrum. Meth. A **580** (2007) 1485.
- [14] T.K. Gaisser and A.M. Hillas, Proc. 15th ICRC, Plovdiv, Bulgaria **8** (1977) 353.
- [15] M. Unger et al., Nucl. Instrum. Meth. A **588** (2008) 433.
- [16] F. Fenu et al. [Pierre Auger Collaboration], PoS (ICRC2017) 486.
- [17] S. Andringa, R. Conceição and M. Pimenta, Astropart. Phys. **34** (2011) 360.
- [18] A. Aab et al. [Pierre Auger Collaboration], JCAP**03** (2019) 18.
- [19] M. Tüeros et al. [Pierre Auger Collaboration], Proc. 33th ICRC 2013, Rio de Janeiro, Brazil [arXiv:1307.5059].
- [20] A. Aab et al. [Pierre Auger Collaboration], “Data-driven estimation of the invisible energy of cosmic ray showers with the Pierre Auger Observatory”, Phys. Rev. D (in press) (2019).
- [21] A. Aab et al. [Pierre Auger Collab.], Phys. Rev. D **91** (2015) 032003; Errata: Phys. Rev. D **91** (2015) 059901.
- [22] P. Abreu et al. [Pierre Auger Collaboration], Astropart. Phys. **35** (2012) 591.
- [23] J. Bellido et al. [Pierre Auger Collaboration], PoS (ICRC2017) 506.



Reconstruction of Vertical Events Recorded by the Surface Detector of the Pierre Auger Observatory

Daniela Mockler^{*a} for the Pierre Auger Collaboration^{†b}

^a*Université Libre de Bruxelles, Brussels, Belgium*

^b*Observatorio Pierre Auger, Av. San Martín Norte 304, 5613 Malargüe, Argentina*

E-mail: auger_spokespersons@fnal.gov

Full author list: http://www.auger.org/archive/authors_icrc_2019.html

At ground level, surface detector arrays sample the secondary particles from extensive air showers induced by primary cosmic rays with ultra-high energy interacting with the Earth's atmosphere. The recorded events are used to study the energy spectrum, arrival directions, and mass composition of the cosmic rays.

The surface detector of the Pierre Auger Observatory comprises 1660 water-Cherenkov stations deployed on a tessellated triangular grid. Each station is filled with 12 tons of ultra-purified water viewed by three 9-inch photomultipliers, which record the Cherenkov light produced mainly by electrons and muons entering the detector. Physics events are selected by exploring the temporal and spatial combination of the individual detector information in real time. The reconstruction algorithm determines the arrival direction and the energy of the primary particle, and will be described for selected events with zenith angles less than 60° (a dataset referred to as *vertical*). The presented reconstruction procedure has been successfully applied to measured and simulated showers.

36th International Cosmic Ray Conference — ICRC2019

24 July – 1 August, 2019

Madison, Wisconsin, USA

*Speaker.

†for collaboration list see PoS(ICRC2019)1177

1. Introduction

The main objective of the Pierre Auger Observatory is the measurement of the energy spectrum, mass composition, and arrival direction of ultra-high energy cosmic rays. The manifold studies profit from the hybrid detector design, combining a large surface detector array with a fluorescence detector [1]. The flux of cosmic rays at the highest energies is as low as one particle per square-kilometer per steradian per century, and as such has to be measured by ground-based detectors. Upon entering the Earth's atmosphere, a primary cosmic ray initiates an extensive air shower. The fluorescence detector (FD) observes the longitudinal development of the shower by recording the fluorescence light emitted along the shower path. The surface detector (SD) measures the lateral distribution at the ground by sampling the secondary particles of the air shower with water-Cherenkov stations. Due to the tessellated array layout and a spacing of 1500 m between the stations, the threshold for full efficiency is reached for primary energies greater than 3×10^{18} eV. A smaller, nested array in the north-west of the Observatory with half of the original spacing extends the threshold of full efficiency down to 3×10^{17} eV [2, 3]. The whole array spans an area of 3000 km². The duty cycle of the surface detector is nearly 100%, while the uptime of the fluorescence detector is limited to clear and almost moonless nights. Thus, the bulk of data is provided by the SD.

In this contribution we present the reconstruction chain for the data measured with the SD, including the data-taking in individual stations, the trigger system deployed to select air shower events, and the reconstruction of these events for zenith angles up to 60° with the corresponding reconstruction uncertainties.

2. Surface detector

The SD array encompasses 1600 water-Cherenkov stations. Each station has a base of 10 m² and is filled with 12 tons of purified water up to a height of 1.2 m. The water volume, which is contained inside a diffusively-reflective liner, is viewed from the top by three 9-inch photomultiplier tubes which record the Cherenkov light produced by relativistic charged particles traversing the water. Each station is equipped with a solar photovoltaic system which provides power for the electronics and communication system, thus making the station self-contained. Due to the limited total bandwidth of only 1200 bits/s for data transmission from the stations to the central data acquisition system (CDAS), the calibration of each station is done automatically by the local electronics. The calibration is based on recording the average charge observed by a PMT for through-going muons from the atmospheric background. Each PMT provides two raw ADC traces for which an individual baseline has to be determined. One signal is directly taken from the anode, the other one is taken from the last dynode after an amplification and inversion within the PMT base electronics to a total nominal signal of 32 times the anode signal. This readout strategy allows for a broad dynamic range. An example of such a signal trace is shown in Fig. 1a. In every recorded trace, a reasonable signal range needs to be selected by defining a start and stop time for each signal trace, as indicated by the dashed vertical lines. For the calibration, a 61 s worth sample of background signals is stored together with the event data. From this, a histogram of integrated charges is created, as depicted in Fig. 1b. The position of the second maximum corresponds to the signal

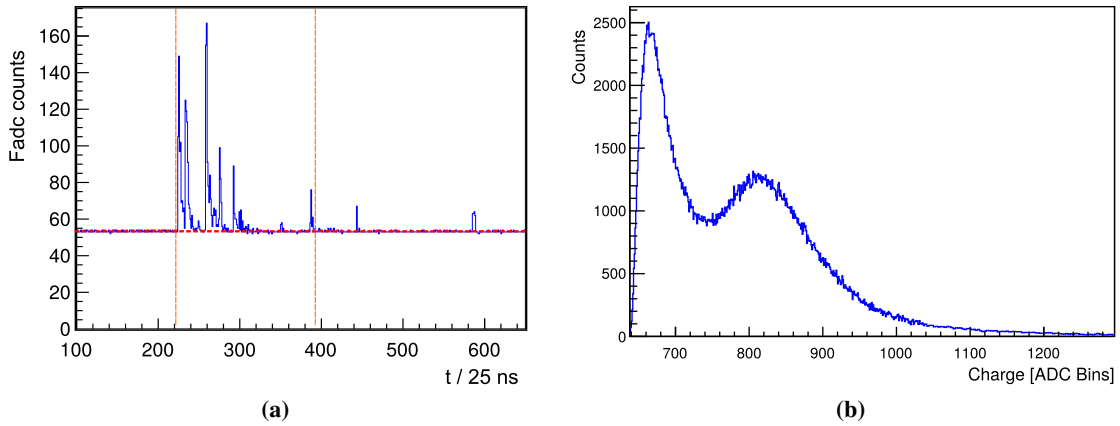


Figure 1: (a) Example of a raw ADC trace. The baseline is shown as horizontal dashed line, while the start and stop times of the signal are indicated by the dashed vertical lines. (b) Each ADC signal is calibrated into units of VEM. The calibration factor is extracted from the position of the maximum in the charge histogram (here at ~ 800 ADC counts).

of background muons and is used to convert the ADC signals into the reference units of a Vertical Equivalent Muon (VEM), which is used as common reference level for the station signals [4]. After subtracting the baseline and calibrating the signal pieces into VEM units, the total station signal is then obtained as the average of the individual PMT signals. When a shower core falls close to a station, the dynamic range of the electronics is not sufficient and the signal saturates. If only the dynode channel saturates, the signal is recovered by reading out the anode channel. For a saturation of the anode channel, a signal-recovery algorithm is applied [5]. Based on the spatial and temporal combination of the first-level station triggers, an array trigger is formed by CDAS and all data satisfying this trigger are permanently stored [6].

3. Data selection and event building

The ingredients for the subsequent shower reconstruction are the start time and the size of the station signals with their respective uncertainties. The uncertainties on the signal start time and the total station signal are determined by analyzing data recorded with doublet stations, a subset of SD stations equipped with partner stations. Being only ~ 11 m apart, the two stations of a doublet sample basically the same part of the air shower. The signal uncertainty can be described by a Poisson-like parameterization, including a dependence on the zenith angle [7]. The station signals and their uncertainties are used in the reconstruction of the lateral distribution function at the ground. The uncertainty of the signal start time affects the angular resolution. The main uncertainty stems from the uncertainty in the arrival time of the shower particles due to the thickness of the shower front. The particle density in the shower front decreases with increasing distance to the shower core and thus fewer particles enter the stations, resulting in a delayed start time of the signal.

At this stage, the events stored at CDAS not only contain real shower events but also accidental events. To select only the events due to air showers, an additional trigger level is applied offline. It requires at least three adjacent stations, whose signal start-times are compatible with a planar

shower-front moving at the speed of light. In next steps, the list of possible event stations has to be cleared from accidental stations, whose signal times coincide by chance. For this, a seed of three neighboring stations with largest signals is required to determine a first approximation of the development of the shower plane,

$$c(t_i - t_1) = -\hat{a}(\vec{x}_i - \vec{x}_1), \quad (3.1)$$

where \vec{x}_1, t_1 are the location and trigger time of the first seed station, respectively. With this, a provisional shower axis \hat{a} is found. Next, all stations with trigger times not matching this shower front are discarded from the event. In addition, triggered stations which have no triggered neighbor station within 1.8 km or two triggered neighbors within 5 km are removed from the station list. As a last step, all active stations which exhibit no trigger but are otherwise functional are flagged as zero-signal stations and are kept for the subsequent event reconstruction as they provide additional constraints for the reconstruction.

4. Event reconstruction

In the following, the list of stations belonging to an event is used for the reconstruction. The shower geometry is approximated by fitting a plane for the shower front, using the information of the event stations:

$$\chi^2 = \sum_i \frac{(t_i - t_{\text{sh}}(\vec{x}_i))^2}{\sigma_i^2}, \quad (4.1)$$

with t_{sh} as the expected time the shower front passes the station location \vec{x}_i and σ_i being the start-time uncertainty of the signal in station i . A more realistic shower model is obtained when allowing for a curvature of the shower front. The true curvature of the shower front is unknown and hence the reconstruction utilizes two slightly different implementations of the shower curvature, a parallel-parabolic and a concentric spherical front-model. Both models are shown in Fig. 2a in addition to the start times of the triggered stations. The signal times are given relative to the planar shower front. The two station sets shown arise due to different modes used to select and calibrate the individual signals.

The reconstruction of the lateral profile of a shower depends on the recorded signal sizes. With increasing distance to the shower axis, the measured signals decrease, which can be described by a lateral distribution function (LDF) as

$$S(r) = S(r_{\text{opt}})f_{\text{LDF}}(r), \quad (4.2)$$

with f_{LDF} being normalized such that $f_{\text{LDF}}(r_{\text{opt}}) \equiv 1$. The optimal distance r_{opt} is 1000 m for the surface array [8]. In general, this distance depends on the grid spacing and describes the optimal distance for which the LDF has the least systematic impact on the shower size estimator $S_{1000} \equiv S(r_{\text{opt}})$. As the true LDF is unknown, the functional form of f_{LDF} was chosen empirically. Similar to the implementation of the curvature model, two realizations of the LDF are available in the two algorithms used for analysis of the data,

$$f_{\text{LDF}}^{\text{NKG}} = \left(\frac{r}{r_{\text{opt}}} \right)^{\beta} \left(\frac{r+r_1}{r_{\text{opt}}+r_1} \right)^{\beta+\gamma}, \quad (4.3)$$

$$f_{\text{LDF}}^{\text{LLP}} = \begin{cases} \exp(\beta\rho + \gamma\rho^2), & r > r_c \\ \exp(\beta\rho + \gamma(2\rho - \rho_c)\rho_c), & r \leq r_c, \end{cases} \quad (4.4)$$

with $r_1 = 700\text{ m}$ and $r_c = 300\text{ m}$, $\rho = \ln(r/r_{\text{opt}})$. In Eq. (4.3), the LDF is described by a modified NKG function [9, 10], while Eq. (4.4) uses a log-log parabola. In both realizations, the LDF slope parameters are given as β and γ . The properties of the primary cosmic ray (mass, energy) as well as the shower development in the atmosphere affect the slopes of the LDF. To account for this, β and γ are parameterized respectively for both LDF realizations as function of zenith angle and shower size. Given the measured signals in the stations and their distances to the shower axis obtained in the previous geometry fit, the fit of the LDF is then maximizing the probability that the shower had a certain core position \vec{x}_c and shower size S_{1000} written as likelihood

$$\log \mathcal{L} = \sum_i \log P(S_{1000}, \vec{x}_c | S_i, \vec{r}_i). \quad (4.5)$$

The probability P includes contributions of both triggered stations with signal and zero-signal stations, whose signals were not sufficient to cause a trigger. The resulting shower size estimator S_{1000} is affected by daily and seasonal atmospheric modulations which change the effective slant depth a shower traversed [11]. In addition, the shower size depends on the azimuth angle of the incident primary particle with respect to the geomagnetic field as charged particles are deflected by the field [12]. To obtain an unbiased shower size estimator both effects are corrected for. In the last step, S_{1000} has to be corrected for attenuation effects in the atmosphere. With increasing zenith angle, the electromagnetic shower component gets more and more attenuated as the amount of traversed atmosphere increases, resulting in a smaller observed shower size at the ground. Using a constant intensity cut method [13], the shower size estimator is converted to the shower size which would have been measured had the shower arrived at an angle of 38° . This shower size is also referred to as S_{38} and is the unbiased energy estimate of the SD. The SD energy is then obtained by calibrating S_{38} to the energy measured by the FD using a subset of showers that can be reconstructed independently by both detectors [14, 15].

5. Reconstruction uncertainties

5.1 Angular resolution

The angular accuracy depends on the start times of the individual stations, which in turn depend on the particle distribution within the shower front as well as on the timing precision of the GPS. The angular resolution (AR) is investigated with full Monte-Carlo simulations for the two primary masses, proton and iron, using EPOS-LHC as hadronic interaction model. Each shower is distributed several times on the array using random core positions and the reconstructed shower directions \hat{a}_{rec} are then compared to the true shower axis \hat{a} by calculating the space-angle η between the arrival directions. The distribution of η can be described by a Rayleigh distribution

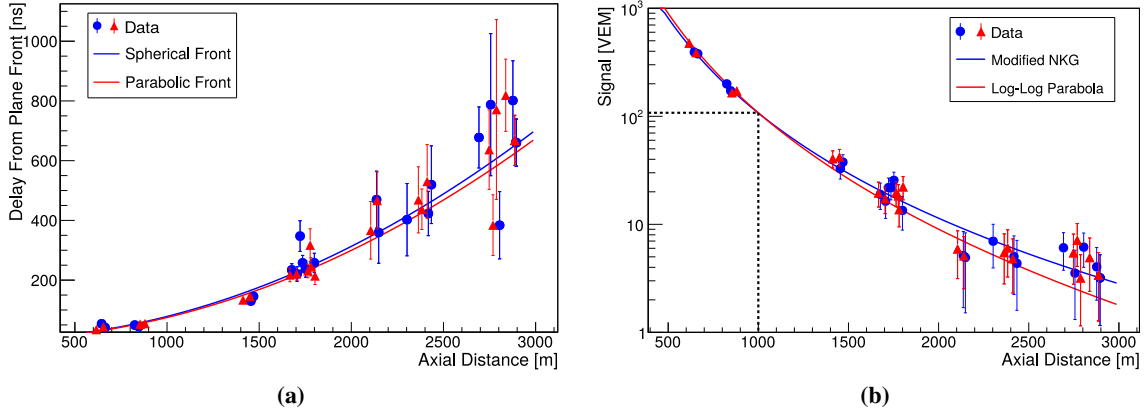


Figure 2: (a) The start times in individual stations as function of the distance to the reconstructed shower axis. The markers show the relative time difference to a planar shower front. Superimposed are the predicted times for the two implemented shower plane models. (b) The individual station signals are shown as a function of the distance to the shower axis. The dashed lines correspond to the signal extracted at 1000 m, which serves as shower-size estimator. The two functions used to fit the lateral distribution of the signals are given as solid lines.

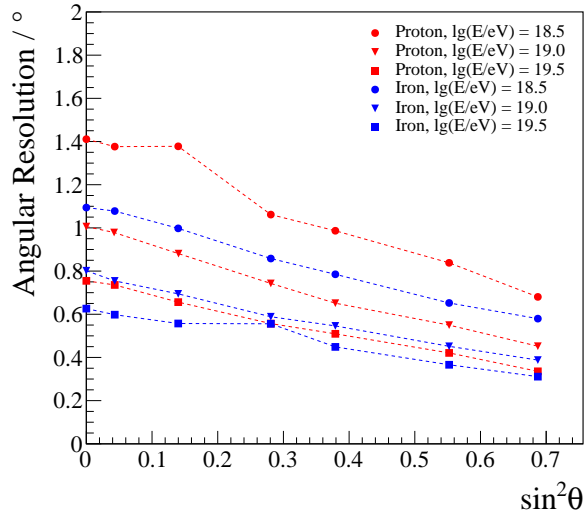


Figure 3: Angular resolution (AR) for the SD as a function of $\sin^2\theta$. The AR is shown for different energies and two primary masses.

$(\eta/\sigma^2) e^{-\eta^2/2\sigma^2}$. The angular resolution is then defined as the angular radius that would contain 68% of the showers, so $AR = 1.5\sigma(\eta)$. As shown in Fig. 3, at the highest energies the angular resolution is better than 1° for all angles and both simulated masses.

5.2 Shower size estimator

The uncertainty of the shower-size estimator can be derived from Monte-Carlo simulations as well as from data. The total uncertainty on S_{1000} from simulations is extracted by comparing the signals in a ring of simulated stations at 1000 m to the reconstructed S_{1000} value given by the LDF

fit. For each simulated energy and zenith angle, the distribution of $\ln(S_{1000}^{\text{rec}}/S_{1000}^{\text{true}})$ is fitted to a Gaussian function. The extracted sigma is then the quadratical combination of the statistical and systematic uncertainty of S_{1000} . For the data-driven method, the statistical uncertainty is directly given by the fitting error in S_{1000} arising from the uncertainty of the signals measured in each station. The systematic uncertainty is due to the unknown true LDF shape for a specific shower. For most events, the slope parameter β is parameterized as function of S_{1000} and zenith angle. Only for a subset of showers with many triggered stations, this parameter is a free parameter in the LDF fit. For this subset of showers, the fitted β_{free} is compared to the fixed value of β_{fix} obtained from the aforementioned parametrization. The dispersion σ_{β} of $\beta_{\text{fix}} - \beta_{\text{free}}$ can be parameterized as function of S_{1000} . Each shower is then reconstructed several times with a value for β sampled from a normal distribution centered at β_{fix} and with a standard deviation of σ_{β} . The systematic uncertainty on S_{1000} is given by the standard deviation of the resulting S_{1000} values. The statistical and systematic uncertainties are shown in Fig. 4a for two data sets, one set with saturated stations and one without. For both data sets, the statistical uncertainty is the dominant error on S_{1000} for values up to 50 VEM. In Fig. 4b, the S_{1000} values with β_{free} are compared to the ones obtained when using the parameterization for β . The difference is less than 3% and hence well within the systematic uncertainties.

As can be seen from the comparison of the combined statistical and systematic uncertainty of S_{1000} shown in Fig. 4c, both methods to derive the uncertainty provide compatible results. The uncertainty decreases from 15% at a shower size of 10 VEM, where the array is fully efficient for more inclined showers, to 5% at the highest shower sizes.

6. Conclusions

We have presented the reconstruction chain for the data measured with the SD. Due to the lack of knowledge of the true curvature of the shower front and the true LDF shape, the Observatory exploits two functional forms in the reconstruction to describe these shower properties. The agreement of both the shower geometry and the shower-size estimator is excellent for the two reconstruction modes. The angular resolution was investigated with simulations and was found to be better than 1% for the highest energies for both simulated primary masses. The same simulations were used to determine the uncertainty of the shower-size estimator. The uncertainty was found to be better than 10% at high energies for events without saturated stations, which is in agreement with the uncertainty derived from data.

References

- [1] A. Aab [Pierre Auger Collaboration], Nucl. Instrum. Meth. A **798** (2015) 172.
- [2] D. Ravignani [Pierre Auger Collaboration], Proc. 33rd ICRC.
- [3] A. Coleman [Pierre Auger Collaboration], PoS(ICRC2019)225.
- [4] X. Bertou [Pierre Auger Collaboration], Nucl. Instrum. Meth. A **568** (2006) 839–846.
- [5] D. Veberič [Pierre Auger Collaboration], Proc. 33rd ICRC.
- [6] J. Abraham [Pierre Auger Collaboration], Nucl. Instrum. Meth. A **613** (2010) 29.
- [7] M. Ave [Pierre Auger Collaboration], Nucl. Instrum. Meth. A **578** (2007) 180.

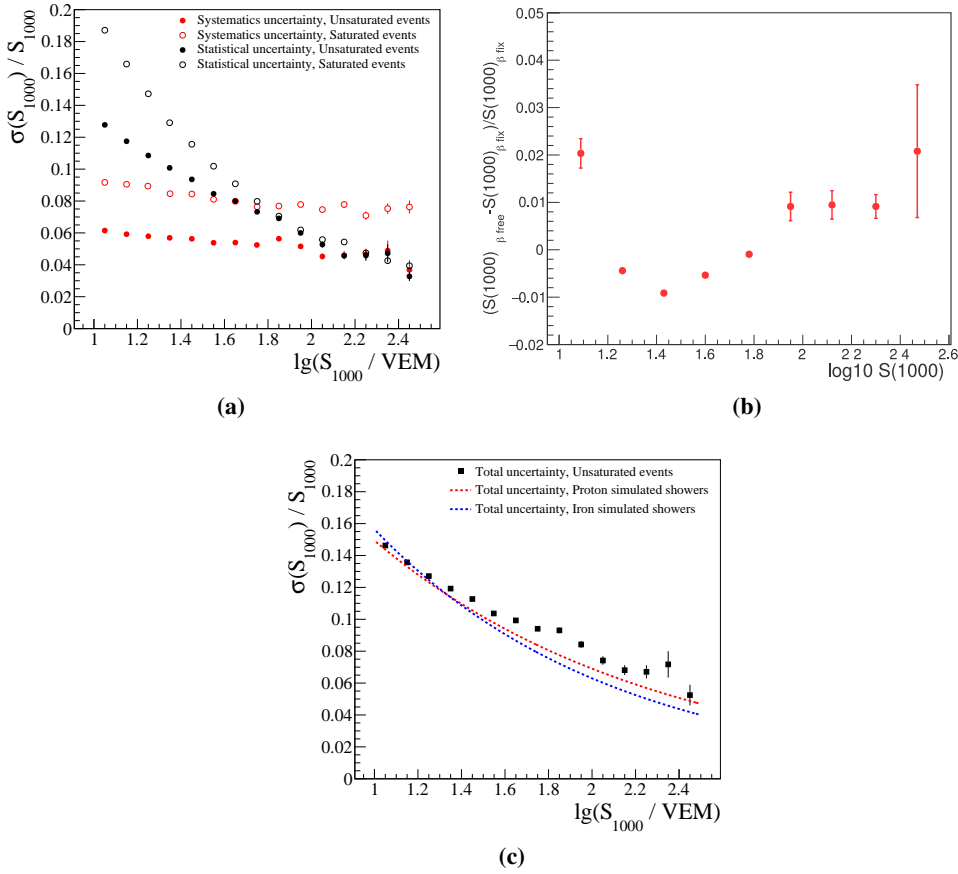


Figure 4: (a) The statistical and systematic uncertainties of the shower size S_{1000} as function of $\lg S_{1000}$. The data are divided into two subsets (with/without saturated stations). (b) Relative difference in S_{1000} for fitting β with respect to using the parameterization of it. (c) The combined statistical and systematic uncertainty derived from data for unsaturated events is compared to the uncertainty obtained from simulations.

- [8] D. Newton and J. Knapp and A.A. Watson, *Astropart. Phys.* **26** (2007) 414–419.
- [9] K. Kamata and J. Nishimura, *Prog. Theor. Phys. Suppl.* **6** (1958) 93.
- [10] K. Greisen, *Prog. Cosmic Ray Physics* **3** (1956) 1.
- [11] A. Aab [Pierre Auger Collaboration], *JINST* **12** (2017) P02006.
- [12] P. Abreu [Pierre Auger Collaboration], *JCAP* **11** (2011) 022.
- [13] J. Hersil et al., *Phys. Rev. Lett.* **6** (1961) 22.
- [14] H.P. Dembinski, B. Kégl, I.C. Mariş, M. Roth, and D. Veberič, *Astropart. Phys.* **73** (2016) 44–51.
- [15] V. Verzi [Pierre Auger Collaboration], *PoS(ICRC2019)*450.

2

Arrival Directions and Anisotropies



PIERRE
AUGER
OBSERVATORY



Search for magnetically-induced signatures in the arrival directions of ultra-high energy cosmic rays measured by the Pierre Auger Observatory

Marcus Wirtz^{*a} for the Pierre Auger Collaboration^{b†}

^a*III. Physikalisches Institut A, RWTH Aachen, Aachen, Germany*

^b*Observatorio Pierre Auger, Av. San Martín Norte 304, 5613 Malargüe, Argentina*

E-mail: auger_spokespersons@fnal.gov

Full author list: http://www.auger.org/archive/authors_icrc_2019.html

The search for magnetically-induced signatures in ultra-high energy cosmic ray data is a promising path for the identification of their sources. We use data of the Pierre Auger Observatory measured between 2004 and 2018, for two energy thresholds, 20 EeV and 40 EeV, providing unprecedented statistics: the number of cosmic rays included in the analyses for these energy thresholds is above 6500 and 1100, respectively. Two analysis approaches are used. In one, we search for inversely energy-ordered deflection patterns, while in the other we analyze the strength of collimation of energy along the local system of principal axes. We apply the analyses for a targeted search in regions around source candidates of active galactic nuclei and starburst galaxies. In addition, for the energy-ordered patterns an all-sky search has been performed. We also report the performance of the method evaluated using simulated data sets, including deflection in a model of the Galactic magnetic field which includes coherent and turbulent components, and with different composition scenarios.

36th International Cosmic Ray Conference — ICRC2019

24 July – 1 August, 2019

Madison, Wisconsin, USA

^{*}Speaker.

[†]for collaboration list see PoS(ICRC2019)1177

1. Introduction

The identification of the sources of ultra-high-energy cosmic rays (UHECRs) remains a challenging task. Being charged particles, they are deflected by the extragalactic and Galactic magnetic fields on their path from their sources to Earth. Despite the considerable experimental efforts [1, 2], the knowledge of these intervening magnetic fields is still poor. Moreover, the composition of UHECRs at the highest energies is also uncertain, given the low statistics and the dependence on the modelling of the hadronic interactions. From measurements of the maximum of the shower development [3], the data indicates that the composition becomes heavier with increasing energy. However, it does not rule out a light nuclei fraction at the highest energies, that may eventually originate in few nearby sources, different from the average ones. In such a case, the identification of several events from the same source can be performed by searching for magnetically-induced signatures in the arrival directions of the measured UHECRs. In this work, we show the results of two different methods that search for such signatures in the data measured by the Pierre Auger Observatory.

2. The Pierre Auger Observatory and the data set

The Pierre Auger Observatory [4], located in Argentina, is with a total area of 3000 km² the world's largest observatory for measuring ultra-high energy cosmic rays (UHECRs). The observatory consists of an array of 1660 water-Cherenkov stations arranged in an equilateral triangular grid (the surface detector), and 27 fluorescence telescopes on four sites (the fluorescence detector), which overlook the atmosphere above the surface detector. While the surface detector measures the lateral distribution of the air shower at ground level, the fluorescence detector can reconstruct the longitudinal profile of the air shower.

We select data recorded with the surface detector between 1 January 2004 and 31 August 2018 with zenith angles up to 80°. We choose energy thresholds 20 EeV and 40 EeV, which yield data sets of 6568 and 1119 events, respectively. The events are required to have at least four (five) active stations surrounding the station with the highest signal for the events with zenith angle smaller (larger) than 60°. For the events with zenith angle smaller than 60°, the reconstructed core must be inside an equilateral or isosceles triangle of active stations.

3. Methods

We investigate the arrival directions and energies of the UHECRs with two different methods. In the first one, we search for sets of events with different energies that come from a single point-like source, showing a correlation between their arrival direction and the inverse of their energy (a “multiplet”). The second method uses an observable built from a principal component analysis in a localized region of the sky, measuring the elongation of a pattern with respect to the region of interest (ROI) center. In the following, we will denote this observable as thrust ratio.

3.1 Multiplet search

Deflections of UHECRs in coherent magnetic fields can be approximated as linear if the total deflection angle $|\vec{\Theta}|$ is small. Thus, with the unit vectors of the source direction $\vec{\Theta}_s$ and the arrival

direction after deflection $\vec{\Theta}$, we can write the deflection behavior as:

$$\vec{\Theta} \simeq \vec{\Theta}_s + \frac{\vec{D}(\vec{\Theta}_s)}{E}, \quad (3.1)$$

where E is the energy of the CR and \vec{D} is the integral along the line of sight of the perpendicular component of the magnetic field \vec{B} times the charge Ze of the particle $\vec{D}(\vec{\Theta}_s) = Ze \int_0^L d\vec{l} \times \vec{B}(\vec{l})$. The “deflection power” $D \equiv |\vec{D}|$ will be given in units $1^\circ \times 100 \text{ EeV}$.

To determine if a set of cosmic rays forms a multiplet, we first use a coordinate system $(\hat{\mathbf{u}}, \hat{\mathbf{w}})$, which is tangential on the surface of the celestial sphere. The system is then rotated around the respective radial unit vector with an angle such that the covariance

$$\text{Cov}(w, 1/E) = \frac{1}{N} \sum_{i=1}^N (w_i - \langle w \rangle)(1/E_i - \langle 1/E \rangle) \quad (3.2)$$

between the cosmic ray coordinates w_i and their inverse energy $1/E_i$ is zero and the covariance $\text{Cov}(u, 1/E)$ is maximal. The correlation between the coordinate u and $1/E$ is measured through the correlation coefficient

$$C(u, 1/E) = \frac{\text{Cov}(u, 1/E)}{\sqrt{\text{Var}(u)\text{Var}(1/E)}} \quad (3.3)$$

where the variances are given by $\text{Var}(x) = \langle (x - \langle x \rangle)^2 \rangle$.

To identify possible candidates among background chance alignments we introduce two cuts: on the one hand, the correlation coefficient $C(u, 1/E) > C_{\min}$ must exceed the threshold C_{\min} , and on the other hand, the spread in the perpendicular direction $\hat{\mathbf{w}}$ of the multiplet may not exceed a threshold $\max(|w_i - \langle w \rangle|) < W_{\max}$. The two parameters were found to perform best on simulations for values of $C_{\min} = 0.9$ and $W_{\max} = 1.5^\circ$. A more detailed description can be found in [5].

3.2 Thrust ratio

Deviations from a clear correlation between the energy and the deflection angle can arise from larger turbulent field components or a mixed nuclear composition of the cosmic rays, as deflections scale also with the nuclear charges Z_i of the particles. In this case, the thrust ratio T_2/T_3 is expected to still find an elongation of the arising pattern in the arrival directions. The thrust observables T_k are constructed by successively maximizing the values

$$T_k = \max_{\hat{n}_k} \left(\frac{\sum_i |\omega_i^{-1} \vec{p}_i \cdot \hat{n}_k|}{\sum_i |\omega_i^{-1} \vec{p}_i|} \right) \quad (3.4)$$

with respect to the axes \hat{n}_k starting with $k = 1$. The sum iterates over all cosmic rays in the chosen ROI, $\vec{p}_i = E_i \hat{e}_{r_i}$ is the momentum of particle i , and ω_i is the exposure towards this direction. The principal axes \hat{n}_k are perpendicular to each other ($\hat{n}_1 \perp \hat{n}_2 \perp \hat{n}_3$), thus, by construction we obtain for the thrust observables the relation $T_1 > T_2 > T_3$.

While the thrust axis \hat{n}_1 points radially to the local barycenter of the energy distribution within the ROI, the axes \hat{n}_2 and \hat{n}_3 form an orthonormal coordinate system tangential to the local spherical plane. In this system, a signal like structure would be characterized by a strong collimation of arrival directions around the \hat{n}_2 -axis, and therefore by a high thrust observable T_2 . To be less affected by the radial cosmic ray distribution within the ROI, we choose instead the thrust ratio T_2/T_3 as observable. A more detailed description of the procedure can be found in [6].

4. Target selection and benchmark simulation

In this section, we motivate the choice of source candidates for a targeted search and set a benchmark simulation of ultra-high energy cosmic rays originating from these sources and propagating through a model of the Galactic magnetic field.

4.1 Target selection

A recent investigation found a promising hint of UHECR anisotropy in the direction of nearby galaxies, in particular, starburst galaxies (SBG) weighted by their radio flux and to a lesser extent, active galactic nuclei (AGN) weighted by their gamma-ray flux [7]. For the targeted search in this analysis, we test a 'merged' sample of 32 SBGs with distances up to 250 Mpc as described in [7] (section 3.1). We also test active galactic nuclei (AGN) as source candidates. The candidates are taken from the *Third Fermi-LAT Catalog of High-Energy Sources* (3FHL), providing a total number of 33 targets for distances up to 250 Mpc [8].

The expected UHECR flux from a certain source measured on Earth will strongly depend on the propagation distance through the extragalactic space. Therefore, we performed simulations of helium nuclei and preselected the source candidates by a cut on the helium flux contribution of 1% relative to the source with the highest contribution. Table 1 lists the source candidates that survive this cut, and they will be used as targets for the methods defined in section 3:

Nearby AGN from the 3FHL catalog [8]			
Target	gal longitude [°]	gal latitude[°]	distance [Mpc]
Cen A	309.5	19.4	3.7
M87	283.8	74.5	16.5
Fornax A	240.2	-56.7	17.4
Nearby SBG from [7]			
Target	gal longitude [°]	gal latitude [°]	distance [Mpc]
NGC 253	97.4	-88.0	3.6
NGC 4945	305.3	13.3	3.7
Circinus	311.3	-3.8	4.2
M83	314.6	32.0	4.7
NGC 4631	142.8	84.2	7.4
NGC 1808	241.2	-35.9	9.1
NGC 1068	172.1	-51.9	19

Table 1: Target selection of starburst galaxies and active galactic nuclei. For a hypothetical helium acceleration, all sources are expected to still contribute at least 1% the level of the strongest source contribution after suffering from losses during the propagation.

4.2 Benchmark simulation

To evaluate the performance of the above-defined methods, we probe their response on an arrival scenario of UHECRs which originate from the targets defined in table 1 and then propagate

through a model of the Galactic magnetic field. We use the regular model of Jansson and Farrar [9] and as a lower and upper limit two different versions of turbulent fields: the first one contains striation plus a Kolmogorov field with a coherence length of 60 pc as proposed in [10]. In the following, we refer to it as GMF-A model. Recent measurements by the Planck satellite indicate that the turbulent strength of GMF-A model is likely to be too large [11]. Therefore, we also probe a weaker version of the Kolmogorov field with the same coherence length but a downscaled magnetic field strength amplitude of factor 1/3 and no additional striated field. We will refer to this as GMF-B in the following.

For both energy thresholds, 20 EeV and 40 EeV, we test the hypothesis of an outstanding nearby source emitting a certain number of signal cosmic rays N_s with an energy spectrum following a simple power-law spectrum and spectral index of $\gamma = -2$. The arrival directions are obtained by propagating them through either GMF-A or GMF-B magnetic field models. The remaining cosmic ray sky is simulated isotropically following the geometrical exposure and measured energy spectrum at the Pierre Auger Observatory. The source scenarios for the two energy thresholds will only differ in the chemical composition of the accelerated cosmic rays: while in the $E > 40$ EeV scenario the source accelerates helium nuclei up to 200 EeV, in the $E > 20$ EeV scenario also protons are accelerated with proton energies between 20 EeV - 40 EeV and helium energies between 40 EeV - 80 EeV. The flux of arriving helium candidates is assumed to be twice as high as the flux of the proton candidates. Note that with these energy ranges the source features a simple rigidity-dependent acceleration mechanism as expected by a magnetic field based process.

In all simulations, we assumed a total number of 900 events above 40 EeV and 6000 above 20 EeV.¹ We apply an experimental energy uncertainty of 14% and an angular resolution of 1°.

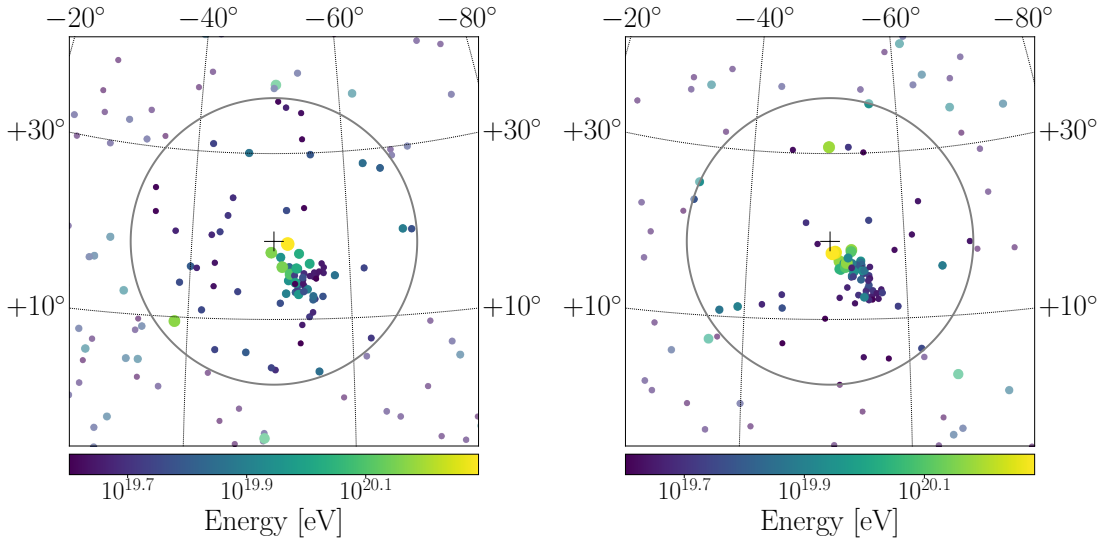


Figure 1: Visualization of arrival directions in Galactic coordinates for the benchmark simulations from target Cen A and energy threshold $E > 40$ EeV for the strong turbulent *GMF-A* Galactic magnetic field model (left) and the weaker version *GMF-B* (right).

¹These numbers are slightly smaller than the actual event number in data, which however is expected to have a minor impact on the sensitivity.

Example simulations for a number of injected signal cosmic rays of $N_s = 50$ from the Cen A source are visualized for the $E > 40$ EeV energy threshold in figure 1.

5. Expected sensitivity

5.1 Multiplets

We present the performance of the multiplet search on the benchmark simulation with the 40 EeV energy cut as specified in section 4. Figure 2 (left) shows the chance probability that the number of found cosmic rays associated with the multiplet occurs in isotropic simulations for the different targets and the simulation with the GMF-A turbulent magnetic field model. The markers indicate different chosen numbers of injected signal cosmic rays from the respective target. Due to the variety of the arrival patterns that arise from the deflection in the Galactic magnetic field and the non-uniform observatory exposure, the sensitivity depends highly on the evaluated target, e.g. nine injected signal cosmic rays for the sources M87 and NGC1068 and 18 injected cosmic rays for the source NGC 4945 are needed to reach a sensitivity of 3σ . This corresponds to signal fractions of 1% and 2%, respectively. As expected, for the weaker GMF-B model, the analysis performs better for almost all targets as can be seen in the right panel of figure 2.

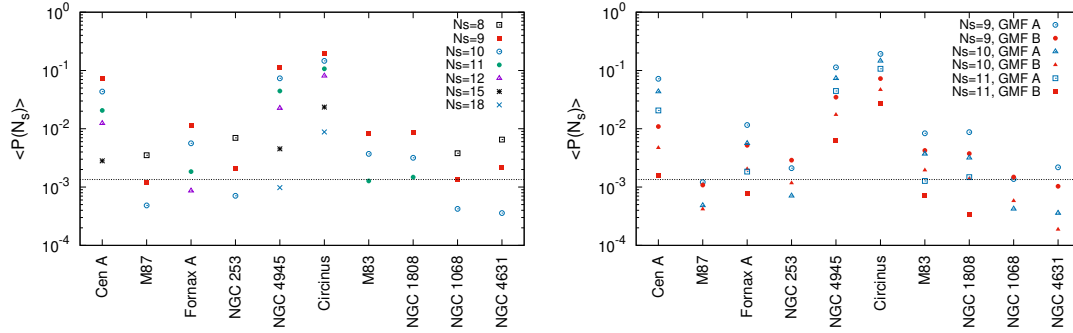


Figure 2: Expected sensitivity for the multiplet search on the benchmark simulation with the energy cut 40 EeV. (Left) Isotropic chance probability for chosen injected signal cosmic rays N_s for the different targets and GMF-A model. (Right) Comparison between GMF-A and GMF-B models.

5.2 Thrust ratio

For the thrust-ratio, the patterns produced by the source candidate have a larger impact on the sensitivity than in the case of the multiplets, as can be seen by the big spread between the lines in figure 3. For the 20 EeV energy cut and GMF-A, most of the targets reach the 3σ confidence level between $N_s \approx 40$ and $N_s \approx 60$ signal cosmic rays, corresponding to small signal fractions between 0.7% and 1.0% as can be seen in the left of figure 3.

In case of the 40 EeV energy cut, a relatively high number of $N_s \approx 30$ to $N_s \approx 60$ injected signal cosmic rays is needed to pass the 3σ confidence level, which correspond to signal fractions between 3% and 6%. This performance is inferior to the multiplet search, which might be explained by the fact that it does not make direct use of the energy information. The weaker turbulent magnetic

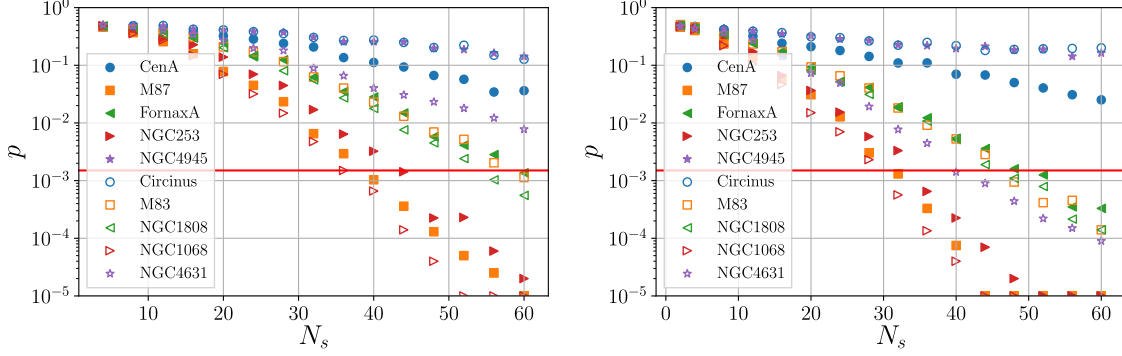


Figure 3: Expected sensitivity for the thrust-ratio observable on the benchmark simulation with the stronger GMF-A turbulent magnetic field model. Shown for the 20 EeV energy cut on the left and the 40 EeV energy cut on the right.

field model GMF-B yields just a minor improvement on the performance: on average, the same sensitivity as in the case of GMF-A is gained when injecting two signal cosmic rays less.

6. Application to data

6.1 Targeted search

In this section, we apply the multiplet and thrust methods to the data of the Pierre Auger Observatory as presented in section 2. All individual chance probabilities that isotropic arrival directions respond at least as strong as found on data are above 1% thus no significant alignment pattern around the chosen targets could be found (cf. table 2).

Target	Isotropic chance probabilities		
	Multiplet (40 EeV)	Thrust-ratio (20 EeV)	Thrust-ratio (40 EeV)
Cen A	1.2×10^{-2}	0.75	0.42
M87	0.61	0.44	0.85
Fornax A	0.96	0.21	1.9×10^{-2}
NGC 253	0.54	0.98	0.88
NGC 4945	0.25	2.9×10^{-2}	3.7×10^{-2}
Circinus	0.99	0.82	0.58
M83	0.20	0.14	0.54
NGC 4631	—	0.59	0.85
NGC 1808	0.61	0.63	0.77
NGC 1068	0.75	6.0×10^{-2}	0.29

Table 2: Isotropic chance probabilities for the targeted search with the multiplet and thrust-ratio observables applied on data of the Pierre Auger Observatory.

The most striking candidate for the multiplet search is in the Cen A region above 40 EeV with a chance probability of 1.2% to arise from isotropic arrival scenarios. The fitted deflection power

is $D = (9 \pm 2)^\circ \times 100$ EeV. In the case of the thrust-ratio, the sources Fornax A above 40 EeV, NGC 1068 above 20 EeV and NGC 4945 for both energy thresholds are most striking with chance probabilities between 2% and 6%. There is barely any overlap between the cosmic rays within the multiplet of the Cen A region and the region of interests evaluated for the thrust observables.

6.2 Blind search

We also perform the multiplet search on the entire sky for the energy threshold above 40 EeV. The largest multiplet found has a multiplicity of 10. The probability that it appears by chance from an isotropic distribution of events is 11%. The second largest multiplet has a multiplicity of nine events. The chance probability of finding at least two multiplets with multiplicity larger or equal than nine in isotropic simulations is 19%. The respective deflection power values are $D = (8.0 \pm 1.3)^\circ \times 100$ EeV and $D = (12 \pm 2)^\circ \times 100$ EeV.

7. Discussion

We introduced two observables to search for magnetically-induced deflection patterns in the energy and arrival direction distribution of ultra-high energy cosmic rays above 20 EeV and 40 EeV in data recorded by the Pierre Auger Observatory.

Neither in a targeted search around chosen sources of active galactic nuclei and starburst galaxies nor in a blind search could any significant pattern be found. The largest deviations from isotropic distributions were found with a p-value of 2% around the Fornax A region for the thrust search above 40 EeV and with a p-value of 1% around the Cen A region for the multiplet search above 40 EeV. The next-to-leading ones were found with p-values of 3 – 6% around the NGC 4945 and NGC 1068 for the thrust search above 20 EeV. These probabilities are not penalized for the use of ten different candidates.

Further investigations to apply the multiplet search for energies down to 20 EeV, and the thrust search on the entire sky are planned.

References

- [1] G. Farrar, M. Unger, PoS (ICRC2017) 558.
- [2] M. Erdmann, G. Müller, M. Urban, M. Wirtz, *Astroparticle Physics* **85** (2016) 54-64.
- [3] A. Aab [Pierre Auger Collaboration], *Phys. Rev. D* **90** (2014) 122006.
- [4] A. Aab [Pierre Auger Collaboration], *Nucl. Instrum. Meth.* **A798** (2015) 172.
- [5] P. Abreu [Pierre Auger Collaboration], *Astroparticle Physics* **35** (2012) pp. 354-361.
- [6] A. Aab [Pierre Auger Collaboration], *European Physical Journal C (EPJ C)* **75** (2015) 269.
- [7] A. Aab [Pierre Auger Collaboration], *The Astrophysical Journal Letters* **853** (2018) 2.
- [8] M. Ajello et al., *The Astrophysical Journal* **232** (2017) 2.
- [9] R. Jansson, G. R. Farrar, *The Astrophysical Journal* **757** (2012) 14.
- [10] R. Jansson, G. R. Farrar, *The Astrophysical Journal* **757** (2012) L11.
- [11] R. Adam [Planck Collaboration], *A&A* **596** (2016) A103.



Large-scale anisotropies above 0.03 EeV measured by the Pierre Auger Observatory

Esteban Roulet^{*a} for the Pierre Auger Collaboration^{b†}

^a*Centro Atómico Bariloche, Comisión Nacional de Energía Atómica
Consejo Nacional de Investigaciones Científicas y Técnicas (CONICET)
Av. Bustillo 9500, R8402AGP, Bariloche, Argentina*

^b*Observatorio Pierre Auger, Av. San Martín Norte 304, 5613 Malargüe, Argentina*

E-mail: auger_spokespersons@fnal.gov

Full author list: http://www.auger.org/archive/authors_icrc_2019.html

We present analyses of the large-scale anisotropies observed by the Pierre Auger Observatory over more than three decades in energy, considering data since 1 January 2004 up to 31 August 2018. For $E \geq 4$ EeV, for which the array with 1500 m separation between detectors is fully efficient, we obtain the dipolar and quadrupolar amplitudes through a combined Fourier analysis of the distribution of events in right ascension and azimuth. A dipolar modulation with an amplitude $d = 6.6_{-0.8}^{+1.2}\%$ and pointing $\sim 125^\circ$ away from the Galactic center is observed above 8 EeV. The dipole amplitude shows an indication of an increase with energy above 4 EeV and the quadrupolar components turn out to be not significant. Astrophysical scenarios that could account for these results are briefly discussed. We also extend the study of the equatorial component of the dipolar modulation down to ~ 0.03 EeV. In the regime in which the efficiencies are small, we use the East-West method, which is largely insensitive to systematic effects. Finally, for the lowest energies we use the data from a subarray with 750 m separation between detectors. The results suggest a change in the phase of the equatorial dipole from values pointing close to the right ascension of the Galactic center below EeV energies towards values indicative of an extragalactic origin for the dipolar anisotropy above a few EeV.

*36th International Cosmic Ray Conference — ICRC2019
24 July – 1 August, 2019
Madison, Wisconsin, USA*

^{*}Speaker.

[†]for collaboration list see PoS(ICRC2019)1177

1. Introduction

The origin of ultrahigh energy cosmic rays is still one of the important open problems in high-energy astrophysics. Besides the information that can be obtained from the observation of the spectrum and the composition of the cosmic rays (CRs), the other crucial handle for this is the study of the anisotropies in their arrival direction distribution. Being charged particles, their deflections in the Galactic and extragalactic magnetic fields make the identification of their sources very challenging. Moreover, the suggested trend towards a heavier composition that is inferred to happen above few EeV leads one to expect that only at the highest observed energies may the average deflections of the CRs from an extragalactic source be smaller than a few tens of degrees. On the other hand, anisotropies on large angular scales, such as a dipole or a quadrupole, may be present at all CR energies. They may arise from the anisotropic distribution of the CR sources themselves, either if the CR propagation is quasi-rectilinear or diffusive. They may also result from individual extragalactic CR sources if the magnetic fields are strong enough so that the propagation is diffusive, and they could also be produced at lower energies by CRs from Galactic sources as they escape from the Galaxy.

2. The dataset

In this work, we consider data collected up to 31 August 2018 at the Pierre Auger Observatory [1]. We consider the data from the surface arrays, since having $\sim 100\%$ duty cycle they provide a significantly larger number of events than the fluorescence telescopes. Another advantage is that their associated exposure has a much simpler angular dependence. We consider the 3000 km^2 array in which the detectors are separated by 1500 m (SD1500), which is fully efficient above $\sim 3 \text{ EeV}$ for events with zenith angles $\theta \leq 60^\circ$ (vertical events) and above 4 EeV for the events with $60^\circ < \theta \leq 80^\circ$ (inclined events).¹ We also use the vertical SD1500 events in the regime below full efficiency, in which case the energy assignment is done by extrapolating the calibration curve established with events having energies above 3 EeV . At the lowest energies, and going down to 0.03 EeV , it proves convenient to use the smaller 23 km^2 sub-array with 750 m separation between detectors (SD750), which is fully efficient down to $\sim 0.3 \text{ EeV}$ for events with $\theta \leq 55^\circ$. For the SD1500 array, we consider events since 1 January 2004, amounting to a total exposure of $92,500 \text{ km}^2 \text{ yr sr}$ for $\theta \leq 80^\circ$ (and a relaxed trigger), and $60,700 \text{ km}^2 \text{ yr sr}$ for $\theta \leq 60^\circ$. For the SD750 array, we use the events since 1 January 2012, amounting to a total exposure of $234 \text{ km}^2 \text{ yr sr}$. We split the data above $\sim 0.03 \text{ EeV}$ into 11 energy bins, with the energies defining the boundaries scaling by factors of two, i.e., $E_n = 2^n \text{ EeV}$, with $n = -5, -4, \dots, 4, 5$, and with the highest energy bin corresponding to $E \geq 32 \text{ EeV}$. We also report the results for the cumulative bin $E \geq 8 \text{ EeV}$ that was considered in previous works. The analyses presented here update those performed above full efficiency of the SD1500 in Refs. [2, 3, 4], and extend those in right ascension down to 0.03 EeV [5] (see also [6, 7, 8]).

¹For energies above 4 EeV , we consider a relaxed trigger in which we allow for the possibility that one of the stations around the one with the highest signal may not be working. Below 4 EeV we do not include the inclined events and require that all six surrounding stations be functioning.

3. Systematic effects

The main difficulty that one has to face in order to determine the large-scale anisotropies is that, besides requiring the detection of a large number of events given the small expected amplitudes, it is also necessary that all possible sources of systematic effects that could lead to spurious signals be well under control and accounted for. The main sources for these systematic effects are:

- The exposure of the array is not perfectly uniform over time, due to the initial detector deployment period, sporadic down-times, etc. To account for this requires one to monitor the number of active detector units (each one corresponding to an hexagon of adjacent working detectors) at every minute and include this information in a weight that is assigned to each event in the Fourier analysis being performed.
- The variation of the atmospheric conditions, such as changes in the air density and pressure, affect the development of the air showers, changing respectively the Molière radius and the total column density traversed [9]. In particular, given the fact that the CR energy is estimated from the reconstructed value of the signal at 1 km from the shower core (450 m for the SD750 array), under hot weather conditions the lower air densities tend to lead to an increased lateral spread of the showers and hence to an overestimate of the primary CR energy. If not accounted for, this would lead to spurious daily and seasonal variations of the CR flux above a given energy threshold. This effect has been studied in detail, and it is taken into account in the energy assignment of the vertical events (the air showers of inclined events are dominated by the muonic component, whose dependence on atmospheric conditions is negligible at these energies).
- The geomagnetic field also affects the shower development, in particular by increasing the lateral spread of the muonic component. This spread is larger for showers that are more perpendicular to the magnetic field direction, what induces spurious dipolar and quadrupolar components in the azimuthal distribution of the events. This is corrected in the energy assignment of the vertical events following Ref. [10] (for inclined showers, the geomagnetic field effects are already accounted for in their standard energy assignment).
- The array has a slight tilt, of about $\theta_t \simeq 0.2^\circ$ on average, towards the SE direction ($\phi_t \simeq -30^\circ$ with respect to the East direction). This tilt could induce a slight net excess of events from the South, which we correct for through the weights introduced for each event in the Fourier analysis.

4. Method

Above the full trigger efficiency of the array, we perform a weighted Fourier analysis in right-ascension and azimuth ($x = \alpha$ or ϕ respectively). The Fourier components are

$$a_k^x = \frac{2}{\mathcal{N}} \sum w_i \cos(kx_i) \quad , \quad b_k^x = \frac{2}{\mathcal{N}} \sum w_i \sin(kx_i), \quad (4.1)$$

where the sums run over all events with $i = 1, N$, the normalization factor is $\mathcal{N} = \sum w_i$, k is the order of the harmonic (e.g., $k = 1$ for the dipolar modulation), and the weights are obtained from

$$w_i^{-1} = \Delta N_{\text{hex}}(\alpha_i^0) [1 + \tan \theta_i \tan \theta_t \cos(\phi_i - \phi_t)], \quad (4.2)$$

with $\Delta N_{\text{hex}}(\alpha_i^0)$ being the normalized differential exposure of the array as a function of the right-ascension of the zenith of the observatory at the time the i -th event is recorded. The amplitudes and phases of the harmonics are then obtained as $r_k^x = \sqrt{(a_k^x)^2 + (b_k^x)^2}$ and $\varphi_k^x = \text{atan}(b_k^x/a_k^x)/k$.

Below full trigger efficiency there are other systematic effects entering into play. Although the efficiency does not depend directly on the right ascension, there is an interplay between the atmospheric effects, which for any given event modify the signals expected at the different stations, and the trigger probability which ultimately depends on those signals. We have found that for the SD1500 array, even accounting for these effects, there are indications of the presence of surviving systematic effects below 2 EeV, as is apparent in the non-negligible amplitudes that remain at the anti-sidereal frequency which suggests that a comparable spurious amplitude could also be present at the sidereal frequency. On the other hand, we have checked that above 2 EeV the first-harmonic amplitudes at both the solar and anti-sidereal frequencies are compatible with being due to statistical fluctuations. Below 2 EeV, one can use instead the East-West (EW) method [11], which relies on the fact that the exposure and atmospheric systematic effects are equal for events coming from the eastern or western hemispheres. This implies that their difference provides a clean measurement of the derivative of the modulation in right ascension, from which the actual modulation can be safely recovered although with a larger uncertainty. For events with energies smaller than 0.25 EeV, it actually turns out to be convenient to use the data from the SD750 array, which although being smaller is more efficient at low energies. Since the SD750 array is not fully efficient below 0.3 EeV, we just use the EW method in this case, extending the analysis down to 0.03 EeV. We note that for the Fourier analysis in right ascension the effect of the tilt of the array and of the geomagnetic corrections are not relevant (they only affect the analysis in azimuth), and hence these corrections are not implemented for the SD750 array.

The computation of the North-South component of the dipole d_z requires the knowledge of the azimuthal modulation of the rates. However, due to the geometry of the surface array layout the trigger efficiency depends on the azimuth angle, and combined with the zenith dependence of the efficiency the exposure ends up having a non-trivial dependence on declination. Moreover, the geomagnetic effects (and also those of the tilt of the array) depend on the azimuth angle, and hence their interplay with the trigger efficiency represents an additional source of systematic effects when one attempts to recover the North-South dipole component (as well as the quadrupole components) in the regime in which there is no full efficiency. We hence restrict the analysis below 4 EeV to the study of the equatorial dipole component \vec{d}_\perp , whose amplitude is related to that of the first harmonic in right ascension via $d_\perp \simeq r_1^\alpha / \langle \cos \delta \rangle$, with $\langle \cos \delta \rangle$ being the average cosine of the declination of the events, and whose phase α_d coincides with the phase φ_1^α .

5. Results

Table 1 contains the values for the dipolar components in the different energy bins above 4 EeV. These values are obtained under the assumption that the higher multipoles are negligible. The most

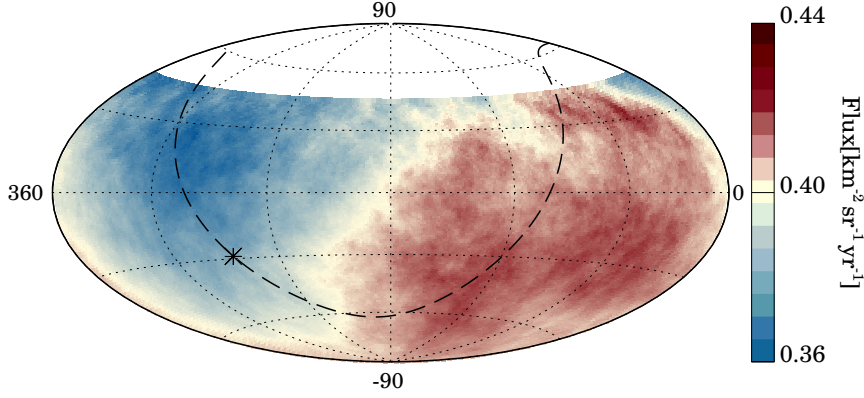


Figure 1: Map in Equatorial coordinates of the CR flux above 8 EeV, averaged on top-hat windows of 45° radius. The location of the Galactic plane is shown with a dashed line, and the Galactic center is indicated with a star.

significant result is the right ascension modulation in the cumulative bin above 8 EeV that was considered in [3], which now gives $d_\perp = 0.060^{+0.010}_{-0.009}$. The overall distribution of the flux in this bin, averaged on top-hat windows of 45° , is displayed in Fig. 1, showing a clear dipolar pattern. The total dipole amplitude in this bin is $d = 0.066^{+0.012}_{-0.008}$, and it points $\sim 125^\circ$ away from the direction of the Galactic centre (shown with an asterisk), indicating that this anisotropy has an extragalactic origin. Considering the four energy bins above 4 EeV, a growth of the dipole amplitude with increasing energy is found, which is approximately reproduced with the expression $d = d_{10}(E/10\text{EeV})^\beta$, with $d_{10} = 0.051 \pm 0.007$ and $\beta = 0.96 \pm 0.16$. A fit with an energy-independent dipole amplitude ($\beta = 0$) is disfavored at the level of 5.1σ by a likelihood ratio test. These results are shown in Fig. 2, where they are also compared to the predictions from Ref. [12] for scenarios of extragalactic sources with a mixed CR composition compatible with that inferred by Auger, having a density 10^{-4} Mpc^{-3} and being sampled either from an isotropic distribution or according to the distribution of galaxies in the 2MRS catalog. The direction of the dipolar anisotropy in the different bins is displayed in Fig. 3, in which the contours of equal probability per unit solid angle, marginalized over the dipole amplitude, that contain the 68%CL range are displayed. In all cases, it turns out to be not

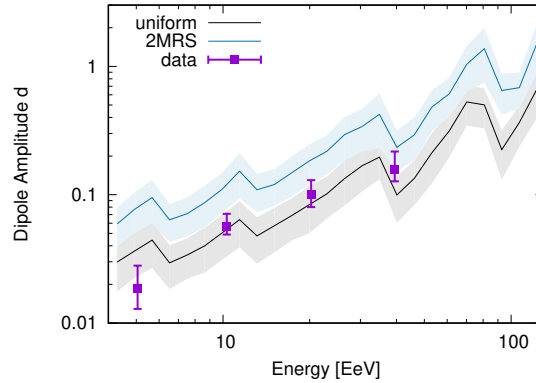


Figure 2: Energy dependence of the dipolar amplitude measured above 4 EeV. Also shown are the predictions from scenarios [12] with extragalactic sources.

Table 1: Dipole reconstruction for $E \geq 4$ EeV. Shown are the number of events in each bin N , the Equatorial amplitude d_{\perp} , the one along the rotation axis of the Earth d_z , and the total 3D amplitude d , as well as the dipole direction (α_d, δ_d) .

Energy [EeV]		N	d_{\perp}	d_z	d	α_d [°]	δ_d [°]
interval	median						
4 - 8	5.0	88,325	$0.010^{+0.007}_{-0.004}$	-0.016 ± 0.009	$0.019^{+0.009}_{-0.006}$	69 ± 46	-57^{+24}_{-20}
≥ 8	11.5	36,928	$0.060^{+0.010}_{-0.009}$	-0.028 ± 0.014	$0.066^{+0.012}_{-0.008}$	98 ± 9	-25 ± 11
8 - 16	10.3	27,271	$0.056^{+0.012}_{-0.010}$	-0.011 ± 0.016	$0.057^{+0.014}_{-0.008}$	97 ± 12	-11 ± 16
16 - 32	20.2	7,664	$0.075^{+0.023}_{-0.018}$	-0.07 ± 0.03	$0.10^{+0.03}_{-0.02}$	80 ± 17	-44 ± 14
≥ 32	39.5	1,993	$0.13^{+0.05}_{-0.03}$	-0.09 ± 0.06	$0.16^{+0.06}_{-0.03}$	152 ± 19	-34^{+19}_{-20}

Table 2: Dipole and quadrupole components in the two energy bins. The x axis is in the direction $\alpha = 0^\circ$.

Energy [EeV]	d_i	Q_{ij}
4 - 8	$d_x = -0.001 \pm 0.008$	$Q_{zz} = -0.003 \pm 0.039$
	$d_y = 0.008 \pm 0.008$	$Q_{xx} - Q_{yy} = -0.004 \pm 0.028$
	$d_z = -0.014 \pm 0.022$	$Q_{xy} = 0.006 \pm 0.014$
		$Q_{xz} = -0.008 \pm 0.018$
		$Q_{yz} = -0.005 \pm 0.018$
≥ 8	$d_x = -0.004 \pm 0.012$	$Q_{zz} = 0.032 \pm 0.061$
	$d_y = 0.054 \pm 0.012$	$Q_{xx} - Q_{yy} = 0.077 \pm 0.048$
	$d_z = -0.011 \pm 0.035$	$Q_{xy} = 0.038 \pm 0.024$
		$Q_{xz} = 0.015 \pm 0.029$
		$Q_{yz} = -0.016 \pm 0.029$

very different from the direction of the outer Galactic spiral arm, at Galactic coordinates $b = 0^\circ$ and $\ell \simeq -100^\circ$. The direction towards the flux-weighted dipole of the 2MRS galaxy distribution, which is dominated by the contribution from galaxies closer than ~ 100 Mpc, is also indicated. In this respect, it is important to keep in mind that the CR deflections induced by the Galactic magnetic field would have the effect of changing the direction of an extragalactic dipolar distribution when it is observed from the Earth, tending to align it closer to the directions towards the spiral arms, as shown in Fig. 4 for different illustrative values of the CR rigidities. These deflections also tend to reduce the resulting dipole amplitude, as indicated with the color code.

Allowing for the presence of a quadrupole, we report the reconstructed dipolar and quadrupolar components of the flux in the bins $[4, 8]$ EeV and $E \geq 8$ EeV in Table 2, obtained as done in [2]. The five independent quadrupolar components turn out to be not significant in any of the energy bins, and hence the resulting dipolar components are consistent with those obtained ignoring the quadrupoles.

The results for the equatorial dipole component d_{\perp} , for all the bins down to $E \simeq 0.03$ EeV, are compiled in Table 3 and plotted in Fig. 5. For the bins in which the measured amplitude is smaller than the value d_{\perp}^{99} within which 99% of the simulations with isotropic distributions of the same number of events would fall, we also report the resulting 99% CL upper bound on the

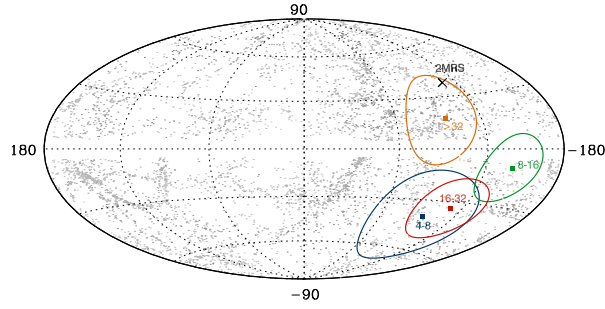


Figure 3: Reconstructed dipole direction in different energy bins, in Galactic coordinates. Dots indicate the 2MRS galaxies within 100 Mpc and the cross is the direction towards the flux weighted dipole.

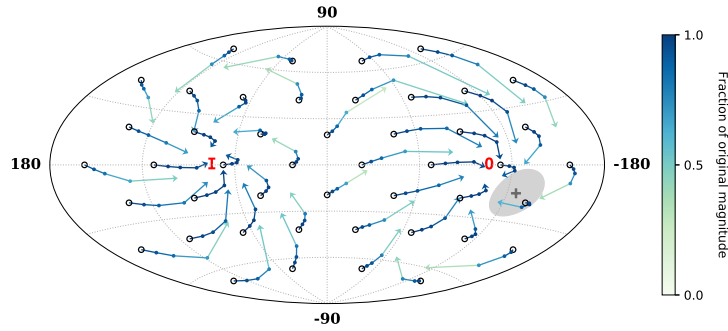


Figure 4: Map in Galactic coordinates illustrating the changes induced by the Galactic magnetic field upon an extragalactic dipolar CR distribution. Circles represent the original dipole direction outside the Galaxy and the different points along the arrows show the directions that would be observed from Earth for $E/Z = 32, 16, 8$ and 4 EeV. The color code indicates the factor by which the observed amplitude gets reduced. The gray ellipse indicates the direction of the reconstructed dipole for $E \geq 8$ EeV.

amplitude that is inferred from the observations. One can appreciate that the measured amplitudes tend to increase with energy, from values typically smaller than about 1% below 1 EeV to values above 6% above 10 EeV. Below 1 EeV the phases in most of the bins point near the Galactic center direction, at $\alpha_{GC} \simeq -94^\circ$, although none of the determined amplitudes are significant. We note that the values obtained at few PeV energies by the IceCube, IceTop and KASCADE-Grande experiments [13, 14, 15], included in the figure, also point near the Galactic center direction.

This would suggest that the transition between a predominantly Galactic and an extragalactic origin for the dipolar anisotropies is taking place somewhere between 1 and few EeV. Further studies of the large-scale anisotropies in this energy regime will help to better characterize this transition.

References

- [1] A. Aab et al. (Pierre Auger Collaboration), Nucl. Instrum. Meth. A **798** (2015) 172
- [2] A. Aab et al. (Pierre Auger Collaboration), Astrophys. J. **802** (2015) 111
- [3] A. Aab et al. (Pierre Auger Collaboration), Science **357** (2017) 1266
- [4] A. Aab et al. (Pierre Auger Collaboration), Astrophys. J. **868** (2018) 4
- [5] A. Aab et al. (Pierre Auger Collaboration), in preparation

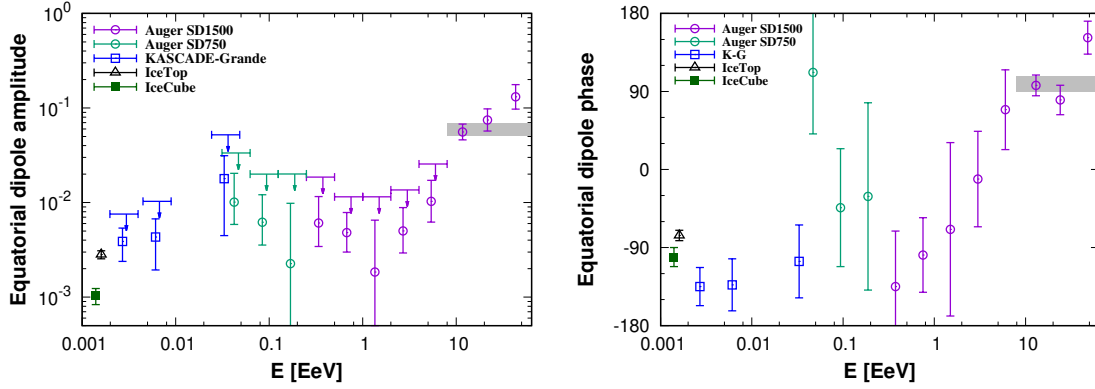


Figure 5: Amplitude (left panel) and phase (right panel) of the equatorial dipole amplitude determined in the different bins. Also shown are the low-energy results from IceCube, IceTop and KASCADE-Grande [13, 14, 15]. For the bins in which $d_{\perp} < d_{\perp}^{99}$, also the upper-limit d_{\perp}^{UL} is indicated with an arrow.

	E [EeV]	N	d_{\perp}	α_d [°]	$P(\geq d_{\perp})$	d_{\perp}^{99}	d_{\perp}^{UL}
East-West (SD750)	0.03125 - 0.0625	432,155	$0.010^{+0.010}_{-0.004}$	112 ± 71	0.54	0.028	0.033
	0.0625 - 0.125	924,856	$0.006^{+0.006}_{-0.003}$	-44 ± 68	0.50	0.016	0.020
	0.125 - 0.25	488,752	$0.002^{+0.008}_{-0.002}$	-31 ± 108	0.94	0.019	0.020
East-West (SD1500)	0.25 - 0.5	770,316	$0.006^{+0.005}_{-0.003}$	-135 ± 64	0.45	0.015	0.018
	0.5 - 1.0	2,388,467	$0.005^{+0.003}_{-0.002}$	-99 ± 43	0.20	0.008	0.011
	1 - 2	1,243,103	$0.0018^{+0.0047}_{-0.0002}$	-69 ± 100	0.87	0.011	0.011
Fourier (SD1500)	2 - 4	283,074	$0.005^{+0.004}_{-0.002}$	-11 ± 55	0.34	0.010	0.014
	4 - 8	88,325	$0.010^{+0.007}_{-0.004}$	69 ± 46	0.23	0.018	0.026
	8 - 16	27,271	$0.056^{+0.012}_{-0.010}$	97 ± 12	2.3×10^{-6}	0.033	–
	16 - 32	7,664	$0.075^{+0.023}_{-0.018}$	80 ± 17	1.5×10^{-3}	0.063	–
	≥ 32	1,993	$0.13^{+0.05}_{-0.03}$	152 ± 19	5.3×10^{-3}	0.12	–
	≥ 8	36,928	$0.060^{+0.010}_{-0.009}$	98 ± 9	1.4×10^{-9}	0.028	–

Table 3: Equatorial dipole reconstruction in different energy bins. Indicated are the number of events, amplitude and phase of d_{\perp} , probability to get a larger amplitude from fluctuations of an isotropic distribution, value within which 99% of the isotropic simulations fall and 99% CL upper limit on the amplitude.

[6] P. Abreu et al. (Pierre Auger Collaboration), *Astrophys. J. Lett.* 762 (2013) L13

[7] I. Sidelnik for the Pierre Auger Collaboration, *Proceeding of the 33rd ICRC*, arXiv:1307.5059

[8] I. Al Samarai for the Pierre Auger Collaboration, *PoS ICRC2015* (2016) 372

[9] A. Aab et al. (Pierre Auger Collaboration), *JINST* 12 (2017) P02006

[10] P. Abreu et al. (Pierre Auger Collaboration), *JCAP* 11 (2011) 022

[11] R. Bonino et al., *Astrophys. J.* 738 (2011) 67

[12] D. Harari, S. Mollerach and E. Roulet, *Phys. Rev. D* 92 (2015) 063014

[13] R. Abbasi et al. (IceCube Collaboration), *Astrophys. J.* 746 (2012) 33

[14] M.G. Aartsen et al. (IceCube Collaboration), *Astrophys. J.* 826 (2016) 220

[15] A. Chiavassa et al. (KASCADE-Grande Collaboration), *Nucl. Part. Phys. Proc.* 279 (2016) 56



Anisotropies of the highest energy cosmic-ray events recorded by the Pierre Auger Observatory in 15 years of operation

Lorenzo Caccianiga^{*a} for the Pierre Auger Collaboration^{b†}

^a*Istituto Nazionale di Fisica Nucleare, Sezione di Milano, Italy*

^b*Observatorio Pierre Auger, Av. San Martín Norte 304, 5613 Malargüe, Argentina*

E-mail: auger_spokespersons@fnal.gov

Full author list: http://www.auger.org/archive/authors_icrc_2019.html

To understand the origin of ultra-high energy cosmic rays (UHECRs), the study of the distribution of their arrival directions has always been of capital importance, despite the difficulties that arise from the deflection they suffer due to magnetic fields. In particular, the highest-energy region, above a few tens of EeV, which extends beyond the observed flux suppression, is of particular interest because of the high rigidities and the suppression of distant sources. We present here the latest results of searches for anisotropies in the arrival directions of the UHECRs detected by the Pierre Auger Observatory. The dataset used for this work is the largest ever recorded from a single observatory at these energies: with nearly 15 years of data, it covers the sky up to a declination of 45° , with an exposure now exceeding $100,000 \text{ km}^2 \text{ sr yr}$. The study of large-scale anisotropy indicates an extragalactic origin for the sources of UHECRs with energies larger than 8 EeV. A search for anisotropies at small to intermediate angular-scales is presented, which enables a model-independent study of flux patterns at the highest energies. We also study the arrival directions of UHECRs against the distribution of nearby extragalactic matter traced by different catalogs of candidate sources. We discuss the most striking features characterized by the Pierre Auger Observatory, which include the most significant indication of anisotropy in the arrival directions of the highest energy cosmic rays.

36th International Cosmic Ray Conference — ICRC2019

24 July – 1 August, 2019

Madison, Wisconsin, USA

^{*}Speaker.

[†]for collaboration list see PoS(ICRC2019)1177

1. Introduction

The quest for the sources of ultra-high energy cosmic rays (UHECRs) is still one of the most important purposes of current high-energy astrophysics. Although recent results on large scale anisotropies have strongly favored an extragalactic origin of the highest energy cosmic rays [1], the specific sources remain unidentified. To pursue this quest, searching for anisotropies and patterns in the arrival directions of the highest energy particles ever recorded is probably one of the most natural paths. Particles above the observed flux suppression [2] at $\sim 40 \text{ EeV}^1$ are supposed to come only from the local universe, within few hundreds of Mpc, because of the interaction they should undergo with the cosmic backgrounds during their propagation. Given that within this horizon the distribution of matter is inhomogeneous, it is worth searching for anisotropies in the arrival direction distribution of ultra-high energy cosmic rays even if their paths are distorted by the Galactic and extragalactic magnetic fields that they encounter in a (so far) unpredictable way.

2. The Pierre Auger Observatory

The Pierre Auger Observatory [3] is the largest detector for UHECRs. It is located in Argentina at a latitude of $\sim -35^\circ$, and covers approximately 3000 km^2 . It is a hybrid detector, using both a surface detector array (SD) composed of 1660 water-Cherenkov detectors and an atmospheric fluorescence detector (FD) made of 27 fluorescence telescopes to observe extensive air showers induced in the atmosphere by primary particles with energies $E > 0.1 \text{ EeV}$. The Pierre Auger Observatory is taking data since January 2004. Cosmic ray events are reliably reconstructed up to a zenith angle of 80° , which translates into a field of view ranging from -90° to $+45^\circ$ in declination. The systematic uncertainty on the energy scale is 14%, and the statistical uncertainty in the energy is smaller than 12% for the highest energy events used in this work [4], while the angular uncertainty is less than 0.9° at these energies.

3. The dataset

For the analyses presented in this work, we used data collected by the Surface Detector of the Pierre Auger Observatory from the 1st of January, 2004 to the 31st of August, 2018. We analyse UHECRs with energy above 32 EeV , which corresponds to the highest energy bin analyzed in large scale anisotropy searches, also presented in these proceedings [5]. Events arriving with a zenith angle below 60° are dubbed as "vertical" while events with zenith angle between 60° and 80° are "inclined". Vertical and inclined events undergo different types of selection and reconstruction, that are described in detail in the contribution to this conference reporting on spectrum [2]. For this work, we apply the same relaxed selection used in previous analyses [6]: for vertical events we require that the station with the largest signal is surrounded by at least 4 active stations and that the reconstructed core of the shower falls within an isosceles triangle of active stations, while for inclined events we require only that the station with the largest signal is surrounded by at least 5 active stations. This is a more relaxed selection than the one used in other works presented in these proceedings, such as the analysis of large scale anisotropies, since it is applicable only to the highest

¹ $1 \text{ EeV} = 10^{18} \text{ eV}$.

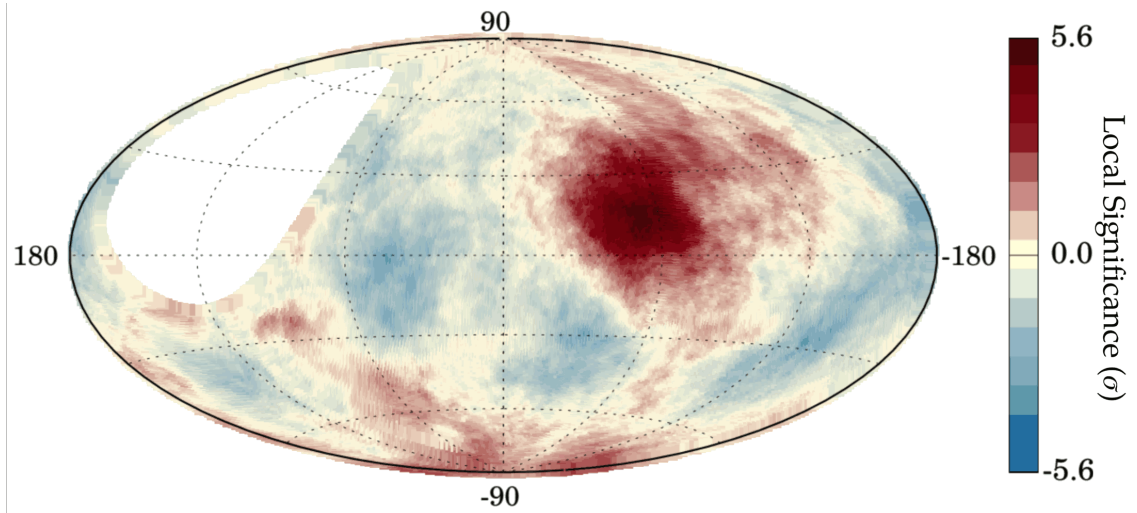


Figure 1: Map in Galactic coordinates of the local significance found when searching for excesses in circular windows with 27° radius above 38 EeV. The post-trial p-value for the most significant excess is 2.5%. See text for details.

energy events that have large footprints on the array. By applying these cuts, we select the highest possible number of events while guaranteeing an accurate reconstruction and exposure estimation. The total number of events selected this way is 2157, with an exposure of $101,400 \text{ km}^2 \text{ sr yr}$.

4. Analyses

4.1 Search for overdensities

The first analysis performed is a model-independent blind search for overdensities over the whole field of view. The search for overdensities was performed with the same methodology used in [6]. The method applied looks for excesses with respect to isotropic expectation in circular regions centered on a $1^\circ \times 1^\circ$ grid covering the whole field of view. The radius of the circular regions, ψ was varied from 1° to 30° in 1° steps. Also the energy threshold of the events was varied from 32 EeV to 80 EeV in 1 EeV steps. The Li-Ma significance was computed for each excess (or deficit) and then penalized for the scanning trials. This penalization was computed by generating simulated isotropic sets of the same size as the real one and counting how many of them showed an excess with a significance equal or larger than the largest found in our data. The most significant excess is found for $E > 38 \text{ EeV}$ at equatorial coordinates $\text{R.A.} = 202^\circ$, $\delta = -45^\circ$ in a 27° radius. In that window, we observe 188 events while we expect 125 from an isotropic distribution of cosmic rays. The local Li-Ma significance is 5.6σ . When performing the same analysis with random isotropic samples 2.5 % gave an excess of equal or higher significance than the one found. The map of the local significance for $E > 38 \text{ EeV}$ in 27° -radius windows over the whole sky is shown in figure 1.

4.2 Correlation with the direction of Cen A

Centaurus A is the nearest radio-loud active galaxy, at a distance of less than 4 Mpc. The

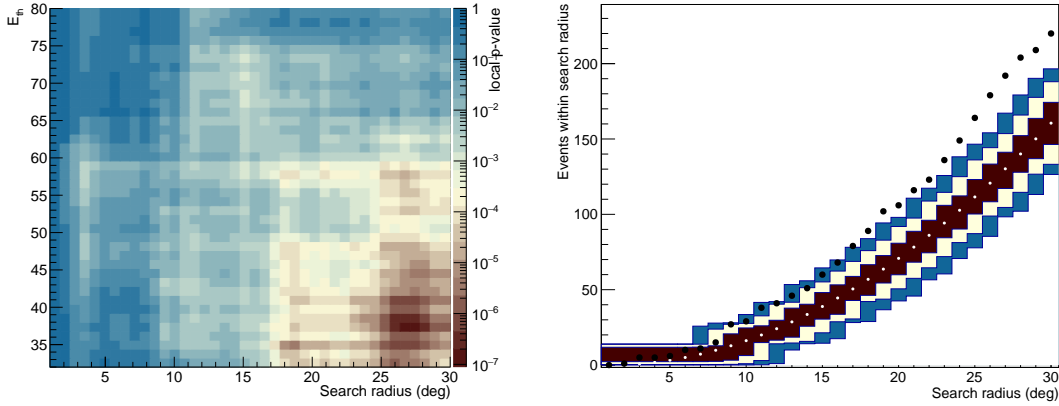


Figure 2: Left: local p-value when searching for excesses around the position of Centaurus A, as a function of search radius and energy threshold. Right: the comparison of number of events with $E > 37$ EeV within a certain angle from Cen A (black dots) compared to the expectation from a isotropic distribution of UHECRs (white dots) and its 1, 2 and 3 – σ dispersion (red, cream and blue respectively).

search for excesses around its direction was performed by counting the number of events within a certain search radius ψ from the AGN position. The number n_{obs} thus obtained is then compared to the one expected given an isotropic distribution of UHECRs, n_{exp} . The binomial probability P of obtaining n_{obs} or more correlating events by chance from an isotropic distribution is computed and considered as local p-values. These values are then penalized as described in the search for overdensities to take into account the trials arising from the scan in energy and in angle. The most significant excess found in the blind search lies $\sim 2^\circ$ away from the position of Cen A. It is not surprising then that when scanning in E_{th} and ψ to find the parameters that give the highest significance, the results are nearly the same as found before: $E_{\text{th}} = 37$ EeV and $\psi = 28^\circ$. For these parameters, 203 events were observed while 141 were expected, and the local significance is 5.1σ which, when penalized for the scan in energy and angle, leads to a one-sided post-trial significance of 3.9σ . This is an increase of significance with respect to the results presented at the 2017 edition of the ICRC [7], where it was 3.1σ .² The local p-values in the $E_{\text{th}} - \psi$ space are shown in figure 2, left. In the right panel of the same figure, it is possible to see the comparison of the number of events within a certain radius from Cen A observed for $E > 37$ EeV to the expectation from an isotropic distribution of cosmic rays (with its 1, 2 and 3 – σ dispersion).

4.3 Likelihood analysis with catalogs of candidate sources

We also update the search for anisotropies published in [8]. This analysis was motivated by the expectation that brighter objects contribute more to the flux, and the likelihood method allowed us to take into account this hypothesis together with the suppression that is expected to increase with distance because of the interactions of UHECRs along their path. In particular, in this method, a probability map of the arrival distribution of cosmic rays is obtained for each model of candidate sources, and compared to the observed distribution of events using an appropriate test statistics

²Note that in that case the energy scan ranged from 40 to 80 EeV.

(TS). The probability maps are smoothed density maps, obtained by modeling the contribution of each individual object with a Fisher-Von Mises distribution with a certain angular width θ . This smearing angle is one of the free parameters of this analysis, and takes into account the unknown deflections of the UHECRs due to magnetic fields. Each object is weighted based on its relative flux, measured in an appropriate band different for each catalog, and on its distance. The attenuation is computed based on the composition scenario at sources that best reproduces the average composition and spectrum measured at the Auger Observatory (scenario A). An isotropic fraction of events was added to the probability maps obtained this way in order to model the diffuse component of UHECRs due to highly deflected events and faint sources not included in the catalogs. The weight of the anisotropic fraction with respect to the isotropic one, f_{aniso} , is the second free parameter for this analysis. The comparison between the model predictions and the observed data is done through a likelihood ratio test. The likelihood function (\mathcal{L}) is the product over the events of the probability map. The likelihood of the null hypothesis (isotropy) \mathcal{L}_0 is obtained as the product over the events of the directional exposure function in the arrival directions. The test statistics used in this analysis is then $TS = 2 \ln \mathcal{L} / \mathcal{L}_0$.

The likelihood analysis was performed on 4 catalogs:

- 2MRS catalog [9], taking out sources closer than 1 Mpc, as selected in [8], which traces the nearby matter.
- Swift-BAT AGNs [10], with the same selection as in [8], which includes both radio loud and quiet AGNs.
- γ -AGN, this time selecting them from the 3FHL catalog [11] recently published by the Fermi collaboration. In [8] the previous 2FHL catalog was used. The selection applied here is the same, with the difference that, since the two catalogs are selected in different energy range, the reference flux used for weighting sources is defined as the integral from 10 GeV to 1 TeV, rather than in the 50 GeV – 1 TeV range as before.
- A sample of starburst galaxies selected based on their continuum emission at 1.4 GHz, used as a proxy of their UHECR flux. This selection has been updated by merging the data from [12] and [13] already reported in [8], with the addition of the Circinus Galaxy and sources selected with HEASARC Radio Master Catalog.³ The number of sources selected this way is 32.

For further details on the catalog selection, please refer to the appropriate section in [8].

The best-fit TS obtained for each catalog at each energy threshold are shown in figure 3, left for starburst and γ -AGN and right for Swift-BAT and 2MRS. It is possible to see that the maximum likelihood-ratio is found with starburst galaxies for $E > 38$ EeV, where a test statistics of 29.5 is obtained. At this energy threshold, the best-fit parameters are $f_{\text{aniso}} = 11_{-4}^{+5}\%$ and $\theta = 15_{-4}^{+5}^\circ$. This corresponds to a local p-value, accounting for the two fit parameters, of 4×10^{-7} , which has then to be penalized for the energy scan, obtaining a post-trial significance of 4.5σ . This is an increase of significance with respect to the results presented in the latest publication of the Collaboration

³<https://heasarc.nasa.gov/W3Browse/master-catalog/radio.html>

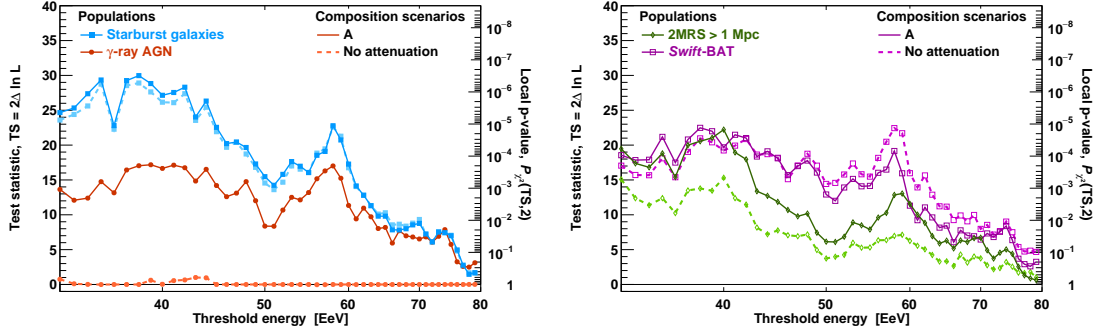


Figure 3: Maximum likelihood-ratio as a function of energy threshold for the models based on starburst galaxies and γ -AGN (left) and Swift-BAT and 2MRS (right). The dashed lines are the same obtained in the no-attenuation scenario.

Catalog	E_{th}	TS	Local p-value	post-trial	f_{aniso}	θ
Starburst	38 EeV	29.5	4×10^{-7}	4.5σ	$11^{+5}_{-4}\%$	$15^{+5}_{-4}^\circ$
γ -AGN	39 EeV	17.8	1×10^{-4}	3.1σ	$6^{+4}_{-3}\%$	$14^{+6}_{-4}^\circ$
Swift-BAT	38 EeV	22.2	2×10^{-5}	3.7σ	$8^{+4}_{-3}\%$	$15^{+6}_{-4}^\circ$
2MRS	40 EeV	22.0	2×10^{-5}	3.7σ	$19^{+10}_{-7}\%$	$15^{+7}_{-4}^\circ$

Table 1: Values of the parameters that maximize the likelihood-ratio test against isotropy for the four different models as described in the text.

[8], where it was 4σ .⁴ A summary of the best-fit parameters obtained for all the four catalogs is reported in table 1.

5. Discussions and conclusion

In this work, we have reported the updated results of searches for anisotropies in the highest energy cosmic rays. All the methods were used in previous analyses and were not changed for this update. With new data up to the end of August 2018, the excess around Centaurus A has increased as well as the significance of rejecting the isotropic hypothesis from a comparison with a starburst galaxies model, reaching 3.9σ and 4.5σ respectively.

Both the blind, full-sky search for excess and that centered on Centaurus A result in a maximum signal obtained at comparable energy thresholds (38 and 37 EeV respectively) and similar top-hat angular scale ($\psi = 27^\circ$ and 28°). Similarly, the catalog-based analysis identifies the largest deviations from isotropy above 38–40 EeV on an angular scale $\theta \sim 15 \pm 5^\circ$. The latter angular spread derives from a Fisher-Von Mises distribution, the equivalent of a Gaussian on the sphere, and would correspond to a top-hat scale $\psi \sim 1.59 \times \theta = 24 \pm 8^\circ$.⁵

We note that the region with the most significant excess flux is densely populated with different types of nearby extragalactic objects. In particular, its center is 2° away from the direction of Cen

⁴Note that in that case the energy scan ranged from 20 to 80 EeV.

⁵The scale factor 1.59, close to the factor $\sqrt{3}$ expected from the scaling of the variances, corresponds to an optimal top-hat window, as used for instance in [14] and [15].

A, which is the object with the largest contribution in the models based on γ -AGNs, Swift-BAT and 2MRS-galaxies, and 6° away from the direction to NGC 4945, which is the object with the largest contribution in the model based on starburst galaxies. The best-fit flux-weighted models derived from the maximum-likelihood analysis predict that the fraction of CRs inside a circle with radius 27° centred at R.A. = 202° , $\delta = -45^\circ$ is 13% (Starburst galaxies and Swift-BAT), 12.2% (γ -AGNs) and 11.5% (2MRS) compared to 14.4% observed in data and 9.5% expected if the flux were isotropic. A more detailed view of this region is shown in figure 4, left panel, in which the black circle has radius 27° and is centered at the position of the most significant overdensity. Also shown are the candidate sources in the models based on γ -AGNs and starburst galaxies, displayed as stars with area proportional to their individual contributions to the expected flux. Note that the model based on starburst galaxies also predicts excess flux around the position of NGC 253 (the galaxy with the second largest contribution in this model) near the southern Galactic pole, in which some excess flux is also indicated in data, as can be seen in figure 1. A more detailed view of this region is shown in figure 4, right panel. As the model based on starburst galaxies, the 2MRS-based model predicts excess flux near the southern Galactic pole, but it does also in other regions in which no excess is found in data, and that partly explains the relatively smaller value of its maximum test-statistics. The models based on γ -AGNs and Swift-BAT do not predict a significant flux excess around the southern Galactic pole. To disentangle between these different scenarios, other types of analyses may be useful, such as the search for magnetically induced signatures also presented in these proceedings [16]. Note also that we do not model in this analysis deflections in intervening magnetic fields that could change the distribution of flux expected from the same source candidates, given the large uncertainties that this modeling would involve.

We presented here the most significant result in a test for anisotropy in the arrival directions of UHECRs. We note that there is no rigorous way of penalizing these results for the numerous analyses performed within and outside the Pierre Auger Observatory Collaboration, in particular since many of such tests were performed using catalogs of astrophysical sources that show similar flux patterns in the sky. We will keep monitoring these interesting excesses, also with the additional information that is coming in the next few years with the observatory upgrade, Auger Prime [17].

References

- [1] The Pierre Auger Collaboration, *Science* **357** (2017) 1266-1270
- [2] V. Verzi for The Pierre Auger Collaboration. These proceedings. [PoS \(ICRC2019\) 450](#)
- [3] The Pierre Auger Collaboration, *Nucl. Instrum. Meth. A* **798** (2015) 172.
- [4] V. Verzi for The Pierre Auger Collaboration. Proceedings for the 33rd International Cosmic Ray Conference (ICRC 2013) arXiv:1307.5059
- [5] E. Roulet for The Pierre Auger Collaboration, These proceedings. [PoS \(ICRC2019\) 408](#)
- [6] The Pierre Auger Collaboration, *Astrophys. J* **804** (2015) 15
- [7] U. Giaccari for The Pierre Auger Collaboration, [PoS \(ICRC2017\) 483](#)
- [8] The Pierre Auger Collaboration, *Astrophys. J. Lett.* **853** (2018) L29
- [9] J. P. Huchra, L. M. Macri, K. L. Masters, et al. *Astrophys. J. Supp.* **199** (2012) 26
- [10] W. H. Baumgartner et al., *Astrophys. J. Supp.* **207** (2013) 19
- [11] M. Ajello, et al. *Astrophys. J. Supp.* **232.2** (2017) 18

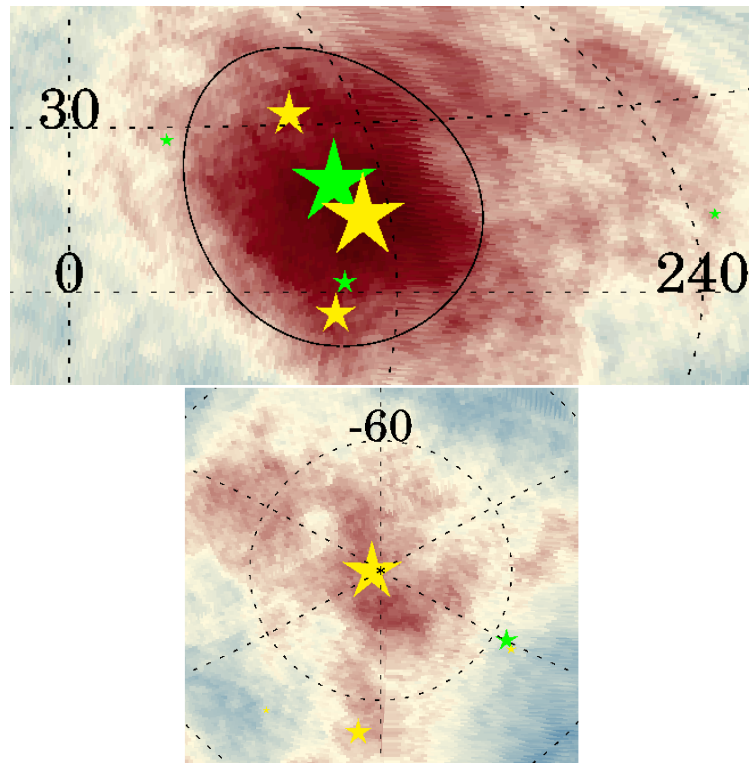


Figure 4: Zoom of the map in Figure 1 with the candidate sources that give the largest contribution to the expected flux in the best-fit models based on γ -AGNs (green) and starburst galaxies (yellow) superimposed. The area of the stars is proportional to their contribution. The left panel displays a black circle with radius 27° centered at the position of the most significant flux excess, with also Cen A (the largest green star) and NGC 4945 (largest yellow star) visible. Right: the south Galactic pole excess, with NGC 253 visible as the largest yellow star.

- [12] M. Ackermann, M. Ajello, A. Allafort, et al. , *Astrophys. J.* **755** (2012) 164
- [13] Becker, J. K., Biermann, P. L., Dreyer, J, Kneiske, T. M. 2009, ArXiv e-prints, arXiv:0901.1775
- [14] The Pierre Auger Collaboration, *Astroparticle Physics* **27** (2007) 244
- [15] The Pierre Auger Collaboration, *Astrophys. J.* , **760** (2012) 148
- [16] M. Wirtz for The Pierre Auger Collaboration, these proceedings *PoS (ICRC2019)* 469
- [17] The Pierre Auger Collaboration, arXiv:1604.03637

3

Nuclear mass composition, photons, and neutrinos



PIERRE
AUGER
OBSERVATORY



Mass composition of cosmic rays with energies above $10^{17.2}$ eV from the hybrid data of the Pierre Auger Observatory

Alexey Yushkov^{*a} for the Pierre Auger Collaboration^{b†}

^a*Institute of Physics of the Czech Academy of Sciences, Prague, Czech Republic*

^b*Observatorio Pierre Auger, Av. San Martín Norte 304, 5613 Malargüe, Argentina*

E-mail: auger_spokespersons@fnal.gov

Full author list: http://www.auger.org/archive/authors_icrc_2019.html

We present updates on the measurements of the depth of the shower maximum X_{\max} and the correlation between X_{\max} and the signal in the water-Cherenkov stations of events registered simultaneously by the fluorescence and the surface detectors of the Pierre Auger Observatory. The measurements of X_{\max} are performed for $E > 10^{17.2}$ eV using observations of the longitudinal development of air showers by the fluorescence telescopes. The evolution of the mean and the fluctuations of X_{\max} with energy, as extracted from the data taken during 2004 – 2017, is interpreted in terms of the evolution of the mean logarithmic mass and the spread of the masses in the primary beam using post-LHC hadronic interaction models.

The measurements of the correlation between X_{\max} and the signal in the surface stations allow one to obtain constraints on the spread of the masses in the primary beam. These constraints are weakly sensitive to the experimental systematic errors and to the uncertainties in the modelling of air showers. Previously, using data taken during 2004 – 2012, we excluded with a significance of 5σ pure compositions and compositions consisting of only protons and helium for energies $10^{18.5} - 10^{19.0}$ eV. In the update of the analysis presented here using the data from years 2004 – 2017 and nearly doubled statistics, these conclusions are confirmed with a significance $> 6.4\sigma$ in the energy range $10^{18.5} - 10^{18.7}$ eV alone, while for higher energies, the correlation in data becomes consistent with less mixed compositions.

36th International Cosmic Ray Conference — ICRC2019

24 July – 1 August, 2019

Madison, Wisconsin, USA

*Speaker.

†for collaboration list see PoS(ICRC2019)1177

1. Introduction

During the last decade, significant progress was achieved in the studies of the mass composition of the ultra-high energy cosmic rays (UHECR). While at energies near and above the flux suppression $E \gtrsim 10^{19.5}$ eV the inferences on the composition still suffer from statistical limitations and uncertainties in the extrapolations of the properties of hadronic interactions, in the region of the possible transition from galactic to extragalactic origins and near the ankle in the UHECR spectrum several results, important for the development and validation of astrophysical models, were obtained.

Measurements of the depth of shower maximum, X_{\max} , published by the Pierre Auger Observatory (Auger) in 2010 [1] were a significant step towards a better understanding of the evolution of the mass composition for $E > 10^{18}$ eV. For the first time, it was shown and later confirmed with higher significance [2, 3, 4] that the mean mass of the UHECRs is decreasing up to $\sim 10^{18.3}$ eV and starts increasing afterwards. This qualitative statement can be derived from the energy dependence of the mean and standard deviation of X_{\max} alone without resorting to hadronic interaction models. The observations, being interpreted in terms of $\ln A$ moments and fractions of individual species, indicate that for energies below the ankle the spread of the masses in the primary beam is larger than for higher energies.

These findings were corroborated by the analysis of the correlation between X_{\max} and the signal in water-Cherenkov detectors (WCD) reported by Auger in 2016 [5]. The observed correlation for energies $10^{18.5} - 10^{19.0}$ eV was found to be negative and compatible with a spread of the masses in the primary beam of $\sigma(\ln A) = 1.35 \pm 0.35$. Since in simulations for all proton-helium mixes the correlation is non-negative, this result is robust evidence that nuclei with $A > 4$ can be accelerated to ultra-high energies and escape the source environment.

In these proceedings, the update of the X_{\max} measurements [4] is presented with data from the years 2016 and 2017 using the latest improvements in the fluorescent technique implemented in Auger [6].

The correlation analysis is updated with five more years of data (2013 – 2017) and contains nearly two times larger event statistics with respect to the published results [5].

2. Data selection

At the Pierre Auger Observatory, the longitudinal development of air showers is measured with the fluorescence detector (FD) consisting of 24 fluorescence telescopes each covering 30° in azimuth and $1.5^\circ - 30^\circ$ in elevation. The telescopes are grouped in units of six at four sites around the surface detector (SD) array of 3000 km^2 in area. Three additional high-elevation ($30^\circ - 58^\circ$) Auger telescopes (HEAT) for the detection of air showers with energies below 10^{18} eV have been operating since 2009 at the Coihueco FD site.

Monitoring of atmospheric conditions, mandatory for the accurate reconstruction of X_{\max} and energy of air showers, is regularly performed at the Observatory (see [7] for more details). Pressure, humidity, temperature profiles, vertical aerosol optical depth (VAOD), the presence of clouds in the field of view of the FD telescopes are monitored in intervals from 15 minutes to 3 hours (depending on the type of monitoring) using a variety of instruments.

Both analyses presented in these proceedings are performed using hybrid events, i.e. events registered by the FD and having at least one triggered SD station. The data selection follows the procedure described in detail in [2]. Good atmospheric conditions are required, meaning that the value of the integral of the VAOD up to 3 km above ground should be lower than 0.1 and that the observations of the longitudinal profile should not be affected by the presence of clouds. The depth of the shower maximum should be in the observed part of the profile and have the expected reconstruction uncertainty $< 40 \text{ g cm}^{-2}$. To avoid a mass composition bias, the difference between SD trigger probabilities for proton and iron should be smaller than 5%. Finally, a fiducial field-of-view selection is applied to guarantee an unbiased FD acceptance of the showers almost independently of their X_{max} and geometries.

Measurements of X_{max} and the analysis of the correlation between SD and FD data from the standard FD sites are performed for the period 12/2004 – 12/2017. For HEAT/Coihueco (HeCo), the X_{max} measurements from the ICRC 2017 [4] are presented using the period 06/2010 – 12/2015. All events with energies below $10^{18.1} \text{ eV}$ detected by HeCo are excluded from the data set of the standard FD. Thus these two data sets are completely independent.

In the analysis of the correlation, for an accurate estimation of the signal at 1000 meters from the core, only events for which at least five stations are active in the hexagon around the WCD with the highest signal are accepted. Events containing saturated stations are excluded, and the analysis is performed up to a zenith angle of 65° where SD reconstruction biases are small. The SD selection applied here is the same as in [5].

3. Measurements of the depth of shower maximum

Measurements of X_{max} with the standard FD are performed at energies above $10^{17.8} \text{ eV}$. Showers of lower energies reach their maximum higher in the atmosphere and because of their fainter profiles are observed only at distances closer to the telescopes. These showers can be reconstructed using information from the combined HeCo telescopes. The extension of X_{max} measurements with the help of HeCo down to $10^{17.2} \text{ eV}$ was previously presented in [3, 4].

Energies and X_{max} of the selected events are corrected for small reconstruction biases determined using Monte-Carlo (MC) simulations generated with CONEX [8] and detector simulations and reconstruction using the Offline Auger software [9] that reproduces the real-time state of the FD and SD. Mean $\langle X_{\text{max}} \rangle$ and $\sigma(X_{\text{max}})$ are calculated using a correction for the residual acceptance biases, and the detector resolution is subtracted from the width of the observed X_{max} distributions. This way, the X_{max} moments measured at Auger are free from detector effects and can be directly compared to predictions from MC simulations. The resolution for the standard FD is $\sim 25 \text{ g cm}^{-2}$ at $10^{17.8} \text{ eV}$ and improves to $\sim 15 \text{ g cm}^{-2}$ at the highest energies. The resolution of HeCo at $\sim 10^{18.0} \text{ eV}$ is slightly worse than that of the standard FD because of the time-dependent corrections required to level the relative calibrations of the HEAT and Coihueco. Systematic uncertainties are below 10 g cm^{-2} for most of the energy range (more details can be found in [2]).

The results of the measurements of $\langle X_{\text{max}} \rangle$ and $\sigma(X_{\text{max}})$ as a function of energy, presented in Fig. 1, agree well with our previous publications [1, 2, 4]. The observed rate of change of $\langle X_{\text{max}} \rangle$ with energy is 77 ± 2 (stat) $\text{g cm}^{-2}/\text{decade}$ below $E_0 = 10^{18.32 \pm 0.03} \text{ eV}$ and is 26 ± 2 (stat) $\text{g cm}^{-2}/\text{decade}$ at the higher energies. In simulations, the elongation rates for the constant primary compo-

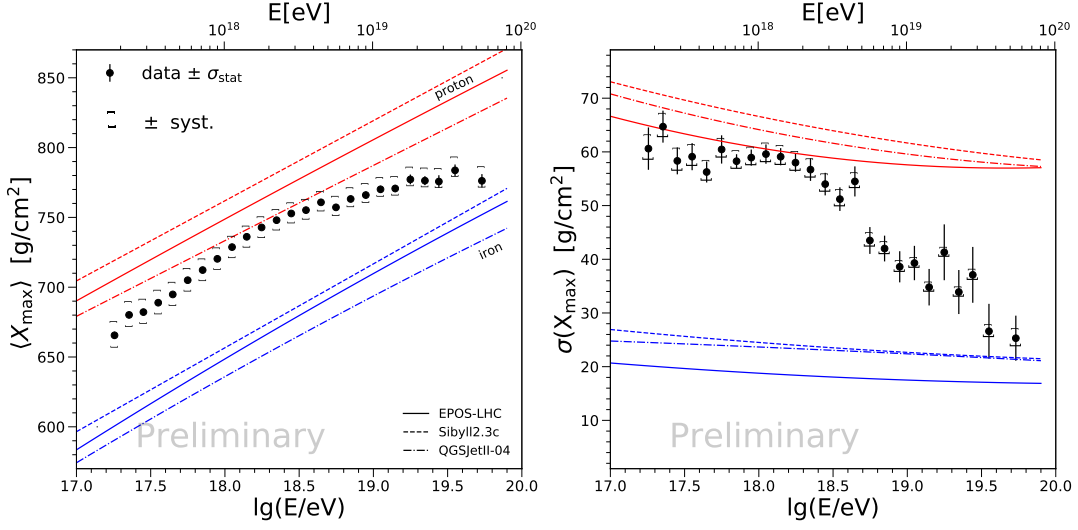


Figure 1: Measurements of $\langle X_{\max} \rangle$ (left) and $\sigma(X_{\max})$ (right) at the Pierre Auger Observatory compared to the predictions for proton and iron nuclei of the hadronic models EPOS-LHC, Sibyll 2.3c and QGSJetII-04.

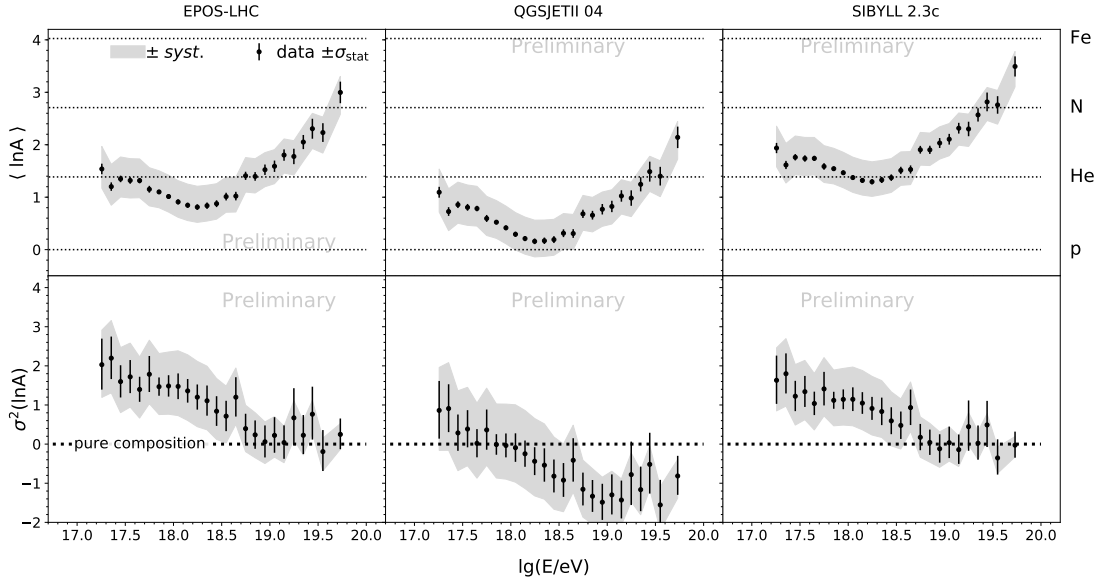


Figure 2: Moments of $\ln A$ distributions from the conversion of the moments of X_{\max} distributions with EPOS-LHC, QGSJetII-04, Sibyll 2.3c.

sitions are close to $\sim 60 \text{ g cm}^{-2}/\text{decade}$ independently of the interaction model used. Thus the mean mass of the UHECRs as a function of energy decreases until E_0 and increases afterwards. The narrowing of the X_{\max} distributions for energies above E_0 (right panel in Fig. 1) is as well in agreement with the MC predictions for $\sigma(X_{\max})$ of heavier nuclei.

Using the method described in [10] the moments of the X_{\max} distributions can be converted to the moments of $\ln A$ distributions. From Fig. 2 one can see that $\langle \ln A \rangle$ reaches the minimum around E_0 . Depending on the interaction model, the values at the minimum vary from ~ 0 for QGSJetII-

04 to 1.4 for Sibyll 2.3c. The spread of the masses is decreasing up to the energies around the ankle ($\sim 10^{18.7}$ eV) and becomes more constant afterwards. In case of QGSJetII-04, the variance of the masses takes non-physical negative values, indicating that using this model the compositions that are preferred are too light and, due to their larger shower-to-shower fluctuations, they do not describe the data well.

4. Correlation between depth of shower maximum and signal in WCDs

The spread of the masses in the primary beam can be estimated from the correlation between X_{\max} and the signal in WCDs at 1000 meters from the core, $S(1000)$ [5, 11]. In this analysis, a general aspect of the development of air showers [12] is used: a smaller X_{\max} ($\Delta X_{\max} \sim -\Delta \ln A$) and larger muon content¹ ($N_{\mu} \sim A^{1-\beta}$, $\beta \simeq 0.9$ [13]) are expected in showers initiated by heavier primary nuclei. While for pure compositions non-negative correlations are found in simulations using CORSIKA [14] and post-LHC hadronic models, in mixed samples smaller values of X_{\max} will be more often found for showers initiated by heavier nuclei with larger N_{μ} . In this way, an anticorrelation between X_{\max} and N_{μ} is expected for mixed compositions. The larger the spread of the masses in the primary beam, the more negative is the correlation. Due to the use of general principles of the development of air showers, the correlation analysis is rather insensitive to the particular details in the modeling of hadronic interactions.

To avoid a decorrelation due to the spreads of energies and zenith angles, we use X_{\max} and $S(1000)$ scaled to a reference energy of 10 EeV. $S(1000)$ is additionally scaled to a zenith angle of 38° . The scaled variables are denoted further as X_{\max}^* and S_{38}^* and thus they are the values of X_{\max} and $S(1000)$ one would have observed, had the shower arrived at 38° and 10 EeV. The correlation between X_{\max}^* and S_{38}^* is evaluated using a ranking correlation coefficient r_G proposed in [15]. The conclusions do not change when other correlation coefficients are used. In Fig. 3 examples of distributions of X_{\max}^* and S_{38}^* are shown for proton and iron showers generated with EPOS-LHC.

The statistical uncertainty can be approximated [5] by $\Delta r_G \simeq 0.9/\sqrt{n}$, where $n = 2652$ is the number of events in the data set and thus $\Delta r_G(\text{data}) = 0.017$. The systematic uncertainty is $\Delta r_G(\text{sys.}) = {}^{+0.01}_{-0.02}$, the negative error is larger due to a small decorrelation (we do not apply any corrections for this effect) in the data sample introduced by long term performances of Auger FD and SD.

As shown in Fig. 3, the correlation found in data is $r_G = -0.069 \pm 0.017$, while in [5] the value of $r_G = -0.125 \pm 0.024$ was reported. We could not individuate any detector effects that could lead to such a change and thus we conclude that it is a result of changes in reconstruction and a statistical fluctuation as will also be discussed below. The main conclusions of [5] remain unchanged: the negative correlation found in data cannot be reproduced using any pure composition. Since the correlation is found to be non-negative for all proton-helium mixes, the data can be explained only by mixed compositions containing primary nuclei heavier than helium $A > 4$. Both these conclusions substantiate our findings from the analysis of X_{\max} .

The spread of the primary masses $\sigma(\ln A)$ can be estimated from Fig. 4 where the correlation found in data is compared to the values in simulated mixtures with all possible combinations of

¹The muon contribution to $S(1000)$ is 40% to 90% depending on zenith angle.

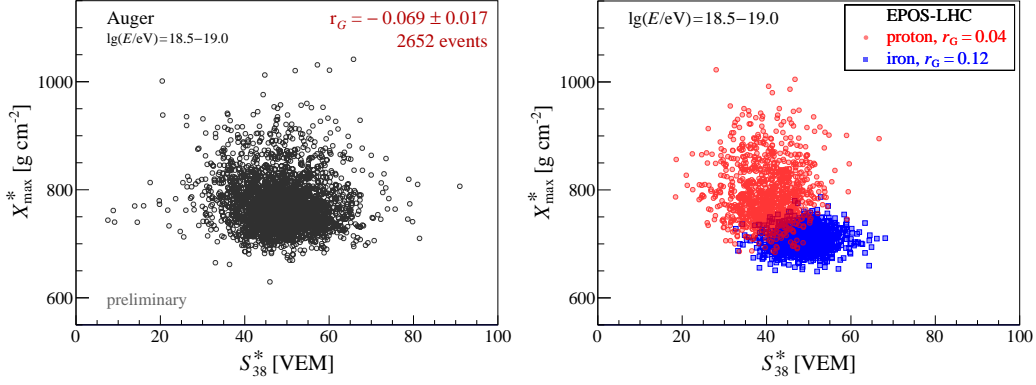


Figure 3: Distribution of X_{\max}^* and S_{38}^* for $\lg(E/eV) = 18.5 - 19.0$ in data (left) and for 1000 proton and 1000 iron showers simulated with EPOS-LHC (right).

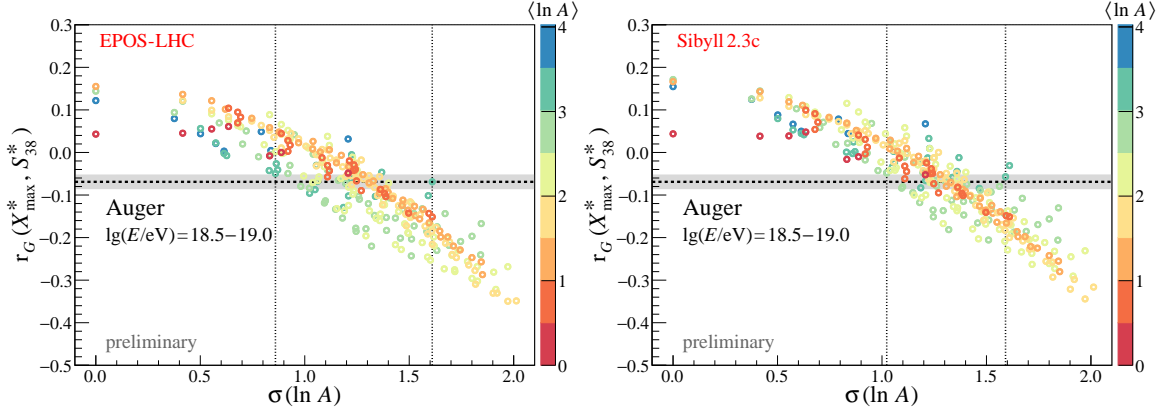


Figure 4: Dependence of the correlation coefficients r_G on $\sigma(\ln A)$ for EPOS-LHC (left) and Sibyll 2.3c (right). Each simulated point corresponds to a mixture with different fractions of (p, He, O, Fe) nuclei, the relative fractions change in 0.1 steps (four points for pure compositions are grouped at $\sigma(\ln A) = 0$). Colors of the points indicate $\langle \ln A \rangle$ of the corresponding simulated mixture. The shaded area shows the observed value for the data. Vertical dotted lines indicate the range of $\sigma(\ln A)$ in simulations compatible with the observed correlation in the data.

relative fractions of (p, He, O, Fe) nuclei changing with a step of 0.1. The correlation $r_G(X_{\max}^*, S_{38}^*)$ gets more negative for the larger spreads of the masses in the mixes. For all models (for QGSJetII-04, not shown in the figure, the results are similar to Sibyll 2.3c) the spread of masses corresponding to the correlation found in data lies in the range compatible to [5]: $0.85 \lesssim \sigma(\ln A) \lesssim 1.6$.

The comparison of the energy dependence of r_G in data to the predictions for proton, iron and extreme mix p/Fe = 1/1 for EPOS-LHC and Sibyll 2.3c interaction models (for QGSJetII-04, not shown here, r_G (proton) is > 0.1 for all energies) is shown in Fig. 5. Compared to [5] an additional energy bin $\lg(E/eV) = 19.0 - 19.5$ has been added.

Combining data in the range $\lg(E/eV) = 18.5 - 18.7$ the observed correlation is $r_G = -0.141 \pm 0.022$, which significantly (6.4σ) differs from zero. For higher energies, the correlation in data becomes consistent with the compositions with smaller mixings. Comparing new data in Fig. 5 to the results of [5] one can see that the change of the correlation in the whole energy range $\lg(E/eV) =$

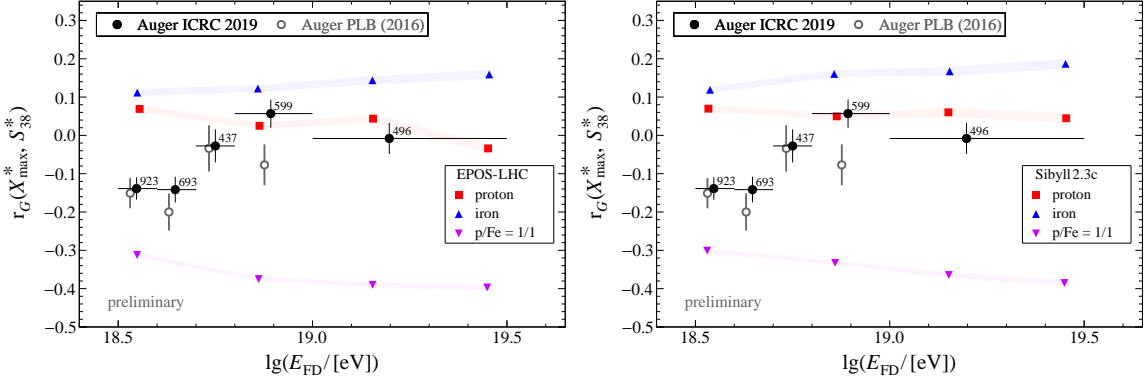


Figure 5: The correlation coefficients r_G for data (full circles) in the energy bins $\lg(E/eV) = 18.5 - 18.6$; $18.6 - 18.7$; $18.7 - 18.8$; $18.8 - 19.0$; $19.0 - 19.5$. Numbers of events in each bin are given next to the data points. For comparison, results from our previous publication [5] are shown with open circles (points are slightly shifted along x -axis to improve visibility). The data sets are statistically compatible with $\chi^2/\text{ndf} = 5.4/4$ (p-value = 0.25). Predictions for proton, iron and extreme mix $p/\text{Fe} = 1/1$ are given for EPOS-LHC (left) and Sibyll 2.3c (right), the widths of the colored bands for the MC results correspond to statistical errors.

$18.5 - 19.0$ from -0.125 to -0.069 is mostly caused by the change of r_G for $\lg(E/eV) = 18.8 - 19.0$ to more positive values. The more negative r_G in [5] for 287 events available then, could result from a statistical fluctuation. With more statistics in the current data set, the results are compatible to a decrease of $\sigma(\ln A)$ above the ankle, as also suggested by the decrease of $\sigma(\ln A)$ in the X_{max} analysis.

5. Summary

In this proceedings, earlier findings of Auger about the evolution of the UHECR composition for $E > 10^{17.2}$ eV have been confirmed with higher significance. The conclusions listed below hold true for all pre- and post-LHC hadronic interaction models, and in the case of the analysis of the correlation between X_{max}^* and S_{38}^* the results, in addition, are robust to modifications of various parameters of nuclear interactions [5].

From the analysis of X_{max} , it follows that the mean mass of the UHECR is getting lighter up to $10^{18.3}$ eV and is becoming heavier afterwards. The spread of the masses $\sigma(\ln A)$ is becoming smaller up to the ankle ($E \sim 10^{18.7}$ eV) and more constant at higher energies. The spread of the masses near the ankle, determined from the analysis of the $(X_{\text{max}}^*, S_{38}^*)$ correlation, is compatible with $0.85 \lesssim \sigma(\ln A) \lesssim 1.6$. For energies below the ankle ($10^{18.5} - 10^{18.7}$ eV) a significantly negative correlation $r_G = -0.141 \pm 0.022$ is observed in the data, that allows us to exclude pure compositions and proton-helium mixes all of which have non-negative correlations.

The conclusions on the increase of the primary mass for $E > 10^{18.3}$ eV, obtained here using hybrid events, are supported by the analysis of the Auger SD data [16]. In the extension of the SD analysis presented at this conference, due to the higher duty cycle of the SD the evolution of the UHECR mass is probed for the energies well beyond 10^{19} eV [17].

References

- [1] **Pierre Auger** Collaboration, J. Abraham et al., *Measurement of the Depth of Maximum of Extensive Air Showers above 10^{18} eV*, *Phys. Rev. Lett.* **104** (2010) 091101, [[arXiv:1002.0699](#)].
- [2] **Pierre Auger** Collaboration, A. Aab et al., *Depth of maximum of air-shower profiles at the Pierre Auger Observatory. I. Measurements at energies above $10^{17.8}$ eV*, *Phys.Rev.* **D90** (2014), no. 12 122005, [[arXiv:1409.4809](#)].
- [3] **Pierre Auger** Collaboration, A. Porcelli, *Measurements of X_{\max} above 10^{17} eV with the fluorescence detector of the Pierre Auger Observatory*, *PoS (ICRC2015)* 420, [[arXiv:1509.0373](#)].
- [4] **Pierre Auger** Collaboration, J. Bellido, *Depth of maximum of air-shower profiles at the Pierre Auger Observatory: Measurements above $10^{17.2}$ eV and Composition Implications*, *PoS (ICRC2017)* 506.
- [5] **Pierre Auger** Collaboration, A. Aab et al., *Evidence for a mixed mass composition at the ‘ankle’ in the cosmic-ray spectrum*, *Phys. Lett.* **B762** (2016) 288–295, [[arXiv:1609.0856](#)].
- [6] **Pierre Auger** Collaboration, B. Dawson, *The Energy Scale of the Pierre Auger Observatory*, *PoS (ICRC2019)* 231.
- [7] **Pierre Auger** Collaboration, A. Aab et al., *The Pierre Auger Cosmic Ray Observatory*, *Nucl. Instrum. Meth.* **A798** (2015) 172–213, [[arXiv:1502.0132](#)].
- [8] T. Bergmann, R. Engel, D. Heck, et al., *One-dimensional hybrid approach to extensive air shower simulation*, *Astropart. Phys.* **26** (2007) 420–432, [[astro-ph/0606564](#)].
- [9] S. Argiro, S. L. C. Barroso, J. Gonzalez, et al., *The Offline Software Framework of the Pierre Auger Observatory*, *Nucl. Instrum. Meth.* **A580** (2007) 1485–1496, [[arXiv:0707.1652](#)].
- [10] **Pierre Auger** Collaboration, P. Abreu et al., *Interpretation of the Depths of Maximum of Extensive Air Showers Measured by the Pierre Auger Observatory*, *JCAP* **1302** (2013) 026, [[arXiv:1301.6637](#)].
- [11] P. Younk and M. Risse, *Sensitivity of the correlation between the depth of shower maximum and the muon shower size to the cosmic ray composition*, *Astropart.Phys.* **35** (2012) 807–812, [[arXiv:1203.3732](#)].
- [12] J. Matthews, *A Heitler model of extensive air showers*, *Astropart.Phys.* **22** (2005) 387–397.
- [13] J. Alvarez-Muñiz, R. Engel, T. K. Gaisser, et al., *Hybrid simulations of extensive air showers*, *Phys. Rev.* **D66** (2002) 033011, [[astro-ph/0205302](#)].
- [14] D. Heck, J. Knapp, J. N. Capdevielle, et al., *CORSIKA: a Monte Carlo code to simulate extensive air showers*. Forschungszentrum, Karlsruhe, 1998. FZKA 6019.
- [15] R. Gideon and R. Hollister, *A rank correlation coefficient resistant to outliers*, *JASA* **82** (1987) 656–666.
- [16] **Pierre Auger** Collaboration, A. Aab et al., *Inferences on mass composition and tests of hadronic interactions from 0.3 to 100 EeV using the water-Cherenkov detectors of the Pierre Auger Observatory*, *Phys. Rev.* **D96** (2017), no. 12 122003, [[arXiv:1710.0724](#)].
- [17] **Pierre Auger** Collaboration, C. Peixoto, *Estimating the Depth of Shower Maximum using the Surface Detectors of the Auger Observatory*, *PoS (ICRC2019)* 440.



Estimating the Depth of Shower Maximum using the Surface Detectors of the Pierre Auger Observatory

Carlos José Todero Peixoto^{*†} for the Pierre Auger Collaboration^{b†}

^a*Escola de Engenharia de Lorena, Universidade de São Paulo, São Paulo, Brazil*

^b*Observatorio Pierre Auger, Av. San Martín Norte 304, 5613 Malargüe, Argentina*

E-mail: auger_spokespersons@fnal.gov

Full author list: http://www.auger.org/archive/authors_icrc_2019.html

The Pierre Auger Collaboration has developed a method for estimating the depth of shower maximum (X_{\max}) using the risetime of the signals recorded by the array of water-Cherenkov detectors. The average value of X_{\max} is determined for energies above 3 EeV, using air showers with zenith angles up to 60° . The work described here considerably extends that reported previously with an increase in the total number of events by a factor 2.1. In total 125,005 events are used, of which 237 are above 50 EeV. The data set is approximately a factor 30 larger than what is available from fluorescence measurements for energies above 3 EeV. The results reinforce previous conclusions: the mean mass of high-energy cosmic rays begins to rise above 3 EeV and extend that finding to higher energies with greater precision. Additionally, we find strong discrepancies when we make a comparison between observations and predictions from simulations with values which are obtained from measurements of the risetime of the recorded signals.

36th International Cosmic Ray Conference — ICRC2019

24 July – 1 August, 2019

Madison, Wisconsin, USA

^{*}Speaker.

[†]for collaboration list see PoS(ICRC2019)1177

1. Introduction

Knowledge of the mass composition of cosmic rays would provide us with crucial information to discriminate between different classes of production, acceleration and propagation models, and to understand the origin of the observed flux suppression; it would allow us to search for a stream of protons at higher energies, thus enhancing the study of small-scale anisotropy. It could further improve previous studies of particle physics at 10 EeV and extend them to energies as high as $\sqrt{s} = 200$ TeV.

Using data from the Pierre Auger Observatory, several methods that enable mass discrimination with ground-based detectors have been developed. Of the several parameters studied, those that presented some relevance were X_{\max} [1] (from measurements of the fluorescence detector, FD), X_{\max}^{μ} [2], Risetime Asymmetries [3] and the Delta Method [4, 5], the latter three using the signals from the surface detector, SD. The X_{\max} parameter has the best resolution for mass composition studies, but the FD only operates during nights without moonlight, only 13% of the operating time of the SD. With the Delta method, we can use the signals from the SD, which has a nearly 100% duty cycle, to calculate a parameter, Δ_S , and to convert this to an estimation of the depth of the shower maximum, X_{\max}^{Delta} .

This work is based on the Delta Method [4], which was originally used with SD data up to zenith angles $\sim 45^\circ$. We now extend the method to events up to 60° . This yields an increase of about 50% in the number of events, thus reducing the statistical uncertainty associated with mass-composition inferences. We have also extended the sample by including three additional years of data. The large data set from the 750 m array has not been updated.

2. Data Selection

This work uses a data sample from the 1500 m array collected from January 2004 to August 2018. We consider events with zenith angles below 60° , and with energies above 3 EeV to guarantee full trigger efficiency.

We also impose conditions at the level of single water-cherenkov detectors (WCD): the total signal must be above 5 VEM, and the distance to the shower core must be in the interval [300, 1400] m for the 1500 m array. For events with energies $\log_{10}(E/\text{eV}) > 19.8$, we extend the distance range up to 2000 m.

After applying these selection criteria, the number of events used in what follows is 125,005.

3. The Delta Method

The Delta Method is explained in Figure 1(Left). We characterize every event with a single parameter Δ_S , which is a function of the risetimes¹ recorded for this event. We have determined relationships (dubbed as *benchmarks*) that describe the risetimes as a function of the distance and zenith angle in a narrow energy range. Risetimes for each WCD are compared to the predicted *benchmark* value, in units of the accuracy with which risetimes are determined, giving a parameter

¹This parameter is the time for the integrated signal to increase from 10% to 50% of the final magnitude of the integrated signal.

Δ_i . Δ_s is the average of the Δ_i values over the N selected WCDs. An example of the dependence of the risetime with the distance to the core is shown in Figure 1(Right).

For each PMT in a detector, there are two Flash Analog-to-Digital Converter (FADC) channels: a high-gain and a low-gain channel (used when the high-gain (HG) channel has saturated). Fits to the data are made using the function

$$t_{1/2}^{\text{low-gain}} = 40 \text{ ns} + \sqrt{A(\theta)^2 + B(\theta) \cdot r^2} - A(\theta), \quad (3.1)$$

where $A[\text{ns}]$ and $B[\text{ns}^2/\text{m}^2]$ are free parameters. With A and B known, a fit to the points from the HG channel is made (shown by grey points in Figure 1(Right)) as

$$t_{1/2}^{\text{high-gain}} = 40 \text{ ns} + N(\theta) \cdot \left(\sqrt{A(\theta)^2 + B(\theta) \cdot r^2} - A(\theta) \right) \quad (3.2)$$

where $N(\theta)$ is a free parameter. In this way, the small differences between the measurements with the two channels are dealt with.

These three parameters are parameterized as a function of $\sec \theta$ in the narrow *benchmark* energy bin. The energy bin used is $\log_{10}(E/\text{eV}) = 19.1-19.2$.

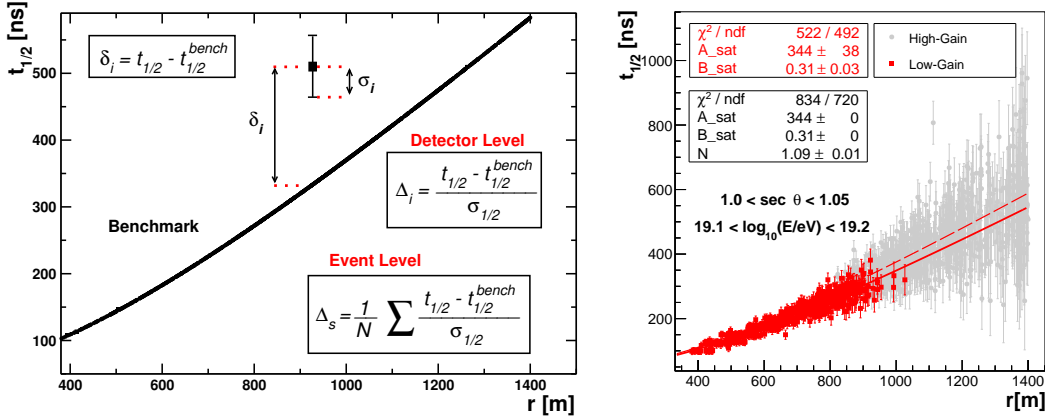


Figure 1: (Left) Description of the Delta Method. (Right) Risetime measurements as a function of the distance to the core for data from the 1500 m array in the energy interval $19.1 < \log_{10}(E/\text{eV}) < 19.2$.

The Delta Method procedures are fully described in [4, 5].

4. Extending to angles up to 60 degrees

Once the functional forms of $A(\theta)$, $B(\theta)$ and $N(\theta)$ are known, the mean value of the Δ_s distribution must be, by definition, compatible with zero for the *benchmark* energy bin, as shown in the Figure 2(a) for events with $\sec \theta < 1.45$. For more inclined events, the parameter A falls rapidly to zero, so that a specific parameterization is needed for this set of events. The result of this new parameterization is shown in the Figure 2(a). As expected, the mean value of the distribution for more inclined events is compatible with zero.

Merging these datasets ($\sec \theta < 1.45$ and $\sec \theta > 1.45$ in Figure 2) we see that the new $\langle \Delta_S \rangle$, Figure 3(a), is consistent with zero. The $\langle \Delta_S \rangle$ as a function of $\sec \theta$ is shown in the Figure 3(b). In the *benchmark* region, Δ_S shows no dependence on the angle.

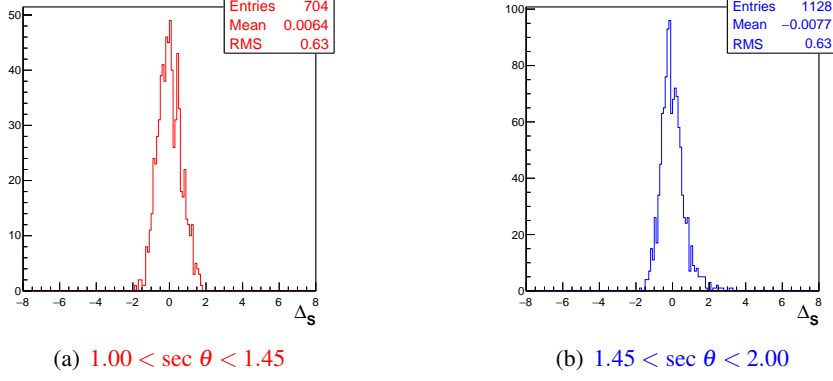


Figure 2: Δ_S values for two zenith angle ranges in the energy bin: $19.1 < \log_{10}(E/eV) < 19.2$.

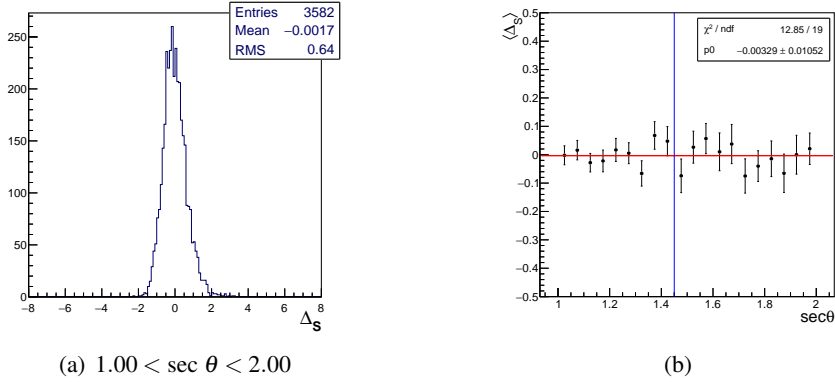


Figure 3: (a) Distribution of Δ_S values for the whole angular range considered in this work. (b) Dependence of $\langle \Delta_S \rangle$ with the zenith angle.

5. $\langle \Delta_S \rangle$ as function of the energy and the evolution for $\langle \ln A \rangle$ with energy

In Figure 4 (Left), the evolution of $\langle \Delta_S \rangle$ as a function of energy is shown. In Figure 4 (Right), a comparison with hadronic models is made. The measurements are well within the predictions from simulations, and they favour a composition dominated by heavier elements as the energy increases. In Figure 5, good agreement between the new and the previously published data is shown. In total, we have more than doubled the number of events. For $\log_{10}(E/eV) > 19.8$, the data set has been increased by a factor 2.1 because of the larger distance range adopted in the signal selection. Our results confirm, with a bigger statistical sample, that as the energy increases, the composition of the flux is dominated by elements heavier than protons.

In Figure 6, we fit our $\langle \Delta_S \rangle$ measurements to different functional forms. The fit to a straight line is poor ($\chi^2 = 75$ for 13 degrees of freedom). When a broken line is considered, the fit is also

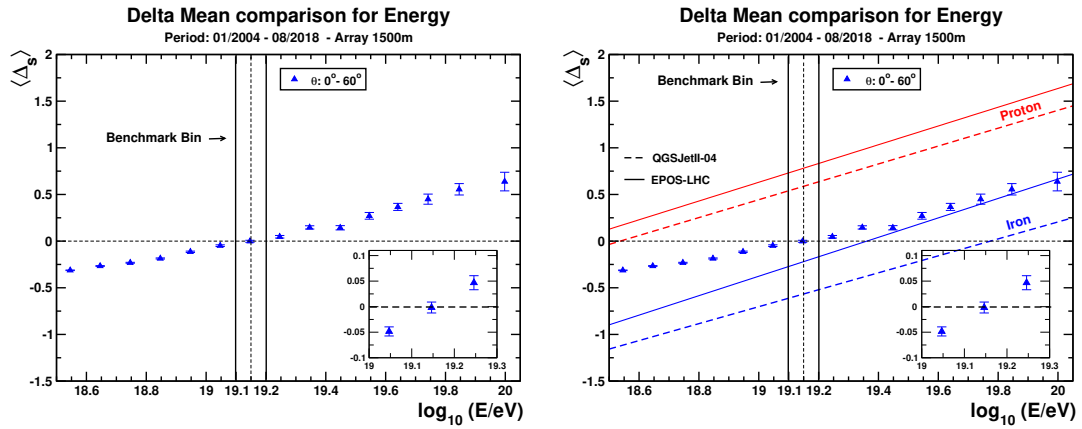


Figure 4: (Left) $\langle \Delta_S \rangle$ as function of the energy for the new dataset. (Right) Comparison of the evolution of $\langle \Delta_S \rangle$ as a function of the energy for data and simulations.

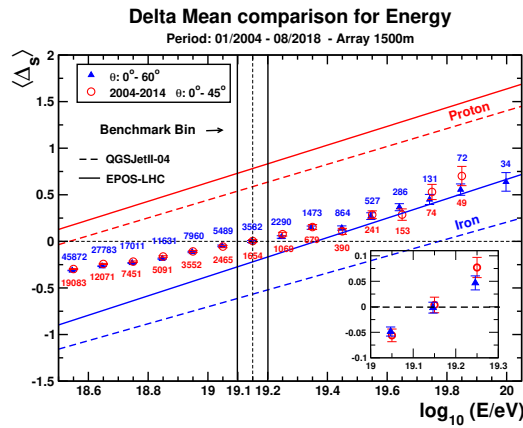


Figure 5: Comparison with previously published results. The numbers indicate the amount of events in each energy bin.

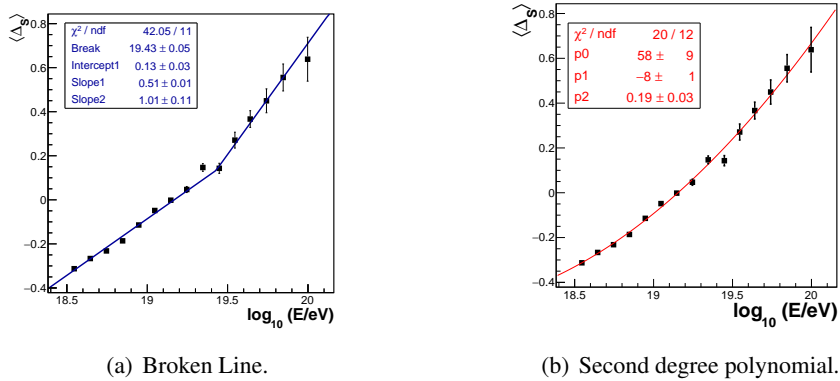


Figure 6: Fits for $\langle \Delta_S \rangle$ as a function of the energy.

poor ($\chi^2/\text{dof} = 42/11$). A better fit is obtained ($\chi^2/\text{dof} = 20/12$) when our measurements are fit to a second degree polynomial. When compared to model predictions, this result clearly indicates that the rate of change of mass composition varies with energy.

Although it is not possible to compare the fluorescence and surface detector data directly, it is possible to transform the X_{max} and the Δ_S values to values of $\langle \ln A \rangle$. In this work, we used the proton and iron primaries for the hadronic models QGSJetII-04 [6] and EPOS-LHC [7].

Figure 7 shows that the QGSJetII-04 and EPOS-LHC models do not describe data adequately. One of the most prominent reasons for this disagreement comes from the difference observed when comparing the number of predicted muons in models with the measurements made with the Pierre Auger data [8].

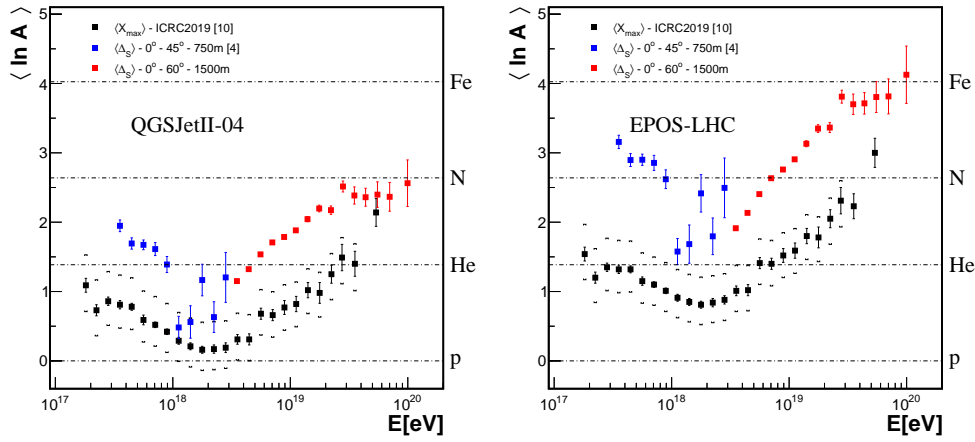


Figure 7: Evolution of the average mass with energy for measurements done with the FD and the SD.

6. Cross Calibration between Δ_S , $X_{\text{max}}^{\text{FD}}$ and Energy

We now address the correlation of Δ_S with X_{max} using hybrid events. We would not expect a 1:1 correlation between these parameters because the position of X_{max} is dominated by the electromagnetic component, whereas Δ_S is dependent on a muon/electromagnetic mix. The values of Δ_S can be calibrated with $\langle X_{\text{max}}^{\text{FD}} \rangle$ providing a correlation from which a new parameter $\langle X_{\text{max}}^{\text{Delta}} \rangle$ can be calculated. These events have been taken from the FD data set discussed in [9] and are shown in Figure 8. There are 2126 events available for calibration. The selected samples of events are unbiased.

Adjusting a linear surface parameterized as

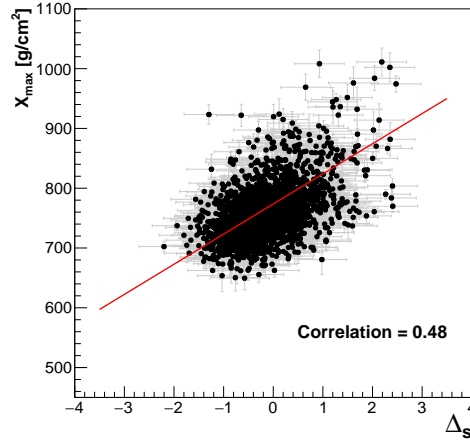
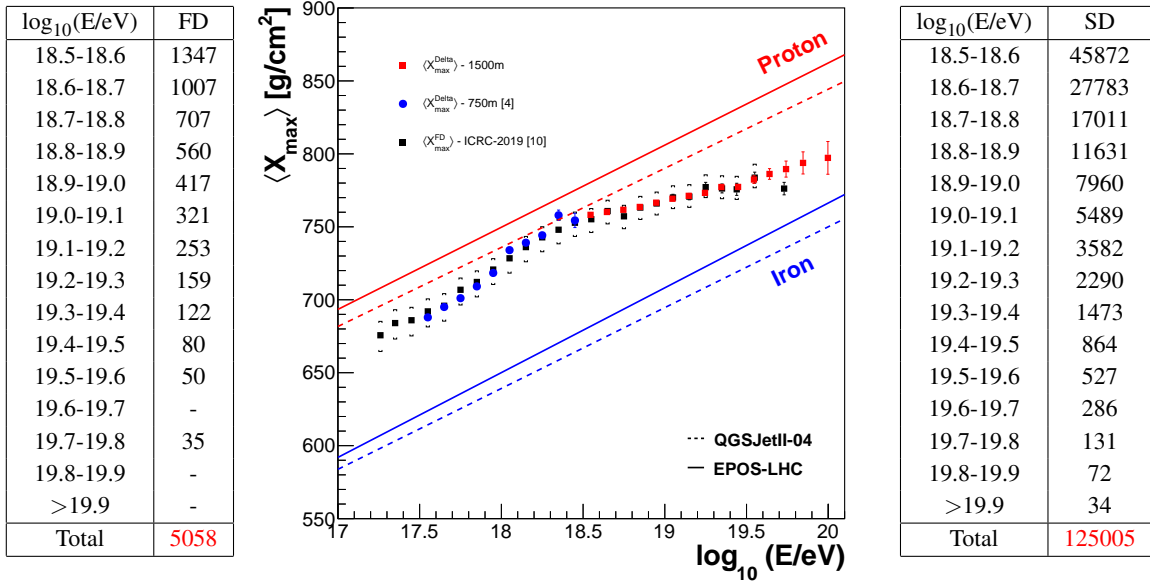
$$\langle X_{\text{max}}^{\text{Delta}} \rangle = a + b \cdot \langle \Delta_S \rangle + c \cdot \log_{10}(E_{SD}/\text{eV}) \quad (6.1)$$

the resulting parameters were used to calculate $\langle X_{\text{max}}^{\text{Delta}} \rangle$. The values of the parameters a , b and c are listed in Table 1.

The $\langle X_{\text{max}}^{\text{Delta}} \rangle$ and $\langle X_{\text{max}}^{\text{FD}} \rangle$ vs energy are shown in Figure 9, together with the number of events (FD and SD) for each energy bin. This analysis confirms with greater precision that, as the energy increases, intermediate/heavy nuclei are preponderant in the flux composition of ultra-high energy cosmic rays.

Table 1: Values for a , b and c for equation 6.1.

Array	$a(\text{g/cm}^2)$	$b(\text{g/cm}^2)$	$c(\text{g/cm}^2)$
1500 m	733 ± 38	34 ± 12	2 ± 1

Figure 8: Correlation between X_{max} and Δ_s for hybrid events.Figure 9: Evolution of $\langle X_{\text{max}}^{\text{Delta}} \rangle$ with energy. The SD measurements are compared with the $\langle X_{\text{max}} \rangle$ measurements done with the FD [10]. The figures in the table correspond to the number of events per energy bin. They are restricted to the energy interval where the Delta method has been updated.

7. Conclusions

The Delta Method uses the information provided by the risetimes of the signals recorded by the WCD of the Surface Detector Array. With it, we can probe the validity of the assumptions contained in state-of-the-art packages that model hadronic interactions at ultra-high energies. Likewise, we can perform mass composition studies with the largest data sample available. This work extends the applicability of the Delta Method up to zenith angles of 60° and adds three more years of data to previously published results. We confirm, with improved precision, that: i) the rate of change of mass composition varies in the energy range covered by our analysis and, that intermediate/heavy nuclei are predominant as the energy increases; ii) simulations do not reproduce correctly the physics of extensive air showers.

Acknowledgements

We acknowledge the support from Fundação de Amparo à Pesquisa do Estado de São Paulo (FAPESP) 2016/19764-9; Conselho Nacional de Desenvolvimento Científico e Tecnológico (CNPq) 404993/2016-8 and Financiadora de Inovação e Pesquisa (FINEP). We also acknowledge the National Laboratory for Scientific Computing (LNCC/MCTI, Brazil) for providing HPC resources of the SDumont and CENAPAD-SP project UNICAMP/FINEP-MCT, which have contributed to the research results reported within this paper.

References

- [1] **Pierre Auger** Collaboration, *Depth of maximum of air-shower profiles at the Pierre Auger Observatory. I. Measurements at energies above $10^{17.8}$ eV*, *Phys. Rev. D* **90** (2014) 122005.
- [2] D. García-Gómez for the **Pierre Auger** Collaboration, *Measurement of atmospheric production depths of muons with the Pierre Auger Observatory*, in *32th ICRC*, (Beijing), August, 2011.
- [3] **Pierre Auger** Collaboration, *Azimuthal asymmetry in the risetime of the surface detector signals of the Pierre Auger Observatory*, *Phys. Rev. D* **93** (2016) 072006.
- [4] **Pierre Auger** Collaboration, *Inferences on mass composition and tests of hadronic interactions from 0.3 to 100 EeV using the water-Cherenkov detectors of the Pierre Auger Observatory*, *Phys. Rev. D* **96** (2017) 122003.
- [5] P. Sánchez-Lucas, Ph.D. thesis: <https://hera.ugr.es/tesisugr/26357422.pdf>.
- [6] S. Ostapchenko, *Non-linear screening effects in high energy hadronic interactions*, *Phys. Rev. D* **74** (2006) 014026.
- [7] K. Werner, F.-M. Liu and T. Pierog, *Parton ladder splitting and the rapidity dependence of transverse momentum spectra in deuteron-gold collisions at the BNL relativistic heavy ion collider*, *Phys. Rev. C* **74** (2006) 044902.
- [8] **Pierre Auger** Collaboration, *Testing hadronic interactions at ultrahigh energies with air showers measured by the Pierre Auger Observatory*, *Phys. Rev. Lett.* **117** (2016) 192001.
- [9] J. A. Bellido for the **Pierre Auger** Collaboration, *Depth of maximum of air-shower profiles at the Pierre Auger Observatory: Measurements above $10^{17.2}$ eV and composition implications*, in *34th ICRC*, (Bexco, Busan, Korea), July, 2017.
- [10] A. Yushkov for the **Pierre Auger** Collaboration, *Mass composition of cosmic rays with energies above $10^{17.2}$ eV from the hybrid data of the pierreauger observatory*, in *PoS(ICRC2019)482*.



Follow-up searches for ultra-high energy neutrinos from transient astrophysical sources with the Pierre Auger Observatory

Michael Schimp^{*a} for the Pierre Auger Collaboration^{†b}

^a*University of Wuppertal, Wuppertal, Germany*

^b*Observatorio Pierre Auger, Av. San Martín Norte 304, 5613 Malargüe, Argentina*

E-mail: auger_spokespersons@fnal.gov

Full author list: http://www.auger.org/archive/authors_icrc_2019.html

We present searches for ultra-high energy (UHE) neutrinos (> 0.1 EeV) with the Pierre Auger Observatory, following the detections of various types of transient astrophysical sources. These include binary black hole (BBH) mergers, detected via gravitational waves (GWs) by the LIGO and Virgo detectors. The results of the searches for a flux of UHE neutrinos from the BBH mergers combined are reported and include events from the currently ongoing third observing run of the LIGO and Virgo GW detectors. Another source of interest in the context of multi-messenger (MM) astrophysics is TXS 0506+056, a blazar that was found to emit both photons and neutrinos in a correlated manner, but at lower energies than accessible with the Pierre Auger Observatory. Follow-up searches for UHE neutrinos were performed during periods of increased emission of high-energy photons and neutrinos from TXS 0506+056 and the corresponding results are reported.

36th International Cosmic Ray Conference — ICRC2019

24 July – 1 August, 2019

Madison, Wisconsin, USA

^{*}Speaker.

[†]for collaboration list see PoS(ICRC2019)1177

1. Introduction

The Pierre Auger Observatory near Malargüe in the Province of Mendoza, Argentina, is the largest and most precise UHE cosmic-ray detector in the world. The Observatory relies on several different detection systems, one of which is the surface detector (SD), a triangular grid consisting of 1660 water-Cherenkov detectors (WCDs) with a spacing of 1.5 km. Overall, the SD covers an area of 3000 km² and has an average altitude of 1400 m a.s.l., corresponding to a vertical atmospheric depth of 875 g/cm². Each WCD is filled with 12 tons of ultra-pure water. When charged particles in extensive air showers (EAS) traverse this water, Cherenkov radiation is emitted and detected using photomultiplier tubes (PMTs). These PMT signals are used to determine EAS properties such as the arrival direction and energy of the primary particle. The Pierre Auger Observatory has been taking data since the beginning of 2004. Its components are described in detail in [1].

Searches for UHE neutrinos and photons with the Pierre Auger Observatory are described in these proceedings [2, 3]. UHE neutrinos and photons are thought to originate from UHE cosmic rays, being produced either at UHE cosmic-ray sources or during their propagation through the Universe [4–8]. Therefore, the established UHE neutrino and photon search procedures are used as an element in MM searches by following up astrophysical observations made by other instruments.

As neutrinos and photons are electrically neutral, they are not deflected in magnetic fields, and their arrival directions thus point back to their sources. In addition, neutrinos are only subject to the weak interaction, leading to almost no attenuation and therefore to virtually no neutrino horizon as opposed to photons, which interact also electromagnetically and therefore have only a finite effective path length. This length is much shorter than the luminosity distances to the sources followed up in this work, $d > 300$ Mpc [9]. Therefore, this work will focus on UHE neutrinos.

One previous example of a MM follow up with the Pierre Auger Observatory is the search for UHE neutrinos from the first ever observed binary neutron star merger, which was detected as GW170817 via GWs by the LIGO Scientific Collaboration and the Virgo Collaboration (LVC) [10]. Additionally, a wide range of signals from this object was found throughout the electromagnetic spectrum [10, 11], leading to a rich set of astronomical and astrophysical insights, and making it a milestone of MM astronomy. At the time of the merger, the source of GW170817 was located about 2° below the horizon at the site of the Pierre Auger Observatory. This direction is in the most sensitive part of the field of view of the Pierre Auger Observatory, the so-called Earth-skimming (ES) region. Accordingly, Auger provided the strongest constraints on the UHE neutrino fluence in the period of 1000 s symmetrically around the merger, which is the a priori fixed search period for prompt emission from this source [12].

Here we focus on two types of potential transient UHE neutrino sources. The first are binary black hole mergers that were found with the LVC GW detectors. The LIGO Scientific Collaboration discovered BBH mergers with the very first directly detected GWs in 2015, initiating the era of GW astronomy [13, 14]. An observation of the BBH mergers by other means has not yet been successful, despite many searches for a signal by a large number of instruments. The other source type is a specific single source, the blazar TXS 0506+056. The IceCube neutrino observatory detected a high-energy (~ 0.3 PeV) neutrino from the direction of TXS 0506+056 in 2017, leading to the so-called IceCube-170922A alert that allowed other observatories to perform follow-up observations [15]. TXS 0506+056 was in a γ -ray flaring state at the time of the detection of the

high-energy neutrino [16]. The coincidence of the neutrino and the γ -ray flare was found not to be accidental with a significance of 3σ [15]. Additionally, and statistically even more significantly, a 3.5σ excess of neutrinos from this source was found in archival data [17]. Naturally, these findings constitute another important step in the development of MM astronomy.

In the following sections, the follow-up search methods, parameters, and results for both source types are described and discussed.

2. Searches for ultra-high energy neutrinos from binary black hole mergers

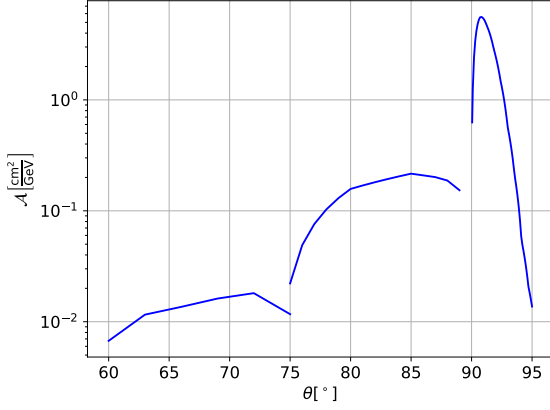
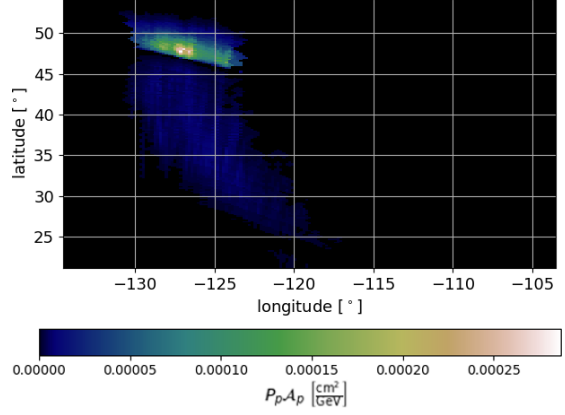
For the 21 events detected and published by the LVC until 2019-06-02 that are most likely originating from BBH mergers [18–29], follow-up searches for UHE neutrinos with the Pierre Auger Observatory have been performed as described below. For the searches, events detected with Auger were only considered to be coincident with a BBH merger if they were detected within 24 hours after the merger and came from within the most probable (90% C.L.) localization quantile in the sky, Ω_{90} , which is provided by the LVC. Using the established UHE neutrino search methods [2], no candidates have been found in such a coincidence with any of the BBH mergers.

In contrast to previous searches, for which follow-up results were expressed in terms of flux or fluence from a single specific source during two fixed search periods, here, the hypothetical fluxes of UHE neutrinos from all followed up BBH mergers are combined as follows. As very little is known about the sources, it is assumed that each has the same isotropic UHE neutrino luminosity as a function of time after the merger. This function, denoted $L(t - t_0)$, with the merger time t_0 , has no a priori constraints. In addition, the differential UHE neutrino flux from each source follows the commonly assumed power law $\frac{d\Phi}{dE_\nu} \propto E_\nu^{-2}$, with the neutrino energy E_ν . These assumptions, together with observational properties, like the localization probability of each source as a function of its direction in the sky, and the neutrino identification efficiency of Auger, allows us to quantify the time-dependent sensitivity to the combined UHE neutrino flux from the sources. As a specific application of this sensitivity, considering that no UHE neutrinos have been found, a 90% C.L. upper bound on $L(t - t_0)$ is calculated and discussed below.

For determining the sensitivity, a key quantity is the effective area $A_{\text{eff}}(E_\nu, \theta, t - t_0)$ of the Observatory, as introduced in [30]. It is proportional to the geometrical area of the SD and to the efficiency of the neutrino detection and identification as a function of E_ν and zenith angle θ . The explicit dependence of A_{eff} on time originates from minor changes in the status of the SD that can lead to SD stations not being considered for data analysis during certain periods of time, changing the Observatory's used geometrical area. The relationship between the number of identified neutrinos N_ν from the considered sources with index s , the universal isotropic UHE neutrino luminosity of each source $L(t - t_0)$, and the effective area $A_{\text{eff}}(E_\nu, \theta, t - t_0)$ can be written in integral form as:

$$N_\nu = \int_{t_0}^{t_0+24 \text{ h}} \iint_{\Omega_{90}} \int_0^\infty \sum_s \frac{L(t)}{d_s^2} P_s(\delta, \alpha) E_\nu^{-2} A_{\text{eff}}(E_\nu, \theta(\delta, \alpha, t), t) dE_\nu d\Omega dt, \quad (2.1)$$

where the BBH mergers as sources with index s have a probability density per solid angle $P_s(\delta, \alpha)$ to be localized at a certain direction and have the best-fit luminosity distance d_s given by the LVC.


 Figure 1: $\mathcal{A}(\theta, t)$ averaged over the year 2016

 Figure 2: Localization probability per pixel P_p times energy-spectrum weighted effective area \mathcal{A}_p in equatorial coordinates for the BBH merger GW event GW170608, 20h40m after the merger

The energy integral $\mathcal{A}(\theta, t) = \int_0^\infty E_V^{-2} A_{\text{eff}}(E_V, \theta, t) dE_V$ is evaluated separately. Figure 1 shows the average of $\mathcal{A}(\theta, t)$ for the year 2016, which is the benchmark time period for effective areas used in [2]. The zenith-angle dependence of the sensitivity is notable and exhibits a strong peak at $\theta = 90.8^\circ$.

For each BBH merger, the localization probability of each source s is provided by the LVC for a set of discrete equally sized pixels that are fixed in equatorial coordinates. The pixels in the 90% C.L. region Ω_{90} will be indexed with p in the following, and accordingly the probability for the source s to be localized within a pixel p is $P_{p,s}$. For the calculation in terms of pixels, the coordinates (δ, α) from Equation 2.1 are converted into the pixels p , while the directional integration is converted into a sum over p . For each source s , the pixels are smaller than the mean point spread function of a reconstructed neutrino with Auger. Therefore, the pixel-wise localization probability provided by LIGO is sufficiently precise for the purpose of this analysis.

Analogously to the direction dependence of $P_{p,s}$, \mathcal{A} is determined for each pixel and source individually, and in this formulation denoted $\mathcal{A}_{p,s}$. Figure 2 shows an example of $P_{p,s} \cdot \mathcal{A}_{p,s}$ in equatorial coordinates for the source GW170608 at $t - t_0 = 74400$ s. A diffuse structure with two distinct regions can be recognized. The bright pixels in the North, representing a large value for $P_{p,s} \cdot \mathcal{A}_{p,s}$, are below the local horizon of Auger and therefore part of the ES angular region ($90^\circ < \theta < 95^\circ$), where the sensitivity to neutrinos is large. The much fainter pixels further south belong to directions above the local horizon, where the sensitivity to neutrinos is much lower [2].

Evaluating the time-dependent quantities from Equation 2.1 in time bins i with a width Δt , the following relation between the number of neutrinos per time bin, $N_{V,i}$, and the corresponding universal isotropic UHE luminosity of the sources in that time bin, L_i , holds:

$$N_{V,i} = L_i \Delta t \sum_s \frac{\sum_p P_{p,s} \mathcal{A}_{p,s,i}}{d_s^2}. \quad (2.2)$$

No neutrinos were found with Auger during any 24-hour time interval after the mergers. Thus,

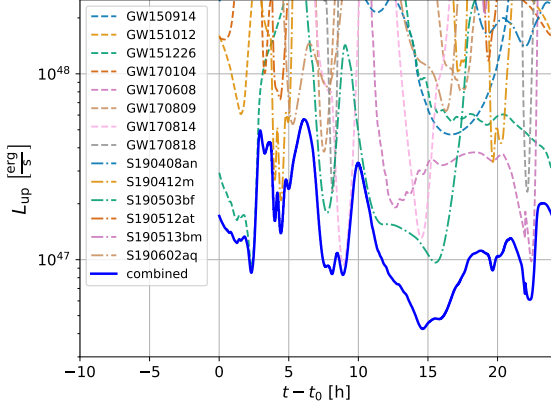


Figure 3: Solid line: upper limit on the time-dependent universal isotropic neutrino luminosity; dashed (dash-dotted) lines: individual single-source contributions from the first two (third) LIGO/Virgo observing runs; sources not indicated here are above the L_{up} -range of the Figure

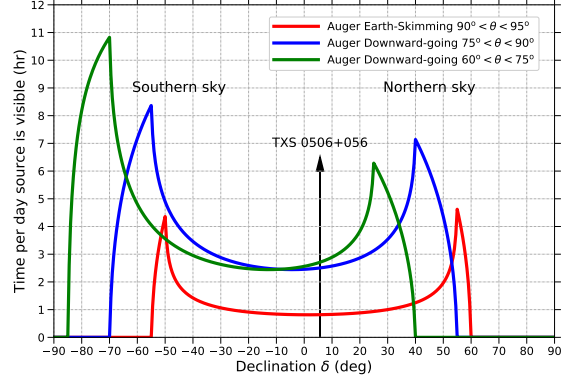


Figure 4: Lines: time per day that a given declination lies in the different neutrino search zenith regions of Auger; arrow: declination of TXS 0506+056

as an application, the 90% C.L. upper bound on the isotropic luminosity, $L_{\text{up},i}$, for all time bins i is derived in the following. The 90% C.L. upper bound on the number of UHE neutrinos identified in the 24 hours after all mergers combined is $N_{\text{up},\text{v},\text{tot}} = 2.44$. The value is the 90% C.L. sensitivity to a Poisson signal when observing zero events with a background expectation of zero [31], which matches the given situation to a very good approximation. The time bins are chosen to have a width of $\Delta t = 1$ s, so the results are calculated for 86400 of these bins, comprising 24 hours in total. This precision in time is high enough to assume that the results for $L_{\text{up},i}$ will very precisely match the upper bound on the true continuous function $L(t - t_0)$.

Using the considerations and assumptions above, the relation $N_{\text{up},\text{v},\text{tot}} = 2.44 = \sum_i N_{\text{up},\text{v},i} = \frac{24 \text{ h}}{\Delta t} N_{\text{up},\text{v},i} \Rightarrow \frac{N_{\text{up},\text{v},i}}{\Delta t} = \frac{2.44}{86400 \text{ s}}$ holds, where $N_{\text{up},\text{v},i}$ is the upper bound on the identified number of neutrinos per time bin i . The assumption that it is the same for all time bins was used here, since both the observed number of detected UHE neutrinos and, to a very good approximation, the expected number of background events are the same (zero) for all time bins. Equation 2.2 can thus be solved for the upper bound on the isotropic luminosity in the time bin i :

$$L_{\text{up},i} = \frac{2.44}{86400 \text{ s}} \left(\sum_s \frac{\sum_p P_{p,s} \mathcal{A}_{p,s,i}}{d_s^2} \right)^{-1}. \quad (2.3)$$

The result for $L_{\text{up},i}$ is shown in Figure 3, where the contributions from the individual sources are indicated as well. For sources whose contribution to the combined sensitivity is more dominant, the corresponding lines in Figure 3 are lower. The universal isotropic luminosity, obtained by combining the sources, is constrained more strongly than the single-source luminosities. This shows that the described combination of sources substantially improves the sensitivity to the source class of BBH mergers as compared to single sources of this class. Still, the combined limit is fully dominated by a single source at some times, e.g. by GW151226 ~ 2.5 hours after the merger.

It should be noted that if this analysis was performed with a longer follow-up search duration, the result would be periodic with a period of 1 sidereal day corresponding to the periodic motion of the field of view of Auger in equatorial coordinates. This, added to the fact that it has been the standard for previous searches [32], substantiates the choice of the 24 hours after each merger as the search duration. With further BBH mergers being detected in the future, the total exposure will increase and either a signal will be eventually detected, or the UHE neutrino emission of the sources can be constrained better over time.

3. Searches for UHE neutrinos from the neutrino-emitting blazar TXS 0506+056

For the blazar TXS 0506+056, the two follow-up search time intervals used in this work are 2014-10-19 – 2015-02-06, and 2017-03-22 – 2017-09-22. The earlier one corresponds to the time of the excess of neutrinos reported by IceCube [17], while the later one is motivated by one of the benchmark durations given by IceCube that represent the γ -ray flare during which the IceCube-170922A high-energy neutrino was found [15]. No neutrinos have been found with Auger during these periods.

TXS 0506+056 is a well located source and the follow-up periods consist of whole days. Therefore, the exposure to it depends only on its declination and, analogous to the BBH merger follow-up searches, small temporary variations in the status of Auger. Figure 4 illustrates the time per day a given declination lies in the different neutrino search regions, where the declination of TXS 0506+056 is indicated.

By taking into account these visibility times and the respective effective areas, the overall sensitivity to the source over a given time interval is obtained. The fluxes corresponding to certain numbers of neutrinos identified with Auger during a given period of time can then be determined in the same way as for the BBH follow-up searches. In the following, we present the fluxes that would correspond to an expectation of one identified UHE neutrino with Auger during each of the mentioned search periods.

In Figure 5, this flux is shown for the first search period (2014-10-19 – 2015-02-06) together with the flux of the neutrino excess measured by IceCube and extrapolations of that measurement to higher energies [17]. These results are shown for different power laws assumed for the flux. The spectrum measured by Fermi-LAT during this time [33] lies mostly below the IceCube flux in this representation. One can see that the flux that would correspond to one UHE neutrino identified by Auger is larger than the extrapolation by IceCube in this E^2 -weighted representation. The ratio between them is ~ 20 for a hard spectrum $\propto E^{-1.9}$. This difference originates largely from the fact that the source is visible only periodically. In particular, it lies in the ES region, the region with the largest sensitivity, for a fraction of only $\sim \frac{1}{25}$ of the time. For a spectrum $\propto E^{-2.3}$, this ratio is ~ 2000 , indicating the lower sensitivity of Auger to softer spectra.

The results for the second search period (2017-03-22 – 2017-09-22) are summarized in Figure 6. It can be inferred that, in this E^2 -weighted representation, the flux associated to the IceCube-170922A alert event is very similar to the photon flux measured by Fermi-LAT in the GeV range [15, 16]. However, the flux that would correspond to one UHE neutrino identified with Auger in this period is ~ 20 times larger than that, again explainable by the periodic visibility of the source, which is not optimal when averaging over time.

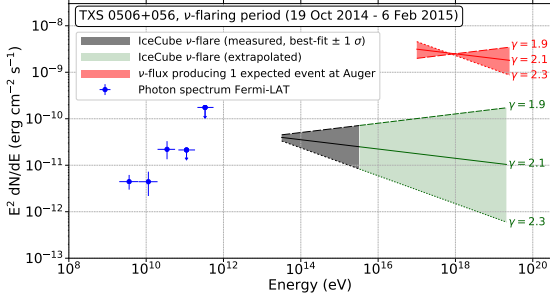


Figure 5: Fluxes associated with the TXS 0506+056 neutrino excess in 2014/2015; blue data points (arrows): measured (upper bounds on) photons from Fermi-LAT; lower shaded region in grey (pale green): IceCube measured (extrapolated) flux of neutrinos for a range of spectral indices; higher shaded region in red: UHE neutrino flux that would correspond to one neutrino being identified with Auger

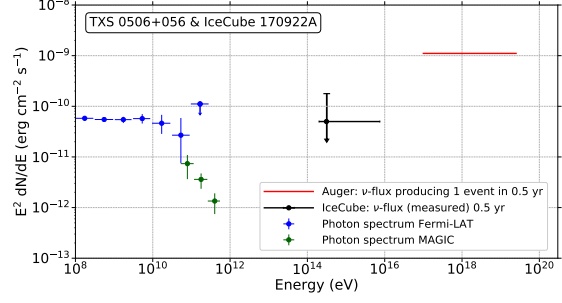


Figure 6: Fluxes from TXS 0506+056 in the time around IceCube-170922A; magenta, blue, and green data points (arrows): measured (upper bounds on) photons by the given instruments; black: neutrino flux of associated IceCube neutrino, assuming this event is the signal for 0.5 years; red: flux from this source that would correspond to one UHE neutrino detected with Auger during the same period

It should also be noted that the neutrino energy ranges regarded for Auger and IceCube in this analysis are about 3 orders of magnitude apart, meaning that both results are meaningful on their own in their respective energy domains.

4. Summary and conclusions

We presented the procedures and results of two different kinds of analyses of searches for UHE neutrinos from transient sources.

Searches for UHE neutrinos from BBH mergers as potential sources were combined and an upper limit obtained on a universal isotropic UHE neutrino luminosity as a function of time after the merger, that would apply to each of the sources. Approximately 14.6 hours after the merger, the combined sensitivity is maximal, and a universal isotropic source UHE neutrino luminosity L_{up} above $\sim 4.3 \cdot 10^{46} \frac{\text{erg}}{\text{s}}$ is excluded due to the non-observation of UHE neutrinos from the 90% C.L. BBH merger localization regions in the sky during the 24-hour periods after all mergers, under the assumption that the sources emit UHE neutrinos with a spectrum $\propto E_{\nu}^{-2}$.

The follow-up searches for UHE neutrinos from the direction of TXS 0506+056 were performed during two different time intervals, 2014-10-19 – 2015-02-06 and 2017-03-22 – 2017-09-22, motivated by a neutrino excess found with IceCube during the earlier one and a γ -ray flare with an associated high-energy neutrino alert lasting the later time interval. No UHE neutrinos have been observed in these searches by Auger. For comparison with the lower-energy IceCube neutrino fluxes from this source, the flux that would correspond to one UHE neutrino from TXS 0506+056 identified with Auger in each of the two follow-up periods has been calculated. For all considered periods and hypothetical energy spectral shapes, the E^2 -weighted flux necessary to produce this one UHE neutrino has been found to be more than an order of magnitude larger than the flux estimations

given by IceCube. While this indicates a smaller sensitivity to neutrinos from the TXS 0506+056 flares, explainable by the periodic visibility with interruptions, the fluxes apply to different energy ranges (TeV/PeV vs. EeV range) and complement each other well.

References

- [1] A.Aab [Pierre Auger Collaboration], *Nucl. Instrum. Meth. A* **798** (2015) 172.
- [2] F.Pedreira for the Pierre Auger Collaboration, *PoS (ICRC2019)* 979.
- [3] J.Rautenberg for the Pierre Auger Collaboration, *PoS (ICRC2019)* 398.
- [4] K.Greisen, *Phys. Rev. Lett.* **16** (1966) 748.
- [5] G.T.Zatsepin, V.A.Kuz'min, *JETP Lett.* **4** (1966) 78.
- [6] D.Hooper, A.Taylor, S.Sarkar, *Astropart. Phys.* **23** (2005) 11.
- [7] M.Ave, N.Busca, A.V.Olinto, A.A.Watson, T.Yamamoto, *Astropart. Phys.* **23** (2005) 19.
- [8] K.Kotera, D.Allard, A.V.Olinto, *JCAP* **2010** (2010) 013.
- [9] M.Risse and P.Homola, *Mod. Phys. Lett. A*, **22** (2007) 749.
- [10] B.P.Abbot et al., *Astrophys. J. Lett.* **848** (2017) L12.
- [11] I.Arcavi et al., *Nature* **551** (2017) 64.
- [12] A.Albert et al., *Astrophys. J. Lett.* **850** (2017) L35.
- [13] B.P.Abbot [LIGO Scientific Collaboration and Virgo Collaboration], *Phys. Rev. Lett.* **116** (2016) 061102.
- [14] B.P.Abbot [LIGO Scientific Collaboration and Virgo Collaboration], *Phys. Rev. Lett.* **116** (2016) 241103.
- [15] IceCube Collaboration, *Science* **361** (2018) eaat1378.
- [16] Y.T.Tanaka, S.Buson, D.Kocevski for the Fermi-LAT collaboration, *Astronomer's Telegram* **10791** (2017).
- [17] IceCube Collaboration, *Science* **361** (2018) 147.
- [18] B.P.Abbot [LIGO Scientific Collaboration and Virgo Collaboration], *arXiv preprint* (2018) arXiv:1811.12907.
- [19] L.Singer [LIGO Scientific Collaboration and Virgo Collaboration], *GCN Circular* **24069** (2019).
- [20] P.Shawhan [LIGO Scientific Collaboration and Virgo Collaboration], *GCN Circular* **24098** (2019).
- [21] D.Chatterjee [LIGO Scientific Collaboration and Virgo Collaboration], *GCN Circular* **24141** (2019).
- [22] S.Ghosh [LIGO Scientific Collaboration and Virgo Collaboration], *GCN Circular* **24377** (2019).
- [23] D.Chatterjee [LIGO Scientific Collaboration and Virgo Collaboration], *GCN Circular* **24503** (2019).
- [24] M.Drago [LIGO Scientific Collaboration and Virgo Collaboration], *GCN Circular* **24522** (2019).
- [25] S.Ghosh [LIGO Scientific Collaboration and Virgo Collaboration], *GCN Circular* **24570** (2019).
- [26] R.De Pietri [LIGO Scientific Collaboration and Virgo Collaboration], *GCN Circular* **24598** (2019).
- [27] G.Mo [LIGO Scientific Collaboration and Virgo Collaboration], *GCN Circular* **24621** (2019).
- [28] S.J.Kapadia [LIGO Scientific Collaboration and Virgo Collaboration], *GCN Circular* **24632** (2019).
- [29] P.Shawhan [LIGO Scientific Collaboration and Virgo Collaboration], *GCN Circular* **24717** (2019).
- [30] A.Aab [Pierre Auger Collaboration], *arXiv preprint* (2019) arXiv:1906.07419, prepared for submission to JCAP.
- [31] G.J.Feldman, R.D.Cousins, *Phys. Rev. D* **57** (1998) 3873.
- [32] A.Aab [Pierre Auger Collaboration], *Phys. Rev. D* **94** (2016) 122007.
- [33] P.Padovani, P.Giommi, E.Resconi, T.Glauch, B.Arsioli, N.Sahakyan, M.Huber, *MNRAS* **480** (2018) 192.



Bounds on diffuse and point source fluxes of ultra-high energy neutrinos with the Pierre Auger Observatory

Francisco Pedreira^{*a} for the Pierre Auger Collaboration^{b†}

^a*IGFAE, Santiago de Compostela, Spain*

^b*Observatorio Pierre Auger, Av. San Martín Norte 304, 5613 Malargüe, Argentina*

E-mail: auger_spokespersons@fnal.gov

Full author list: http://www.auger.org/archive/authors_icrc_2019.html

Neutrinos with energies above 100 PeV are detectable with the Surface Detector array (SD) of the Pierre Auger Observatory. Identification is efficiently done for neutrinos of all flavors interacting in the atmosphere at large zenith angles (downward-going DG), as well as for Earth-skimming (ES) tau neutrinos. No neutrino candidates were found up to 31 August 2018, and this allowed us to put upper bounds on their flux that constrain several models of cosmic-ray and neutrino production at EeV energies. With the SD of Auger we can also search for neutrinos from point-like sources, monitoring a large fraction of the sky (from $\sim -80^\circ$ to $\sim +60^\circ$) in equatorial declination with peak sensitivities at declinations around -53° and $+55^\circ$, unmatched in the northern hemisphere. An excellent sensitivity can also be obtained in the case of transient sources lasting of order an hour or less if they occur when the source is in the field of view of the ES or DG channels.

36th International Cosmic Ray Conference — ICRC2019

24 July – 1 August, 2019

Madison, Wisconsin, USA

^{*}Speaker.

[†]for collaboration list see PoS(ICRC2019)1177

1. Introduction

In this work we report on the search for ultra-high energy (UHE) neutrinos in data taken with the SD of the Pierre Auger Observatory. A blind scan of data from 1 January 2004 up to 31 August 2018 has yielded no neutrino candidates. This corresponds to ~ 14.7 years of data taken or to ~ 9.7 equivalent years of operation of a complete SD (the array was not fully deployed until 2008) representing an increase of 5.2 years of data taken over previous searches [1]. The non-observation of neutrino candidates allows us to place stringent constraints on the diffuse flux of UHE neutrinos with relevant implications for the origin of the ultra-high energy cosmic rays (UHECRs). Here we report upper limits to the diffuse flux of UHE neutrinos [2] and also corresponding limits to the neutrino flux from point-like sources as a function of declination [3].

2. The neutrino search with the Pierre Auger Observatory

The Pierre Auger Observatory is located in the province of Mendoza, Argentina, at a mean altitude of 1400 m above sea level. It has been running and taking data since 2004, and although it was primarily designed to measure extensive air showers (EAS) induced by UHECRs, the Observatory can also identify UHE neutrinos using its SD. This is an array of 1660 water-Cherenkov detectors (“stations”), each SD station containing 12 tonnes of water and located 1.5 km from its neighbors arranged in a hexagonal pattern.

There are two different ways to detect neutrinos with the SD. Firstly, neutrinos of all flavors can undergo charged current (CC) or neutral current (NC) interactions in the atmosphere and induce a “downward-going” shower that can be detected. Secondly, tau neutrinos (ν_τ) can produce in the Earth crust a tau lepton (through CC interactions) that exits the Earth surface and decays in the atmosphere inducing an “Earth-skimming” upward-going shower. Neutrino-induced showers must be identified in Auger data against the background of showers initiated by UHECRs. The identification is based on a simple idea: protons, heavier nuclei and photons interact shortly after entering the atmosphere, while neutrinos can initiate showers deep in the atmosphere. At large zenith angles, the atmosphere is thick enough that the electromagnetic component of showers initiated by nucleonic cosmic rays gets absorbed, and the shower front at ground level is mainly composed of muons producing signals in the SD stations that have characteristic large peaks associated to individual muons which are spread over short time intervals. On the other hand, showers induced by neutrinos deep in the atmosphere have a considerable electromagnetic component at the ground, in several of the triggered SD stations producing signals that are spread over time.

The search strategy consists in selecting showers that arrive at the SD array in the inclined directions (with zenith angle between $60^\circ < \theta < 90^\circ$ for DG and $90^\circ < \theta < 95^\circ$ for ES) and identifying those that show a broad time structure in the signals detected for the SD stations. In the following we briefly explain the main steps involved in the selection algorithm. The first step is the selection of inclined events. For geometrical reasons, in inclined events the pattern of the triggered SD stations typically exhibits an elliptical shape on the ground. These patterns can be characterized by a length L (major axis) and a width W (minor axis) and inclined events typically exhibit large values of L/W [4]. The different set of cuts applied to select DG and ES events is detailed in [2].

The second step is identifying those inclined events that interact deep in the atmosphere. The main observable used to discriminate broad from narrow shower fronts is the Area-over-Peak¹ (AoP) [1]. Inclined background showers of hadronic origin exhibit AoP values close to one, in contrast with neutrino-induced showers where the values of AoP are typically larger.

To select ES ν_τ , we use the AoP averaged over all the triggered stations ($\langle \text{AoP} \rangle$). For DG showers, we construct a multivariate analysis combining several observables that carry information on the time spread of the signals in the SD stations. For optimization purposes the DG category of events is subdivided into two sets for Low (DGL) and High (DGH) zenith angles, between $60^\circ < \theta < 75^\circ$ and $75^\circ < \theta < 90^\circ$ [1], respectively. Full details can be found in [2].

A search for ES and DG neutrino-induced showers was performed in the Observatory data from 1 January 2004 when data taking started, up to 31 August 2018. No neutrino candidates were identified. In Fig. 1 (left) we show the distribution of $\langle \text{AoP} \rangle$ for inclined events in the ES sample in the whole data period compared to that expected in Monte Carlo simulations of ν_τ -induced ES showers, along with the optimized value of the cut ($\langle \text{AoP} \rangle = 1.83$) above which an event would be regarded as a neutrino candidate [2]. After the inclined selection and the neutrino identification criteria $\sim 95\%$ of the simulated neutrinos that induce triggers are identified. This proves that the Pierre Auger Observatory is highly efficient as a neutrino detector. The Fisher distribution for inclined events in the DGH sample in the whole data period with $N_{\text{stations}} \geq 12$ compared to that expected in Monte Carlo simulations is also shown in Fig. 1 (right).

3. Exposure

The non-observation of neutrino candidates let us calculate an upper limit to the diffuse flux of UHE neutrinos. For this purpose the exposure of the SD of Auger needs to be obtained for

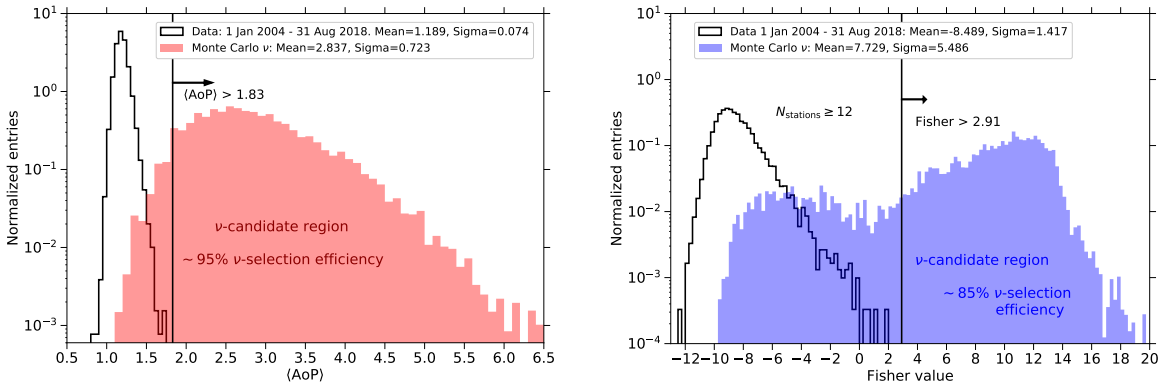


Figure 1: Left: Distribution of $\langle \text{AoP} \rangle$ after the Earth-Skimming inclined selection. Right: Distribution of the Fisher variable after the DGH inclined event selection for events with a number of triggered stations larger than 11. The filled red and blue histograms are the distributions of $\langle \text{AoP} \rangle$ and Fisher value in Monte Carlo (MC) simulations of ν . Black histograms refer to the corresponding selection for data (25904 inclined events in left, 12139 inclined events in right).

¹The Area-over-Peak is defined as the ratio of the integral of the time trace to its peak value normalized to the average signal produced by a single vertical muon.

the period unblinded using Monte Carlo simulations of neutrino-induced showers, as well as the same selection and identification criteria applied to the data. The identification efficiencies for each channel are shown in [4].

For downward-going neutrinos the detection efficiency, $\varepsilon_{i,c}$, depends mainly on neutrino flavor $i = \nu_e, \nu_\mu, \nu_\tau$, the type of interaction ($c = \text{CC}, \text{NC}$), neutrino energy E_ν , zenith θ and azimuth φ angles, the point of impact of the shower core on the ground, and the depth at which the neutrino interacts. In the ν_τ Earth-skimming channel the efficiency ε_{ES} depends on the energy of the emerging τ leptons E_τ , the position of the signal pattern on the ground, on the zenith θ and azimuth φ angles, and on the altitude of the decay point of the τ above the ground. The total exposure \mathcal{E}_{tot} is obtained assuming a flavor mixture of $\nu_e : \nu_\mu : \nu_\tau = 1 : 1 : 1$. Full details can be found in [2].

4. Limits to diffuse fluxes

The total exposure \mathcal{E}_{tot} folded with a single-flavor flux of UHE neutrinos per unit energy, area A , solid angle Ω and time, and integrated in energy gives the expected number of events for that flux:

$$N_{\text{evt}} = \int_{E_\nu} \mathcal{E}(E_\nu) \phi(E_\nu) dE_\nu. \quad (4.1)$$

Assuming a differential neutrino flux $\phi = k \cdot E_\nu^{-2}$, an upper limit to the value of k at 90% C.L. is obtained as

$$k_{90} = \frac{2.39}{\int_{E_\nu} E_\nu^{-2} \mathcal{E}_{\text{tot}}(E_\nu) dE_\nu}, \quad (4.2)$$

where 2.39 is the Feldman-Cousins factor for non-observation of events in the absence of expected background accounting for systematic uncertainties [1]. The single-flavor 90% C.L. integrated limit is $k_{90} < 4.4 \times 10^{-9} \text{ GeV cm}^{-2} \text{ s}^{-1} \text{ sr}^{-1}$. It mostly applies in the energy interval $10^{17} \text{ eV} - 2.5 \times 10^{19} \text{ eV}$ for which $\sim 90\%$ of the total event rate is expected in the case of a E_ν^{-2} spectral flux. The integrated limit represents the value of the normalization of a E_ν^{-2} differential neutrino flux needed to predict ~ 2.39 expected events. For such a spectral shape tau neutrinos contribute up to $\sim 86\%$ of the total event rate, and in particular ES neutrinos dominate the rate of ν_τ events over the downward-going ν_τ . The contribution of ν_e and ν_μ together is smaller than 15% in this case.

The denominator of Eq. (4.2) can also be integrated in bins of neutrino energy of width ΔE_ν , and a limit \hat{k}_{90} can be obtained in each energy bin. This is shown in Fig. 2 (left) for logarithmic energy intervals $\Delta \log_{10} E_\nu = 0.5$. The differential limit is an effective way of characterizing the energy dependence of the sensitivity of a neutrino experiment. It can be seen in Fig. 2 that the best sensitivity is achieved for energies around 1 EeV in Auger.

5. Constraints on the origin of UHECRs

Employing the upper limit obtained with the Observatory, we can constrain several models of neutrino production in interactions of UHECRs with the cosmic microwave background, often referred to as cosmogenic neutrino models. For example, scenarios assuming sources that accelerate only protons and which have a strong evolution with z , similar to Fanaroff-Riley type II (FR II) radio-loud active galactic nuclei (AGN) [5], are strongly constrained (probability of observing 0 neutrinos is $\sim 2.7 \times 10^{-3}$) by the Auger results at more than 90% C.L.

To explore the constraining power of the Auger upper limits to EeV neutrinos, we performed an extensive scanning of the evolution function of the sources with redshift, $\Psi(z) \propto (1+z)^m$ up to z_{\max} (maximal redshift at which UHECRs are accelerated). For each pair of m and z_{\max} , the cosmogenic flux was calculated, and the expected number of neutrino events in Auger was obtained. Models predicting more than 2.39 neutrinos are disfavored at $> 90\%$ C.L. The resultant exclusion plot is shown in Fig. 2 (right) with the contours representing the 68% and 90% C.L. exclusion limits, respectively. The non-observation of neutrino candidates in the Observatory data allows us to exclude a significant region of the parameter space (m, z_{\max}) [4].

6. Sensitivity of the Observatory to point-like neutrino sources

As the Pierre Auger Observatory has a good angular resolution (typically better than 2.5°) [10], we can also obtain a limit to point-like sources of UHE ν . Each neutrino search channel, ES, DGH and DGL, corresponds to a given range of zenith angles, and the three combined cover between $\theta = 60^\circ$ and 95° . The neutrino identification efficiency is different in each channel, making the sensitivity of the Observatory dependent on the direction in the sky where the search is performed. The sensitivity in each direction can be quantified in terms of the effective area $\mathcal{A}_i(E_\nu)$, to neutrinos of flavor $i = \nu_e, \nu_\mu, \nu_\tau$ and energy E_ν , defined such that \mathcal{A}_i multiplied by the spectral flux of flavor i from a point source gives the energy spectrum of the instantaneous rate of detected events. The instantaneous effective area for the ES, DGH and DGL neutrinos as a function of neutrino energy is displayed in Fig. 3 (left). The Pierre Auger Observatory has optimal effective area in the EeV

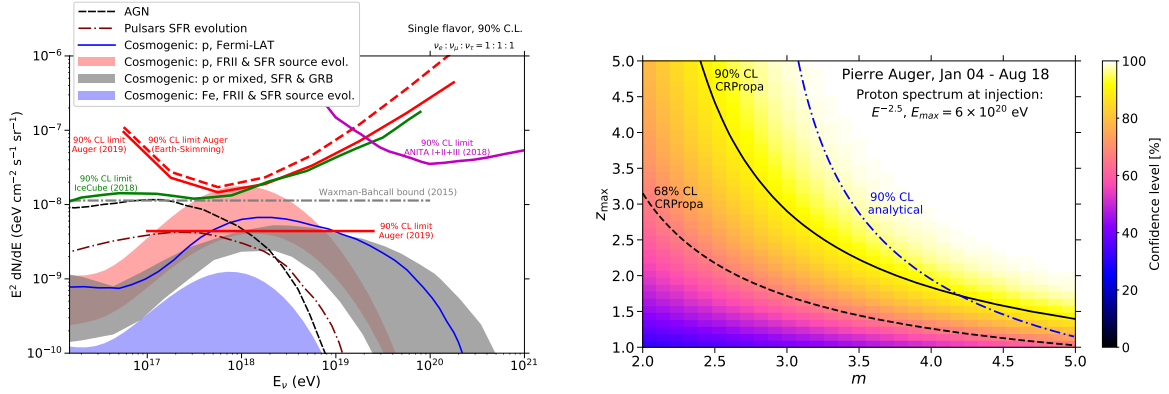


Figure 2: Left: Pierre Auger Observatory upper limit (90% C.L.) to the normalization k of the diffuse flux of UHE neutrinos $\phi_\nu = k E_\nu^{-2}$ as given in text (solid straight red line). Also plotted are the upper limits to the normalization of the diffuse flux (differential limits) when integrating the denominator of Eq. (4.2) in bins of width 0.5 in $\log_{10} E_\nu$ (solid red line - Auger all channels and flavors; dashed red line - Auger Earth-skimming ν_τ only). Similar limits from ANITA I+II+III [6] and IceCube [7] are displayed along with predictions for several neutrino models. All limits and fluxes are converted to a single flavor. Right: Constraints on UHECR source evolution models parameterized as $\psi(z) \propto (1+z)^m$ for sources distributed homogeneously up to a maximum redshift z_{\max} and emitting protons following a power-law $dN/dE \propto E^{-2.5}$ up to $E = 6 \cdot 10^{20}$ eV. A proton-only flux is matched to the Auger spectrum at $7 \cdot 10^{18}$ eV. The cosmogenic neutrino fluxes for each combination of m and z_{\max} were calculated with the MC propagation code CRPropa [8]. See [2] for further references and details on these plots.

energy range beyond the published effective area of IceCube and, for favorable source positions as seen from the SD, the effective area of the Pierre Auger Observatory is significantly larger.

As neutrinos at the Pierre Auger Observatory are searched for θ between 90° and 95° in the ES analysis, and between 60° and 90° in the DG analysis, at each instant, neutrinos can be effectively detected only from a specific region of the sky corresponding to this zenith angle range. A point-like source at a declination δ , right ascension α (equatorial coordinates) and a local sidereal time t , is seen from the latitude of the Observatory ($\lambda = -35.2^\circ$) with a time-dependent zenith angle $\theta(t)$ given by $\cos \theta(t) = \sin \lambda \sin \delta + \cos \lambda \cos \delta \sin(2\pi t/T - \alpha)$ where T is the duration of one sidereal day. At any given instant, the field of view (FoV) of the Observatory for neutrino searches is limited by the selection imposed on θ . In fact, the three channels ES, DGH and DGL correspond to different FoV. This is shown in Fig. 3 (right) where the corresponding FoV bands are plotted in equatorial coordinates as a function of $\alpha - t_{\text{GS}}$, where $t_{\text{GS}} = 2\pi t/T + \ell$ is the Greenwich Sidereal Time (GST) converted to angle and ℓ is the mean longitude of the Observatory. For any given α the instantaneous declination range for neutrino search at 00:00 GST ($t_{\text{GS}} = 0$) can be read from the plot at a value α of the abscissa. At any other t_{GS} the corresponding declination range is simply read from Fig. 3 at $\alpha - t_{\text{GS}}$.

The SD of the Pierre Auger Observatory is sensitive to point-like sources of neutrinos over a broad declination range between $\delta \sim -85^\circ$ and $\delta \sim 60^\circ$ (see Fig. 3). In particular ES showers can be efficiently identified between $\delta \sim -55^\circ$ and $\delta \sim 60^\circ$ (red band), for DGH showers between $\delta \sim -70^\circ$ and $\delta \sim 55^\circ$ (blue band), and for DGL between $\delta \sim -85^\circ$ and $\delta \sim 40^\circ$ (green band). In the case of a steady flux we can calculate the expected energy distribution of the detected events by multiplying the exposure $\mathcal{E}(\delta)$ to a point-like source of UHE neutrinos by the spectral flux. The exposure depends on neutrino energy E_ν and on the declination δ of the source and is obtained by integrating the effective area \mathcal{A} over a given time interval. For a given source position δ , the effective area \mathcal{A} is dependent on θ which changes with time.

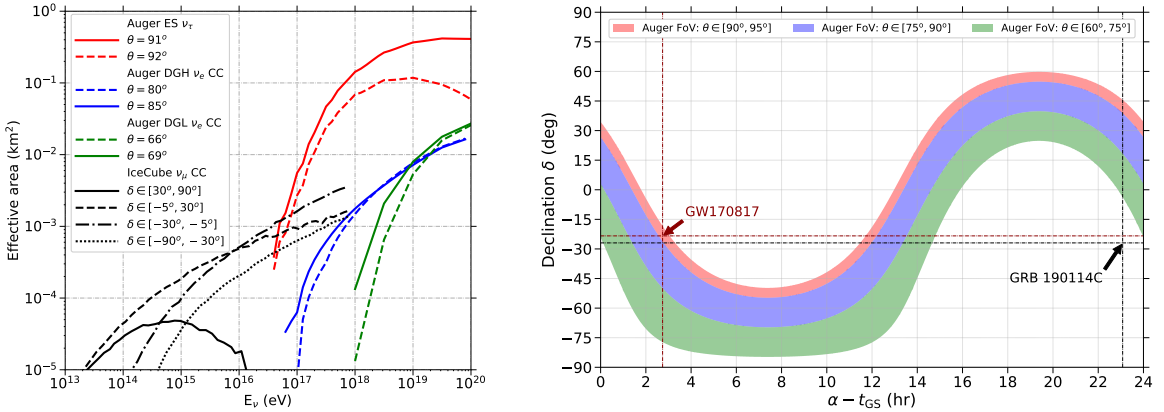


Figure 3: Left panel: Instantaneous effective areas for all the channels as a function of neutrino energy for selected zenith angles as labeled, compared to those of IceCube [11]. Right panel: Instantaneous FoV of the Pierre Auger Observatory for ES, DGH and DGL neutrinos as a function of the hour angle (see text). Two source examples are shown: GW170817 visible in Auger in the ES at the time of emission [12], and GRB 190114C [13] not visible in Auger in the inclined directions at the time of the burst.

The directional exposure obtained daily for the ES, DGH and DGL selections at fixed energies, averaged over the period between 1 May 2008 and 31 August 2018 (excluding the intervals over which the array was unstable) is shown in Fig. 4 (left) as a function of the source declination. Two sets of curves for each selection group have been combined in Fig. 4 for 10^{18} eV and $10^{19.5}$ eV to illustrate that the relative weight of the channels depends strongly on the energy. The position of the source relative to the Observatory during the search period plays a crucial role in the case of searches for short time intervals. When the source lies just below the horizon, at a zenith angle $\theta \sim 90^\circ - 93^\circ$, the effective area is maximal and the integrated exposure is competitive with dedicated ν experiments such as IceCube and ANTARES.

7. Limits for steady sources of UHE neutrinos

As stated in section 4, a blind search for UHE neutrinos in the data period analyzed has yielded no candidate neutrino events in the ES, DGH, and DGL analyses. Under the same conditions that we consider in section 4, a bound on $k_{\text{PS}}(\delta)$ can be obtained separately for the ES, DGH, and DGL channels. In each of the DG channels the contributions from different flavors having both NC and CC are combined in the equal flavor assumption. In the calculation of the limits, the dependence of the neutrino detection efficiency on the zenith angle and its change with time as the source transits in the Observatory field of view are taken into account.

The limits are shown in Fig. 4 (right) as a function of declination in comparison to those obtained by IceCube [11] and ANTARES [14]. It must be emphasized that the energy ranges where the three experiments are sensitive, are different and complementary. The limits reported by ANTARES and IceCube apply to energies below the energy range of the search of neutrinos with Auger.

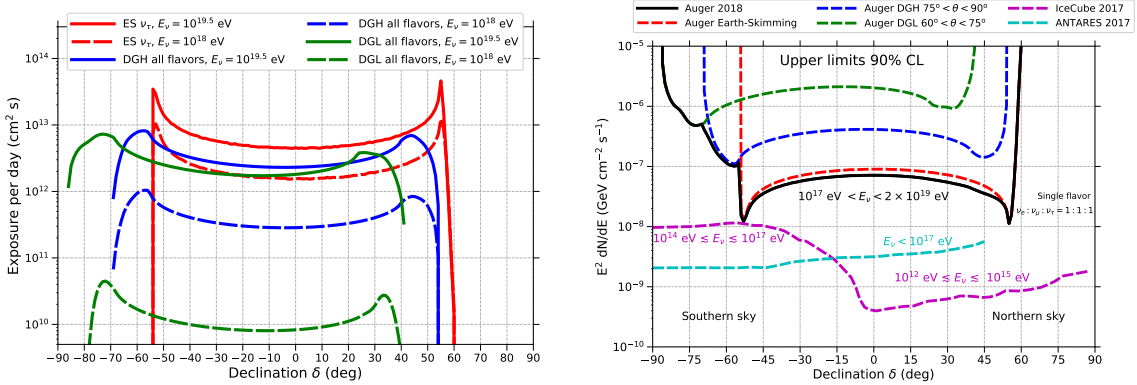


Figure 4: Left panel: Average exposure per day at $E_\nu = 10^{18}$ eV and 3×10^{19} eV as a function of declination δ for the ES, DGH and DGL channels. Right panel: Pierre Auger Observatory upper limits (1 Jan 2004 - 31 Aug 2018) at 90% C.L. on the normalization k^{PS} of a single flavor point-like flux of UHE neutrinos $dN/dE_\nu = k^{\text{PS}} E_\nu^{-2}$ as a function of the source declination δ . The limits for IceCube (2008 - 2015) [11] and ANTARES (2007 - 2015) [14] are also shown. Note the different energy ranges for each observatory.

8. Discussion and conclusions

With the Pierre Auger Observatory we can detect UHE neutrinos from a large fraction of the sky, from very close to the South Celestial Pole to declination values up to $\delta \sim 60^\circ$. For a steady source in this range there is always a time window during a sidereal day in which the source would be in the field-of-view of the ES, DGH or DGL channels.

No neutrino candidates have been identified in Auger data until 31 Aug 2018. The upper limits to the diffuse flux of UHE ν obtained with the Pierre Auger Observatory are competitive at energies around 10^{18} eV. The SD of the Pierre Auger Observatory has an unmatched sensitivity to potential sources of EeV neutrinos in the Northern terrestrial hemisphere. This region in the sky cannot be searched for in the EeV energy range by experiments such as IceCube because of the opacity of the Earth to neutrinos in those directions when seen from the South Pole.

The sensitivity of the SD of the Pierre Auger Observatory to transient sources of UHE neutrinos is crucially dependent on the efficiency of the detection during the time interval of the transient. Thus, depending on the inclination of the event in the local coordinate system of the Observatory, the sensitivity can exceed by far that of other dedicated neutrino detectors. For instance, at about 10^{18} eV, the Pierre Auger Observatory's effective area is maximal for sources slightly below the horizon, and therefore its sensitivity to transients from these directions is larger than that of IceCube by more than an order of magnitude. This is particularly interesting because the location of the GW170817 event, the first known binary neutron star merger, was slightly below the horizon at the time around the merger as reported in [12] and seen in Fig. 3.

The Pierre Auger Observatory is placed in an excellent position to contribute to the recently started era of multi-messenger astronomy, which is likely to bring new exciting discoveries in the near future, by looking for neutrinos in the EeV range in correlation with the detection of gamma rays or gravitational waves.

References

- [1] A. Aab *et al.* (Pierre Auger Collab.), Phys. Rev. D **91**, 092008 (2015).
- [2] A. Aab *et al.* (Pierre Auger Collab.), submitted to JCAP (2019) arXiv:1906.07422.
- [3] A. Aab *et al.* (Pierre Auger Collab.), submitted to JCAP (2019) arXiv:1906.07419.
- [4] E. Zas for the Pierre Auger Collab., PoS(ICRC2017) 972.
- [5] K.-H. Kampert, and M. Unger, Astropart. Phys. **35**, 660 (2012).
- [6] P. W. Gorham *et al.* (ANITA Collab.), Phys. Rev. D **98**, 022001 (2018).
- [7] M. G. Aartsen *et al.* (IceCube Collab.), Phys. Rev. D **98**, 062003 (2018).
- [8] R. Alves Batista *et al.*, JCAP **05**, 038 (2016).
- [9] A. Ishihara and S. Yoshida, Phys. Rev. D **85**, 063002 (2012).
- [10] A. Aab *et al.* (Pierre Auger Collab.), JCAP **08**, 019 (2014).
- [11] M. G. Aartsen *et al.* (IceCube Collab.), Astrophys. J. **835**, 151 (2017).
- [12] A. Albert *et al.* (ANTARES, IceCube, Pierre Auger & LIGO/Virgo Collabs.), Astrophys. J. Lett. **850**, L35 (2017).
- [13] <http://tevcat.uchicago.edu/?mode=1;id=324>
- [14] A. Albert *et al.* (ANTARES Collab.), Phys. Rev. D **96**, 082001 (2017).



Limits on ultra-high energy photons with the Pierre Auger Observatory

Julian Rautenberg^{*,a} for the Pierre Auger Collaboration^{†b}

^a*Bergische Universität Wuppertal, Wuppertal, Germany*

^b*Observatorio Pierre Auger, Av. San Martín Norte 304, 5613 Malargüe, Argentina*

E-mail: auger_spokespersons@fnal.gov

Full author list: http://www.auger.org/archive/authors_icrc_2019.html

The Pierre Auger Observatory is the most sensitive air-shower detector for primary photons with energies above ~ 0.2 EeV. Using the Surface Detector array (SD), photons in the zenith angle range from 30° to 60° can be identified through the broad time-structure of the signals expected to be induced in the SD stations. An additional signature for photon-induced air showers is the steeper lateral distribution of secondary particles at the ground with respect to nucleonic showers. Stringent limits are set to the diffuse flux of ultra-high energy (UHE) photons above 10 EeV, using SD data collected between 2004 and mid-2018 with an exposure of $40000 \text{ km}^2 \text{ sr yr}$. Below 1 EeV, unprecedented separation power between primary photons and hadrons can be achieved by combining observables from the low-energy enhancements of the Pierre Auger Observatory, namely three upwards-pointing fluorescence telescopes, which can directly measure the atmospheric depth of the shower maximum, and the 750 m SD array, which again accesses the steeper lateral distribution of photon-induced air showers. For the first time, limits on the integral photon flux below 1 EeV are presented using data collected by the Pierre Auger Observatory between mid-2010 and 2015. This extends the range of photon searches at the Pierre Auger Observatory to about three decades in energy.

36th International Cosmic Ray Conference — ICRC2019

24 July – 1 August, 2019

Madison, Wisconsin, USA

*Speaker.

†for collaboration list see PoS(ICRC2019)1177

1. Introduction

The search for ultra-high energy (UHE) photons is a key to reveal the origin of the highest energetic cosmic rays. Nuclei interacting with the extra-galactic background light, dominantly the cosmic microwave background (CMB), are expected to produce a flux of UHE photons that can propagate over several Mpc. The expected cosmogenic flux depends on the composition and energy distribution of the source emission, as well as the distribution and cosmological evolution of the sources themselves.

The Pierre Auger Observatory [1] is a hybrid detector, consisting of a Surface Detector (SD) with 1600 stations distributed over 3000 km^2 in a triangular grid with a spacing of 1.5 km, as well as a Fluorescence Detector (FD) of 27 telescopes overlooking the area from four sites from the boarder of the array. To extend the exposure to smaller energies below 10^{18} eV, an area of 23.5 km^2 is equipped with 60 additional SD stations to achieve half spacing of 750 m and three of the FD telescopes (HEAT) have a field of view inclined by 30° with respect to the standard FD telescopes above the 750 m array.

2. Photon searches at the Pierre Auger Observatory

SD observables that have the potential to separate the photon showers from the hadronic ones are based on the difference in the signals in the particle detectors due to the later shower development, measured in the depth of the shower-maximum, X_{max} . For a photon, the electromagnetic shower on average has a steeper lateral fall-off and a slower rise of the signal in the SD stations on ground than hadronic showers.

Besides the use of the SD for the shower measurements on the ground, the Pierre Auger Observatory can exploit the hybrid setup and directly measure the longitudinal profile of the showers with the FD. X_{max} gives a direct and powerful estimator for the composition, thus discriminating photons from hadrons as primary cosmic ray particles. The hybrid measurements are limited by the about 15% uptime of the FD, though. Searches for photons and the derived upper limits on the flux of photons as well as on the photon fractions of the measured cosmic ray flux have been already published, using the SD data [2, 3] as well as hybrid ones [4, 5, 6]. In addition, the hybrid search has been extended to search for point-like sources [7] and stacking of a source catalogue [8].

This contribution presents in the next section an extension of the previous analysis based on the SD observables to the current data-set. Then the extension of the hybrid photon search towards lower energies is described.

3. Diffuse photon flux at the highest energies

The measurement for energies above 10 EeV follows the one presented in [3]. The range in zenith angle used is $30^\circ < \theta < 60^\circ$. The data-period has been extended, and covers the period from 1 Jan 2004 to 30 Jun 2018. The corresponding exposure for that zenith angle range has been determined to $40000\text{ km}^2\text{ sryr}$. To estimate the efficiency and the optimal separation, a photon signal Monte Carlo (MC) sample has been simulated using CORSIKA [9] with EPOS-LHC [10] as hadronic interaction model. The conversion of UHE photons in the geomagnetic field is simulated

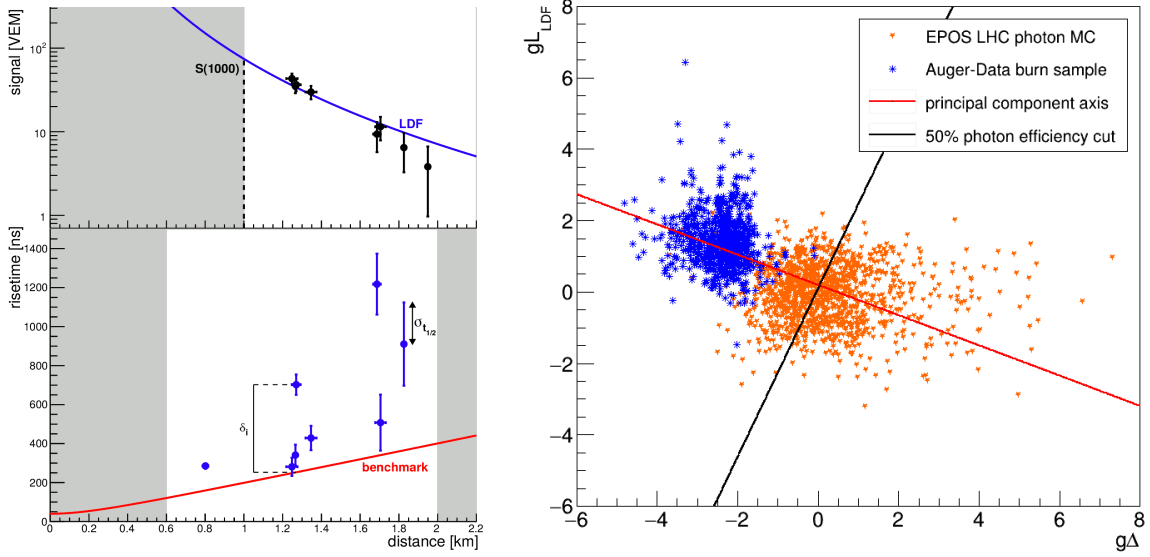


Figure 1: Left: Signal (top) and risetime of the SD stations (bottom) vs. distance to the shower axis for a simulated photon event, together with the LDF (top) and risetime-benchmark (bottom) parametrization. Right: Principal Component Analysis of the data (blue) and the MC prediction for photons (orange) for the normalized observables $g\Delta$ and gL_{LDF} described in the text.

using PRESHOWER [11]. The Landau-Pomeranchuk-Migdal (LPM) effect is also implemented in the simulation. The photon MC has been reweighted to an energy distribution according to a E^{-2} spectrum. For this analysis aiming at identifying photons in the UHECR-flux we do not use any simulation of nucleonic primary cosmic rays (background MC sample) to avoid the large uncertainties in the tail of the distributions due to the use of hadronic interaction models. Where needed, 2% of the data are used as background sample, which are excluded from the measurement (burned). With respect to [3] the hadronic interaction model has changed, which has only a minor effect on the photon simulations. The simulation and reconstruction show minor improvement, i.e. for the data reconstruction in terms of the automatic and therefore less biased detection of the rare peculiarities in photomultipliers of the SD stations. These usually have no significant effect on the integral, and therefore signal estimation, but on the shape which is used for the composition estimation. The reconstruction of the energy is done using the observable S_{1000} , the signal at 1000 m from the shower axis estimated using a fit of a lateral distribution function parametrized to describe the Auger data. The conversion of S_{1000} to the energy corresponding to a photon shower is done in an iterative procedure [12]. To avoid biases only showers which are almost fully developed are selected by requiring the X_{max} to be no more than 50 g/cm^2 below ground.

The selection of the photon candidates has been performed using two estimators. The first one uses the steeper lateral distribution function (LDF) of electromagnetic showers. For this, the ratio of the measured signal, S_i , and the expected signal according to the LDF fit at the distance r_i of that SD station i to the shower axis, $S_{\text{LDF}}(r_i)$, is determined. The observable is the logarithm of the average of these ratios:

$$L_{\text{LDF}} = \log_{10} \left(\frac{1}{N} \sum_{i=1}^N \frac{S_i}{S_{\text{LDF}}(r_i)} \right),$$

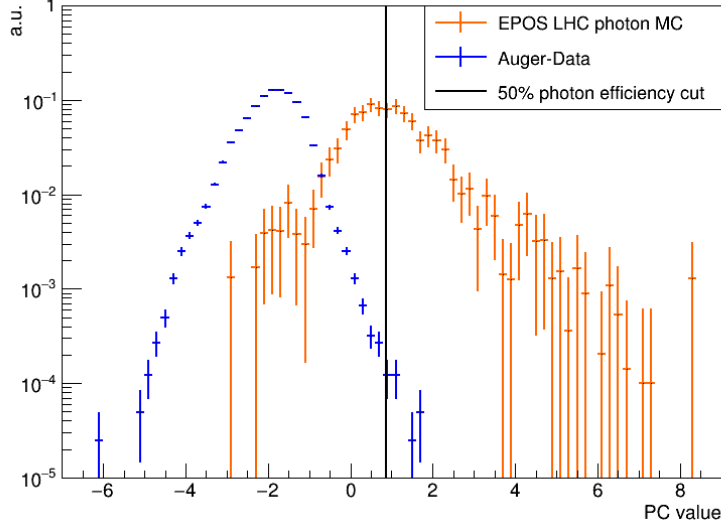


Figure 2: Distribution of the data (blue) and the MC prediction for photons (orange) along the principal component axis. For better comparison, the two distributions are normalized to an integral of one. The line indicates the signal selection at the median of the photon MC sample. 11 data events are above the threshold.

using only SD stations with $r_i > 1000\text{m}$. Photon candidates are expected to have smaller signals at larger distances to the shower axis, resulting in a negative L_{LDF} . The second observable is based on the electromagnetic signal in the stations, which is on average delayed compared to the fast-rising signal of the muons. We therefore calculate the *risetime*, $t_{1/2}$, as the time between the 0.1 and the 0.5 quantile of the time trace. It should be noted, that the difference in the muonic and electromagnetic signal decreases with smaller distance of the observer to the X_{max} for pure geometrical reasons, additionally increasing the $t_{1/2}$ for the larger X_{max} of photon showers. The measured $t_{1/2}$ shows a clear asymmetry in the azimuth angle with respect to the shower direction. This asymmetry, depending also on distance to the shower axis as well as the zenith angle, can be parametrized and thus corrected for, resulting in the corrected SD station risetime, $t_{1/2}^i$. To select photon candidates, an observable is constructed from the average $t_{1/2}^i$ and its uncertainty from the data, the so called *benchmark*, $t_{1/2}^{\text{bench}}$. To obtain an event-wise observable, Δ , the residuals of $t_{1/2}^i$ of the SD stations from the benchmark are averaged similarly as described in [13],

$$\Delta = \frac{1}{N} \sum_{i=1}^N \frac{t_{1/2}^i - t_{1/2}^{\text{bench}}}{\sigma_{t_{1/2}^i}}$$

Here, only SD stations with an observed signal of minimally 6 VEM¹ and a distance to the shower axis $600\text{m} < r_i < 2000\text{m}$ are considered. The deviation from the average LDF leading to L_{LDF} and the deviation of the risetime from the benchmark leading to Δ are illustrated for a simulated photon event in Fig. 1 left.

To obtain an optimal discrimination, the two observables are transformed using a Principal Component Analysis (PCA). For this, the observables are normalized for the photon MC sample so

¹the signal as calibrated to a vertical equivalent muon

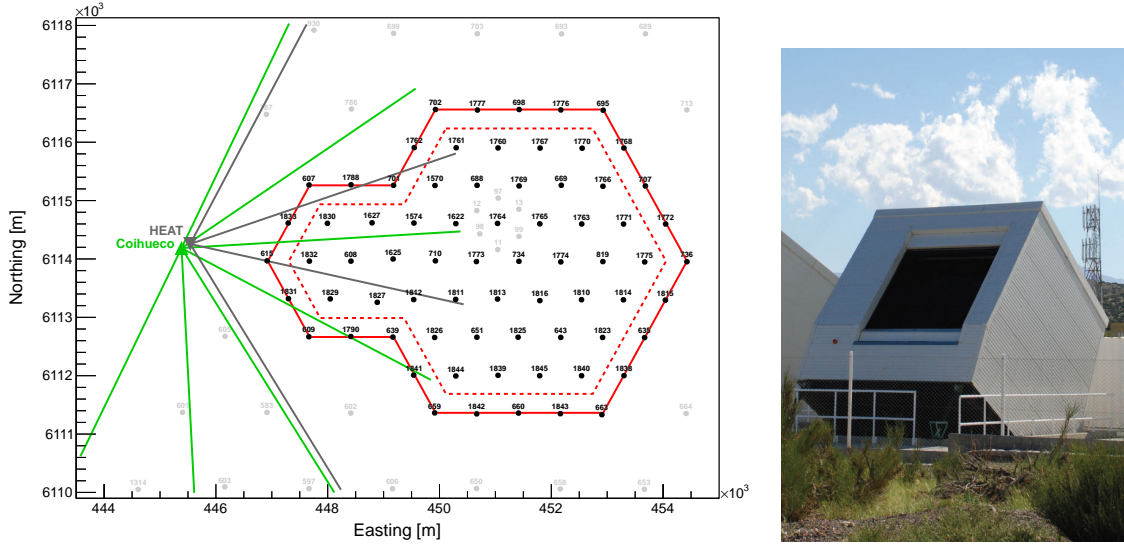


Figure 3: Left: layout of the dense 750m array in the field of view of the FD builds Coihueco and HEAT. Right: Picture of one HEAT telescope with the field of view inclined by 30°

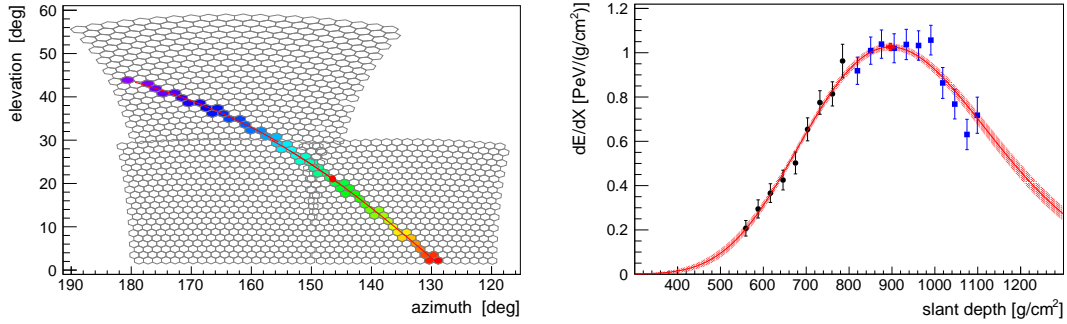


Figure 4: Example of a simulated photon with the energy of 0.5 EeV . Left: the camera view with the color encoding the timing from early (blue) to late (red). Right: the longitudinal profile measured by HEAT (black circles) and Coihueco (blue squares) with the Gaisser-Hillas fit (red line). The red cross indicates the X_{max} position.

that the mean is equal to zero and the standard deviation equal to one, resulting in gL_{LDF} and $g\Delta$. The PCA is performed on the burn sample of 2% of the Auger data and a part of the MC of about equal statistics. The PCA axis is shown in Fig. 1 right.

The selection cut for the signal has been fixed in [2] to an efficiency on the non-preshowering photon signal of 50%. We keep this cut-value for consistency here, noting that at energies closely above 10 EeV the background rejection is not guaranteed to be 100%. Applying the analysis to the search data-set resulted in the distribution of the data and the photon MC in the PCA variable as shown in Fig. 2. In the tail of the data-distribution, 11 events are above the threshold, two of them at an energy above 20 EeV . The number of candidates evolved with respect to [3] due to the increase of exposure and slight changes in the reconstructed shower parameters. Further analysis using proton simulations for the geometry and energy of the candidates are not excluding the background hypothesis of the candidates. Here the large uncertainties of the hadronic interactions in the tail of

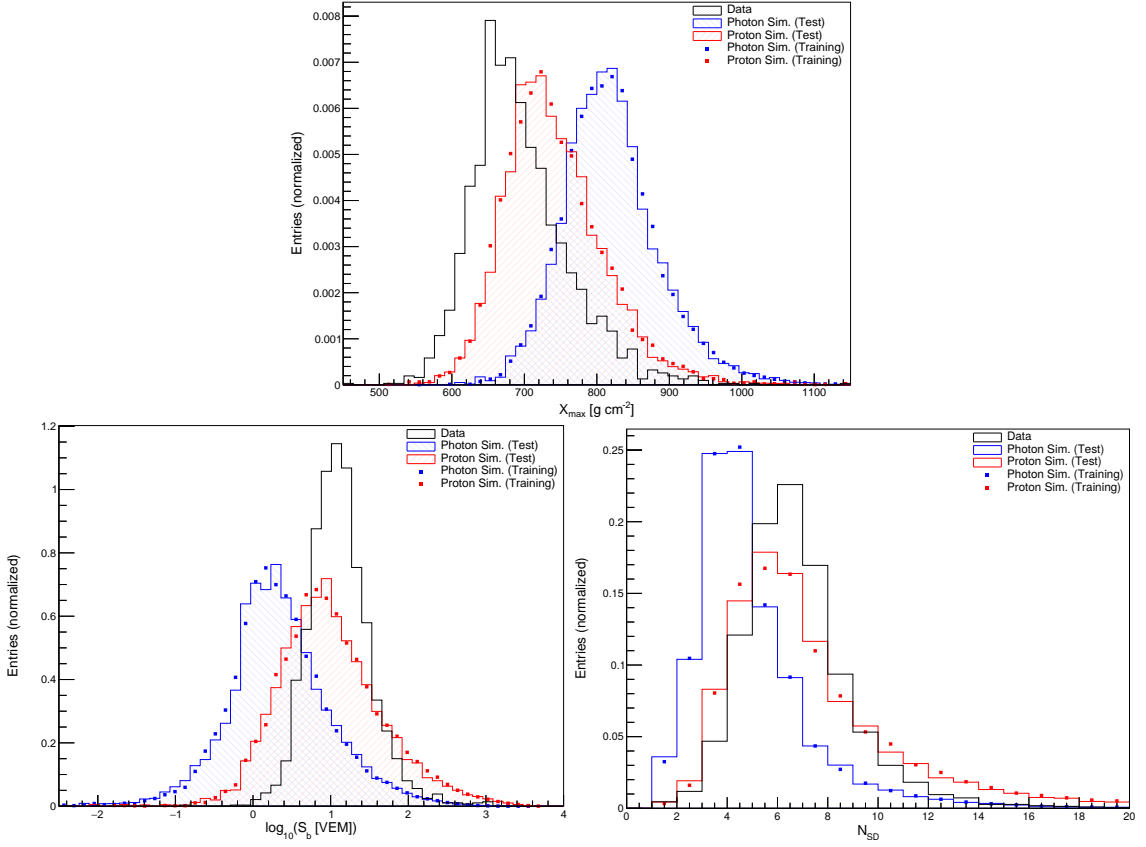


Figure 5: Observables used as input for the BDT as described in the text are shown for the photon signal MC (blue), the proton background MC (red), and the data-set (black): X_{\max} measured by FD (top), S_b (bottom left) as well as N_{SD} (bottom right) as measured by SD.

the distributions limit the significance of such a test. As we can neither exclude the hypothesis of the candidates to be hadronic, nor can we prove the candidates to be photons, we conservatively determine the upper limit on the photon flux at 95% confidence level, as shown in Fig. 7. Therefore, though improving the exposure by almost a factor of two, the limit for the lower energy of 10EeV is background limited and even slightly worse than in [3]. For energies above 20EeV the limits are significantly improved due to the large increase in exposure while not obtaining any new candidate.

4. Diffuse photon flux at lower energies

At energies below 10EeV the number of SD stations with signal is too small to have a significant separation of photon-induced and nucleus-induced showers. But the increased event statistics allows to use the direct X_{\max} measurement for the 15% uptime of the FD. We follow the measurement in [6] combining the X_{\max} with the SD observables S_b [20],

$$S_b = \sum_i^{N_{SD}} S_i(r_i) \left(\frac{r_i}{1000\text{m}} \right)^b,$$

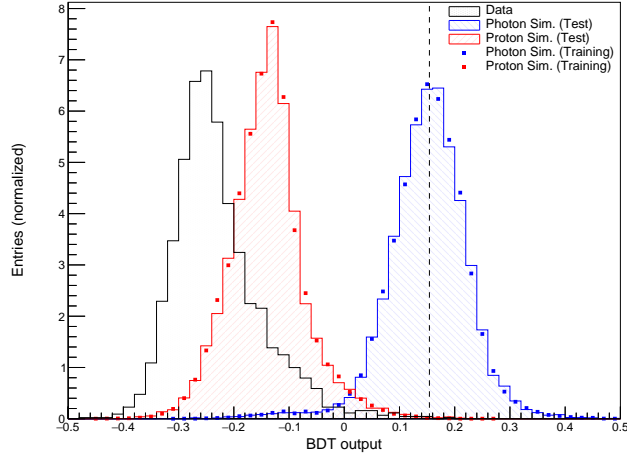


Figure 6: Output variable of the BDT trained on simulations together with the distributions for the photon signal MC (blue), the proton background MC (red), and the data-set (black).

with $b = 4$ and the number of SD stations, N_{SD} . Here, the measurement is extended towards energies below 1 EeV by using data of the sub-array at smaller spacing of 750m as shown in Fig. 3 and the measurement of X_{max} with the FD extension HEAT. The event selection is done according to [21]. MC simulations for photons and protons have been generated similar to Sec. 3. Using these as signal and background, a Boosted Decision Tree (BDT) has been trained. To take the energy and zenith angle dependence of the three discriminating observables into account they are used as additional inputs to the BDT. An example for a simulated photon event can be seen in Fig. 4. Before applying the BDT on the data it has been tested on a 5% burn-sample subsequently excluded from the measurement. The data period used in this analysis is 1 Jun 2010 to 31 Dec 2015. The distributions of the input variables for the different MC samples and the data-sample are shown in Fig. 5. The separation power of the input variables is in this projection reduced due to their energy dependence. The resulting distribution of the BDT output variable is plotted in Fig. 6. Again, the selection cut on the BDT output variable is a-priori set to the median of the photon distribution, leading to a selection efficiency of 50%. After application of the photon selection cut to the data sample only one candidate event is selected. This number is compatible with the background expectation from the proton MC. Evaluating the hybrid exposure for the given time-period, we determine the upper limits on the integral photon flux for the thresholds of 0.2, 0.3, 0.5 and 1 EeV at 95% confidence level. These flux limits are displayed together with the flux limits at the highest energy described in Sec. 3 in Fig. 7. They are compared to other measurements, partially derived at 90% confidence level.

5. Conclusion

With the increase in exposure at the highest energies and the extension towards lower energies using the enhancements of the Pierre Auger Observatory, the 750m SD array and the FD HEAT, most stringent limits on the photon flux can be achieved. In combination with [6], the measurements presented here form the most sensitive UHECR photon search over about three orders of magnitude starting at 0.2 EeV.

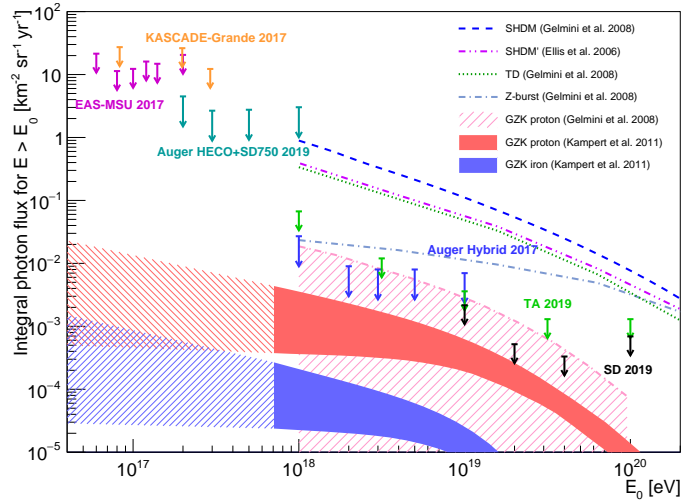


Figure 7: Photon flux limits at 95% C.L. for the different analysis of the Pierre Auger Observatory, compared to model predictions [14, 15, 16] and other experimental limits at 95% C.L. [17], as well as at 90% C.L. [18, 19].

References

- [1] A. Aab [Pierre Auger Collaboration], *Nucl. Instrum. Meth. A* **798** (2015) 172.
- [2] The Pierre Auger Collaboration, *Astropart. Phys.* **29** (2008) 243 [arXiv:0712.1147].
- [3] C. Bleve for the Pierre Auger Collaboration, PoS(ICRC2015)1103, 2015.
- [4] The Pierre Auger Collaboration, *Astropart. Phys.* **27** (2007) 155 [arXiv:astro-ph/0606619].
- [5] The Pierre Auger Collaboration, *Astropart. Phys.* **31** (2009) 399 [arXiv:0903.1127].
- [6] The Pierre Auger Collaboration, *JCAP* **04** (2017) 009 [arXiv:1612.01517].
- [7] The Pierre Auger Collaboration, *ApJ* **789** (2014) 160 [arXiv:1406.2912].
- [8] The Pierre Auger Collaboration, *ApJL* **837** (2017) L25 [arXiv:1612.04155].
- [9] D. Heck *et al.*, Report FZKA **6019** (1998).
- [10] T. Pierog *et al.*, *Phys. Rev. C* **92** (2017) 034906 [arXiv:1306.0121].
- [11] P. Homola *et al.*, *Comput. Phys. Comm.* **173** (2005) 71 [arXiv:astro-ph/0311442].
- [12] P. Billoir *et al.* arXiv:astro-ph/0701583.
- [13] The Pierre Auger Collaboration, *Phys. Rev. D* **96** (2017) 122003 [arXiv:1710.07249].
- [14] G. Gelmini, O. Kalashev, D. Semikoz, *JETP* **106** (2008) 1061 [arXiv:astro-ph/0506128].
- [15] J. Ellis, V. E. Mayes, D. V. Nanopoulos, *Phys. Rev. D* **74** (2006) 115003 [arXiv:astro-ph/0512303].
- [16] K.-H. Kampert *et al.*, Proceedings ICRC **2** (2011) 198.
- [17] Telescope Array Collaboration, *Astropart. Phys.* **110** (2019) 8 [arXiv:[arXiv:1811.03920].
- [18] KASCADE-Grande Collaboration, *ApJ* **848** (2017) 1.
- [19] Yu. Fomin *et al.*, *Phys. Rev. D* **95** (2017) 123011.
- [20] G. Ros *et al.*, *Astropart. Phys.* **35** (2011) 140 [arXiv:1104.3399].
- [21] J. Bellido for the Pierre Auger Collaboration, PoS(ICRC2017)506, 2017.

4

Hadronic Interactions and Shower Physics





The muon component of extensive air showers above $10^{17.5}$ eV measured with the Pierre Auger Observatory

Federico Sánchez^{*a} for the Pierre Auger Collaboration^{b†}

^a*Instituto de Tecnologías en Detección y Astropartículas, CNEA-CONICET-UNSAM, Buenos Aires, Argentina*

^b*Observatorio Pierre Auger, Av. San Martín Norte 304, 5613 Malargüe, Argentina*

E-mail: auger_spokespersons@fnal.gov

Full author list: http://www.auger.org/archive/authors_icrc_2019.html

The muon densities at 450 m from the core for showers above $10^{17.5}$ eV and zenith angle between 0° and 45° are presented. Results are based on 1 year of calibrated data collected by the engineering array of the Auger Muons and Infill for Ground Array (AMIGA) detector. Taking into account systematic uncertainties as well as attenuation effects, the observations suggest that the current hadronic interaction models fail in reproducing the measured number of muons with energies >1 GeV. Simulations at $10^{17.5}$ eV and $10^{18.0}$ eV show that for EPOS-LHC an increase of 38% is required at both energies, while for QGSJetII-04 an increment of 50% and 53% is needed at respective energies. Data have been combined with previous results on muon densities at higher energies showing the match in the evolution of the composition derived with the measurements of depth of the maximum development of the showers in the atmosphere (X_{\max}). The current AMIGA observations show that the variation of the primary masses has no sudden changes in the energy range $10^{17.5}$ to $10^{18.0}$ eV.

*36th International Cosmic Ray Conference — ICRC2019
July 24th – August 1st, 2019
Madison, Wisconsin, USA*

^{*}Speaker.

[†]for collaboration list see PoS(ICRC2019)1177

1. The AMIGA engineering array

The surface detector (SD) of the Pierre Auger Observatory [1] consists of an array of water-Cherenkov detector (WCD) placed in a triangular grid with spacing of 1500 m covering an area of 3000 km² (SD-1500), a smaller embedded array of 23.5 km² with 750 m spacing (SD-750), and finally an even denser array with 433 m spacing (SD-433) over 1.9 km². The fluorescence detector (FD) consists of 27 air-fluorescence telescopes overlooking the SD area from four sites. The contribution of Auger Muons and Infill for the Ground Array (AMIGA), alongside with the SD-750 and SD-433 arrays, is to provide a dedicated device to directly measure the muonic component of extensive air showers, the underground muon detector (UMD). Before proceeding to the construction of the full-size UMD, an array of prototypes operated until November 2017 to validate and optimize the detector design, and to evaluate its performances. This array, deployed at a depth of 2.3 m (~ 540 g/cm²) to shield the electromagnetic component, was made with seven stations consisting in 30 m² of plastic scintillator. A detailed description of the present status of the underground muon detector array may be found in [2]. Once completed in the full SD-750 area, the UMD will serve as part of AugerPrime, the upgrade of the Observatory currently being deployed with the aim of improving the mass composition determination [3]. In this work, the first results based on the direct measurement of the muon densities of EAS in an energy region between 3×10^{17} eV and 2×10^{18} eV are presented. The analyzed data were collected during one year by the engineering array of AMIGA. In total, 1742 events with zenith angle up to 45° were analyzed. The full-sized UMD array will include 61 stations in the whole SD-750 area and is foreseen to be completed between the end of 2019 and mid 2020.

2. Detector efficiency and resolution

To determine the detector efficiency and to assess the resolution of the procedure for counting particles, one position of the array was equipped with identical *twin* underground scintillators triggered by the same water-Cherenkov detector. One unit was deployed towards the South of the surface detector, the other towards the North. For the resolution studies, we exploit the fact that two identical close-by detectors basically measure the same spot of the shower. Therefore, by analyzing the difference of their signals for a given event, it is possible to estimate signal fluctuations. As the separation between the twin detectors is ~ 20 m, only signals at least 200 m away from the shower core are considered to be sampling the same muon density.

On the other hand, for efficiency analysis the different areas of the devices constituting the twin detector are used. In fact, the units of 30 m² are segmented into 2×10 m² and 2×5 m². The expected ratio of counts of two detectors of different areas is $r = \epsilon_1/\epsilon_2 \cdot a_1/a_2$ where ϵ_i is the efficiency of the detector with area a_i . An ideal counter of area a will record twice as many particles as a counter with an area $a/2$, and the ratio of counts between detectors will be $r = 2$. In the real case, a deviation from this behavior might arise, in particular if there are detection inefficiencies associated with the dimensions of the detectors. The joint probability to measure n_i and m_i particles for a single event i over two independent Poissonian detectors can be explicitly written in terms of the ratio of the expectation numbers $r = \mu_i/\nu_i$. The estimator for the ratio \hat{r} is found by maximizing the corresponding likelihood function for N events leading to an estimator of the relative efficiency

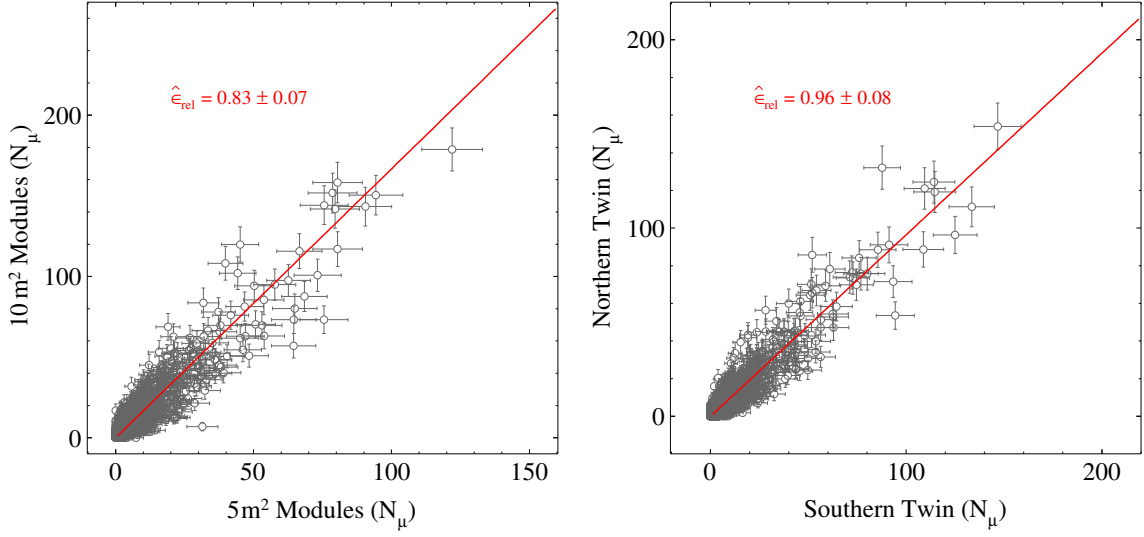


Figure 1: Relative efficiency between detectors of different (left) and identical (right) areas. The estimation $\hat{\epsilon}_{\text{rel}}$ is obtained by fitting the data (red solid line).

between units of different area that can be written as $\hat{\epsilon}_{\text{rel}} = a_2/a_1 \cdot \bar{n}/\bar{m}$. The fraction \bar{n}/\bar{m} is the ratio of the sample averages measured by the detectors with areas a_1 and a_2 .

The twin position has eight modules, four of each area. By comparing the measurements on the four modules of 10 m^2 with those of the four with 5 m^2 area composing the *twin*, the relative efficiency between detectors can be assessed. The result of this comparison is shown in Fig. 1-(left). The relative signal efficiency estimation yields $\hat{\epsilon}_{\text{rel}} = 0.83 \pm 0.07$. Within uncertainties, the obtained $\hat{\epsilon}_{\text{rel}}$ is compatible with laboratory measurements [5]. This result is mainly driven by the attenuation of light along the fibers in the modules with larger area. Nevertheless, as soon as equal areas are compared, the twin devices behave as identical detectors. As an example, the case for 30 m^2 is shown in Fig. 1-(right). This latter result is of major importance since it implies that the data from the twin detectors can be used to determine the resolution of the counting procedure.

Exploiting the same method used in the past to obtain the accuracy in the signal measurements of the SD stations [4], the sample variance σ^2 and mean N_μ estimators are calculated from the number N_i of muons measured by each twin on an event-by-event basis. Subsequently, the estimator

$$\Delta^2 \equiv \left(\frac{\sigma}{N_\mu} \right)^2 = 2 \left(\frac{N_1 - N_2}{N_1 + N_2} \right)^2 \quad (2.1)$$

is evaluated for each event. The mean value of Δ^2 within bins of average number of muons is shown in Fig. 2-(left) as a function of the muon count. For an ideal counter, the resolution should be $\Delta_{\text{Poisson}}^2 = 1/N_\mu$. The blue line is the fit of a Poissonian model to the data. The counting uncertainty as a function of the number of counted muons results in

$$\Delta^2(N_\mu) = \frac{1.7 \pm 0.9}{N_\mu^{(1.0 \pm 0.2)}}. \quad (2.2)$$

As an illustration of the behavior of the UMD counters, the bin contents centered at 5 muons in Fig. 2-(right) are separately displayed and fitted with a Poissonian distribution. It is important to

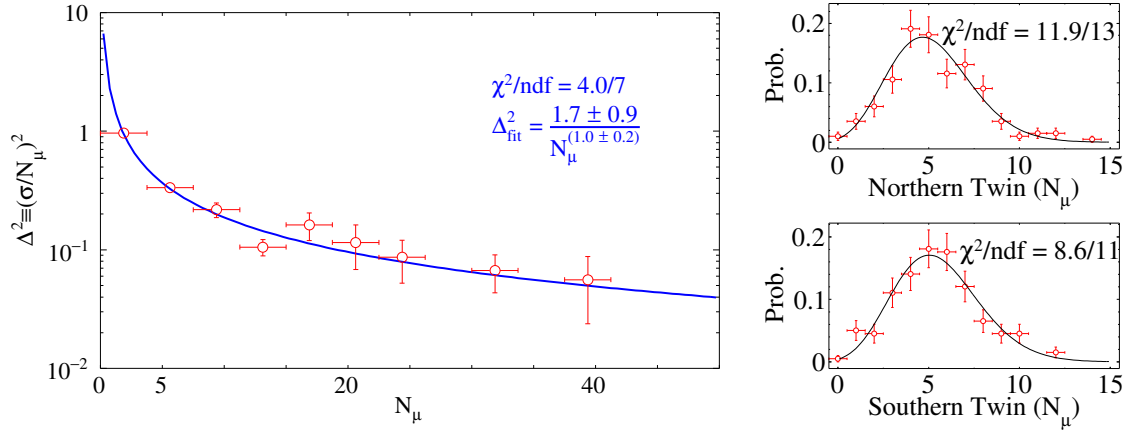


Figure 2: Resolution of the UMD. *Left*: Δ^2 as function of of average measured muons. The blue line is the fit of a Poissonian model. *Right*: From the bin $N_\mu = 5$, the distribution in each twin is shown alongside with its Poisson fit.

Source of Uncertainty	Relative Systematic
Calibration	3.9%
Soil density	2.8%
MLDF	8.8%
Efficiency correction	9.9%
CIC correction	2.3%
Total	14.3%

Table 1: Summary of analyzed systematic uncertainties (see text).

note that an ideal behavior of the counters is assumed for the construction of the likelihood model implemented in the muon lateral distribution function. Such an assumption is clearly supported by the data.

3. Systematic uncertainties

Five sources of systematic uncertainties have been studied in the present work [5]. These are: (i) the calibration procedure, (ii) the density variations of the soil covering the area of the detector, (iii) the unknown shape of the muon lateral distribution function, (iv) the area-dependent efficiency correction, and finally (v) the *Constant Intensity Cut* (CIC) correction to take into account the attenuation of muons in inclined showers. The impact of each source of uncertainty over the reconstructed muon density at the optimal distance of 450 m, ρ_{450} , is summarized in Tab. 1.

In the engineering UMD array, the counting of particles relied only on the signal amplitude, not on its charge. During this testing and developing phase, the selected optical sensors were multi-anode photo-multiplier tubes (sMPMTs). The aim of the calibration was, therefore, to set the threshold of discrimination (V_{thr}) of each MPMT channel at the level of 30% of the single photo-

electron amplitude (V_{SPE}). In total, 2240 channels were calibrated individually and the spread of thresholds after calibration routine was $\sigma = 21$ mV. Therefore, the detector response has been simulated for different values of V_{thr} ranging from 20% to 40% of V_{SPE} to estimate the effect of a 3σ variation. A relative uncertainty of $\sigma/\rho_{450} = 3.9\%$ is obtained from the linear fit.

The shielding of the electromagnetic component of EAS, as well as the energy of the muons that can reach the underground detectors, depends on the density of the soil. In-situ measurements of the density in three positions (two in the periphery and one in the center) of the SD-750 array were performed at depths of 1 m, 2 m, and 3 m. The mean measured soil density was 2.380 g/cm^3 with a dispersion of $\sigma = 0.051 \text{ g/cm}^3$ between surveyed sites. Averaged over all considered angles, a relative systematic of $\sigma/\rho_{450} = 2.8\%$ is found.

When an extensive air shower falls within the detector array, each triggered station samples the density of muons ρ_{μ} at discrete distances from the shower core. The reconstruction procedure implies a fit with a pre-selected muon lateral distribution function (MLDF). For the underground muon detector, the chosen parametrization followed the KASCADE-Grande experiment [6],

$$\rho_{\mu}(r, E, \theta; \mathbf{p}) = \frac{A_{\mu}(E)}{A_0} \left(\frac{r}{r^*}\right)^{-\alpha} \left(1 + \frac{r}{r^*}\right)^{-\beta(\theta; \mathbf{q})} \left(1 + \left(\frac{r}{10r^*}\right)^2\right)^{-\gamma} \quad (3.1)$$

where $\mathbf{p} = \{r^*, \alpha, \gamma, \mathbf{q}\}$ are fixed parameters which were optimized with simulations and A_0 is a normalization factor. Only $A_{\mu}(E)$ is a free parameter. The simulation-based parametrization of the slope $\beta(\theta)$ adds additional systematic uncertainty. A conservative estimation of the corresponding uncertainty was performed by varying the slopes in $\pm 0.15 \beta(\theta)$. Averaging over all angles $\theta \leq 48^\circ$, a mean relative systematic of $\sigma/\rho_{450} = 8.8\%$ is obtained.

During the reconstruction procedure the measured muon densities are corrected by area-dependent efficiency ϵ according to $\rho_{\mu}^{\text{corr}} = \rho_{\mu}/\epsilon$. But the values of ϵ also depend on the time window in the signal used to identify muons [5]. To evaluate the associated systematic, the variation in ρ_{450} was calculated considering two cases: (i) when efficiencies associated to a time window of 22 ns are used, and (ii) when no inhibition window is set during the reconstruction procedure. Averaged over the energy range from $10^{17.4}$ to $10^{18.3}$ eV, an uncertainty of $\sigma/\rho_{450} = 9.9\%$ is found.

As a result of the longer path in the atmosphere and the increased amount of soil covering the buried detectors, the muonic component of inclined air showers gets attenuated. Using UMD data, the attenuation function $f_{\text{att}}(\theta; \mathbf{a}, \mathbf{b})$ using the CIC method [7] was found. The muon density corrected by attenuation is therefore $\rho_{35} = \rho_{450}/f_{\text{att}}(\theta)$. The uncertainties in the parameters $\{\mathbf{a}, \mathbf{b}\}$ add additional systematic uncertainty. Averaged over the zenith-angle range $0^\circ \leq \theta \leq 45^\circ$ the mean relative uncertainty is 2.3%.

4. Results: ρ_{35} vs. Energy

For the analysis of data, the SD quality cuts were applied as for previous official reconstruction [8]. On top of that, as the UMD engineering array has seven stations, to ensure a good sampling of the shower by the underground detectors, the largest SD signal is required to be within the hexagon that constitutes the array of buried scintillators. The zenith-angle range was restricted to $\theta \leq 45^\circ$ to avoid large attenuation effects and statistical uncertainties due to the reduced areas of the scintillator plane. The energy as well as the geometry of the events are reconstructed using data

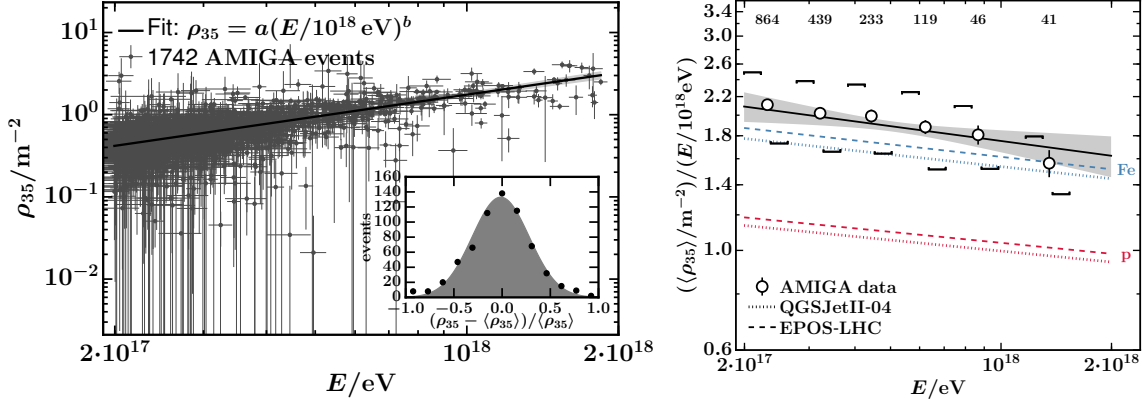


Figure 3: *Left*: Fit of the energy dependence $\rho_{35}(E; a, b)$ for AMIGA data. Vertical and horizontal error bars for single events correspond to the statistical errors. The inset shows the normalized residuals. *Right*: Energy-normalized densities as a function of E compared to expectations. Error bars denote the statistical uncertainties. Systematic uncertainties are indicated by square brackets. The number of events per bin is stated at the top. The obtained fit is shown by a black solid line with a shaded band corresponding to the statistical uncertainties.

from the SD-750 array alone. The reconstructed muon densities ρ_{35} as a function of the energy are shown in Fig. 3-(left). The evolution of ρ_{35} is fitted with a power law

$$\rho_{35}(E; a, b) = a(E/10^{18} \text{ eV})^b \quad (4.1)$$

by maximizing the log-likelihood function

$$\ln \mathcal{L} = \sum_k \ln \left(\sum_i e^{-\frac{(E_k - E_i)^2}{2\sigma_{E_i}^2}} e^{-\frac{(\rho_{35k} - \rho_{35}(E_i; a, b))^2}{2\sigma_{\rho_{35i}}^2}} \right). \quad (4.2)$$

The function of Eq. (4.2) accounts for the threshold effect that is caused by the application of an energy cut and accommodates the uncertainties both in the signal and energy estimate [9]. The energy uncertainty is σ_E (determined by the SD) while the uncertainty of the reconstructed muon densities is $\sigma_{\rho_{35}}$. The index k runs over events with energies above $10^{17.5}$ eV where the SD-750 array becomes fully efficient. The second sum with index i accounts for the migration of events below the full efficiency into the accepted energy range, by including events with energies above $10^{17.3}$ eV. The maximum considered energy is $10^{18.3}$ eV. The best fit solution is displayed by a solid line in Fig. 3-(left). The obtained values are $a = (1.75 \pm 0.05(\text{stat}) \pm 0.05(\text{sys}))/\text{m}^2$ and $b = 0.89 \pm 0.04(\text{stat}) \pm 0.04(\text{sys})$ for the average muon density a at 10^{18} eV and the logarithmic gain b . The evolution of the muon content in data is compared to simulations with proton and iron primaries in Fig. 3-(right). To soften the strong energy dependence, the muon densities have been normalized by the energy. The slopes obtained from both hadronic interaction models are 0.91 for iron and 0.92 for proton, slightly steeper than found in the data. More strikingly, simulations fail to reproduce the observed muon densities which are between 8% (EPOS-LHC) and 14% (QGSJetII-04) larger than those obtained for iron showers at an energy of 10^{18} eV. In order to

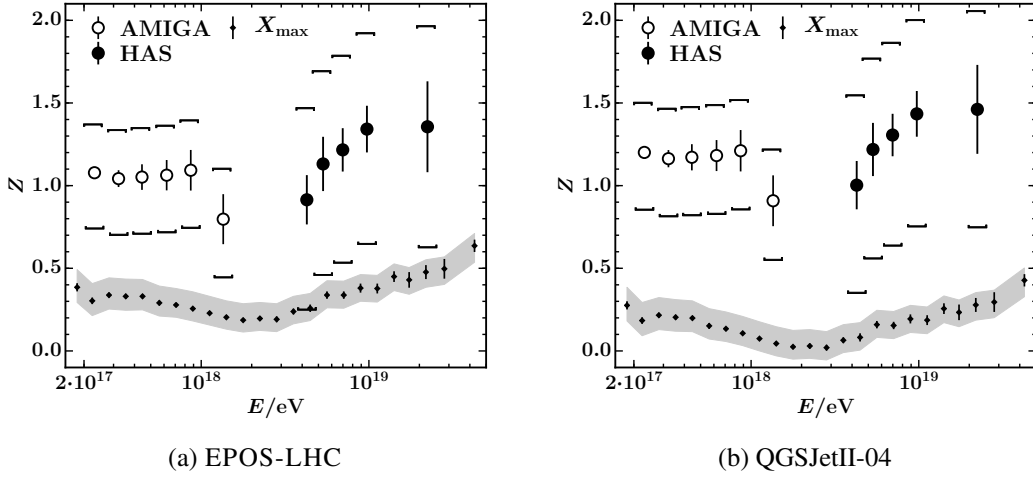


Figure 4: z -factor from direct measurements of muons by AMIGA and the analysis of horizontal air showers (sHASs) compared to the value coming from $\langle X_{\max} \rangle$ by the FD.

compare the muon densities measured by the AMIGA prototype array with the results of the study of the average number of muons in horizontal air shower (HAS) [10, 11], the z -factor [12]

$$z = \frac{\langle \ln \rho_{35} \rangle - \langle \ln \rho_{35} \rangle_{\text{p}}}{\langle \ln \rho_{35} \rangle_{\text{Fe}} - \langle \ln \rho_{35} \rangle_{\text{p}}} \quad (4.3)$$

is calculated using simulations for proton and iron primary particles for a fixed energy and a specific hadronic interaction model. Replacing ρ_{35} by R_{μ} in Eq. (4.3), the z -factor is similarly obtained for the analysis of HAS. The results of both muon analyses are shown in Fig. 4 together with the corresponding values of $z = \ln A / \ln 56$ that are obtained from measurements of the depth of shower maximum X_{\max} [13]. Within the statistical and systematic uncertainties, the z -factors derived by the two muon studies seem to be in agreement at the intermediate energies between their distinct energy ranges. Moreover, the combined muon measurements match the trend of z derived from X_{\max} measurements as a function of the energy. To quantify the disagreement of the muon content between simulations and data, the combination of AMIGA muon densities with independent measurements of the mean depth of shower maximum of the fluorescence detector at fixed energies of $10^{17.5}$ and 10^{18} eV is presented. Using their linear dependence on the mean logarithmic mass, the mean logarithmic muon densities $\langle \ln \rho_{35} \rangle$ in simulations are related to the mean depth of shower maximum $\langle X_{\max} \rangle$ based on proton and iron simulations for both hadronic interaction models and primary energies. Comparing the muon densities measured by AMIGA with those in simulations in Fig. 5, we find that the muon content in simulations would need to be increased by 38% at both energies for EPOS-LHC while an increment of 50% at $10^{17.5}$ eV and 53% at 10^{18} eV is required for the QGSJetII-04 model to match the data.

5. Conclusions

Direct measurements of the muonic component of EAS with the Pierre Auger Observatory were presented for the first time. The observed muon densities, which are larger than for those from

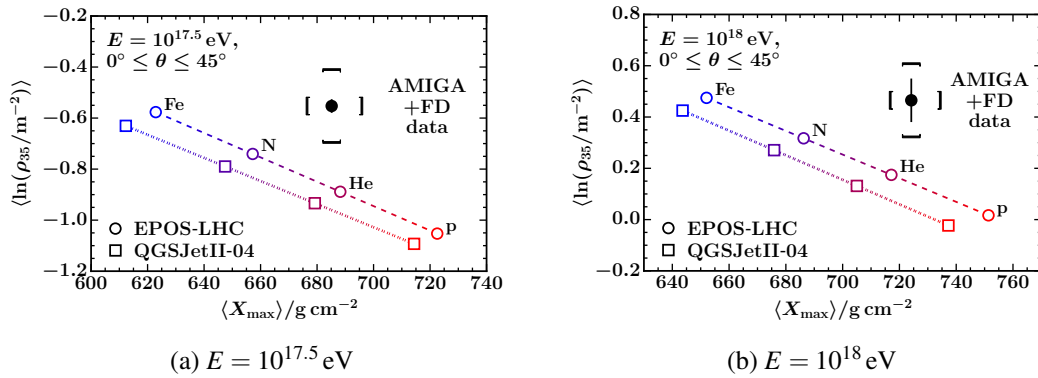


Figure 5: Mean logarithmic muon density $\langle \ln \rho_{35} \rangle$ as a function of the mean depth of shower maximum $\langle X_{\text{max}} \rangle$ for simulations with primary energies of $10^{17.5}$ eV (a) and 10^{18} eV (b) compared to Auger measurements with the FD ($\langle X_{\text{max}} \rangle$) and AMIGA ($\langle \ln \rho_{35} \rangle$).

simulations, show the failure of current hadronic interaction models to reproduce the measurements in the considered energy range. The AMIGA prototype array results are in accordance to the previous Auger muon measurements of horizontal air showers at higher energies. Furthermore, the energy evolution of the combined muon measurements matches the expectations from the X_{max} measurements. The disagreement of the muon content measured by AMIGA and simulations has been quantified with the independent FD measurements of the mean depth of shower maxima. Similar evidence for a muon deficit in simulations were obtained by previous experiments, although direct comparisons are hindered by the different energy thresholds of the observed muons.

References

- [1] The Pierre Auger Collaboration, Nucl. Instrum. Meth. A **798** (2015) 172–213
- [2] A.M. Botti for the Pierre Auger Observatory, PoS (ICRC2019) 202.
- [3] A. Castellina for the Pierre Auger Observatory, EPJ Web Conf 210 (2019) 06002.
- [4] M. Ave *et al.*, Nucl. Instrum. Meth. A **578** (2007) 180–184.
- [5] S. Muller for the Pierre Auger Observatory, EPJ Web Conf 210 (2019) 02013.
- [6] W.D. Apel *et al.*, Nucl. Instrum. Meth. A **620** (2010) 202–216.
- [7] J. Hersil *et al.*, Phys. Rev. Lett. **6** (1961) 22–23.
- [8] F. Fenu for the Pierre Auger Collaboration, PoS (ICRC2017) 486.
- [9] H. Dembinski for the Pierre Auger Collaboration, Proc. 32th ICRC, (2011).
- [10] L. Cazón for the Pierre Auger Collaboration, EPJ Web Conf 210 (2019) 02002.
- [11] The Pierre Auger Collaboration, Phys. Rev. D **91** (2015) 032003.
- [12] H. Dembinski for the Working Group on Hadronic Interactions and Shower Physics, EPJ Web Conf 210 (2019) 02004.
- [13] J. Bellido for the Pierre Auger Collaboration, PoS (ICRC2017) 506.



Measurement of the fluctuations in the number of muons in inclined air showers with the Pierre Auger Observatory

Felix Riehn^{*a} for the Pierre Auger Collaboration^{†b}

^a*Laboratório de Instrumentação e Física Experimental de Partículas (LIP), Lisbon, Portugal*

^b*Observatorio Pierre Auger, Av. San Martín Norte 304, 5613 Malargüe, Argentina*

E-mail: auger_spokespersons@fnal.gov

Full author list: Pierre Auger Collaboration and additional author(s):

http://www.auger.org/archive/authors_icrc_2019_a.html

We present the first measurement of the fluctuations in the number of muons in inclined air showers with energies above 4EeV measured with the Pierre Auger Observatory. We find that the results agree well with simulations within the experimental uncertainties. In contrast, the measurement of the average number of muons has previously been found to deviate substantially from the predictions by high-energy hadronic interaction models. We analyse the implications of these findings for our understanding of hadronic interactions, especially to those at the highest energies.

36th International Cosmic Ray Conference — ICRC2019

24 July – 1 August, 2019

Madison, Wisconsin, USA

*Speaker.

†for collaboration list see PoS(ICRC2019)1177

1. Introduction

From early on, the study of cosmic rays has been dual in nature. We wonder about their origin in the cosmos, and whether they can teach us something about the extreme side of the universe. At the same time, we use their interactions in the atmosphere to study the microcosmos. Much of the early developments in particle physics was driven by cosmic-ray research [1]. While most of particle physics nowadays is done at accelerator facilities, the high-energy frontier is still held by ultrahigh-energy cosmic rays (UHECR), easily reaching center-of-mass energies ten times larger than CERN's Large Hadron Collider.

Not surprisingly, the observation of an excess in the number of muons, that was initially reported by the Pierre Auger Observatory [2, 3, 4], has raised secret hopes of another breakthrough in particle physics from cosmic rays. It certainly has stirred theorists imagination [5, 6, 7]. Other observables from ultrahigh-energy showers, like the average depth of shower maximum (X_{\max}) and its fluctuations [8, 9], or the muon production depth (X_{\max}^{μ}) [10], limit the allowed range for explanations of the muon excess with new physics but do not definitely exclude it. This is the case because X_{\max} and X_{\max}^{μ} mostly depend on the cross-section, i.e. the geometrical shape of hadrons, while the number of muons depends more strongly on particle production, which is more related to the deep, internal structure of hadrons [11, 12].

In these proceedings, we report the measurement of another observable of ultrahigh-energy air showers with the Pierre Auger Observatory which severely constrains the available phase space for exotic explanations of the muon excess: the shower-to-shower fluctuations in the number of muons.

2. Measurement of the shower-to-shower fluctuations

2.1 Reconstruction of the number of muons

The measurement of the fluctuations in the number of muons is based on the sample of inclined air showers detected at the Pierre Auger Observatory [13] between 01/01/2004 and 10/06/2019. Only air showers that were simultaneously detected with the surface detector array (SD) and at least one of the fluorescence detectors (FD), are used (hybrid detection).

The reconstruction of the number of muons relies on the fact that for inclined air showers, the electromagnetic cascade is mostly absorbed in the atmosphere so that signals at the ground are dominated by muons. By fitting the normalization factor of a reference model¹ for the muon density at the ground to the observed distribution of signals in the SD array, the number of muons can be extracted [14]. The reconstructed quantity R_{μ} , is the total number of muons at the ground relative to the average of the total number of muons in a shower with primary energy 10^{19} eV.

The reconstruction of the energy of the air showers is done by integrating the longitudinal shower profiles observed with the FD [15].

An event selection is applied to ensure a high quality of the reconstruction. For the FD, this means, for example, only events measured during good atmospheric conditions are selected. For the SD, only events with reconstructed energies above 4EeV and zenith angles above 62° are

¹QGSJET II-03

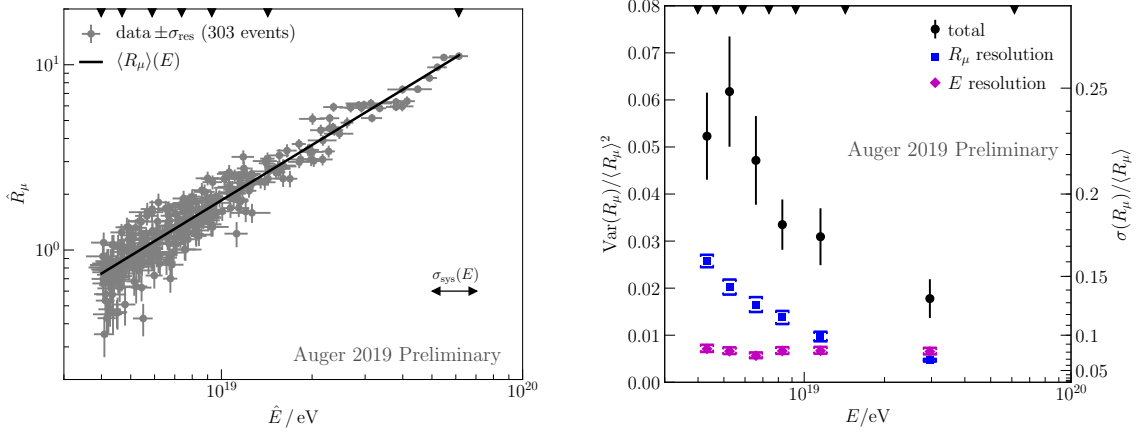


Figure 1: Left: Correlation between the reconstructed energy and the reconstructed number of muons in inclined air showers. The black line is the resulting evolution of the average number of muons after the unfolding procedure. Measured quantities are marked with a hat. Right: Raw variance of the number of muons (black) and the contributions from the detector (blue) and energy resolution (purple). The axis on the right shows the value of the standard deviation. The energy ranges for which the fluctuations are evaluated are marked by the black triangles at the top of the figure.

accepted to ensure a triggering probability of 100% and to avoid contamination of the signals at the ground by the electromagnetic component respectively. For each event, a minimum of four detector stations with signal in the SD was required to ensure high-quality reconstruction of R_μ . The selection criteria are described in detail in the previous publication [2]. The initial sample contains 52587 hybrid air showers, and after the selection without applying the energy threshold, 860 remain. There are 303 events above 4 EeV.

2.2 Intrinsic fluctuations

The relative shower-to-shower fluctuations in the number of muons $\sigma(R_\mu)/\langle R_\mu \rangle$ (intrinsic fluctuations) are extracted from the data, by fitting a statistical model to the measured pairs of energy \hat{E} and number of muons \hat{R}_μ . Measured quantities are marked with a hat to distinguish them from true quantities that contain only intrinsic fluctuations.

The model is based on the assumptions that: FD & SD measurements have fluctuations that follow Gaussian distributions, with widths given by the detector resolutions $\sigma_{\text{res}}(\hat{E})$ and $\sigma_{\text{res}}(\hat{R}_\mu)$; intrinsic fluctuations follow a Gaussian distribution; the average number of muons as a function of the primary energy is given by a power-law $\langle R_\mu \rangle(E) = a(E/(10^{19} \text{ eV}))^b$. The model is fitted by maximizing the log-likelihood

$$\ln \mathcal{L}(a, b, s) = \sum_i \ln \left[\sum_k C_k \exp \left(-\frac{1}{2} \frac{(\hat{E}_i - \hat{E}_k)^2}{\hat{\sigma}_{\hat{E},k}^2} \right) \exp \left(-\frac{1}{2} \frac{(\hat{R}_{\mu,i} - \langle R_\mu \rangle(\hat{E}_k))^2}{\hat{\sigma}_{\hat{R}_\mu,k}^2 + (s(\hat{E}_k) \cdot \langle R_\mu \rangle(\hat{E}_k))^2} \right) \right], \quad (2.1)$$

where the outer sum over the index i , the usual sum over the log-likelihoods of events, includes only events above the energy threshold of 4 EeV. The inner sum over the index k includes all events, also below the threshold, to account for migration effects which, given the steeply falling spectrum

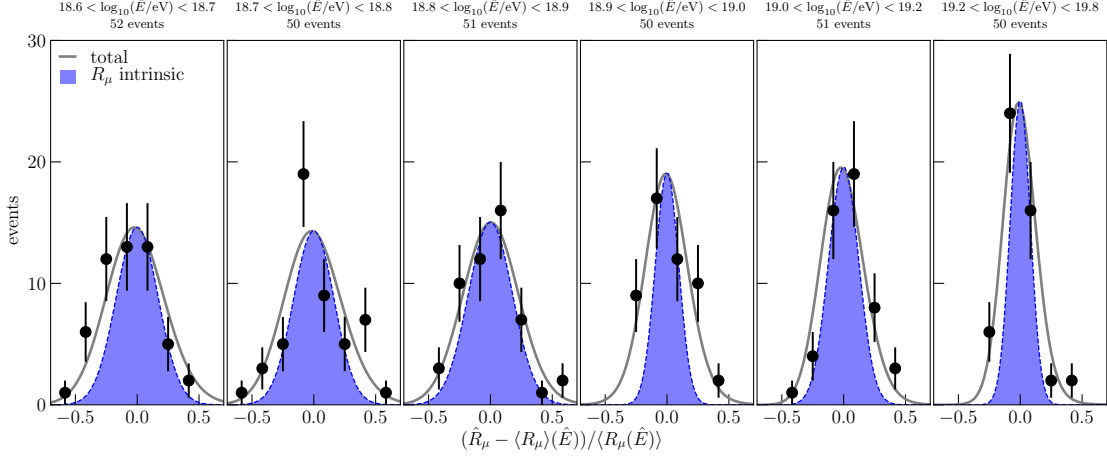


Figure 2: Distribution of the relative number of muons in six bins of energy from $10^{18.6}$ eV to $10^{19.8}$ eV. The model for the full distribution is shown in gray, the inferred intrinsic distribution of the number of muons is shown by the filled-in curve.

of CRs, can be sizable [16]. The factor C_k contains the normalization factors from the double Gaussian. The relative intrinsic fluctuations at energy \hat{E}_k are written as $s(\hat{E}_k) \equiv \sigma(\hat{E}_k)/\langle R_\mu \rangle(\hat{E}_k)$.

The detector resolutions enter Eq. (2.1) through the variances $\hat{\sigma}_{\hat{E},k}^2$ and $\hat{\sigma}_{\hat{R}_\mu,k}^2$, which are the uncertainties in the individual measurements. We have tested the assumption that on average the $\hat{\sigma}_k^2$ describe the detector resolution with simulations and data.

To obtain the energy dependence of the fluctuations we split $s(\hat{E}_k)$ in Eq. (2.1) into six independent parameters for the different energy bins (see markers at the top of Figs. 1). Within one bin the fluctuations are constant. The bins are chosen such that the number of events in each is similar.

The distribution of events above the threshold that enter the fit is shown in Fig. 1 (left).

In the right panel of Fig. 1, the raw variance in the data and the average contributions from the SD and FD resolutions are shown for illustration. In Fig. 2, the distribution of the relative number of muons $(\hat{R}_\mu - \langle R_\mu \rangle)/\langle R_\mu \rangle$ in the six energy bins is shown together with the best-fit model of Eq. (2.1) as well as the corresponding intrinsic distributions. For the current number of events, the assumption of Gaussian distributions for the detector and intrinsic fluctuations seems to hold.

2.3 Systematic uncertainties & corrections

The intrinsic fluctuations extracted in the unfolding will only represent the true intrinsic fluctuations if all other sources of fluctuations have been correctly accounted for. Since the detector fluctuations are sizable (see Fig. 1 right), we first check whether the distribution of the detector resolutions is estimated correctly.

The Pierre Auger Observatory is equipped with four FD stations which overlook a common area covered by the SD array. By using events which are simultaneously observed by telescopes in two FD stations, we get two estimates for the energy and the resolution. On average, these should be the same. We find that a small correction of -1% for the energy resolution is necessary.

For the SD resolution, we find two corrections are necessary. One is found by using simulations where one can reconstruct the same shower multiple times, leaving only fluctuations due to

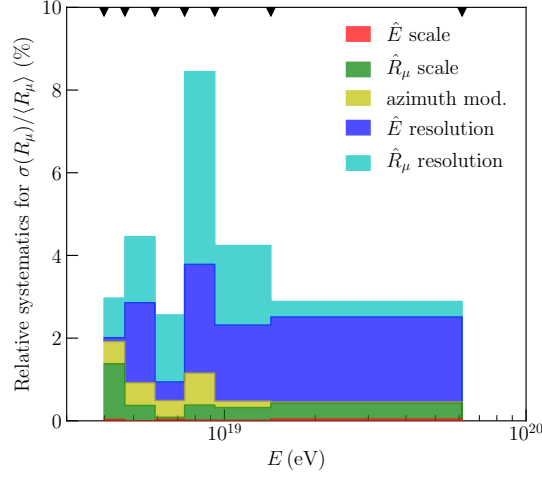


Figure 3: Stacked histogram of the contributions to the systematic uncertainty in the standard deviation. The dominant contributions are from the uncertainties in the SD and FD resolutions.

the detection process and the reconstruction. Comparing the variance in the reconstructed muon scale in this sample with the expectation, i.e. the detector resolution $\sigma_{\text{res}}(\hat{R}_\mu)^2$, we find a correction of +1% is necessary. While many sources of detector fluctuations can be included in the simulation, a difference to real data remains. To estimate that remaining difference, we calculate and compare the jackknife variance [17] for both data and simulations. We find that in this case, a correction of -1% to the estimated resolution is necessary. In combination these corrections almost entirely cancel each other.

In addition to the accuracy of the resolution, we investigate for a possible presence of drifts or modulations in the data, as these would also increase fluctuations. We do this by splitting the data in percentiles along a specific variable and compare. We find no significant trends, except for a modulation of the average number of muons with azimuth angle. This modulation is most probably related to the approximations going into the modeling of the muon densities at the ground [14]. For the average number of muons the modulation averages out. For the fluctuations, we calculate the contribution from the modulation to be $\sigma_\phi/\langle R_\mu \rangle = (-0.04 \pm 0.02)/\sqrt{2}$ and correct the final result accordingly.

For all corrections, we apply half of their value directly and report the second half as a systematic uncertainty. In case of the SD resolution, this means even though the two corrections that are discussed above, cancel each other, there is still a contribution to the systematic uncertainty. The effects of the energy scale uncertainty (14%) and the systematic uncertainty in the number of muons R_μ (11%) are small. Largest contributions are from the uncertainties in the resolutions. The impact of the systematic uncertainties on the relative fluctuations is shown in Fig. 3. Overall systematic effects on the fluctuations are below the level of 8%.

3. Results & discussion

The final result for the relative fluctuations is shown in Fig. 4 on the left. We find that the observed fluctuations fall in the range of the predictions from air shower simulations with current

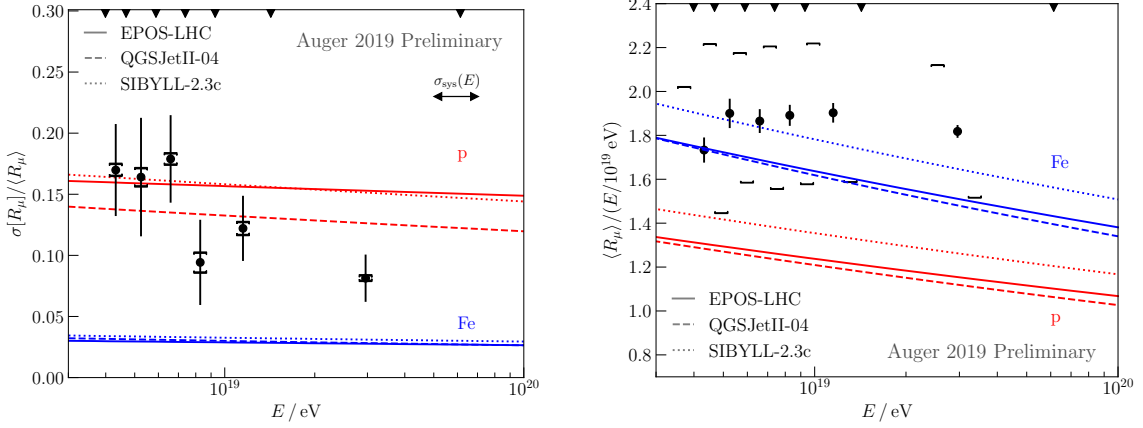


Figure 4: Shower-to-shower fluctuations (left) and the average number of muons (right) in inclined air showers as a function of the primary energy. For the fluctuations, the statistical uncertainty (error bars) is dominant, while for $\langle R_\mu \rangle$ the systematic uncertainty (square brackets) is dominant. The shift in the markers for the systematic uncertainty in the average number of muons represents the uncertainty in the energy scale.

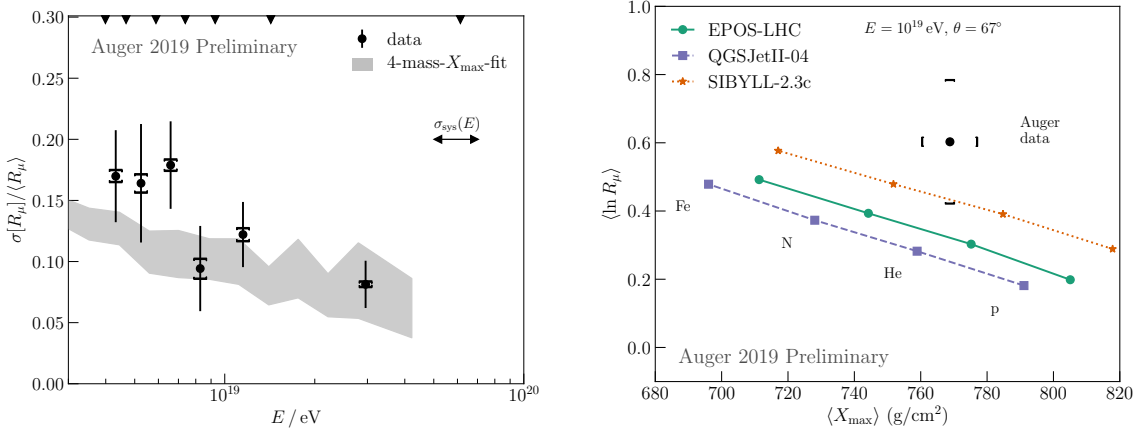


Figure 5: Left: Comparison of the measured fluctuations of the number of muons as a function of the primary energy with the expectation derived from hadronic models and the CR composition from the fit of four primary mass components to the measured X_{max} -distributions [21, 22]. Right: Average number of muons as a function of the average depth of shower maximum at 10^{19} eV .

hadronic interaction models [18, 19, 20]. The measured fluctuations seem to slightly decrease with the primary energy. Fitting $p_0 + p_1 \log_{10}(E/eV)$ to the fluctuations, we find a significant non-zero value for the slope with $p_1 = -0.11 \pm 0.04$.

In addition to the fluctuations, we also obtain new results for the measurement of the average number of muons. The results are shown on the right in Fig. 4. Note that in the figure, $\langle R_\mu \rangle$ is divided by the factor $(E/10^{19} \text{ eV})$. In contrast to the fluctuations, the measurement here falls outside the range of the predictions from simulations (see also the discussion in [4]).

For the parameters of the energy evolution of the number of muons, $\langle R_\mu \rangle = a(E/(10^{19} \text{ eV}))^b$,

we find:

$$\begin{aligned} a &= 1.85 \pm 0.02(\text{stat.})^{+0.36}_{-0.31}(\text{syst.}) \\ b &= 0.99 \pm 0.02(\text{stat.})^{+0.03}_{-0.03}(\text{syst.}), \end{aligned}$$

which is compatible with our previous results [2].

A comparison between the measured fluctuations in the number of muons and the predictions from interaction models given the measured CR composition is shown in Fig. 5 left. The composition that is used here is inferred from the measured distributions of X_{max} by assuming proton, helium, nitrogen and iron as primary components and fitting the fractions to the overall distributions [21, 22]. Although there are some differences in the estimated composition for the different interaction models, and the predictions for the relative fluctuations for protons also differ between models, the results for the fluctuations in the number of muons are very similar. In the figure, the phase space covered by interaction models with the statistical and systematic uncertainties from the composition fit added in quadrature is shown by the gray band. The measured fluctuations in the number of muons (black points) are compatible with the expectation from composition and interaction models. Fitting a linear evolution in energy to the central value of the model band and comparing with the data, we get a p-value of 34%.

In Fig. 5 right, the average logarithm of the number of muons is shown as a function of the average X_{max} for a primary energy of 10^{19} eV. Since both $\langle \ln R_{\mu} \rangle$ and $\langle X_{\text{max}} \rangle$ depend linearly on $\ln A$, the model predictions for an arbitrary composition between proton and iron reduce to the lines shown in the figure. Also here the results are consistent with the previous publication. A notable difference is the new prediction from SIBYLL 2.3c, which is just compatible with the data.

The fluctuations and the average of the number of muons depend on different stages in the development of air showers. While the average number of muons is influenced by the entire chain of interactions [11, 12, 23], the fluctuations are dominated by the first interaction, in particular by the partition of energy in the hadronic and the electromagnetic cascade [24, 25]. The good agreement between measurement and predictions for the relative fluctuations in the number of muons indicates that the first, high energy interaction is reasonably well described by hadronic interaction models. Given the good agreement for the fluctuations, the likely explanation for the disagreement in the average is that a small discrepancy in the particle production exists at all energies, which then is accumulated as the showers develop to create the deficit in the number of muons finally observed at the ground. This mechanism is also used to enhance the number of muons in SIBYLL 2.3c [26]. Explanations invoking modifications in the first interaction that change the intrinsic fluctuations are disfavored.

4. Summary

We report the first measurement of the fluctuations in the number of muons in extensive air showers above an energy of 4EeV and an update to our previous measurement of the average number of muons. We find that the fluctuations are compatible with the predictions from air shower simulations with current hadronic interaction models and the measured composition of cosmic rays. We confirm our previous measurement of the average number of muons and note

that SIBYLL 2.3c now gives a consistent interpretation when combining $\langle R_\mu \rangle$ and $\langle X_{\max} \rangle$ measurements. The agreement between measured fluctuations and predictions by standard hadronic interaction models means the models give a sufficiently good description of particle production in the first interaction between $10^{18.6}$ eV and $10^{19.8}$ eV.

References

- [1] C. D. Anderson and S. H. Neddermeyer *Phys. Rev.* **50** (1936) 263–271.
- [2] A. Aab [Pierre Auger Collaboration], *Phys. Rev. D* **91** (2015), no. 3 032003, [[1408.1421](#)].
[Erratum: *Phys. Rev. D* 91, no. 5, 059901 (2015)].
- [3] A. Aab [Pierre Auger Collaboration], *Phys. Rev. Lett.* **117** (2016), no. 19 192001, [[1610.08509](#)].
- [4] L. Cazon, Working group on hadronic interactions and shower physics *PoS (ICRC2019)* 214.
- [5] G. R. Farrar [[1902.11271](#)].
- [6] G. R. Farrar and J. D. Allen *EPJ Web Conf.* **53** (2013) 07007, [[1307.2322](#)].
- [7] L. A. Anchordoqui, H. Goldberg, and T. J. Weiler *Phys. Rev. D* **95** (2017), no. 6 063005, [[1612.07328](#)].
- [8] A. Aab [Pierre Auger Collaboration], *Phys. Rev. D* **90** (2014), no. 12 122005, [[1409.4809](#)].
- [9] P. Abreu [Pierre Auger Collaboration], *Phys. Rev. Lett.* **109** (2012) 062002, [[1208.1520](#)].
- [10] A. Aab [Pierre Auger Collaboration], *Phys. Rev. D* **90** (2014), no. 1 012012, [[1407.5919](#)].
[Erratum: *Phys. Rev. D* 92, no. 1, 019903 (2015)].
- [11] R. Ulrich, R. Engel, and M. Unger *Phys. Rev. D* **83** (2011) 054026.
- [12] R. Engel, D. Heck, and T. Pierog *Ann. Rev. Nucl. Part. Sci.* **61** (2011) 467–489.
- [13] A. Aab [Pierre Auger Collaboration], *Nucl. Instrum. Meth. A* **798** (2015) 172–213, [[1502.01323](#)].
- [14] A. Aab [Pierre Auger Collaboration], *JCAP* **1408** (2014), no. 08 019, [[1407.3214](#)].
- [15] J. Abraham [Pierre Auger Collaboration], *Nucl. Instrum. Meth. A* **620** (2010) 227–251, [[0907.4282](#)].
- [16] H. P. Dembinski, B. Kégl, I. C. Mariş, M. Roth, and D. Veberič *Astropart. Phys.* **73** (2016) 44–51, [[1503.09027](#)].
- [17] B. Efron and C. Stein *Ann. Statist.* **9** (05, 1981) 586–596.
- [18] T. Pierog, I. Karpenko, J. M. Katzy, E. Yatsenko, and K. Werner *Phys. Rev. C* **92** (2015), no. 3 034906, [[1306.0121](#)].
- [19] S. Ostapchenko *Phys. Rev. D* **83** (2011) 014018, [[1010.1869](#)].
- [20] F. Riehn, H. P. Dembinski, R. Engel, A. Fedynitch, T. K. Gaisser, and T. Stanev
PoS (ICRC2017) 301 [[1709.07227](#)].
- [21] A. Aab [Pierre Auger Collaboration], *Phys. Rev. D* **90** (2014), no. 12 122006, [[1409.5083](#)].
- [22] J. Bellido [Pierre Auger Collaboration], *PoS (ICRC2017)* 506.
- [23] J. Matthews *Astropart. Phys.* **22** (2005) 387–397.
- [24] L. Cazon, R. Conceição, and F. Riehn *Phys. Lett. B* **784** (2018) 68–76, [[1803.05699](#)].
- [25] R. Conceição et al. *PoS (ICRC2019)* 226.
- [26] F. Riehn, R. Engel, A. Fedynitch T.K. Gaisser and T. Stanev *EPJ Web Conf.* **208** (2019) 11002.

5

Cosmology and Geophysics





Testing Lorentz Invariance Violation at the Pierre Auger Observatory

Rodrigo Guedes Lang^{*a} for the Pierre Auger Collaboration^{†b}

^a*Instituto de Física de São Carlos, Universidade de São Paulo, Avenida Trabalhador São-Carlense 400, CEP 13566-590, São Carlos, SP, Brazil*

^b*Observatorio Pierre Auger, Av. San Martín Norte 304, 5613 Malargüe, Argentina*

E-mail: auger_spokespersons@fnal.gov

Full author list: http://www.auger.org/archive/authors_icrc_2019.html

In this work, we present the capabilities of testing Lorentz invariance violation (LIV) using data from the Pierre Auger Observatory. Two independent scenarios are treated. Firstly, LIV on the hadron sector is considered and the modified UHECR propagation obtained. An updated combined fit of the spectrum and composition data is performed for each LIV assumption. The data is better described with a low maximum rigidity at sources, which leads to a poor sensitivity to LIV effects. Secondly, subluminal LIV on the photon sector is considered and the propagation of GZK photons is modified. For one of the scenarios considered, very competitive limits on the LIV coefficient of the order of $\delta_\gamma^{(1)} \gtrsim -10^{-40} \text{ eV}^{-1}$ and $\delta_\gamma^{(2)} \gtrsim -10^{-60} \text{ eV}^{-2}$ are imposed. Finally, we discuss a promising possibility of testing LIV using the development of UHE air-showers.

36th International Cosmic Ray Conference — ICRC2019

24 July – 1 August, 2019

Madison, Wisconsin, USA

^{*}Speaker.

[†]for collaboration list see PoS(ICRC2019)1177

1. Introduction

Relativity has been widely established and well tested during the last century. However, departures from relativity such as Lorentz invariance violation (LIV) have been proposed by several high energy models [1]. Potential LIV signatures are expected from several different astrophysical contexts. Previous studies have searched for LIV signals using distinct results, such as the time of flight of photons generated in gamma-ray bursts [2, 3, 4], modulations of the energy spectrum in TeV gamma-rays [5, 6, 7] and ultra-high energy cosmic rays (UHECR) [8, 9], and upper limits on the flux of EeV photons [10, 11]. No LIV signal has yet been found [1] and, thus, restrictive limits on the violation have been set [12].

LIV effects are expected to be suppressed at low energies and for short travel distances [1]. Consequently, UHECRs represent a unique possibility for testing it, being the most energetic known particles in the Universe [13] and coming from extragalactic sources [14].

The Pierre Auger Observatory is the largest experiment ever built to study UHECRs. It uses a hybrid technique composed of a surface detector (SD) with 1660 water-Cherenkov stations and a fluorescence detector (FD) with 27 fluorescence telescopes covering an area of 3000 km². In this study, three important results obtained by the Observatory are used to search for LIV signals: (i) the energy spectrum of UHECR measured with unprecedented statistics [15], (ii) the distribution of depths of maximum of air-shower profiles, X_{\max} [16], and (iii) the upper limits on the photon flux [17].

A generic phenomenological approach based on the Coleman & Glashow formalism [18] is used here to introduce LIV as presented in section 2. Two different and independent LIV scenarios are tested: (a) LIV in the hadronic sector is tested by searching the best description of the energy spectrum and X_{\max} distributions under LIV assumptions and (b) LIV in the photon sector is limited by the upper limits in the photon flux. A third promising scenario to search for LIV signals in the pion section by looking into the development of extensive air showers (EAS) is also discussed.

2. Lorentz invariance violation framework

The phenomenological approach of Coleman & Glashow [18] summarizes LIV effects in a perturbative modification of the particle dispersion relation,

$$E_i^2 = p_i^2 + m_i^2 + \sum_{n=0}^{\infty} \delta_i^{(n)} E_i^{n+2}, \quad (2.1)$$

where E , p and m are, respectively, the energy, the momentum and the mass of the particle; i denotes the particle species and n the approximation order, while $\delta_i^{(n)}$ is the LIV coefficient for each particle at a given order. Searches for LIV use data to measure or limit values of $\delta_i^{(n)}$. It is usual to consider in each LIV analysis only one particle species and specific order, leaving $\delta_i^{(n)} \neq 0$ as a free parameter. Modifying the dispersion relation may lead to several effects depending on the particle considered and on the sign of $\delta_i^{(n)}$. In particular, the kinematics of some interactions are expected to be modified, resulting in a shift in their energy threshold.

In this work, two different and independent LIV scenarios are tested against Auger data: (a) positive LIV coefficients for the hadron sector ($\delta_{\text{had}} = \delta_p = \delta_\pi > 0$) and (b) negative LIV coeffi-

coefficients for the photon sector ($\delta_\gamma < 0$). A third hypothesis is discussed for negative LIV coefficients for the pion sector ($\delta_\pi < 0$).

3. UHECR propagation

The spectrum of UHECRs propagating in the intergalactic medium is shaped by their interaction with the photon background. For the highest energies, the most relevant interactions are the photodisintegration for nuclei, ${}^A Z + \gamma_{\text{bkg}} \rightarrow {}^{A'} Z' + p(n)$, and the photopion production for protons, $p + \gamma_{\text{bkg}} \rightarrow p + \pi$. Changing the particle dispersion relation leads to a change in the kinematics of the interactions, causing modifications in the extragalactic propagation of the UHECRs. For this reason, LIV effects are expected to be visible in the measured spectrum and composition [8, 9] and, thus, these measurements can be used to search for LIV signatures.

In this section, LIV is considered in the hadron sector, $\delta_p = \delta_\pi = \delta_{\text{had}} > 0$, and the modified kinematics of the photopion production and photodisintegration as published in [19] are used. The main effect of LIV is an increase in the mean free path of the interactions. The difference from the LI scenario becomes significant above a given energy for each LIV coefficient. The modified mean free paths are implemented in the *SimProp* code [20] and the resulting spectra and composition on Earth for each LIV assumption are obtained.

Identical and homogeneously distributed UHECR sources are considered emitting four different nuclear species (${}^1\text{H}$, ${}^4\text{He}$, ${}^{14}\text{N}$, ${}^{28}\text{Si}$) with an energy spectrum given by a power law with a broken exponential cutoff,

$$\frac{dN_A}{dE} = J_A(E) = f_A J_0 \left(\frac{E}{10^{18} \text{ eV}} \right)^{-\gamma} \times \begin{cases} 1 & \text{for } E < Z_A R_{\text{cut}} \\ \exp\left(1 - \frac{E}{Z_A R_{\text{cut}}}\right) & \text{otherwise} \end{cases}, \quad (3.1)$$

where f_A is the fraction of the injected isotope over the total and is defined at fixed energy, $E = 10^{18}$ eV, γ is the spectral index, R_{cut} is the maximum rigidity at the sources.

The simulations took into account three LIV coefficients for the leading order $n = 0$, $\delta_{\text{had}}^{(0)} = \{5 \times 10^{-24}, 10^{-23}, 10^{-22}\}$. The two limiting cases, LI ($\delta_{\text{had}} = 0$) and maximum LIV ($\delta_{\text{had}} \rightarrow \infty$), were also considered. The maximum LIV scenario represents the propagation of UHECR with no interactions with the photon backgrounds at all energies, taking into account only the adiabatic energy losses due to the expansion of the universe.

The analysis searches for the values of the parameters which best describe the energy spectrum [15] and the X_{max} distributions [16] for each LIV assumption, updating the results reported in [9]. The fit procedure follows a method similar to the one described in [21]. Only energies above $E > 10^{18.7}$ eV are considered; the combined energy spectrum is employed and Gumbel parametrizations are used to fit the X_{max} distributions. The goodness of fit is obtained using a generalized χ^2 (the deviance, $D = -2(\ln(L_J/L_J^{\text{sat}}) + \ln(L_{X_{\text{max}}}/L_{X_{\text{max}}}^{\text{sat}}))$). EPOS-LHC [22] is used as hadronic model for interactions in the atmosphere.

Tab. 1 shows the results of the fits for each of the LIV assumptions. The results using the 2017 data set [15, 16] confirm the finding of [9], where the best fit found using the 2015 data set [23, 24] is located in an elongated region extended below $\gamma = 1$. The value of the deviance is worse with respect to the one reported in [9], both for the LIV and the LI cases, due to the increased statistics

Scenario	γ	$\lg(R_{\text{cut}}/V)$	f_{H}	f_{He}	f_{N}	f_{Si}	$D(J)$	$D(X_{\text{max}})$	D_{total}
LI, $\delta_{\text{had}} = 0$	-1.13	18.25	70.1	29.5	0.4	0.02	19.9	236.6	256.5
LIV, $\delta_{\text{had}}^{(0)} = 5 \times 10^{-24}$	-1.26	18.24	68.9	30.8	0.3	0.02	19.5	235.6	255.1
LIV, $\delta_{\text{had}}^{(0)} = 1 \times 10^{-23}$	-1.20	18.25	67.4	32.2	0.4	0.02	19.9	236.1	256.0
LIV, $\delta_{\text{had}}^{(0)} = 1 \times 10^{-22}$	-1.42	18.22	68.4	31.4	0.2	0.01	17.7	231.8	249.5
max LIV, $\delta_{\text{had}} \rightarrow \infty$	0.91	18.47	52.3	42.3	5.4	0.	34.4	189.7	224.1

Table 1: Best fit parameters for the LI reference model and LIV cases (using *SimProp* simulations).

of the data set. A better separation between the values of the minimum with respect to what is shown in Fig. 1 can be obtained for example using a different hadronic model in the atmosphere.

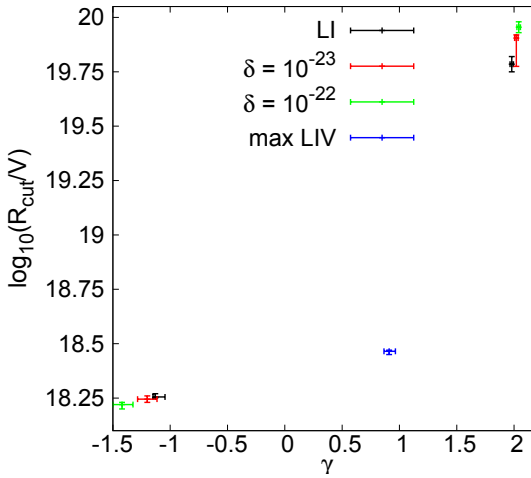


Figure 1: Position of the best-fit values as a function of the spectral index and rigidity cutoff, for the LI case and some of the LIV cases, are reported in the lower-left part of the figure. The error bars are computed from the interval $D \leq D_{\text{min}} + 1$. The local minima are reported in the upper-right part of the plot: in this case the error bars are computed from the interval $D \leq D_{\text{local}} + 1$.

4. GZK photons propagation

Propagating UHECRs interact with the background photons, emitting pions via photopion production. Neutral pions rapidly decay into EeV photons, called GZK photons, which may arrive on Earth. The Pierre Auger Observatory has the capability of detecting these photons. Nevertheless, no event has yet been detected and, consequently, restrictive upper limits on the photon flux have been imposed [17].

Propagating EeV photons interact with the background radiation via pair production, $\gamma + \gamma_{\text{bg}} \rightarrow e^+ + e^-$, which strongly suppresses the expected flux of GZK photons [25]. In this section, we consider subluminal LIV in the photon sector for the leading orders $n = 1, 2$ ($\delta_\gamma < 0$). The kinematics of the pair production considering LIV is obtained following the procedure described in Ref. [11]. The main effect in the propagation is an increase in the mean free path when LIV is considered, which leads to photons traveling farther and, consequently, to an enhanced flux of GZK photons.

Since the GZK photons are emitted during the propagation of UHECR, the assumptions about the UHECR sources, such as the injection energy, composition and redshift evolution, play an important role in the expected flux of GZK photons [11]. In this work, two astrophysical scenarios

Scenario	γ	$\lg(R_{\text{cut}}/V)$	f_{H}	f_{He}	f_{N}	f_{Si}	f_{Fe}
A	-1.5	18.185	60.00	39.70	0.20	0.02	0.00
B	1.97	19.86	0.01	0.00	47.10	52.90	0.00

Table 2: Best fit parameters (corresponding to the the global, A, and local, B, minima of the combined fit) for the LI model obtained with CRPropa simulations.

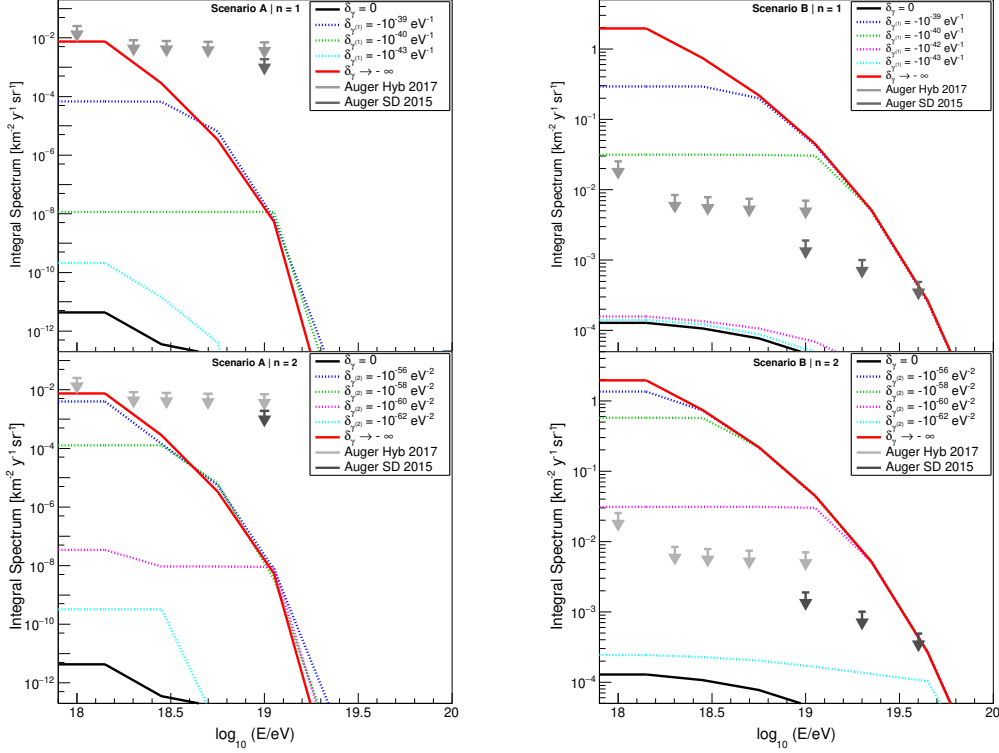


Figure 2: Integral flux of GZK photons. The left and right panels represents scenarios A and B, respectively. Top and bottom panels represents LIV approximation orders $n = 1$ and $n = 2$, respectively. The continuous black line represents the LI scenario, the continuous red line represents the maximum LIV scenario and the dashed colored lines represent intermediate LIV scenarios. Gray and black arrows show the upper limits from the Pierre Auger Observatory [17].

are considered. These scenarios come from the combined fit described in the previous section, using a LI propagation simulated with CRPropa3 [26]. The first one, A, is the best fit, with hard spectral index, while the second one, B, is a local minimum, corresponding to a softer spectral index (see Tab. 2). Both scenarios consider identical and homogeneous sources distributed up to 9600 Mpc.

The LIV photon mean free paths were implemented in CRPropa3/EleCa [26] and several intermediate LIV scenarios are considered for the leading orders $n = 1, 2$. The two limiting cases are also considered, i.e., LI ($\delta_\gamma = 0$) and maximum LIV ($\delta_\gamma \rightarrow -\infty$).

Fig. 2 shows the resulting integral fluxes of GZK photons compared to the upper limits on the flux from the Pierre Auger Observatory. As expected, when LIV is considered, the flux is stronger.

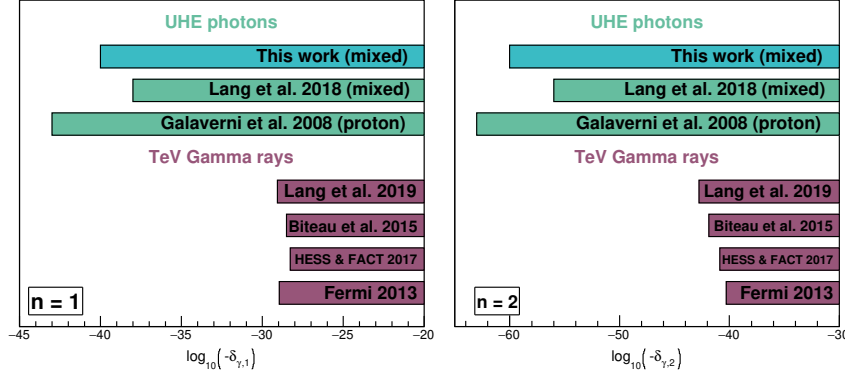


Figure 3: Limits on the subluminal LIV coefficient. The left and right panels show the limits for $n = 1$ and $n = 2$, respectively. The green bars show limits coming from UHE photons [10, 11] and the purple bars show limits coming from TeV gamma-rays [7, 5, 6, 2].

For the astrophysical scenario A, not even in the most extreme case, $\delta_\gamma \rightarrow -\infty$, the flux becomes larger than the upper limits and, thus, no LIV limits can be imposed. For the astrophysical scenario B, on the other hand, some of the LIV coefficients considered are enough to create a flux larger than the upper limits and, consequently, limits on the LIV coefficient can be imposed. For this scenario, the imposed limits are $\delta_\gamma^{(1)} \gtrsim -10^{-40} \text{ eV}^{-1}$ and $\delta_\gamma^{(2)} \gtrsim -10^{-60} \text{ eV}^{-2}$.

Fig. 3 shows a comparison between the limits on the LIV coefficient for the subluminal photon sector imposed in this work and previous limits imposed from astrophysical tests. The comparison with limits from the TeV gamma-rays are not straight-forward since different astrophysical assumptions, photon energies and systematic uncertainties are considered in each case. Limits from refs. [10, 11] were imposed using a similar approach. Galaverni et al. considers pure proton composition at the source and the upper limits of the photon fluxes published in 2007 and 2008. A pure proton composition, however, is not favored by the X_{max} data [16]. Lang et al. [11] updated the analysis using mixed composition and the upper limits of the photon fluxes published in 2017. The limits imposed here are directly derived from the latest Pierre Auger data and are 2 and 4 orders of magnitude more restrictive than those imposed Lang et al. [11] for $n = 1$ and $n = 2$ respectively.

5. Extensive air showers development

One of the key interactions which governs the EAS development is the neutral pion decay, $\pi^0 \rightarrow \gamma + \gamma$, because it connects the hadronic and electromagnetic components of the shower. If LIV is considered in the pion sector, the kinematics of the pion decay are affected and thus the shower development.

Considering the total energy of the pion, $s_i^2 = E_\pi^2 - p_\pi^2 = m_\pi^2 + \sum \delta_\pi^{(n)} E_\pi^{n+2} = s_f^2$, one can show that for certain values $\delta_\pi < 0$, the decay becomes kinematically forbidden above $E_\pi^{(n)} > m_\pi^2 / \delta_{\pi,n}$.

In this work, the changes in the pion decay due to possible LIV were implemented in the CONEX [27] software. In particular, a LIV coefficient of $\delta_\pi = -1/M_{\text{Pl}} \approx -8.2 \times 10^{-29} \text{ eV}^{-1}$ has been considered. About 5000 air-showers were simulated for each mass (hydrogen, helium, nitrogen, iron) and each energy bin in the range from 10^{17} up to 10^{20} eV in logarithmic steps of 0.25. In

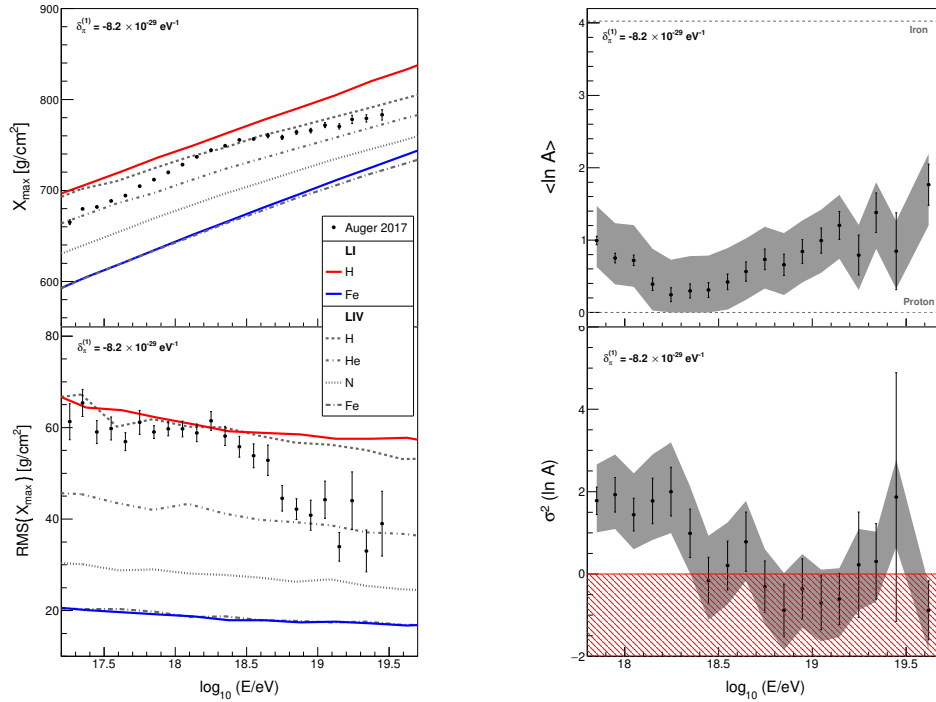


Figure 4: Left panel: First two moments of the X_{\max} distribution. The red and blue continuous lines show the simulated moments for a pure composition of proton and iron, respectively, in a LI scenario. The dashed lines show the simulated moments for a LIV scenario with $\delta_\pi^{(1)} = -8.2 \times 10^{-29} \text{eV}^{-1}$. The black points show data measured by the Pierre Auger Observatory [16]. **Right panel:** First two moments of the $\ln A$ distribution for a LIV scenario with $\delta_\pi^{(1)} = -8.2 \times 10^{-29} \text{eV}^{-1}$. The black dots represent the simulated data and the gray area represents the systematic uncertainties of the Observatory.

Fig. 4, on the left panel, the first and second moments of the X_{\max} distributions for the LI and LIV scenarios are shown. As it can be noted, the $\langle X_{\max} \rangle$ is sensitive to LIV and the composition behaves as if it were lighter in the LIV scenario. On the right panel, the resulting $\langle \ln A \rangle$ and $\sigma^2(\ln A)$ obtained from the first two moments, using the modified hadronic interaction model EPOS-LHC, are shown. It is straightforward to notice that, in presence of LIV, the $\sigma^2(\ln A)$ ends up into the nonphysical region below zero. This behaviour is more pronounced in the LIV scenario with respect to what has been found in the LI case with the same hadronic interaction model [28, 16].

6. Conclusions

This paper tests Lorentz invariance violation using the Pierre Auger Observatory data.

First, an update of our previous work [9] was presented. LIV was considered in the propagation of UHECRs by modifying the photopion production and photodisintegration. The LIV simulations were fitted to updated data of the spectrum and X_{\max} distribution. The data is better described by a scenario with relatively low maximum rigidity, reducing the potentiality of the measurements to reveal LIV effects, which are suppressed by the energy.

In the second scenario, the procedure proposed in Ref. [11] is followed for GZK photons. Considering a scenario in which the UHECR spectrum is described by a model with high rigidity

at the sources, limits of the order of $\delta_\gamma^{(1)} \gtrsim -10^{-40} \text{ eV}^{-1}$ and $\delta_\gamma^{(2)} \gtrsim -10^{-60} \text{ eV}^{-2}$ are imposed. These limits are 2 and 4 orders of magnitude more restrictive than the most updated ones using the same technique [11] for $n = 1$ and $n = 2$, respectively.

Finally, we discuss the possibility of using extensive air shower to test LIV. The pion decay is changed and promising preliminary results show that its effects on the X_{max} distribution can be used in the future to impose limits on LIV.

Acknowledgements

We acknowledge the support from Fundação de Amparo à Pesquisa do Estado de São Paulo (FAPESP) through grants 2015/15897-1, 2016/24943-0 and 2019/01653-4. We also acknowledge the National Laboratory for Scientific Computing (LNCC/MCTI, Brazil) for providing HPC resources of the SDumont supercomputer, which have contributed to the research results reported within this paper (sdumont.lncc.br).

References

- [1] D. Mattingly, Living Rev. Rel. **8**, 5 (2005) doi:10.12942/lrr-2005-5 [gr-qc/0502097].
- [2] V. Vasileiou *et al.*, Phys. Rev. D **87**, 122001 (2013) [arXiv:1305.3463].
- [3] J. Ellis *et al.*, Phys. Rev. D **99**, 083009 (2019) [arXiv:1807.00189].
- [4] H. Abdalla and M. Böttcher, Astrophys. J. **865**, 159 (2018) [arXiv:1809.00477].
- [5] J. Biteau and D.A. Williams, Astrophys. J. **812**, 60 (2015) [arXiv:1502.04166].
- [6] G. Cologna *et al.* [H.E.S.S. and FACT Collaborations], AIP Conf. Proc. **1792**, 050019 (2017) [arXiv:1611.03983].
- [7] R.G. Lang *et al.*, Phys. Rev. D **99**, 043015 (2019) [arXiv:1810.13215].
- [8] D. Boncioli *et al.*, PoS ICRC **2015**, 521 (2016) [arXiv:1509.01046].
- [9] D. Boncioli [Pierre Auger Collaboration], PoS ICRC **2017**, 561 (2018).
- [10] M. Galaverni and G. Sigl, Phys. Rev. Lett. **100**, 021102 (2008) [arXiv:0708.1737].
- [11] R. Guedes Lang *et al.*, Astrophys. J. **853**, 23 (2018) [arXiv:1701.04865].
- [12] S. Liberati and L. Maccione, Ann. Rev. Nucl. Part. Sci. **59**, 245 (2009) [arXiv:0906.0681].
- [13] A. Aab *et al.* [Pierre Auger Collaboration], JCAP **1508**, 049 (2015) [arXiv:1503.07786].
- [14] A. Aab *et al.* [Pierre Auger Collaboration], Science **357**, no. 6537, 1266 (2017) [arXiv:1709.07321].
- [15] F. Fenu [Pierre Auger Collaboration], PoS ICRC **2017**, 486 (2018).
- [16] J. Bellido [Pierre Auger Collaboration], PoS ICRC **2017**, 506 (2018).
- [17] A. Aab *et al.* [Pierre Auger Collaboration], JCAP **1704**, 009 (2017) [arXiv:1612.01517].
- [18] S.R. Coleman and S.L. Glashow, Phys. Rev. D **59**, 116008 (1999) [hep-ph/9812418].
- [19] R.G. Lang, Master Thesis, University of São Paulo, Brazil (2017).
- [20] R. Aloisio *et al.*, JCAP **1711**, 009 (2017) [arXiv:1705.03729].
- [21] A. Aab *et al.* [Pierre Auger Collaboration], JCAP **1704**, 038 (2017), Erratum: [JCAP **1803**, E02 (2018)] [arXiv:1612.07155].
- [22] T. Pierog *et al.*, Phys. Rev. C **92**, 034906 (2015) [arXiv:1306.0121].
- [23] I. Valino [Pierre Auger Collaboration], PoS ICRC **2015**, 271 (2016).
- [24] A. Porcelli [Pierre Auger Collaboration], PoS ICRC **2015**, 420 (2016).
- [25] A. De Angelis *et al.*, Mon. Not. Roy. Astron. Soc. **432**, 3245 (2013) [arXiv:1302.6460].
- [26] R. Alves Batista *et al.*, JCAP **1605**, 038 (2016) [arXiv:1603.07142].
- [27] T. Bergmann *et al.*, Astropart. Phys. **26**, 420 (2007) [astro-ph/0606564].
- [28] P. Abreu *et al.* [Pierre Auger Collaboration], JCAP **02**, 026 (2013).



ELVES reconstruction and characterization at the Pierre Auger Observatory

Roberto Mussa^{*a} for the Pierre Auger Collaboration^{b†}

^a*Istituto Nazionale di Fisica Nucleare, Sezione di Torino, Italy*

^b*Observatorio Pierre Auger, Av. San Martín Norte 304, 5613 Malargüe, Argentina*

E-mail: auger_spokespersons@fnal.gov

Full author list: http://www.auger.org/archive/authors_icrc_2019.html

Since 2013, the four sites of the Fluorescence Detector (FD) of the Pierre Auger Observatory have been recording transient luminous events called ELVES with a dedicated trigger. These light emissions are correlated to distant lightning strikes. The length of recorded traces has been increased from 100 μs (2013) to 300 μs (2014-16) and 900 μs (2017-present), to calculate better the total energy of the UV light emitted at the base of the ionosphere and its angular distribution above the lightning strike. The reconstruction of the time evolution of the light front allows an accurate determination of the lightning bolt location, within a few kilometers, as confirmed by the comparison with ground-based lightning detection networks. The time resolution of the FD applied to the observation of ELVES is a novel approach to probe fundamental physics in thunderstorms such as their charge distribution and lightning initiation processes. Argentina has been flagged as one of the most active regions on Earth for the most extreme lightning strikes, which highlight the serendipitous opportunity the Auger Observatory is offering to the geophysics community.

36th International Cosmic Ray Conference — ICRC2019

24 July – 1 August, 2019

Madison, Wisconsin, USA

^{*}Speaker.

[†]For collaboration list see PoS(ICRC2019)1177

1. Introduction

Besides its main activity, the study of the ultra-high-energy cosmic rays, the Pierre Auger Observatory has started a program of cosmo-geophysics studies, which exploits some of the unique features of its detectors. Since 2013, during the hours of operation of the Fluorescence Detector (FD), a dedicated data stream is devoted to the study of ELVES. This phenomenon, predicted in the early 1990s [1] and discovered one year later [2], are transient luminous events occurring at an altitude of about 90 km when an intense electromagnetic pulse (EMP) emitted during the development of lightning reaches the base of the ionosphere. For an observer at the ground, with a camera capable to record images at the speed of more than one million frames per second, ELVES appear as rapidly expanding rings, starting from a point at mid-distance between source and observer, progressively increasing in brightness as the front drifts towards the horizon, to form a projected *smile* into the camera. With longer integration time (e.g. more than 5 ms per frame) the ELVES will appear like a flat ring in the sky, approximately centered above the vertical of the lightning. The 24 FD telescopes of the Auger Observatory [3], each with an 11 m² mirror, 440 PMTs with high photon sensitivity in the close UV band ($\lambda=300$ to 420 nm), and a time resolution of 100 ns, are ideally suited for such type of observations. These studies have required a series of modifications to the online selection of the events, based on a three-stage trigger described in the next section.

2. Triggering ELVES with the Auger FD

The first level trigger operates at the pixel level with an adjustable threshold that keeps the PMT trigger rate constant at 100 Hz. The second level trigger (SLT) searches for track segments made of at least five adjacent pixels which passed the first level trigger. The third level trigger (TLT) was originally designed to efficiently veto events due to close lightning, featuring a high multiplicity of triggered pixels randomly distributed in time across the camera within a 100 μ s time window.

After the serendipitous discovery of ELVES in our early data sets [4], the upgrade of the multiplicity-based TLT prevented the further recording of ELVES candidates in the standard data stream. A four-year long study of prescaled SLT events, which yielded 58 new ELVES candidates [5], facilitated the design of a TLT algorithm which was able to both reject close lightning and accept the ELVES events, when the direct flash from the causative lightning is below the horizon. The new TLT is performing a check on the angular evolution of the light front around the first triggered pixel. The pixels in the rows and the columns adjacent to the first triggered pixel are checked; their pulse peak time is required to grow continuously with the distance from the first pixel. To account for statistical fluctuations, 20% of the time increments between two triggered adjacent pixels are allowed to show the wrong slope. As ELVES candidates release a large amount of light in comparison to cosmic rays, the trigger also requires at least one pixel with a pulse amplitude larger than 50 ADC counts.

3. ELVES data taken from 2013 to 2016

The ELVES trigger was at first implemented in March 2013 at the FD site of Los Leones, and then extended to all FD sites during the following FD shift. During the first year of commissioning,

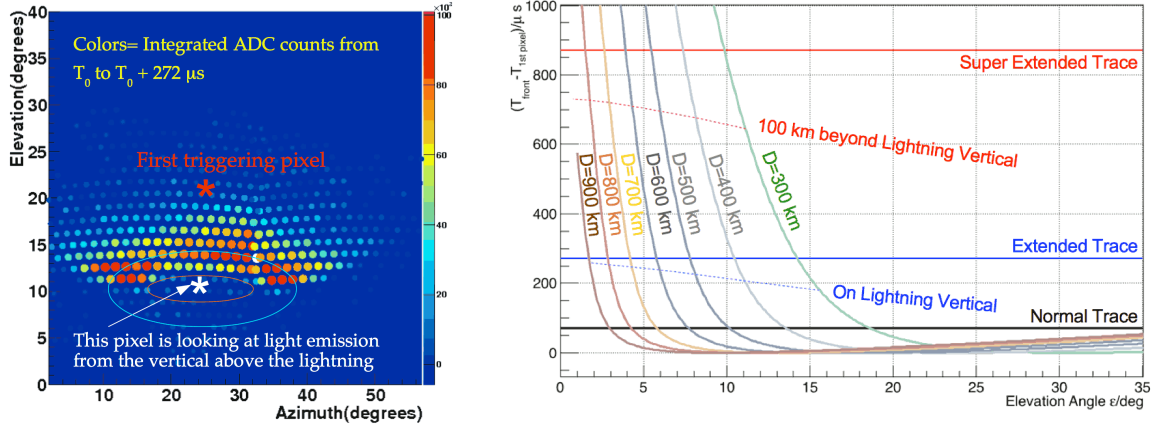


Figure 1: Light distribution after $272 \mu\text{s}$ (left); time evolution of the light front in the central column (right) for ELVES caused by lightning at distances from 300 to 900 km (green to brown curves); the solid horizontal lines show the trace length in 2013 (black), 2014-16 (blue), 2017-present (red). The dashed oblique lines show when the light front reaches the vertical above the lightning and the region of maximum intensity, about 100 km beyond the vertical.

we learned that the standard FD traces (which are $100 \mu\text{s}$ long) did not allow us to see the light emitted from the region of the ionosphere located vertically above the lightning source. Therefore, the FD readout scheme was modified in order to acquire three consecutive frames for the ELVES triggers (Extended Readout). This change enables the study of the angular distribution of light emission above the lightning, which contains information on the dynamics of this process. It must be stressed that the time width of the large EMP generating the ELVES is of the order of 10^{-5} s , four to five orders of magnitude shorter than the full development of the lightning bolt, and two orders of magnitude shorter than the time needed for the light wave to propagate across the base of the ionosphere. In addition, the size of the central gap is related to the electrons' speed in the return stroke of the lightning [6].

The 2014-2016 ELVES dataset was taken with a maximum trace length of $300 \mu\text{s}$. A typical example of an event taken with the extended readout is shown in Fig.1, where the distribution of light, integrated over the first $272 \mu\text{s}$ after a $28 \mu\text{s}$ buffer used for pedestal calculation, is shown. The vertical above the lightning is represented by a white star; the red star indicates the first triggered pixel, while the red ellipse indicates the region where the light emission dies down. Modelling the EMP emission from the lightning source as an ideal vertical dipole, we expect an azimuthal symmetry of the light emission around the vertical above the lightning. Partial reconstruction of the amount of light emitted by a fraction of the region of peak intensity would allow an estimate of the total light emission in the UV band. During the three-year period, we collected about $2.3 \cdot 10^3$ ELVES candidate triggers: 80% are mono (i.e. seen from only one FD site), 17% are stereo (simultaneously seen from two sites), and 2.2% are triplet (seen from three sites). Further quality checks were used to increase the purity of the sample.

The multiple eye capability of the Observatory has been exploited to have a first estimate of the trigger efficiency of each FD. After correcting for on-time of operation [7] of each site, and accounting for the geographically not uniform distribution of lightning strikes in the field of view,

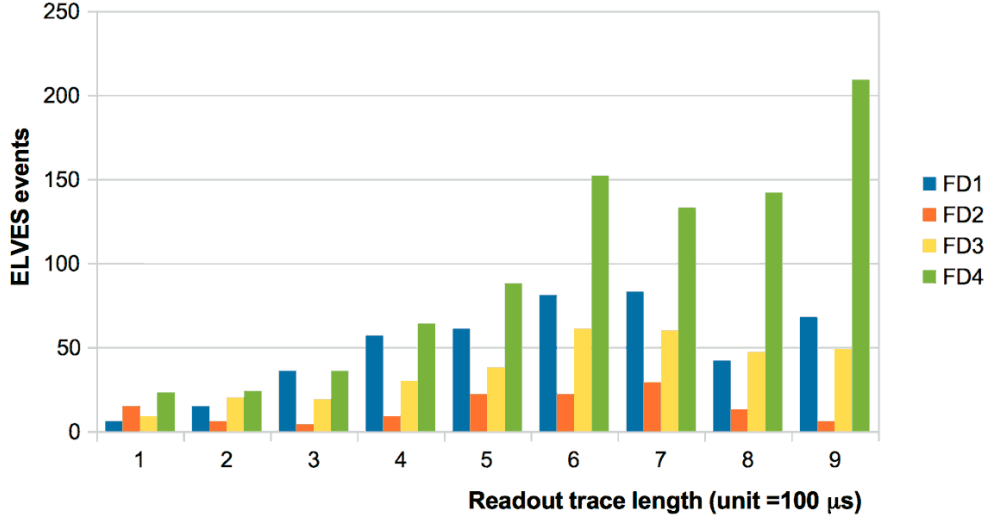


Figure 2: Distribution of the trace lengths for ELVES triggers for each FD site, in units of $100 \mu\text{s}$, for the period 2017-2018. The FD4 site (Coihueco) sees more ELVES because the majority of thunderstorms occur in its field of view.

we could estimate a single FD efficiency $\varepsilon_{FD} = 35 \pm 8\%$.

The study of the ELVES events taken in the period 2014-2016 has shown that a more complex variety of emission patterns has to be considered. The estimate of the total UV emission, to be compared with the energy of the original EMP pulse, requires the measurement of the intensity of light through the full region of maximum emission, outlined by the cyan ellipse on the left panel of Fig.1. In order to explore the light emission from angular regions at lower elevation angles, it was necessary to largely increase the integration time. In the right panel of Fig.1, the difference between the time of arrival of the light front on the central column of the ELVES and the time of the first triggered pixel, is shown, as a function of the pixel elevation, for ELVES produced by lightning at distances from 300 to 900 km.

Since January 2017, the ELVES trace length has been extended to a maximum of $900 \mu\text{s}$ (Super Extended Readout scheme) in order to observe the peak intensity region of most events through the whole azimuth range around the lightning generating the ELVES. In Fig.2, the distribution of the size of the traces recorded in the four FD sites from 2017 to 2018 is shown in units of $100 \mu\text{s}$, which is the standard for cosmic ray triggers.

4. Reconstruction of lightning location

The geometrical reconstruction of the light front propagation aims to a precise time and space location of lightning which caused the ELVES, and to a good measurement of the angular distribution of the light emission from the base of the ionosphere, located at an average altitude $H_{EM} = 92$ km. The lightning location algorithm is based on two very simple assumptions: (a) the emission of the EMP at the lightning can be considered point-like in space-time from the FD observer, and (b) the de-excitation time scale of the base of the ionosphere is negligible with respect to the prop-

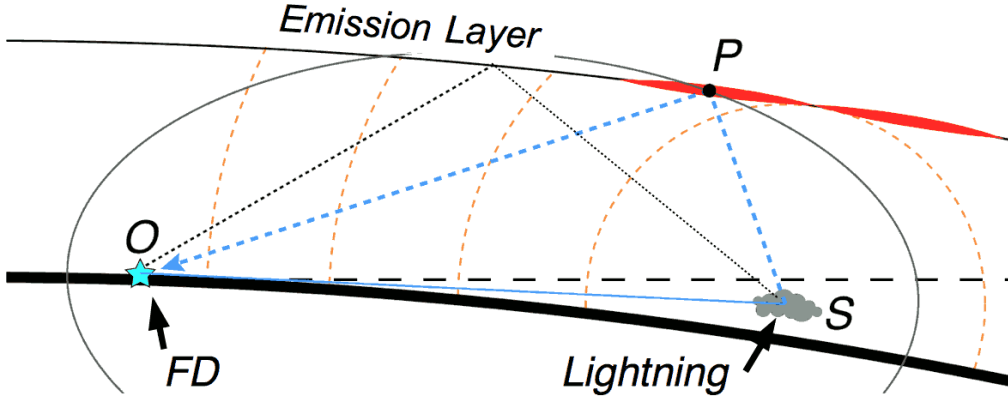


Figure 3: ELVES reconstruction geometry.

agation time. With these two simple assumptions we can conclude that, at any given instant, the emitting surface at the base of the ionosphere can be calculated as the intersection of an ellipsoid, whose focal points are the source S and the observer O , with a sphere whose radius is $R_{earth} + H_{EM}$. The azimuthal expansion of this curve is expected to be symmetric with respect to the vertical, while the front going towards the FD is expected to move faster than that going in the opposite direction.

In the first step of the reconstruction, we fit the ADC trace of each FD pixel to one or more asymmetric gaussians. If less than ten pixels feature a double peak, the reconstruction proceeds with a precise calculation of the time and location of the lightning strike. When ten or more pixels have a double peak, the reconstruction requires a more complex algorithm, which is briefly described in the following sections.

The reconstruction of the lightning location is performed as a two-step process:

1. a set of polynomial fits is performed on the pulse times T_i of each row and column, to obtain a first rough estimate of the lightning longitude and latitude; the results are inputs to the second fit;
2. we perform a second fit to minimize the $\chi^2 = \sum_{i=1}^N (T_i - \Delta T_0 - \overline{OPS}_i/c)^2 / \sigma_{T,i}^2$, where N is the number of pixels contributing to the minimisation, ΔT_0 is the time lag between the emission of the EMP from the source and the observation of the first light at the FD diaphragm, and \overline{OPS}_i is the sum of the distances \overline{SP} (from the source to the emission layer) and \overline{PO} (from the emission layer, assumed to have zero thickness and altitude $H_{EM} = 92$ km, to the FD); the lightning is assumed to be at sea level.

In this way, the location of the lightning source for almost 1600 events is reconstructed. These have then been compared with the lightning recorded by the World Wide Lightning Location Network (WWLLN, [8]) within 1500 km from the centre of the Observatory. We found that $\simeq 70\%$ of our events are correlated with a bolt of lightning detected by the WWLLN within 5 ms.

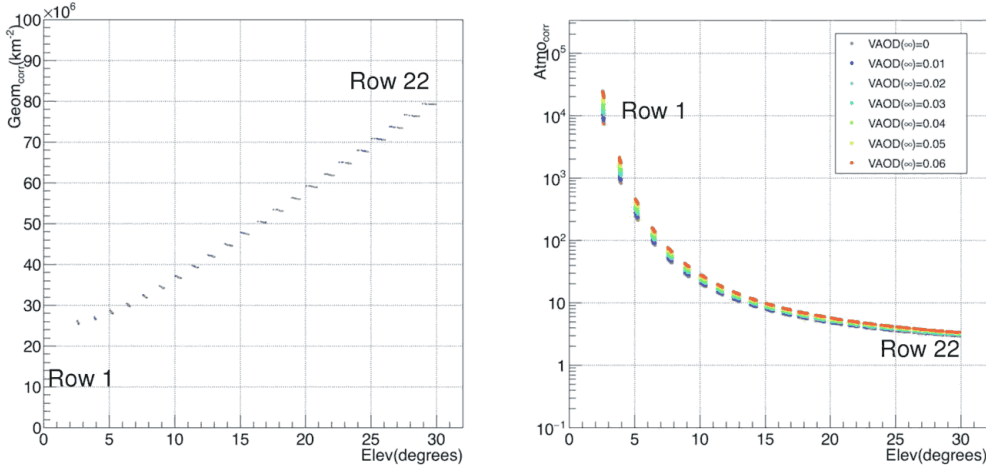


Figure 4: Geometric corrections at the centre of each pixel (left), atmospheric corrections with total VAOD ranging from 0 to 0.06 (right) .

5. Reconstruction of the angular distribution of the light emitted at the base of the ionosphere

After having located the lightning source, in order to calculate the total amount of photons radiated by the ELVES, it is necessary to transform the amount of light observed in each pixel, $P_i(FD)$, to the photon surface density $\Phi_i = P_i(FD) * C_i(geom) * C_i(atmo)$ at the base of ionosphere. The geometric correction

$$C_i(geom) = \overline{OP}^2 / (A_{mirror} A_{EM})$$

accounts for the solid angle subtended by the FD diaphragm, and the size of the emitting surface at the base of the ionosphere A_{EM} , constructed projecting the six vertices of each pixel to an altitude of 92 km.

The atmospheric correction:

$$C_i(atmo) = \exp((VMOD(\infty) + VAOD(\infty)) * AM(\theta_i))$$

accounts for the absorption of light through the atmosphere, using the total vertical optical depths of molecules, $VMOD(\infty)$, and aerosols, $VAOD(\infty)$, through the atmosphere, measured by the instruments on site [9]. The airmass $AM(\theta)$ is calculated using the formula in ref.[10].

The corrections (shown in Fig.4 for the center of each pixel) are strongly dependent on the row number and weakly dependent on the column number. After applying these corrections, in the rare case of a perfectly vertical current source, the total amount of light emitted from the base of the ionosphere can be easily extrapolated. Further work is needed to model tilted dipoles or more complex emission patterns.

6. Classification of Multiple ELVES

About one fifth of the ELVES identified at the Auger Observatory are composed of more than one distinct flash of light. When more than ten pixels show more than one pulse in the traces, the

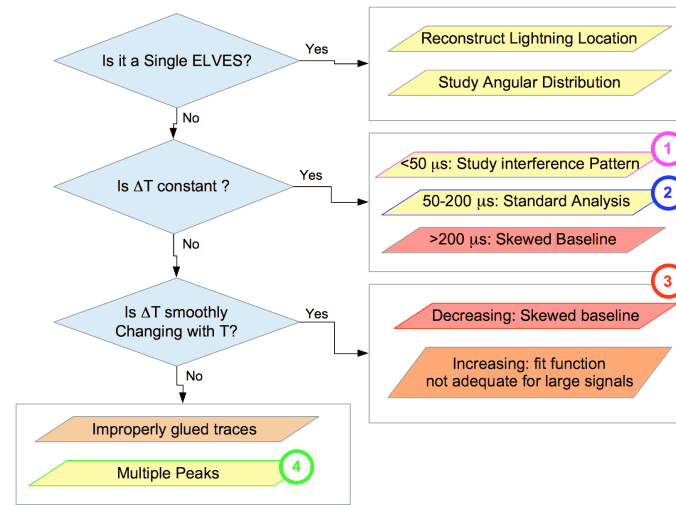


Figure 5: Flowchart of ELVES analysis chains.

ELVES is labeled as *multiple* and a different type of analysis (summarised in Fig.5) is performed. The first step consists in plotting the time difference between any two pulses, as shown in Fig.6, where one event for each of the four categories found by the current analysis is depicted.

The first two categories are characterized by a constant ΔT : when it is very short ($<50 \mu\text{s}$) it may be explained as the interference pattern produced by the EMP emitted by an intracloud lightning when a fraction of the pulse is bouncing off the ground. If the gap is larger than $50 \mu\text{s}$, the events are likely to be related to the initial breakdown stages of the lightning, or to a more complex profile of the return stroke. The third category consists of events with a ΔT linearly decreasing with pulse time, which appear as single ELVES overlapped to another class of light transient, maybe a halo [11], with a much longer risetime. The fourth group, showing abruptly changing ΔT , is related to ELVES with more than two peaks. This pattern has been proposed as a possible signature of production of terrestrial gamma-ray flashes [12]. A simple linear fit of ΔT vs the time T of the first peak allows differentiating these four categories, as shown in the right part of Fig.6. The first three categories account for 80% (respectively 11%, 57%, 22%) of the total number of events. The remaining events, with a large positive slope, are very likely to be triple or quadruple ELVES and deserve further analysis.

7. Conclusions and future prospects

Since 2013, the Auger Observatory has been taking data with a special trigger devoted to the study of ELVES. The time resolution of our FD gives us unique opportunities for the study of these phenomena. We changed the length of the trace readout in two steps: (a) since 2014, we sampled $300 \mu\text{s}$ in order to see the light emission from the vertical of the causative lightning; (b) since 2017, we read up to $900 \mu\text{s}$, to study the angular distribution of the entire region of maximum emission around the lightning.

In most cases, we have learned that simple models are not able to describe the rich variety of ELVES events, and larger statistics are required to fully understand the variety of features shown

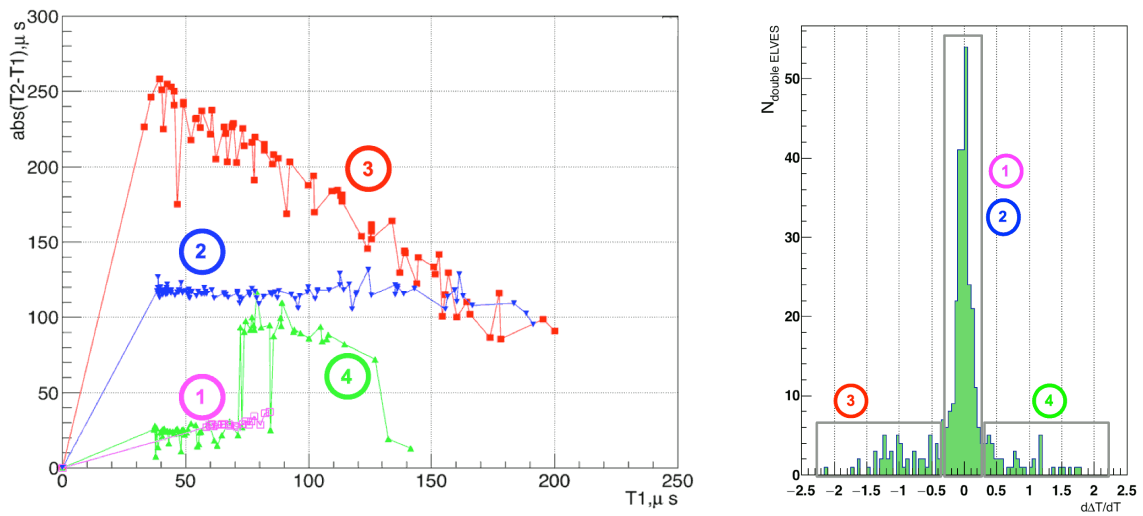


Figure 6: Time difference between two pulses vs time of the first pulse in multiple ELVES (left). Distribution of the slopes of the time between the first and the second pulse in multiple ELVES (right): the numbers indicate the categories shown in the left plot and described in the text.

by such interesting phenomena.

For future analyses, we envisage further upgrades of the TLT selection criteria to increase the selection efficiency. We are also planning to enhance our lightning detection network to gain more insights on the mechanisms leading to the production of multiple ELVES.

References

- [1] U. S. Inan, T. F. Bell, J. V. Rodriguez, *Geophys. Res. Lett.* **18**, (1991) 705
- [2] W. L. Boeck *et al.*, *Geophys. Res. Lett.* **19**, (1992) 99
- [3] J. Abraham *et al.* [Pierre Auger Collaboration], *Nucl. Instrum. Meth. A* **620** (2010) 227.
- [4] R. Mussa *et al.* [Pierre Auger Collaboration], *Eur. Phys. J. Plus* **127** (2012) 94.
- [5] A. Aab *et al.* [Pierre Auger Collaboration], arXiv:1307.5059 [astro-ph.HE].
- [6] P. R. Blaes *et al.*, *Geophys. Res. Lett.* **41** (2014) 9182.
- [7] P. Abreu *et al.* [Pierre Auger Collaboration], *Astropart. Phys.* **34** (2011) 368.
- [8] <http://wwlln.net>.
- [9] J. Abraham *et al.* [Pierre Auger Collaboration], *Astropart. Phys.* **33** (2010) 108.
- [10] F. Kasten and A. T. Young, *Applied Optics* **28** (1989) 4735.
- [11] C.P. Barrington-Leigh *et al.*, *J. Geophys. Res.* **106** (2001) 1141.
- [12] N. Liu *et al.*, *J. Geophys. Res.* **122** (2017) 10563.



Analysis of Data from the Low-energy Modes of the Surface Detector of the Pierre Auger Observatory

Martin Schimassek^{*a} for the Pierre Auger Collaboration^{†b}

^a*Karlsruhe Institute of Technology (KIT), ETP, Germany*

^b*Observatorio Pierre Auger, Av. San Martín Norte 304, 5613 Malargüe, Argentina*

E-mail: auger_spokespersons@fnal.gov

Full author list: http://www.auger.org/archive/authors_icrc_2019.html

The Pierre Auger Observatory is the largest cosmic-ray observatory in existence and covers an area of about 3000 km² with its 1660 surface detectors. Each of these detector stations records signals of relativistic particles in 12 tonnes of ultra-pure water, measured with three 9-inch photomultipliers. With a collecting area of about 10 m², each surface detector station is sensitive to single particles down to MeV energies. Such particles are recorded in counters and histograms for each detector that are transmitted to the central data acquisition system at regular time intervals. The background flux of particles is measured with very high statistics by combining all surface detector stations and therefore enables investigations of the source of variations in this flux. We present an updated analysis of the particle-counter data and highlight the long-term stability of the corrected rates. With these corrected rates, we present the frequency spectrum of the observed variations and highlight the expected solar contributions, show an in-depth analysis of the diurnal variation, and update the observation of the eleven-year solar-cycle from 2006 until the end of 2018.

36th International Cosmic Ray Conference — ICRC2019

24 July – 1 August, 2019

Madison, Wisconsin, USA

^{*}Speaker.

[†]for collaboration list see PoS(ICRC2019)1177

1. Introduction

The rate of cosmic rays measured at the top of Earth's atmosphere is modulated by changes in the interplanetary medium. Solar activity and transient events modify the magnetic deflections of high-energy particles and thus change the cosmic-ray intensity at Earth.

The standard detectors for measuring this intensity are neutron monitors, that measure the hadronic component of the particle cascades formed in Earth's atmosphere. However, also different detector systems are able to track the evolution of the cosmic-ray intensity, for example muon telescopes and particle counters from high-energy experiments.

The Pierre Auger Observatory [1] is designed to measure the highest energy cosmic rays. It is located in Malargüe, Argentina (69.3°W, 35.3°S, 1400 m a.s.l.) and covers 3000 km² with its surface detector (SD). The surface detector is built as a triangular grid with 1500 m spacing of 1660 water-Cherenkov detector stations. Each of these detector stations is constantly measuring the rate of particles for stability monitoring and calibration [1, 2].

This data has been previously employed in studies of solar transient events like Forbush decreases [2, 3, 4], searches for indications of gamma-ray bursts [5], and identification of modulations related to the solar cycle [6].

In detail, the rate of particles in the SD stations is measured using a counting trigger, the so-called scaler mode, with a very low current threshold range of $3 < I_{\text{peak}} < 21$ ADC channels above baseline [2]. A coincidence of all 3 PMTs of the station is required. This counter is sensitive to a deposition of energy in the range $15 \text{ MeV} \lesssim E_d \lesssim 100 \text{ MeV}$ [3] and results in an average count rate of $\sim 1.8 \times 10^8$ counts per minute, where the rate is reported every second via a radio transmission. These energy depositions arise from showers initiated by primary cosmic-rays with energies from 10 GeV to a few TeV [3]. A different source of data are pulse-height and pulse-charge histograms collected for calibration purposes, and are available together with the high-energy cosmic ray events. These can also be used to study the background intensity of particles [6].

In this work, we focus on the scaler data and present an updated analysis of the existing data set. In Section 2 we present the detection of lightning strikes using the scaler mode. The updated data treatment is discussed in Section 3. In the following Sections we present a first spectral analysis of the corrected scaler data, a detailed analysis of the diurnal modulation, as well as updated analyses on the modulations during Forbush decreases and during the solar cycle, with data covering 13 years.

2. Lightning Events

Since the implemented threshold is low, the scaler rate is sensitive to the electromagnetic pulse associated with lightning strikes. Identifying seconds with lightning strikes is thus important for background rejection in analyses of the scaler rate. In addition, other analyses, carried out with the Auger SD, can profit from the identification power for these events.

The general concept for identifying seconds with lightning strikes is similar to the search of rate increase correlated with gamma-ray bursts [5]. By comparing the scaler rate measured in the test second $\Gamma(t_i)$ with the mean rate recorded in a five minute interval $\langle \Gamma \rangle$, significant excesses are selected. In this analysis we take the median of 300-second intervals as a robust estimate of the

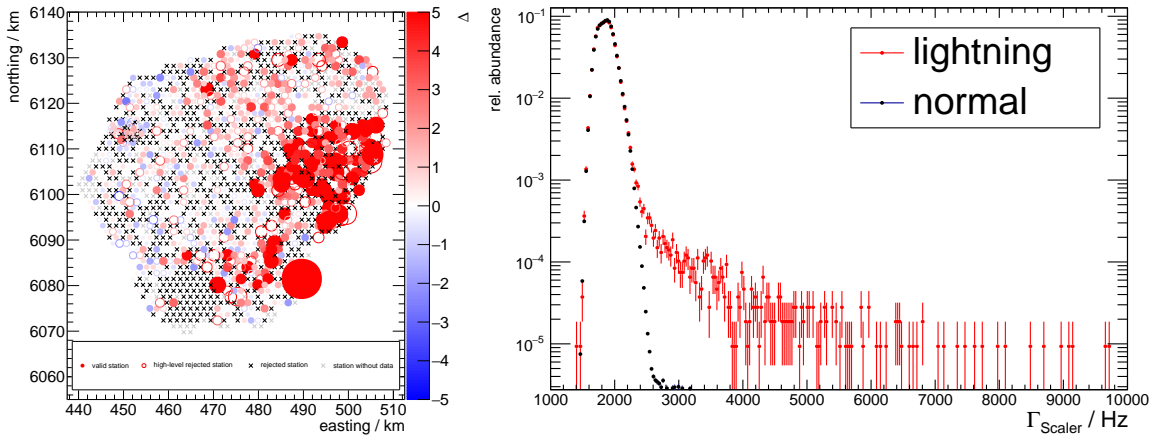


Figure 1: *Left:* Visualization of a lightning-strike event. The color and sizes of the markers represent the deviation of the measured scaler rate from the median rate within a 5-min interval. See text for more details. *Right:* Distribution of measured scaler rates during seconds including lightning strikes (red) and during normal conditions (black).

mean rate $\langle \Gamma \rangle$, and estimate the current standard deviation $\hat{\sigma}$ with the median absolute deviation under a Gaussian assumption. These quantities are defined for each available SD station separately.

We use a Gaussian background model with a common additional signal s to estimate the significance of excesses. With the rates of all stations $\vec{\Gamma}$, their respective median rates $\langle \vec{\Gamma} \rangle$, and the estimated standard deviations $\vec{\hat{\sigma}}$, the likelihood of an additional excess signal is

$$\mathcal{L}(\vec{\Gamma} | \langle \vec{\Gamma} \rangle, \vec{\hat{\sigma}}, s) = \prod_i \frac{1}{\sqrt{2\pi}\sigma_i} \exp \left[- \left(\frac{\Gamma_i - \langle \Gamma \rangle_i - s}{\sqrt{2}\sigma_i} \right)^2 \right]. \quad (2.1)$$

After maximising with respect to s , Wilk's theorem is used to estimate its significance. We discriminate lightning seconds from other increases using the fit-quality of selected significant excess seconds. When the excess is originating from a lightning strike, the SD stations with a high signal are few and localised so that the quantity

$$\chi^2 = \sum_i \frac{(\Gamma_i - \langle \Gamma \rangle_i - \hat{s})^2}{\sigma_i^2 + \hat{s}} \quad (2.2)$$

where \hat{s} is the estimated common signal, is very large due to the rest of the SD array showing no excess. Seconds with lightning strikes can be identified by using the Gaussian transformation of the goodness-of-fit χ^2 with the criterion $(\chi^2 - N_{\text{DoF}}) / \sqrt{2N_{\text{DoF}}} \gtrsim 100$.

For a lightning-strike event the pull $\Delta = (\Gamma - \langle \Gamma \rangle) / \hat{\sigma}$ of each station is visualised in the left panel of Fig. 1. A localised excess is clearly visible in the eastern part of the SD. Stations that are not used in the analysis of the scaler data are drawn with crosses and the criteria for their selection is described in the next Section.

By stacking all identified seconds with lightning strikes during the single day 24 January 2016, as well as the “quiet” seconds, the difference in the distribution of the scaler counts during lightning strikes is made visible. In the right panel of Fig. 1, histograms for this example day are shown. A clear deviation from the Gaussian distribution during lightning periods is visible. The seconds

identified as affected by lightning strikes are not used in the analyses presented in the following Sections.

3. Data Treatment

We have shown in previous work [2, 6] that the scaler data has to be handled carefully due to the low threshold employed. Additionally, for its interpretation over longer time scales ($\gtrsim 5$ minutes), corrections have to be applied [4, 6].

Here we present an update of the data treatment presented in [6]. This update is based on a change of a paradigm: To recover more data, all selections and corrections are performed on the single-station level. To ensure good data quality, the PMT-status information from the analysis of air-shower traces [7] is used to select stations with three well working PMTs. This selection replaces also cuts based purely on the extrema of the scaler-rate distribution.

Similarly to the previous analyses, the atmospheric overburden altering the rate of measurable particles, is then corrected by the means of a linear fit of the pressure dependency. Under the assumption that the count rate scales with the pressure difference $\Delta P = P - \langle P \rangle$, we use the fit function

$$\Gamma = (1 + \alpha_p \Delta P) \Gamma_0 \quad (3.1)$$

with now station-specific constants α_p and Γ_0 . The final pressure correction is then in a form of a scaling factor $\gamma_p(t) = 1 - \alpha_p \Delta P$ available for each SD station.

As we have shown in [6], the changes in the optical properties of the water-Cherenkov detectors influence the detection threshold of low-energy particles over longer time periods of several years [8]. To measure these optical properties of an SD station we use the so-called ‘‘area-over-peak’’ quantity: the measured charge of a muon-produced pulse, divided by its height. This quantity is computed for each PMT of an SD station and the average per station is used for this correction. We use it to calculate a time-dependent correction factor $\gamma_{AoP}(t)$ for each station, similar to the procedure in [6].

Using both corrections, the corrected scaler rate $\hat{\Gamma}$ of station i is calculated as

$$\hat{\Gamma}_i(t) = \Gamma_i(t) \gamma_p(t) \gamma_{AoP}(t). \quad (3.2)$$

To account for differences in the SD stations, as for example different altitudes, we will use in the following a relative quantity based on the scaled count rates of the stations. For each station a reference rate $\Gamma_0^{(i)}$ is calculated as its mean rate during the year 2013. We then use the average of these rescaled rates

$$r_{\text{scaler}}(t) = \frac{1}{n} \sum_i \hat{\Gamma}_i(t) / \Gamma_0^{(i)} \quad (3.3)$$

averaged over five-minute intervals as basic scaler data quantity.

4. Observed Frequency Spectrum

As pointed out in the introduction, the intensity of cosmic-rays with energies lower than 100 GeV measured at Earth is modulated by solar effects. In this analysis we want to discuss the periodic parts of this modulation as observed in the Auger scaler rate.

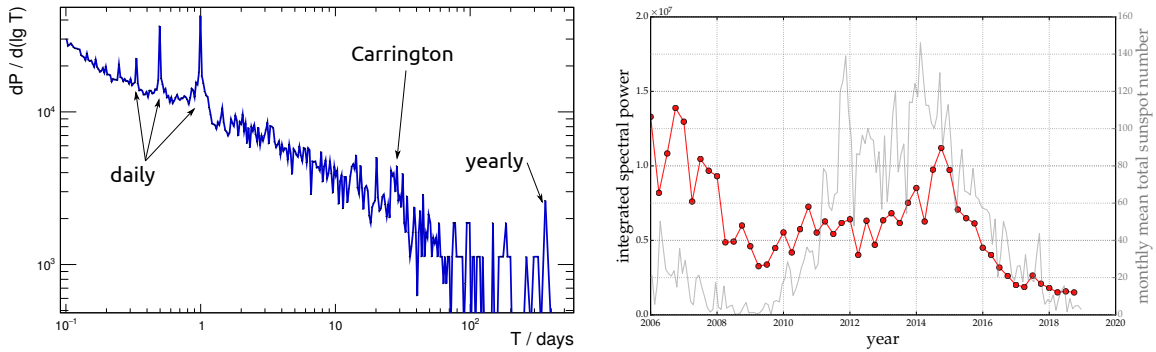


Figure 2: *Left:* Observed frequency spectrum over the full data period from 2006 to 2018. *Right:* Time dependence of the integrated spectral power around the Carrington frequency $T \in [20, 70]$ days including overtones. For reference, the solar sunspot-number data from [9] is shown in gray.

The left panel of Fig. 2 shows the discrete Fourier-series expansion of the observed scalar rates in logarithmic scale. The sharpest peaks in the spectral power are visible for a signal with a frequency of one solar day and the corresponding overtones. This diurnal signal is due to the Earth’s rotation in the magnetized solar wind and has been observed with Auger before [4]. A more detailed analysis of this signal is presented in the next section.

Another expected periodicity of the cosmic-ray intensity is associated with the rotation of the Sun and corresponding magnetic features. Therefore, an enhancement in the spectrum at frequencies corresponding to the Carrington period is expected. On the logarithmic scale of Fig. 2 this is not clearly visible. However, small enhancements at the indicated range are visible and the frequency spectrum is not expected to show a clear peak at the Carrington frequency, because of the different frequencies of individual transient events contributing.

Because the rate of magnetic features of the Sun correlates with the solar cycle, a time dependence of the spectral power of these frequencies is expected. The right panel of Fig. 2 shows the integrated spectral-power for Fourier modes with periods between 20 and 70 days. For reference, the number of sunspots is shown during the same period as well. The minima and the solar maximum in sunspot number also appear as minima and a maximum of the spectral power. But, as expected from the presence of non-periodic solar events like Forbush decreases, there is no one-to-one correlation of the spectral power with the sunspot number.

In the long-period domain an enhancement of the Fourier modes with a period of 365 days is visible, corresponding to the movement of the Earth around the Sun. The 11-year solar cycle cannot be resolved with this Fourier analysis and the length of the data set of only 13 years. A time correlation based approach for this observation is presented in the last Section of this work.

5. Diurnal Signal

The rotation of the Earth in the magnetized solar wind gives rise to a diurnal change in the measured rate of particles at the ground. Due to the tilt of the Earth’s rotation axis and the location of Auger at about 35° south latitude, as well as the minor changes in distance to the Sun, yearly modulations of this signal are also expected.

The data set of the corrected Auger scalers show these modulations that are not correlated with pressure or temperature very clearly. The left panel of Fig. 3 shows these daily modulations of the measured scaler rates. For each month the Auger scaler rates are averaged in five-minute bins in time of day (UTC) and rescaled with the average scaler rate in this month. This rescaling emphasizes the shape of the diurnal signal, with an amplitude of about 1%, instead of highlighting the long-term variations caused by the 11-year solar-cycle which is measured with an amplitude of about 4%.

From Fig. 3 the seasonal variation of the diurnal signal is clearly visible. The peak position of the signal is shifting by three hours over the course of a year. In January the daily signal peaks at about 14:00 UTC, whereas in austral winter the peak moves to 17:00 UTC.

During the solar maximum in the years from 2012 to 2014 the daily signals are less similar. In this period the regular structure is washed out by a higher rate of transient events and higher variability.

The long-term stability of the daily profiles can be derived from comparing the daily profiles across the 13 years shown in Fig. 3. Apart from resolution effects from the SD still being deployed during 2006, the profiles of 2006 match those measured in 2018.

With the high statistics available at the Auger, the diurnal modulation of on average 1.2% peak-to-peak is resolved every day. This is also the reason for the strong enhancement of the spectral power for frequencies of one per day and its overtones in the Fourier spectrum, shown in the left panel of Fig. 2.

In the right panel of Fig. 3 this ability to resolve the signal is visualized by comparing the average profile of June 2018, drawn in black, with the profiles of two individual days of this month.

The data of the individual days are rescaled with their average rate, to enable the comparison of the shapes themselves. For both chosen days the diurnal variation is clearly visible. However, the amplitudes and details of the signals are distinctively different: the peak-to-peak amplitude for June 1st with 0.7% is smaller than in the average profile, which shows an amplitude of 1.4%. In contrast to June 1st, the peak-to-peak amplitude of June 5th is very similar to the average profile, but this day also shows that with the high statistics of the Auger scaler rate, other features, only present in singular days, are resolved. In this example of June 5th there is an additional rate enhancement at about 8:00 UTC, as well as two additional depressions of the rate at 2:00 and 6:00 UTC.

This comparison highlights the abilities of the Auger scaler rates in resolving structures on hourly scales with high statistics. This is the basis for future analysis of the rates on these scales also during transient events like Forbush decreases.

6. Observation of Forbush Decreases

The time resolution of the Auger scaler rate of up to 1 s can be used to search for transient events. One example of transient solar events are Forbush decreases. After applying the pressure correction the Auger scaler rates are sensitive to Forbush decreases and they have been observed and analysed before [3].

With this updated analysis and corrections, these observations are possible as well and profit from the updated corrections. In the right panel of Fig. 4 an example of a Forbush decrease, as observed with this new Auger scaler data set, is shown. For comparison, data from three different

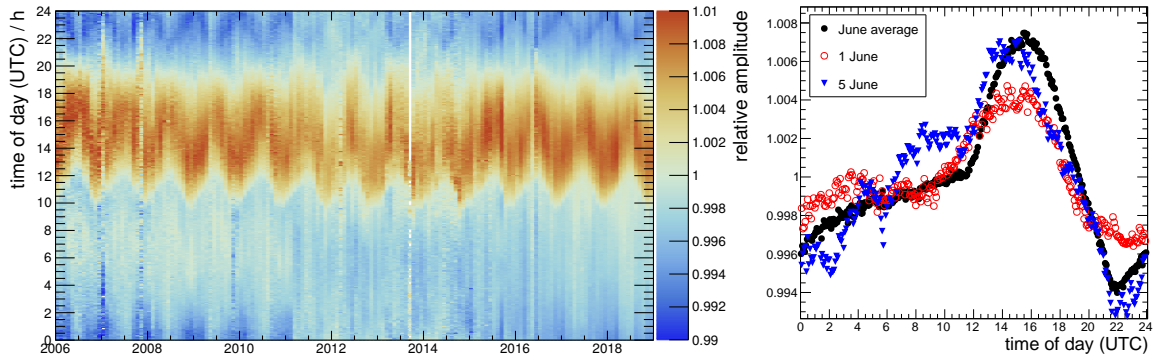


Figure 3: The observed daily pattern of the scaler rate as a function of the time of day (UTC). *Left:* The monthly average values. Each month is normalized separately to emphasize the shape. *Right:* For June 2018: the average daily shape of the observed diurnal pattern together with two single days as examples of the variations in this diurnal pattern.

neutron monitors [10], Athens [12] in the northern hemisphere, McMurdo [13] in the Antarctic, and Tsumeb in Namibia [11] are shown for the same time period. The Forbush decrease during mid of June 2015 is clearly visible in all stations, with the Auger scaler rate showing the smallest relative amplitude due to the high magnetic cut-off.

Besides the Forbush decrease itself, there are more features in the neutron-monitor time-series which can also be observed in the Auger scaler rate. One example is the enhancement in the rates during the end of July 2015.

This shows the potential of the Auger scaler rate to complement neutron-monitor data at high-rigidity cut-off in the southern hemisphere.

7. Long-Term Observations

The Auger scaler rate can be used for long-term measurements of solar modulations of the cosmic-ray intensity as it was shown in previous work [6]. To achieve this long-term stability of the measurements, the corrections, as presented in [6] and their adaptation to a station-based approach in Eq. (3.2), are essential. Here we present an updated version of the 11-year solar-cycle modulation of the cosmic-ray intensity. The left panel of Fig. 4 displays the measured scaler rate from January 2006 until the end of 2018. For comparison, the rate as measured by the Tsumeb neutron monitor [11] is shown during the same time period.

Over the whole period we observe a variation in the average scaler rate of about 4%. With a maximum of +3% relative to Jan 2006 in 2009 and a minimum with -1% in 2015. In June 2018 the amplitude reaches again about +3% relative to Jan 2006 during the current solar minimum. The correlation with the neutron monitor - as well as the match with the expected behaviour from solar sunspot data [9] - showing a recovery of the scaler rate towards the second solar minimum during the operation of Auger, highlight the long-term stability and reliability of the corrected scaler rate.

8. Conclusion and Outlook

We have shown that with the appropriate corrections the Auger Scaler mode is a useful data set

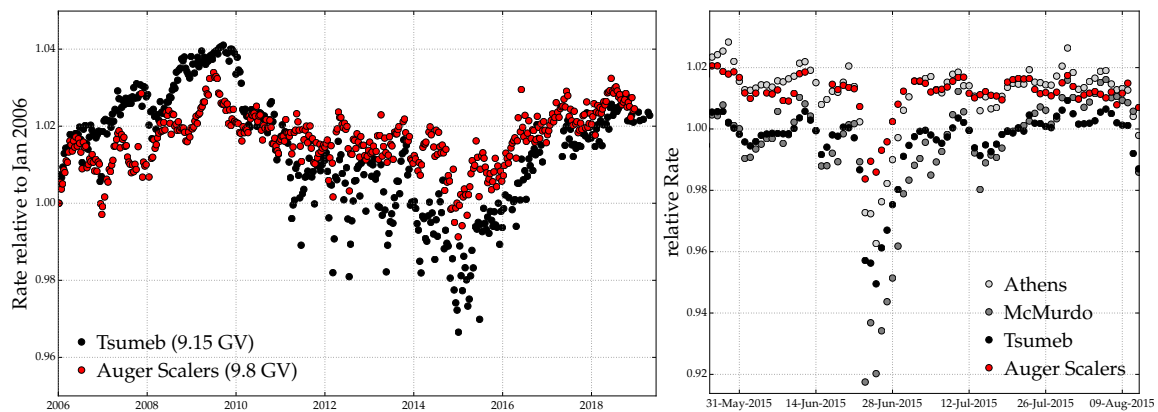


Figure 4: *Left:* Long-term comparison of the measured rates of the Tsumeb [11] neutron monitor with the corrected Auger scaler rate. Data from 2006 until the end of 2018 is shown, averaged in 10 day intervals. *Right:* Comparison of the measured Auger scaler rates during a Forbush decrease with data from the Athens [12], McMurdo [13], and Tsumeb [11] neutron monitors.

to measure modulations of the cosmic-ray intensity at time scales from hours to several years. The good correlation of the long-term measurements with neutron-monitor data highlights the validity of our corrections. An additional proof of the stability of our data and the corrections is the stability of the phase and amplitude of the diurnal variation in the measured rate over the range of 13 years.

In the near future there is also the possibility to extend the set of low-energy data collected with Auger because of the new possibilities introduced with the upgraded detectors [14]. With new electronics [15] and a complementary type of particle detector, new possibilities to measure the total cosmic-ray intensity will be explored.

References

- [1] A. Aab [Pierre Auger Collaboration], Nucl. Instrum. Meth. A, **798** (2015) 172.
- [2] The Pierre Auger collaboration, JINST, **6** (2011) P01003, doi: 10.1088/1748-0221/6/01/P01003.
- [3] S. Dasso, H. Asorey *et al.* [Pierre Auger Collaboration], Adv. Space Res., **49** (2012) 1563–1569, doi: 10.1016/j.asr.2011.12.028.
- [4] H. Asorey [Pierre Auger Collaboration], 31st Int. Cosmic Ray Conf., Łódź, Poland (2009), 41.
- [5] X. Bertou [Pierre Auger Collaboration], ICRC (2007), 1042.
- [6] J.J. Masias-Meza [Pierre Auger Collaboration], PoS(ICRC 2015) 074, arXiv: 1509.03732.
- [7] D. Mockler [Pierre Auger Collaboration], PoS(ICRC2019)353.
- [8] K. Choi [Pierre Auger Collaboration], PoS(ICRC2019)222.
- [9] SILSO World Data Center, International Sunspot Number Monthly Bulletin and online catalogue, 2006–2018.
- [10] The NMDB database (www.nmdb.eu), founded under the European Union’s FP7 programme provided the data.
- [11] TSUMEB Neutron Monitor, North-West University of South Africa. Data accessed via NMDB.eu.
- [12] H. Mavromichalaki *et al.*, Ann. Geophys., **23** (2005) 1–8.
- [13] Data kindly provided by the Univ. of Delaware Dep. of Physics and Astronomy and the Bartol Research Institute.
- [14] A. Aab *et al.* [Pierre Auger Collaboration], arXiv: 1604.03637.
- [15] D. Nitz [Pierre Auger Collaboration], PoS(ICRC2019)370.

6

Detectors and AugerPrime Upgrade





Real-time Measurements with Atmospheric Instruments at the Pierre Auger Observatory

Violet M. Harvey^{*a} for the Pierre Auger Collaboration^{†b}

^a*Department of Physics, University of Adelaide, Adelaide, S.A. 5005, Australia*

^b*Observatorio Pierre Auger, Av. San Martín Norte 304, 5613 Malargüe, Argentina*

E-mail: auger_spokespersons@fnal.gov

Full author list: http://www.auger.org/archive/authors_icrc_2019.html

The state of the atmosphere regarding the air density profile, the vertical distribution of aerosols, and the location of clouds is closely monitored at the Pierre Auger Observatory because the troposphere serves as a giant calorimeter for the air fluorescence technique. We present an overview of the atmospheric monitoring instruments at our disposal, with a focus on their capabilities for real-time measurements and their importance to extensive air shower reconstruction. We detail the improvement of our database of aerosol attenuation measurements that has been extended by two more years to the end of 2017 and fully recalculated with new software that brings a range of enhancements. We also address the importance of using hourly measurements of aerosol distributions for analyses rather than static models of average atmospheric conditions.

36th International Cosmic Ray Conference — ICRC2019

24 July – 1 August, 2019

Madison, Wisconsin, USA

^{*}Speaker.

[†]For collaboration list see PoS(ICRC2019)1177.

1. Introduction

The Pierre Auger Observatory [1], located at approximately 1400 m above sea level (ASL) in the Mendoza province of Argentina, is the world's largest detector of cosmic rays. It operates as a hybrid detector, with a 3000 km² surface detector array (SD) composed of over 1600 water-Cherenkov stations overlooked by a fluorescence detector (FD) composed of 27 telescopes divided among four sites. The FD detects fluorescence light from nitrogen molecules in the atmosphere excited by the passage of the secondary particles produced in an extensive air shower, while the SD detects the secondary particles at ground.

The air fluorescence technique for observing cosmic ray events and reconstructing the primary particle energy, the depth of shower maximum, and the arrival direction is nearly calorimetric because the quantity of isotropically radiated ultraviolet (UV) light is proportional to the total energy deposited. However, it is highly sensitive to the assumptions made in determining the fraction of light scattered out of the shower toward the detector and attenuated on the path to the detector. This necessitates an extensive system of instruments to monitor the properties of the troposphere above the observatory.

The vertical description of pressure, temperature, and humidity (as well as derived state variables such as air density and atmospheric depth) is essential for accurate calculation of the Rayleigh (molecular) attenuation length and the air fluorescence yield. Although molecular scattering is the dominating attenuation effect, we must also consider scattering due to aerosol particles. Vertical aerosol distributions can change significantly from hour to hour, as well as throughout the year.

Clouds may partly obscure the FD view of the shower, causing a break in the shower light profile and an underestimate of the energy, or they may lie directly in the path of the shower development, increasing the fraction of Cherenkov light scattered towards the FD and causing an overestimate of the energy. Thin cloud can also subtly distort the shape of the shower light profile.

2. Instruments and data processing

2.1 Molecular monitoring

From 2002 until the end of 2008, radiosondes were intermittently launched from the observatory to measure important air properties as a function of height and produce vertical profiles [2].

The Global Data Assimilation System (GDAS), provided by the United States National Center for Environmental Prediction, is a freely-available source of 3-hourly molecular state parameters produced by a model combining data from radiosondes, surface observations, radar observations, and satellite observations. In 2011 these vertical profiles replaced local radiosonde data in the event reconstruction for all air showers seen by the Auger Observatory since 2005 [3].

The observatory additionally uses five ground-based weather stations – one at each of the four FD buildings and one at the CLF (see Sec. 2.2) – to monitor the ground-level pressure, temperature, humidity, and wind velocity with a time resolution of 5 min.

2.2 Aerosol monitoring

The Auger Observatory operates two laser facilities within the surface array, both relatively near the centre. The Central Laser Facility (CLF) has been operational since the commissioning

of the first FD site, while the eXtreme Laser Facility was constructed later to benefit the FD sites furthest from the CLF. Each facility houses a UV laser which fires 50 vertical pulses every 15 min. Each pulse has a width of 7 ns and the average pulse energy is 6.5 mJ. Each of the two lasers are observed from each of the four FD sites, creating a bistatic lidar system of eight laser-FD pairs. For each laser-FD pair, the average of the 200 pulses in each hour creates a trace of photons at the detector as a function of height (hourly light profile).

Since 2013 there has also been a monostatic Raman lidar system at the CLF [4], used to make three measurements of the vertical aerosol profile each night: before, during, and after the FD observations. The Raman lidar cannot be operated while the FD is running, but this only interrupts data acquisition for four of the 27 fluorescence telescopes and only for 20 min each night.

In order to calculate vertical aerosol distributions with the bistatic lidar, we normalise our data periodically with “reference” nights, typically one for each year, for which the aerosol attenuation is negligible. To find a reference night we select candidates with hourly light profiles which match closely to profiles simulated under aerosol-free conditions, and cross-reference to other sources such as the Raman lidar to determine the clearest night. The data-normalised method for aerosol analysis at the Auger Observatory [5] uses the reference light profile to cancel out all detector systematics and molecular scattering effects in other light profiles each year, leaving just aerosols to explain any difference in magnitude and shape.

2.3 Cloud monitoring

At each FD site is a monostatic elastic backscatter lidar which automatically scans for cloud outside of the field of view (FOV) of the FD every 15 min [1]. The time delay and magnitude of the returned signal indicates the distance and density of scattering centres. In Fig. 1a an overhead FD lidar scan indicates a localised cloud base height (CBH) of 4 km above ground level. During event reconstruction, the minimum CBH and the overhead cloud coverage (0 % to 100 %) are considered.

The bistatic lidar system described above, though primarily intended for aerosol monitoring, will detect cloud when it lies either directly over the lasers or along a path between the lasers and an FD site. In the first case this provides a measurement of the CBH over the surface array, and in the second case an upper limit which we can still use. The overall CBH for an hour is taken as the lowest seen by any laser-FD pair in any 15 min block of laser shots.

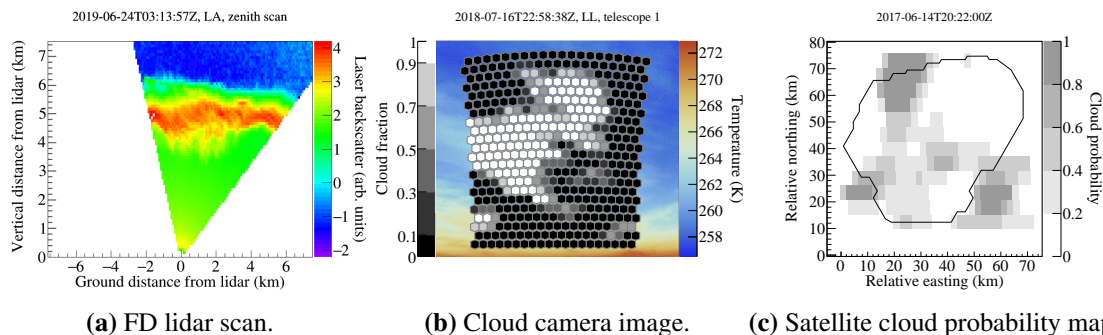


Figure 1: Examples of real data from an FD lidar, a cloud camera (masked to the pixels of one fluorescence telescope), and GOES.

Atop each FD building is an infrared (IR) camera on a motorised mount, sensitive to the band from $8\ \mu\text{m}$ to $14\ \mu\text{m}$ where clouds appear warmer than clear sky. Every 5 min the cameras scan the FOV of the FD sites, and every 15 min they scan the full sky. An example cloud camera image for one fluorescence telescope, with cloud in the FOV, is shown in Fig. 1b. The images are analysed and a cloud fraction (0 % to 100 %) is associated with each FD pixel. Near the horizon (elevation $\leq 5.5^\circ$) the atmosphere becomes optically thick in this IR band and the higher radiative temperature of water vapour makes discerning clouds very difficult, so these cloud fractions are considered less reliable. During data acquisition, the cloud camera images are used by FD operators for guidance on outside conditions. During event reconstruction, the cloud fraction of each FD pixel along the shower track is considered.

The Geostationary Operational Environmental Satellite system (GOES) is operated by the United States National Oceanic and Atmospheric Administration. The raw data are freely available, and an algorithm tuned for use at the Auger Observatory is applied to convert aerial measurements across four IR bands into cloud probability maps every 30 min. Fig. 1c is an example of such a map, which allocates a probability of cloud (0 % to 100 %, in 20 % steps) to each $2.4\ \text{km} \times 5.5\ \text{km}$ satellite imagery pixel across the surface array [6]. During event reconstruction, the cloud probability of each satellite pixel between the FD and the shower axis from above is considered.

3. Application of data during air shower analysis

3.1 Molecular data

The atmospheric density profile plays a fundamental role in converting the light emitted at the shower track as a function of height, to the energy deposited in the atmosphere per unit depth as a function of depth. It is also used to account for molecular scattering and attenuation when converting the observed fluorescence light into energy deposited at the shower.

The pressure, temperature, and humidity profiles are used to calculate the fluorescence yield along the track of the air shower. This includes accounting for the temperature dependence of the collisional cross-sections of atmospheric nitrogen with nitrogen or oxygen, the frequency of collisions, and additional de-excitation by water vapour [3].

Variations in pressure and air density close to the ground affect the signal observed in the SD due to changes in particle scattering. This modulates the reconstructed shower energy, and for studies using a fixed energy cut the diurnally modulated arrival rate can appear as a large scale anisotropy. Hence, the real-time estimations of these variables are used to apply a “weather correction” [7].

3.2 Aerosol data

A quality cut is placed on the value of vertical aerosol optical depth at 4.5 km ASL. Events are discarded from analysis when this value exceeds 0.1, which corresponds to a $\sim 10\%$ reduction in vertical light transmission. As indicated in Fig. 2, this is a significant minority of all events.

For studies needing high quality FD observations, we require that real aerosol data be available from the time the event occurred. We have extended the aerosol database with two more years of measurements, up to the end of 2017, allowing a larger sample of FD events to meet this requirement and potentially be used in analysis.

Important corrections to the data-normalised method for aerosol analysis were previously described by the Auger Collaboration [8]. The effect of these changes was to remove the assumptions that aerosol scattering out of the laser beam is negligible and that multiple scattering of photons en route to the detector is negligible. These corrections were effectively incorporated to the existing software, however they could not be fully realised until the software used laser light profiles calculated with the same technique of light integration across the FD cameras as that employed for air shower reconstructions. This represented a fundamental change, and ultimately it could only be realised after a complete rewrite of the software. This work has been completed, and as a benefit several other improvements have been made.

At very low altitudes, the integrated optical depth remains the same but we have improved the determination of the exact shape. At higher altitudes we now more rigorously apply a smoothing algorithm that prevents statistical fluctuations in the aerosol profile being interpreted as a significant step in aerosol content. We also reviewed the technique used to propagate uncertainties from the initial light profiles to the final aerosol profile, and replaced a numerical method with a much faster and more accurate analytical one. The software now has a modular structure, and any future corrections will be easier to incorporate.

All new results have been cross-checked with the separate laser simulation technique [5], finding good agreement. The new software produced the complete aerosol database used in air shower reconstructions referred to throughout Auger Collaboration contributions to these proceedings.

3.3 Cloud data

Data from all cloud monitoring instruments are brought together during analysis to determine if an event as viewed from a particular FD site is affected by cloud and should be discarded. These “cloud cuts” have been briefly described previously [9], but we shall now discuss them in detail.

As illustrated by Fig. 3, we test the instruments in a preferred order to determine if any indicate the event is *not* affected by cloud. Only when all available instruments suggest the event is cloud-affected do we conclude this is the case.

In the following list we refer to the “best approximation” for the cloud base height (CBH) or cloud coverage from FD lidars. The best approximation is defined as the sole measurement from the FD lidar at the same FD site as viewed the event, or if unavailable then it is the average of the measurement from all other FD lidars. With reference to the labelled steps in Fig. 3:

- (a) If all FD pixels which received light from the shower axis have cloud fractions (from cloud camera) of 0 %, then the event is clear. Cloud fractions are ignored for any FD pixels that view part of the shower below 5.5° elevation, due to cloud camera limitations (see Sec. 2.3).

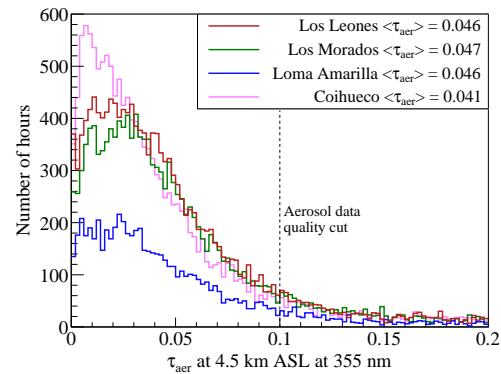


Figure 2: Distributions of vertical aerosol optical depth (τ_{aer}) at 4.5 km ASL for each FD site. Loma Amarilla has six fewer years of data.

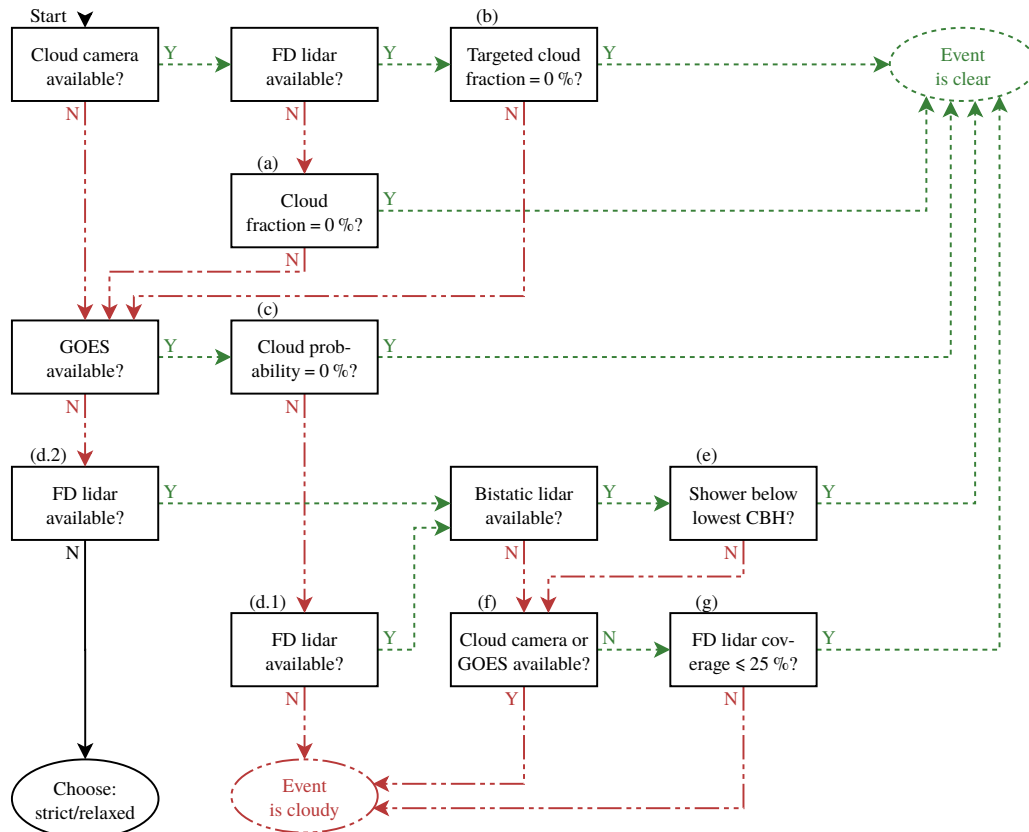


Figure 3: The cloud cut procedure for event analysis. Boxes represent steps of the procedure and ellipses represent exit points. Each step poses a question which may be answered “yes” (Y) or “no” (N). Refer to the text for detail on the steps labelled (a) through (g).

- (b) As step (a), but also disregarding cloud fractions for any FD pixels viewing parts of the shower below the CBH of the nearest available FD lidar, because such cloud must actually be behind the shower and couldn’t have affected it.
- (c) If all satellite pixels between the FD site and the observed points along the shower axis have cloud probabilities of 0 %, then the event is clear.
- (d) We cannot attempt any further tests without FD lidar, so if it is unavailable:
 - (d.1) Step (c) indicated cloud, so we conclude the event is cloudy.
 - (d.2) We cannot make a definitive conclusion and we may choose to discard or retain the event for a “strict” or “relaxed” cut respectively. The relaxed cut is generally used, but this choice depends on the specific analysis being performed.
- (e) Consider the lower of the bistatic lidar CBH (see Sec. 2.3) and the best approximation of the FD lidar CBH. If the field of view of the event observation is below this CBH, as determined by two metrics beyond the scope of this discussion [9], then the event is clear.
- (f) If cloud camera or GOES are available, then steps (b) or (c) indicated the event is cloudy.
- (g) If the best approximation of the FD lidar cloud coverage is less than 25 %, then the event is clear. Otherwise the event is cloudy.

Even if an event affected by cloud mistakenly passes the cloud cuts, it can still be removed by the

independent profile quality cuts. These cuts ensure that there are no large gaps in the shower light profile, that it isn't too short, and that the goodness of fit parameter is acceptable [9].

4. Effect on reconstruction results

4.1 Molecular atmosphere

Using GDAS 3-hourly data in air shower reconstructions brings improvements over the models initially employed at the observatory, which were derived from radiosonde data.

The exact effect on uncertainties was assessed by simulating events using known atmospheric profiles collected with radiosondes, reconstructing once with the old models and once with GDAS. The statistical uncertainty on energy measurements due to the molecular atmosphere is reduced by up to 50 % at high energies, and for depth of shower maximum it is halved at all energies [3].

Applying the weather correction rescales the SD signal – and hence the reconstructed energy – by up to 2 % for most events and up to 7 % in extreme cases, with some zenith angle dependence [7]. It also accounts for modulation in the daily and hourly event rates above a fixed energy threshold.

4.2 Aerosol atmosphere

To assess the importance of hourly aerosol measurements, we have studied the effect of using a fixed average vertical distribution of aerosols on measurements of energy (E) and depth of shower maximum (X_{\max}). A similar study has been done in the past [10], but here we update that work with greater statistics and a more recent aerosol analysis. We consider two average vertical aerosol profiles, one for the three FD sites at 1.4 km ASL and one for the site at 1.7 km ASL. We reconstruct well-measured air showers twice, once each with the average and hourly aerosol profiles, and produce the plots in Fig. 4 showing the changes in reconstructed E and X_{\max} and their energy-dependence when using these different sources of aerosol information.

These distributions exhibit large non-Gaussian tails, and an increasing standard deviation with increasing shower energy. This is a consequence of the average shower distance increasing with energy, and the hourly aerosol measurements being increasingly important for those showers. We note that the current statistical uncertainty on FD measurements of energy is 8 % [11], and from 15 g cm^{-2} to 25 g cm^{-2} for depth of shower maximum [9], using hourly aerosol profiles. The use of an average profile instead would significantly worsen these resolutions at high energies, and would complicate analysis given the non-Gaussian tails.

5. Conclusion

An extensive range of instruments is used to monitor the state of the atmosphere at the Auger Observatory, of which a subset have been outlined here. We have discussed exactly how these instruments are used in analysis, detailing both the recent upgrades to the aerosol software as well as the full procedure for selecting and removing cloud-affected events. Finally, we have shown the effects that using real-time molecular and aerosol data have on air shower reconstructions, contrasting each against the use of average models. It is clear that the real-time aspect of these monitoring systems is a significant advantage to the science results of the Auger Observatory.

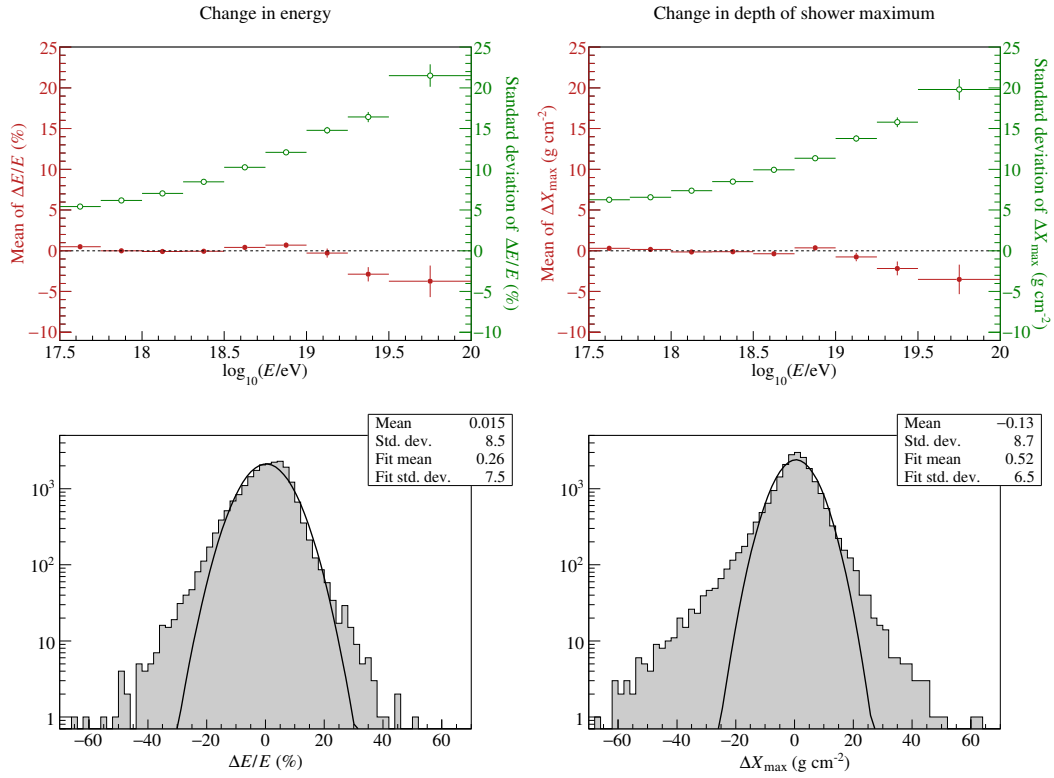


Figure 4: Results from air shower reconstructions using an average aerosol profile minus those from an hourly profile. *Top:* shifts in the reconstruction of FD energy (E) and depth of shower maximum (X_{max}) as a function of the shower energy. Filled red circles plot the mean of the distribution in each energy bin, and open green circles plot the standard deviation. *Bottom:* distributions of the shifts in E and X_{max} combining all energy bins, plotted with Gaussian fits.

References

- [1] A. Aab et al., *Nucl. Instrum. Methods Phys. Res., Sect. A* **798**, 172 (2015).
- [2] P. Abreu et al., *J. Instrum.* **7**, P09001 (2012).
- [3] P. Abreu et al., *Astropart. Phys.* **35**, 591 (2012).
- [4] V. Rizi et al., *EPJ Web Conf.* **197**, 02003 (2019).
- [5] P. Abreu et al., *J. Instrum.* **8**, P04009 (2013).
- [6] P. Abreu et al., *Astropart. Phys.* **50 - 52**, 92 (2013).
- [7] A. Aab et al., *J. Instrum.* **12**, P02006 (2017).
- [8] M. Malacari, *Proc. Int. Cosm. Ray Conf., PoS(ICRC2017)* 398.
- [9] A. Aab et al., *Phys. Rev. D* **90**, 122005 (2014).
- [10] J. Abraham et al., *Astropart. Phys.* **33**, 108 (2010).
- [11] B. Dawson, *Proc. Int. Cosm. Ray Conf., PoS(ICRC2019)* 231.



Long Term Performance of the Pierre Auger Observatory

Koun Choi^{*a} for the Pierre Auger Collaboration^{†b}

^a*Université Libre de Bruxelles, Brussels, Belgium*

^b*Observatorio Pierre Auger, Av. San Martín Norte 304, 5613 Malargüe, Argentina*

E-mail: auger_spokespersons@fnal.gov

Full author list: http://www.auger.org/archive/authors_icrc_2019.html

The Pierre Auger Observatory is the largest detector ever built to measure ultra-high energy cosmic rays. It employs a hybrid technique, combining a surface detector consisting of 1660 water-Cherenkov stations and a fluorescence detector composed of 27 Schmidt telescopes. The construction of the Observatory started in 2004, and since then, it has been continuously taking data in a stable manner. We will present the behavior of the Observatory over more than 14 years and the expected response into the future with the AugerPrime upgrade now underway. Key performance indicators such as the on-time and the event rates will be presented, along with reference to calibration and monitor instruments.

36th International Cosmic Ray Conference — ICRC2019

24 July – 1 August, 2019

Madison, Wisconsin, USA

^{*}Speaker.

[†]for collaboration list see PoS(ICRC2019)1177

1. Overview of the Pierre Auger Observatory

The Pierre Auger Observatory is the world's largest cosmic ray air-shower detector. The Observatory is built on a 3000 km² high plain in the province of Mendoza, Argentina. It adopts a hybrid design which combines a Surface Detector (SD) consisting of 1660 water-Cherenkov stations and a Fluorescence Detector (FD) composed of 27 Schmidt telescopes deployed at four different sites overlooking the SD array. The SD captures the lateral spread of air-showers at ground level, while the FD observes their longitudinal profiles.

The construction of the SD started in January 2004, and it has been running in full configuration since 2008. After the completion of the *SD-1500 array* with 1.5 km spacing between the stations placed on a triangular grid, the low-energy extension of the SD, *SD-750 array*, was started. It comprises 61 stations with a grid spacing of 750 m and has been taking data since 2011. An SD station is composed of a water tank of 3.6 m diameter and 1.2 m height housing a liner bag made from reflective Tyvek. The liner bag is filled with ultra-pure water, and three 9-inch photomultiplier tubes (PMTs) optically coupled to water look downwards into the tank. When relativistic charged particles from an air shower pass through the inner volume, emitted Cherenkov light is reflected on the inner Tyvek surface and detected by the PMTs. Each station is equipped with a solar power battery and panel, a front-end electronics board, GPS, and a communication antenna for autonomous operation. The Cherenkov light observed by each PMT is digitized at 40 MHz by a 10 bit Flash Analog-to-Digital Convertor (FADC) channels for the output from the last PMT dynode and the anode.

The FD detects nitrogen fluorescence light induced by air-showers in the atmosphere. A single telescope has a field of view of ($30^\circ \times 30^\circ$) in azimuth and elevation angles, with a minimum elevation of 1.5° above the horizon. The combination of the six telescopes in each site covers 180° in azimuth angle. A spherical mirror of 3.4 m radius of curvature focuses light onto a camera composed of 440 hexagonal PMTs assembled in a (22×20) matrix taking data at a frequency of 10 MHz. The number of photons detected by each camera pixel is used to evaluate the energy deposited in the atmosphere as a function of depth. Twelve fluorescence telescopes in the Los Leones and Coihueco sites started data taking in January 2004. Another six telescopes entered in acquisition in May 2005 at the Los Morados site, and finally, six telescopes in the Loma Amarilla site became operational in March 2007. Since September 2009, three additional telescopes (HEAT: High Elevation Auger Telescope) with an elevated field of view ($30^\circ \sim 60^\circ$) have also been operating to study lower-energy cosmic rays.

The atmosphere is the medium where the air showers develop and thus an important part of the Observatory is dedicated to measuring the atmospheric conditions and the concentration of aerosols present in the air. The Observatory includes a set of high-quality devices for monitoring clouds and aerosols such as infrared cameras and laser facilities. Details on the design and previous studies on the performance of the Observatory can be found in [1].

Currently, the Observatory is undergoing the AugerPrime upgrade program whose major aim is to enhance the sensitivity of the SD to the mass composition at the highest energies by the deployment of the SSD (Surface Scintillator Detector) on top of the SD stations. The upgrade plan also includes a radio detector deployment, the AMIGA (Auger Muons and Infill for the Ground Array) project, as well as an increase of the duty cycle of the FD [2]. Thus it is important to ensure

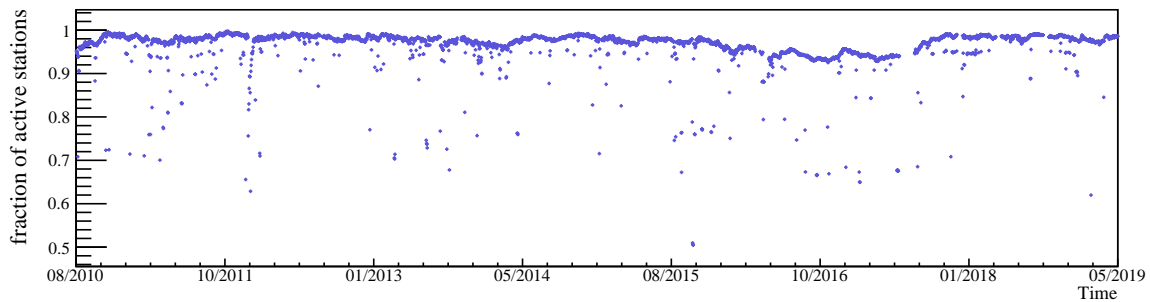


Figure 1: Number of active SD stations normalized to the number of deployed SD stations as a function of time.

that the detectors will continue to take high-quality data over the next decade.

The functioning of the SD, the FD and the other instruments is constantly monitored, from observables related to the PMTs to higher-level variables used in advanced analyses. In this work, we will provide information on the long term performance of the Pierre Auger Observatory by reviewing its behavior over more than 14 years. In section 2, we will describe the performance of the SD and its expected performance in the next decade. We will review the performance of the FD and of the calibration and atmosphere monitoring instruments in section 3, and conclude in section 4.

2. Long term performance of the Surface Detector

The SD tank and the electronics are exposed to unstable weather conditions such as a large temperature variation, lightning, high salinity, dust and humidity. These environmental conditions can damage the detector and influence the quality of data. To constantly monitor the detector condition and response, various sensors are installed in every SD station. Variables related to temperature, battery power, PMT voltage and current, and dynode/anode ratio (the ratio of the amplitude of the output from the last PMT dynode to the one from the anode) are sent to the Central Data Acquisition System (CDAS) and then exported to a MySQL database server [1, 3, 4]. Besides monitoring the conditions of the station hardware, the number of triggers a station is transmitting is continuously surveyed. Each station has two levels of triggers (called $T1$ and $T2$). Due to the limited data transmission bandwidth, the trigger algorithms are implemented locally in the station software. The $T2$ trigger selects signals with amplitudes exceeding a threshold (TH), or signals that are spread in time (*time over threshold* or ToT), and are sent to CDAS to form the trigger for air-showers based on time and spatial coincidence of the signals [5]. The number of active stations able to send $T2$ signals is constantly monitored. The ratio of active stations to the total number of deployed stations is depicted in Fig. 1. Since the beginning of the deployment, on average more than 95% of all stations have been functioning. Lower values correspond to DAQ downtime, communication issues in the data transmission to CDAS or other on-site problems occasionally occurring for individual stations. The time fraction when the entire array was not transmitting data was less than 1% since 2004.

The particles produced in air showers initiated by low-energy cosmic rays pass through the stations

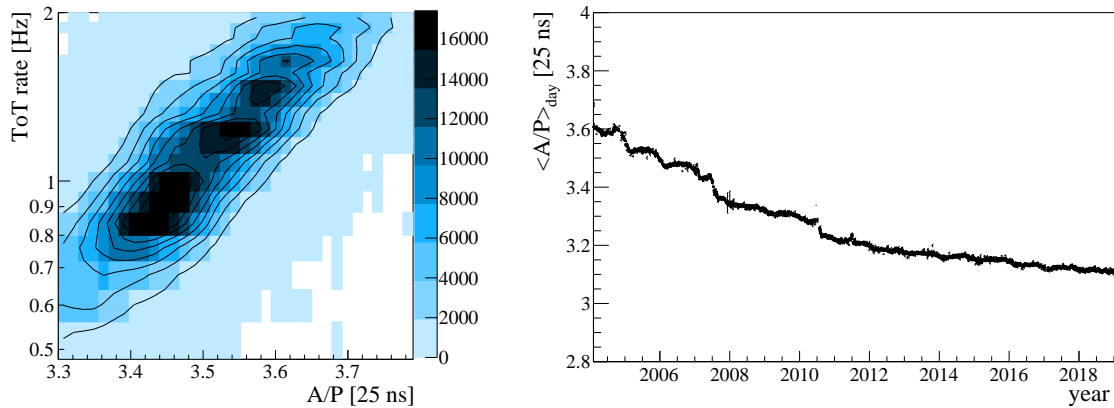


Figure 2: *Left:* Correlation between A/P and ToT rate plotted using monitoring data from October 2006. *Right:* Daily average of A/P of one of the three PMTs in the station Rocio (station id 270) as a function of time.

at a rate of ~ 3000 per second. Selected by a simple threshold calibration trigger, the amplitude and the charge of each signal are compiled in individual histograms for each PMT. The calibration histograms are filled during one minute. Among the particles entering the tank, the muons produce a larger amount of Cherenkov photons and provide a distinctive larger area and a higher peak than the electrons and photons. These values are computed in the station software and then sent to CDAS every six minutes. Entire calibration histograms are transmitted to CDAS with each triggered air-shower. By employing the uniform flux of the atmospheric muons, a uniform calibration for the entire array is achieved.

A good variable to assess and understand the slow changes in the detectors is the area over peak ratio (A/P) of the atmospheric muon signals. This variable is related to the reflectivity of the Tyvek liner and water transparency, as well as the response of PMTs and of the electronics. The correlation with the ToT trigger, which depends on the shape of the muon pulse and therefore on the A/P, is illustrated in Fig. 2 (left). The right plot of Fig. 2 is an example of A/P evolution showing a typical behavior, of one PMT in a station which has been taking data since 2004. After deployment, most stations experience a rapid decrease in A/P, followed by a milder slope which tends to become flat. An annual modulation related to the seasonal temperature variation is also seen. In 2007 and 2010, some of the stations experienced sudden changes in A/P, which are correlated to very cold winters with temperature drops below -10°C [6]. In the last nine years, the freezing temperatures in winters no longer influenced A/P behavior, as can be seen in the winter of 2018, where the temperature dropped below -10°C , but no significant change in A/P has been observed.

The stacked distribution of the A/P loss is shown in the left plot of Fig. 3. For each A/P profile, the average A/P in 2018 is computed, and the A/P loss is defined as the ratio of this value to the one at the initial deployment year. Among the 4175 PMTs used in the evaluation, less than 18.5% of the PMTs have experienced a decrease of more than 15% compared to their initial values. Shown in the same plot is the stacked distribution of the A/P loss since 2013. In the last five years, A/P has stabilized, with a loss of less than 5% for 95% of the PMTs.

The long-term evolution of A/P is described by a model characterizing the exponential de-

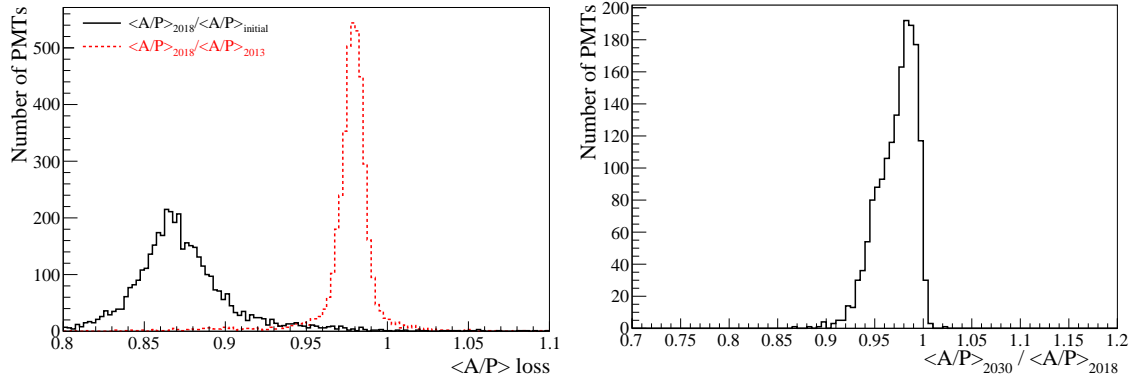


Figure 3: *Left:* Stacked distribution of A/P loss, defined as $\langle A/P \rangle_{2018}$ divided by $\langle A/P \rangle_{\text{initial}}$ (solid, black) and by $\langle A/P \rangle_{2013}$ (dashed, red) of each PMT. *Right:* $\langle A/P \rangle$ expected in 2030 divided by $\langle A/P \rangle_{2018}$.

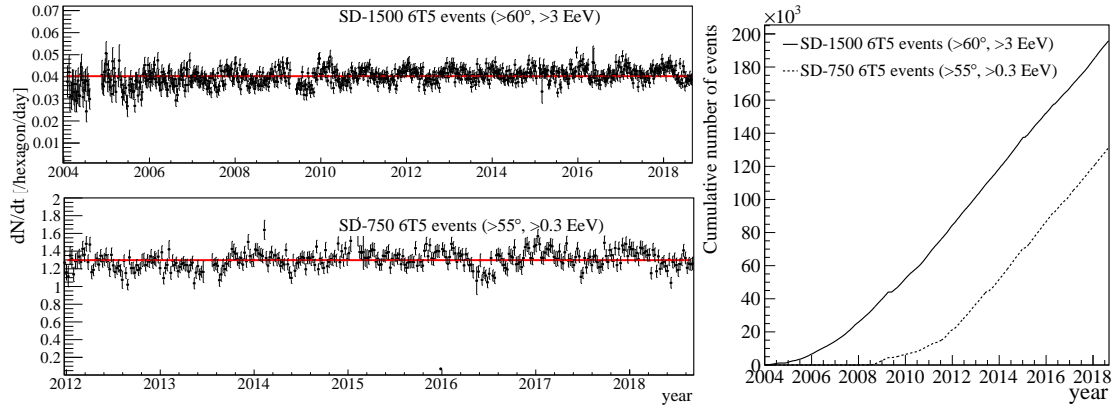


Figure 4: *Left:* Evolution of the daily 6T5 rate normalized to the number of hexagons. *Top:* Number of the SD-1500 array events with energy $>3 \times 10^{18}$ eV and zenith angle $<60^\circ$. *Bottom:* Number of the SD-750 array events with energy $>0.3 \times 10^{18}$ eV and zenith angle $<55^\circ$. Red lines indicate the averages (see text). Note that the bin size is chosen to be a week, and error bars represent the corresponding statistical uncertainties. *Right:* Cumulative number of 6T5 events for the SD-1500 array (solid) and the SD-750 array (dashed).

ray combined with an annual modulation [6]. The A/P evolution is extrapolated to estimate the expected A/P in the future. By selecting PMTs with having data for more than five months and without a discontinuity in the most recent two years of data, 1655 PMTs are fitted. As a result, 85% of these PMTs are expected to have an A/P larger than 95% of their current values in 2030 (Fig. 3). Based on this extrapolation, we can assume that the SD stations will not experience a significant change in their behavior within the operation time of the Pierre Auger Observatory.

The air-shower trigger is formed by requiring a time coincidence of at least three neighbouring stations [5]. For accurate reconstruction, a trigger condition, named as *6T5 trigger*, further ensures that showers are contained in the array, by requiring that at the time of the event all six neighbouring stations of the station with the highest signal are active. The 6T5 events are the basis of high-level analyses like the measurements of the energy spectrum [7]. Thus a stable 6T5 rate is crucial. For

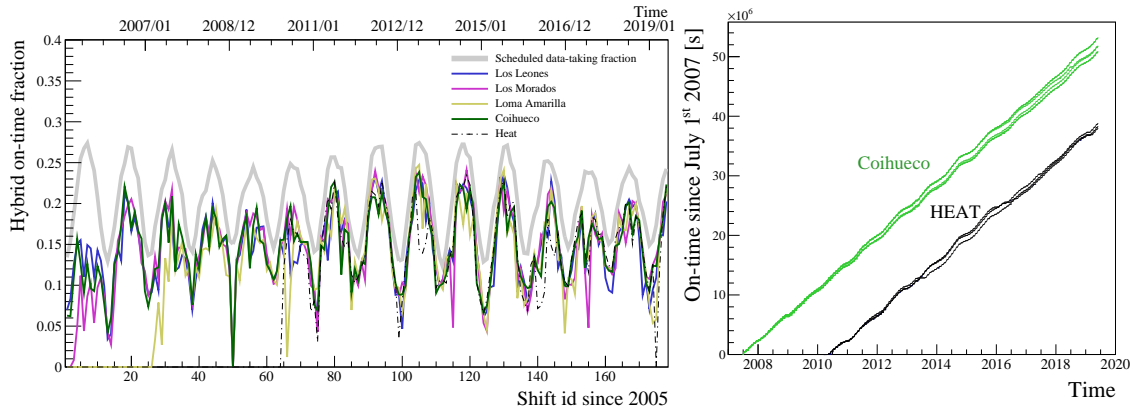


Figure 5: *Left:* The on-time fraction is shown for the four FD sites (Los Leones, Los Morados, Loma Amarilla and Coihueco) and the HEAT for hybrid events. The X-axis indicates shift ID, where each shift covers a moon cycle. *Right:* The accumulated on-time since July 1, 2007 for the six telescopes of Coihueco and the three telescopes of HEAT.

cosmic rays with zenith angle less than 60° and energy larger than 3 EeV , the trigger efficiency for the SD-1500 array is array is close to 1, irrespective of the nature of the primary particle. For the SD-750 array, full efficiency is achieved above 0.3 EeV and for zenith angle less than 55° . The time evolution of the daily rate of 6T5 events passing the full trigger efficiency conditions per hexagon is shown in Fig. 4 (left). The 6T5 rate has been constant over more than 14 years, being 0.040 ± 0.004 events/day/hexagon for the SD-1500 array and 1.3 ± 0.1 events/day/hexagon for the SD-750 array. In 2013 new station triggers have been implemented which do not depend strongly on the shape of the signal. Being sensitive to small signals, they lower the energy threshold for full efficiency of the arrays, assuring a constant event rate above this threshold [8].

The cumulative number of 6T5 events is illustrated in Fig. 4 (right). The SD has been running with high efficiency of data accumulation throughout the 15 years of the data-taking history. The SD-1500 array data sets currently contain more than 4.5 million 6T5 events out of which more than 200,000 events are above 3 EeV .

3. Long term performance of the Fluorescence Detector

The fluorescence telescopes operate during dark, clear nights. Data taking requires the sun to be lower than 18° below the horizon (evening and morning astronomical twilights) and the moon to be below the horizon for longer than three hours. In addition, the illuminated moon fraction has to be lower than 70%. The sky background photon flux (Night Sky Brightness) and the artificial lights in the field of view of the FD telescopes should also be marginal. The data taking can also be affected by bad weather conditions such as rain, snow, strong winds and lightning. The weather conditions and the background noise (electronic and Night Sky Brightness) for the FD are continuously monitored during the data taking [9, 10].

When an air shower is observed by the FD in coincidence with at least one triggered SD station, a better reconstruction of the shower geometry is achieved with respect to the one using the FD alone [11]. These events are called *hybrid events*. Knowing the hybrid on-time is crucial

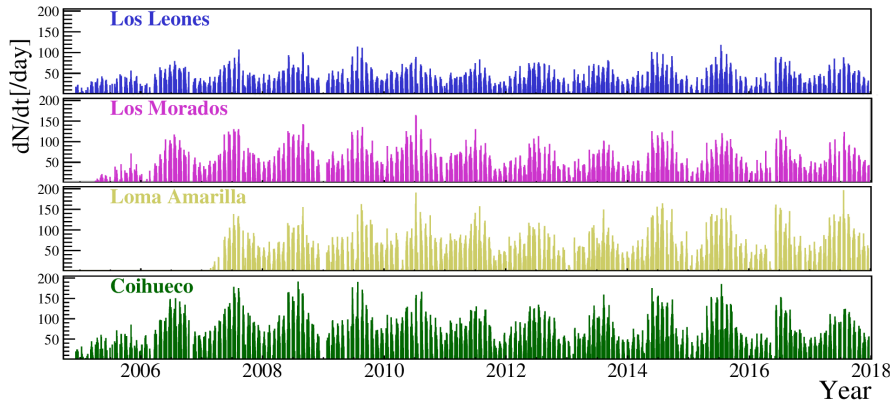


Figure 6: Number of events taken in each day are shown for the four FD sites, respectively.

for an accurate evaluation of the FD hybrid exposure [11]. The time evolution of the hybrid on-time fraction is shown in Fig. 5 (left) for four FD sites and the HEAT telescopes. The on-time of the hybrid detector is compared to the nominal Data Acquisition (DAQ) time fraction calculated according to the Sun and the Moon positions as previously described. In addition to the Night Sky Brightness and the weather conditions, technical problems such as DAQ failure can cause inefficiency of the FD operation. Excluding the initial phase when the telescopes were not fully operational, the on-time has been about 15% for all FD sites. Also, seasonal modulations are visible due to longer nights during winter. On the right side of Fig. 5, the accumulated on-time in seconds since July 1, 2007, for Coihueco and HEAT telescopes is shown. The stability of the hybrid detector is shown in Fig. 6 in terms of the daily number of hybrid events observed by individual FD sites with the same seasonal modulations being visible as in the on-time plot (Fig. 5).

Different methods are used to calibrate the FD. Absolute calibrations have been performed over the years to follow the long-term behavior, while a relative calibration is performed daily to follow the short- and medium-term changes due to different contributions, i.e. filters, mirrors, and PMTs. The absolute end-to-end calibration [12] used a drum-shaped tool, in which a pulsed UV-LED source illuminates the interior of a 2.5 m diameter cylindrical drum of 1.4 m depth, that can be mounted at the entrance aperture of each telescope. Three different relative calibration measurements [13], using light sources injected at three different positions on each telescope, are performed twice per night, before and after the FD data acquisition, to track daily variations as well as variations between two consecutive absolute calibrations. As an example, the mean of the calibration constants from all PMTs of telescope 3 at the Loma Amarilla site are shown in Fig. 7 (left) for the period from 2007 to 2019. A stable behaviour is reported after an initial drift [14].

Monitoring the atmospheric properties around the air-shower development is also critical for a reconstruction of the shower energies. Especially atmospheric transmission through aerosols needs rigorous monitoring due to their large and fast time variation and the significant effect on air-shower reconstruction [1]. The Central Laser Facility (CLF) and the eXtreme Laser Facility (XLF) continuously take data to measure the aerosol optical depth vertical profiles in the FD field of view on an hourly basis [15]. During FD data acquisition, the two facilities vertically shoot a set of 50 collimated UV laser pulses every 15 minutes, which can be simultaneously detected by different

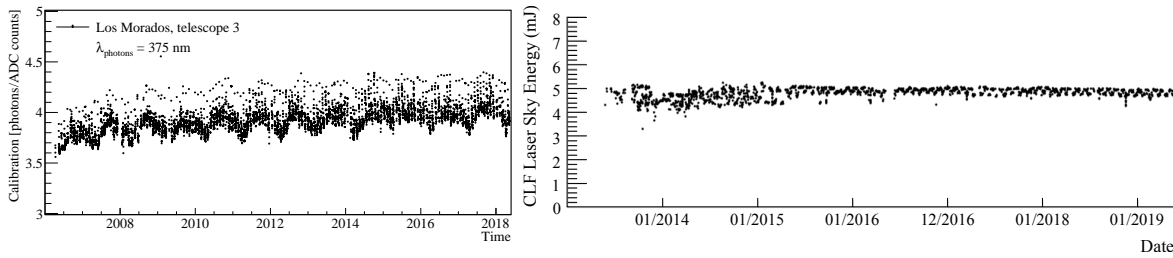


Figure 7: *Left:* Mean of the calibration constants from all PMTs of telescope 3 in the Loma Amarilla site, taken in each shift. *Right:* The CLF laser energy as a function of time.

FD telescopes. The CLF has been operating since 2003, and a major upgrade was done in 2013 to add a beam calibration system and a backscatter Raman lidar receiver. For absolute calibrations of the CLF beam, the entire laser beam is sent to the sky and captured with an external radiometer before and after each night's operation. Fig. 7 (right) illustrates the stability of the energy of the CLF beam measured by the calibration system. For more information about the CLF and XLF facilities and the analyses refer to [1, 9, 15].

4. Conclusion

We have presented the long term performance of the Pierre Auger Observatory over more than 15 years of data-taking history. The SD has been functioning stably with a duty cycle higher than 95%. The study carried out on atmospheric muons shows that the SD have stabilized, the area over peak loss is expected to be less than 5% for most of the PMTs in the next decade. The FD, as well as the instruments for calibration and monitoring of the detectors, have also been operating in a stable and efficient manner.

References

- [1] The Pierre Auger Collaboration, Nucl. Instrum. Meth. A 798 (2015)
- [2] The Pierre Auger Collaboration, arXiv:1604.03637 [astro-ph.IM]
- [3] X. Bertou *et al.* for the Pierre Auger Collaboration, Nucl. Instrum. Meth. A 568 (2006)
- [4] C. Bonifazi for the Pierre Auger Collaboration, ICRC (2013) 1079
- [5] The Pierre Auger Collaboration, Nucl. Instrum. Meth. A 613 (2010)
- [6] R. Sato for the Pierre Auger Collaboration, ICRC (2011) 204
- [7] V. Verzi for the Pierre Auger Collaboration, PoS(ICRC2019) 450
- [8] A. Coleman [Pierre Auger Collaboration], PoS(ICRC2019) 225
- [9] The Pierre Auger Collaboration, Astropart. Phys. 33, 108 (2010)
- [10] M. Kleifges, et al., IEEE Trans. Nucl. Sci. 50, 1204 (2003)
- [11] P. Abreu, et al., Astropart. Phys. 34, 368 (2011)
- [12] Brack J. et al., Astropart. Phys. 20, 653 (2004)
- [13] R. Caruso for the Pierre Auger Collaboration, ICRC (2009) 473
- [14] G. Salina for the Pierre Auger Collaboration, PoS(ICRC2015) 594
- [15] V. Harvey for the Pierre Auger Collaboration, PoS(ICRC2019) 283



Analysis of Data from Surface Detector Stations of the AugerPrime Upgrade

Álvaro Taboada^{*a,b} for the Pierre Auger Collaboration^{†c}

^aKarlsruher Institut für Technologie (KIT), Institut für Kernphysik (IKP), Karlsruhe, Germany

^bInstituto de Tecnologías en Detección y Astropartículas (ITeDA), Buenos Aires, Argentina

^cObservatorio Pierre Auger, Av. San Martín Norte 304, 5613 Malargüe, Argentina

E-mail: auger_spokespersons@fnal.gov

Full author list: http://www.auger.org/archive/authors_icrc_2019.html

Measuring the different components of extensive air showers is of key importance in reconstructing the mass composition of ultra-high energy cosmic rays. AugerPrime, the upgrade of the Pierre Auger Observatory, aims to enhance the sensitivity of its surface detector to the masses of cosmic rays by installing a 3.8 m² plastic scintillator detector on top of each of the 1660 Water-Cherenkov Detectors (WCDs). This Scintillator Surface Detector (SSD) provides a complementary measurement which allows for disentanglement of the electromagnetic and muonic shower components. Another important improvement of AugerPrime are the surface-detector electronics. The new electronics will process signals from the WCD and the SSD with higher sampling frequency and enhanced resolution in signal amplitude. Furthermore, a smaller photomultiplier tube will be added to each WCD, thus increasing its dynamic range. Twelve upgraded surface detector stations have been operating since September 2016. Additionally, seventy-seven SSDs have been deployed and are taking data since March 2019. In this work, the analysis of the data from these detectors is presented.

36th International Cosmic Ray Conference — ICRC2019

24 July – 1 August, 2019

Madison, Wisconsin, USA

*Speaker.

†for collaboration list see PoS(ICRC2019)1177

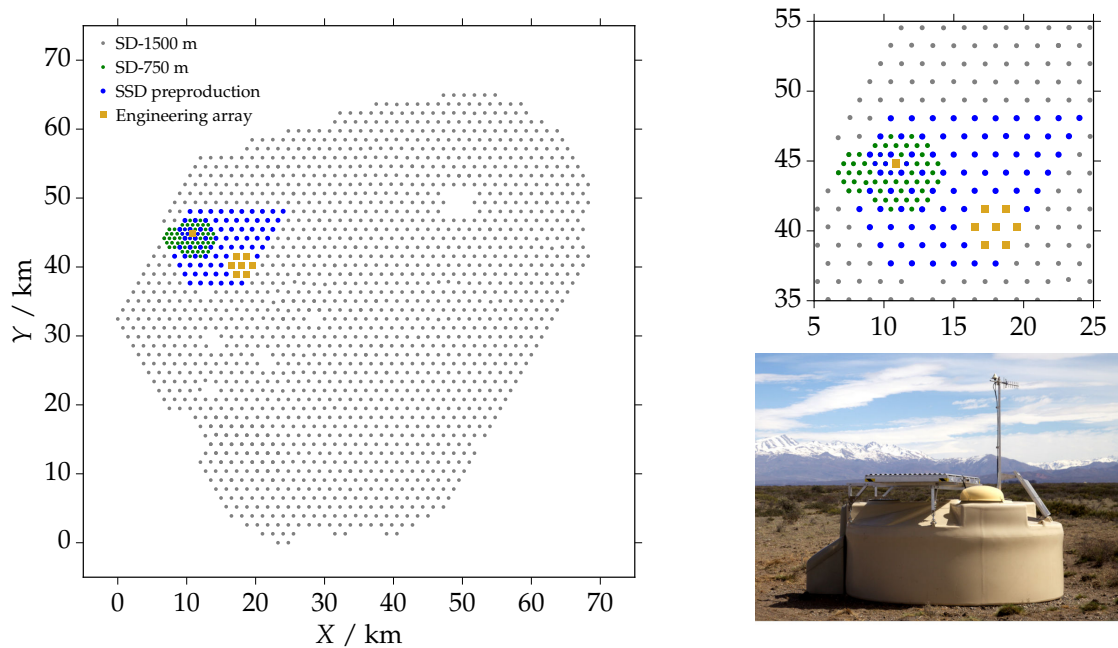


Figure 1: *Left*: Layout of the surface detector. *Top right*: Zoomed area containing the engineering array (golden squares) and SSD preproduction locations (blue dots). *Bottom right*: Photograph of an upgraded station of the surface detector.

1. Introduction

The main goal of the AugerPrime upgrade [1, 2] is to provide additional measurements of air showers which will allow for a better estimation of the mass composition of ultra-high energy cosmic rays. The key part of the upgrade is the installation of scintillator surface detectors on top of each of the existing water-Cherenkov detectors in the 3000 km² surface detector (SD) array which can be seen in Fig. 1 (left). A complementary response of the two sub-detectors to shower particles allows us to disentangle the electromagnetic and the muonic shower components at the ground.

The SSD unit consists of an aluminum housing filled with 48 scintillator bars distributed between two modules covering a total area of 3.8 m². Wavelength-shifting fibers guide photons produced in the scintillation process to a photomultiplier tube (PMT) located between the two modules. An additional element of AugerPrime is the upgrade of the SD electronics [3]. The upgraded board processes both of the SSD and WCD signals with higher sampling frequency (120 MHz instead of 40 MHz) and improved resolution in pulse amplitude (12 bits instead of 10 bits). Furthermore, an additional Small PMT (SPMT) in the WCD will increase the dynamic range of signals allowing measurements as close as 250 m from the shower core. A picture of an upgraded station can be seen in the bottom right of Fig. 1.

The first SSD units together with upgraded electronics and SPMT were deployed in the field in September of 2016. Twelve stations constitute the Engineering Array (EA) where nine are positioned using the standard 1500 m spacing and the remaining three form a multiplet at a 750 m spacing [4]. In March 2019, seventy-seven SSDs were connected to stations with non-upgraded

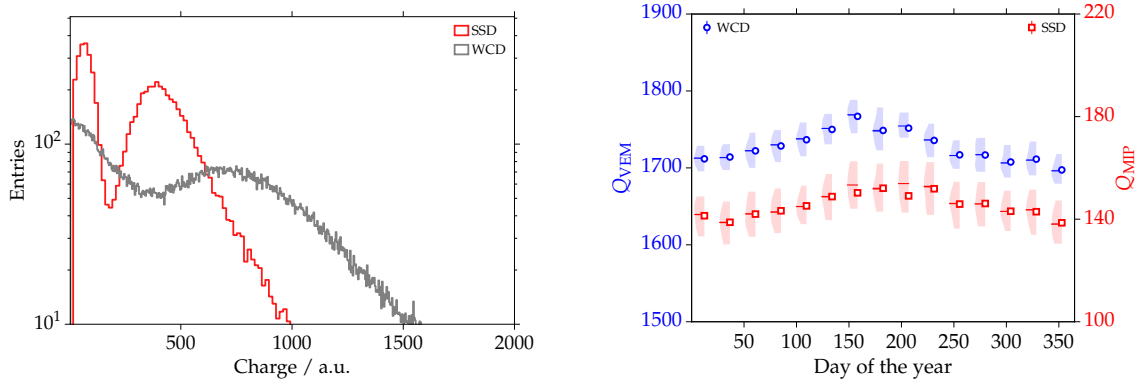


Figure 2: *Left:* Example of the “charge” distribution for the WCD (gray) and SSD (red) of an upgraded station at the engineering array. As the SSD is triggered by the WCD, the first peak of the charge distribution in the SSD is a pedestal (integral of baseline) in cases where the muon triggered the WCD but did not pass through the scintillator. *Right:* Profile of the variation with time of the VEM (blue circles) and MIP (red squares) charge. For each bin the spread of the distribution of Q_{VEM} and Q_{MIP} is shown by the blue and red shaded bands, respectively.

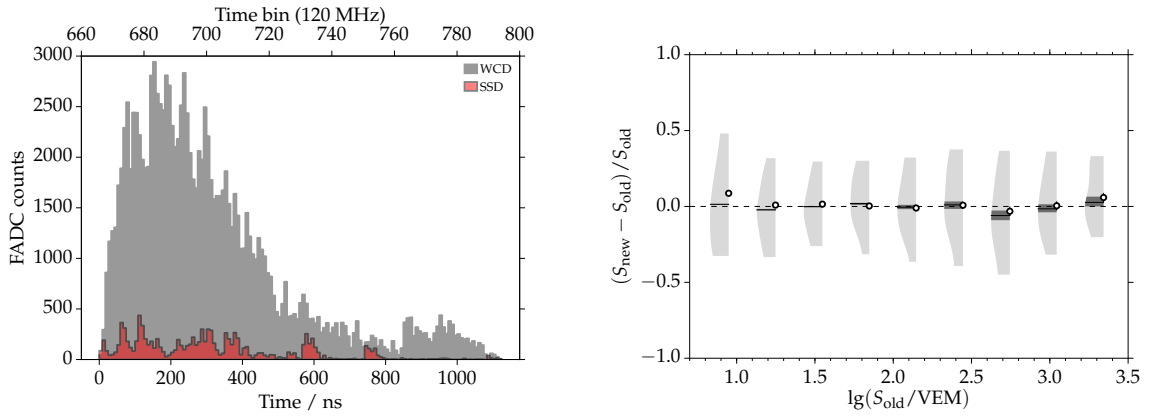


Figure 3: *Left:* Example of a time trace of an upgraded station located at 847 m from the shower core. The trace corresponds to one of the WCD PMTs (gray) and to the SSD (red). *Right:* Signal comparison from doublet measurements between old and new electronics as a function of the measured signal in a non-upgraded station. For this analysis 19337 doublet events with unsaturated signals were used.

electronics constituting the so-called SSD preproduction array. The area (of $\sim 120 \text{ km}^2$) containing the engineering array and SSD preproduction locations can be seen in the top right of Fig. 1.

2. Calibration and performance of the detectors

The flux of particles that reach the ground is constantly measured and is used to provide a common reference for all signals recorded by the SD stations. Signals from the WCDs are expressed in units of VEM (*vertical-equivalent muon*), which corresponds to the average signal

resulting from a vertical and centered muon traversing the tank, measured as the integrated PMT pulse over time, thus a “charge”. An estimation of the VEM can be obtained from the spectrum of signals generated by atmospheric muons passing through the tank. An example of a “charge” distribution in a WCD can be seen in Fig. 2 (left). Such histograms exhibit two characteristic peaks. For the WCD, the first peak is due to small signals which are produced mainly by electromagnetic particles (e^\pm , γ) due to their low average energy deposited in water. The second peak is produced by atmospheric muons where the integrated signal is the result of a convolution of effects related to the muons’ angular and energy spectra. By fitting the muon peak position, the value of the VEM charge (Q_{VEM}) is obtained [5]. Due to its dimensions, no direct calibration of the SPMT with muons is feasible. Selecting small shower events, the SPMT can be cross-calibrated with the large PMTs in such a way that the signal spectrum is correctly reconstructed up to about 20000 VEM. In the SSD muons and electrons deposit on average the same energy for a given traversed distance. The term MIP (*minimum ionizing particle*) is used to express the signals from the SSD. Analogous to the WCD, the average charge deposited by a MIP can be seen in the second peak of the charge histogram and the value of the MIP charge (Q_{MIP}) can be inferred from the fit to that distribution. The evolution of the VEM and MIP charge with time can give us insight on the performance of the calibration. The violin plot¹ in Fig. 2 (right), shows the average behavior of the VEM and MIP charge for a station in the engineering array over one year of acquisition. The variation of Q_{VEM} and Q_{MIP} related to seasonal modulations is apparent. At the same time, no aging effects seem to be present in the SSD.

When shower particles cross the detector, they produce time traces as a result of a convolution of the deposited energy with the response of the PMT. An example of a time trace can be seen in Fig. 3 (left). The calibrated signal S is obtained from the integral of the trace and it is expressed in units of VEM and MIP for the WCD and SSD, respectively. A comparison of the WCD signals between stations with old and upgraded electronics is shown as a function of the signal in Fig. 3 (right). This comparison is performed using upgraded stations in the engineering array, which are part of a doublet with a non-upgraded station. A good agreement between the old and new electronics can be seen for a wide range of signals.

3. Shower measurements with AugerPrime detectors

Since the first SSD units were deployed in the engineering array, more than 28000 showers have been measured including both upgraded and standard stations in the event reconstruction. Due to its higher trigger rate, the majority of these showers were measured by EA stations at the SD-750 m array and with energies $\gtrsim 10^{17.5}$ eV. Fewer showers (but more energetic) have also triggered the upgraded stations of the SD-1500 m array. With the addition of the SSD units in the preproduction array, more than 150 showers at energies above 3 EeV were measured including scintillator signals.

3.1 Analysis of shower signals

The SSD operates in slave mode to the WCD meaning that when a shower triggers the WCD,

¹For each bin, the “violin” (shaded area) extends up to the 1σ standard deviations of the distribution. The mean and median of the distribution are represented by markers and lines, respectively. The standard error on the mean is shown by the error bars while the darker area around the median line represents the 1σ uncertainties on the median.

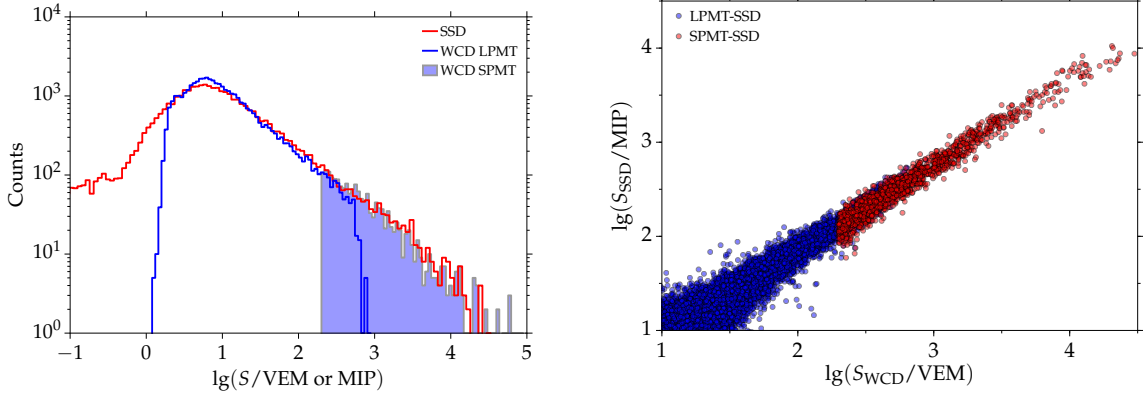


Figure 4: *Left*: Distributions of SSD (red) and WCD (blue) signals. The filled histogram shows signals from the SPMT. *Right*: Correlation between SSD and WCD signals using the large PMTs (blue) and the SPMT (red).

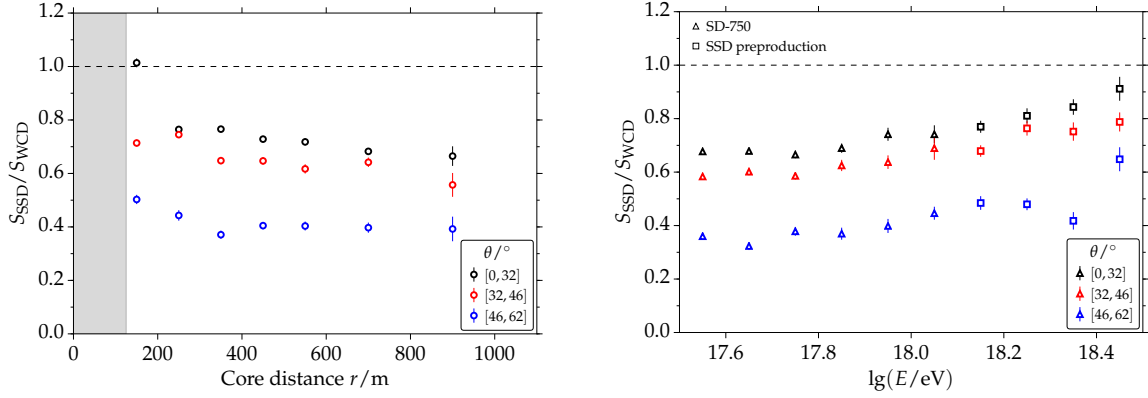


Figure 5: *Left*: Ratio of SSD and WCD signals as a function of the core distance, for different zenith angles of incidence. The gray area shows the region of saturated signals. *Right*: Ratio of signals as a function of the reconstructed energy. Data from the SD-750 m array (triangles) and SSD preproduction array (squares) are used. Ranges in zenith are chosen according to equal bins in $\sin^2 \theta$.

the information of the corresponding SSD is also read out. The signal distribution of both detectors is shown in Fig. 4 (left). The physics trigger is visible for the WCD with a sharp cut-off at low signals while for the SSD the signals can go down to baseline fluctuations in cases where no particles passed through the scintillator. The shape of the signal distribution in the SSD can be understood as a transition between the signal distribution due to baseline integration (no particle passing through) and/or small energy deposits in the scintillator (e.g., photons, corner-clipping particles, etc), and eventually the signal distribution produced by one or many particles traversing the detector. With the addition of the SPMT, the non saturated range of the WCD extends up to ≈ 20000 VEM, as seen in Fig. 4 (right). The correlation between the signals measured by the SSD and the SPMT is also shown there.

The idea of using a scintillator detector in order to enhance the sensitivity of the surface de-

detector to the mass of ultra-high energy cosmic rays relies on the differences in the SSD and WCD responses to shower components. While electromagnetic particles have smaller energy deposits than muons in water, both components deposit on average the same amount of energy in the scintillator. In this sense, the SSD is more sensitive to the electromagnetic component of the shower.

The ratio of SSD signals to WCD signals is shown in Fig. 5 (left) as a function of the distance to the shower core. The trend changes with the zenith angle. For vertical showers, the ratio $S_{\text{SSD}}/S_{\text{WCD}}$ is closer to 1 at distances closer to the shower core and decreases with increasing distance. For inclined showers, the ratio becomes nearly constant for distances $r > 300$ m. In Fig. 5 (right) the same ratio is shown as a function of the reconstructed energy, using data from the EA stations located in the SD-750 m spacing array at energies below $10^{18.1}$ eV and data from stations of the SSD preproduction array above that energy. The sensitivity of the SSD to the electromagnetic component, which has a faster increase with energy than muons, is shown by the up-going trend in this figure.

3.2 Event reconstruction

The surface detector records the footprint of the air shower at the ground. After passing the event selection criteria, standard shower reconstruction methods are applied to estimate the intrinsic properties of the primary cosmic ray. In the SD event reconstruction [6], the information about start times is used to reconstruct the arrival direction of the primary using a spherical model of the shower front.

After a first estimation of the arrival direction, a fit of the lateral distribution function (LDF) of signals at the ground is performed. This distribution arises from a convolution of the energy spectrum and the incoming direction of shower particles with the detector response. Different functional forms are used to describe signals at the ground which generally follow a power law with changing index. In this work, a modified Nishimura-Kamata-Greisen function is employed:

$$S(r) = S(r_{\text{opt}}) \left(\frac{r}{r_{\text{opt}}} \right)^{\beta} \left(\frac{r + r_s}{r_{\text{opt}} + r_s} \right)^{\beta + \gamma}, \quad (3.1)$$

where β and γ are the two slope parameters, and r_{opt} and r_s are the optimal and scale distances, respectively. The optimal distance depends on the grid spacing and was determined to be 1000 m for the SD-1500 m array and 450 m for the SD-750 m array. The signal at the optimal distance is called the shower size (S_{1000} , S_{450}) and is used to reconstruct the energy of the primary. The scale distance and the slope parameter γ allow for more flexibility in the fit at distances far from the core. A change in the steepness of the LDF is expected due to the transition of the electromagnetic and the muonic lateral distributions, the latter being dominant at large distances as electromagnetic particles suffer from attenuation in the atmosphere.

A first example of an event reconstruction can be seen in Fig. 6 (left). The SPMT allows us to extend the unsaturated measure of the signal very close to the core of the shower. It can be seen how signals of the saturated stations can be corrected from ≈ 3000 VEM to ≈ 7000 VEM. The saturated and unsaturated traces of one of these stations are shown in Fig. 6 (right). Another example of an event measured with both the WCD and SSD is shown in Fig. 7 (left). The energy and arrival direction as well as the core position are estimated from the fit to the WCD signals. This information is then used for the fit of the SSD LDF. The profile of the average LDF for the WCD

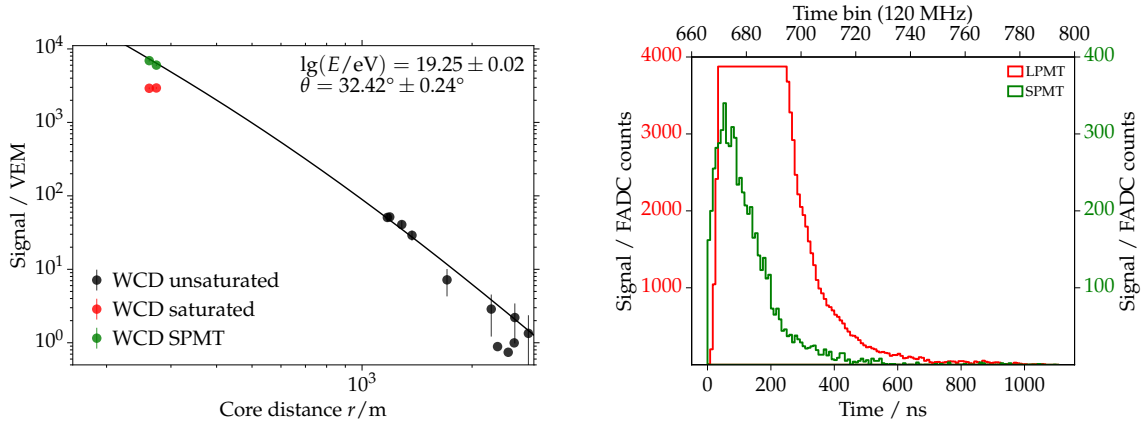


Figure 6: *Left*: Reconstruction of the event with ID: 46663172. The SPMT allows us to measure unsaturated signals close to the core improving the quality of the fit of the LDF. *Right*: Saturated (red) and unsaturated (green) traces of an upgraded station located at 260 m from the shower core.

and SSD signals can be seen in Fig. 7 (right). Each signal was normalized by the corresponding shower size to eliminate any degeneracy due to showers with different energies. As expected, the SSD has a steeper LDF than the WCD, with slightly larger signals close to the shower core and a faster fall off at large distances.

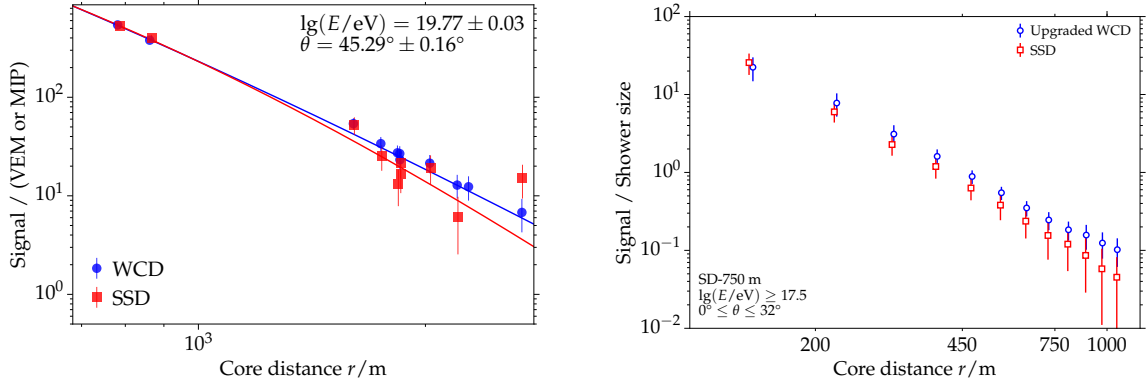


Figure 7: *Left*: Reconstruction of the event with ID: 53431866, with an energy of ≈ 60 EeV. The solid lines show the fit of the lateral distribution function of the WCD (blue) and the SSD (red) signals. *Right*: Profiles of the WCD and SSD signals (no saturation) normalized by the shower size. Reconstructed events of the SD-750 m array with energies $\geq 10^{17.5}$ eV and zenith $\theta \in [0^\circ, 32^\circ]$ were used.

The contribution of the different components to the total signal is encoded in the time traces. The time structure is affected by the distance particles travel from their point of origin in the shower to the detector. In addition, both detectors have different time responses, for example, the signal in the WCD has a relatively larger spread due to the multiple reflections of Cherenkov light in the tank while in the SSD the time spread can be indicative of particles that were produced later in the shower development. An example of calibrated traces for the WCD and SSD can be seen in Fig. 8.

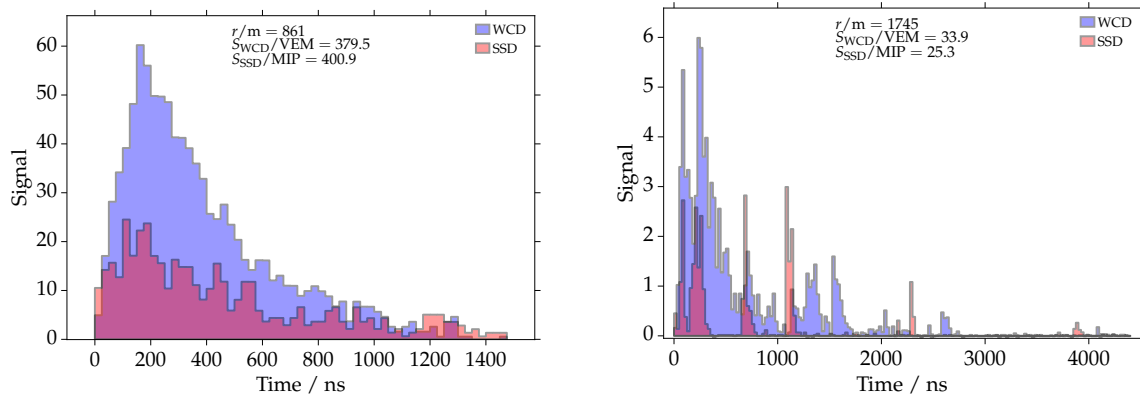


Figure 8: WCD and SSD traces from stations of the event shown in Fig. 7 (left), at different positions.

4. Summary

Stations of the AugerPrime upgrade have been taking data since they were deployed as part of the engineering array at the end of 2016. The results from the calibration have shown a good performance of the detectors as well as good agreement in the WCD signals comparing old and upgraded electronics. In addition, seventy-seven SSDs were deployed and started data acquisition in March 2019 increasing the wealth of events at higher energies. The dependency of the signal ratio with zenith, energy and distance, as well as the normalized LDFs, demonstrate the differences in the sensitivity of the two detectors to the different shower components. Furthermore, the additional SPMT extends the dynamic range of the WCD signals up to about 20000 VEM, allowing for a better reconstruction of events with stations close to the shower core.

References

- [1] Pierre Auger Collaboration, *The Pierre Auger Observatory Upgrade - Preliminary Design Report*, arXiv:1604.03637
- [2] A. Castellina for the Pierre Auger Collaboration, *AugerPrime: the Pierre Auger Observatory Upgrade*, proceedings of the Ultra High Energy Cosmic Rays 2018 Conference, EPJ Web Conf., 210, 06002 (2019).
- [3] D. Nitz for the Pierre Auger Collaboration, these proceedings, PoS(ICRC2019)370.
- [4] Z. Zong for the Pierre Auger Collaboration, proceedings of the 35th ICRC (Busan South Korea), PoS(ICRC2017)449.
- [5] X. Bertou for the Pierre Auger Collaboration, *Calibration of the surface array of the Pierre Auger Observatory*, Nucl. Instrum. Meth. A **568**, 839 (2006).
- [6] D. Mockler for the Pierre Auger Collaboration, these proceedings, PoS(ICRC2019)353



Measurements of Inclined Air Showers with the Auger Engineering Radio Array at the Pierre Auger Observatory

Marvin Gottowik^{*a} for the Pierre Auger Collaboration^{†b}

^a*Bergische Universität Wuppertal, Gaußstraße 20, 42097 Wuppertal, Germany*

^b*Observatorio Pierre Auger, Av. San Martín Norte 304, 5613 Malargüe, Argentina*

E-mail: auger_spokespersons@fnal.gov

Full author list: http://www.auger.org/archive/authors_icrc_2019.html

The Auger Engineering Radio Array (AERA) comprises 153 autonomous radio antenna stations distributed over an area of 17 km². It is operated in coincidence with the surface detector array and fluorescence telescopes of the Pierre Auger Observatory so that hybrid observations of extensive air showers initiated by cosmic rays in the EeV energy range can be performed. A first analysis of the radio emission of more than 500 inclined air showers with zenith angles between 60° and 84° was published last year. Here, we provide an update of the analysis including recent data, approximately quadrupling the event statistics. For inclined showers, the radio signal is found to be distributed over an area of several km², allowing air showers to be measured with radio antennas on a grid as sparse as the 1500 m spacing of the 1600 water-Cherenkov Detector (WCD) stations. For a subset of these inclined events, for which the primary energy can be reconstructed with the data from the WCD array, we verify that the measured radio amplitudes agree with Monte Carlo simulations made using CoREAS. Special challenges of a radio event reconstruction dedicated to inclined air showers will also be discussed.

36th International Cosmic Ray Conference — ICRC2019

24 July – 1 August, 2019

Madison, Wisconsin, USA

^{*}Speaker.

[†]for collaboration list see PoS(ICRC2019)1177

1. Introduction

Ultrahigh energy cosmic rays interact with the Earth's atmosphere and produce an extensive air shower of secondary particles. The detection of air showers using the emitted radio signals has become a standard technique for modern cosmic ray experiments and yields a resolution in the reconstruction of important air shower observables that is competitive with particle and fluorescence detectors [1, 2]. Radio detection combines the advantages of originating from the well-understood electromagnetic component of the air shower, being sensitive to the longitudinal shower profile and having an operational time of nearly 100 %.

As the radio emission is strongly forward-beamed it only illuminates areas with a diameter of a few hundred meters on the ground in the case of vertical showers. This requires a dense antenna grid. However, for inclined air showers the shower develops geometrically more distant to the ground. As there is no absorption or scattering of the emitted radio signal in the atmosphere it is expected that an area of several km² on the ground is illuminated [3]. This would enable measurements of inclined air showers with a sparse antenna array.

2. The Auger Engineering Radio Array

The Pierre Auger Observatory is a hybrid detector for the measurement of ultra high energy cosmic rays located in Mendoza Province, Argentina [4]. Its baseline detectors comprise the world's largest surface detector (SD) array of 1660 water Cherenkov particle detectors covering in total an area of 3000 km², and a fluorescence detector (FD) overlooking the array from 4 sites with 27 telescopes. The Auger Engineering Radio Array (AERA) [5] is situated in the north-western part within the 750 m spaced SD array and in the field of view of the Coihueco and HEAT FD telescopes.

AERA is an engineering array, hence different antenna types, electronics and spacings of the stations have been tested. The deployment was done in three phases starting in summer 2011, the current layout (AERA III) was finalized in March 2015. Today, AERA comprises 153 autonomous radio stations spread over an area of ~ 17 km². In Fig. 1, a map of AERA is shown and the individual deployment phases are indicated. For the dense center of AERA (phase I) 24 logarithmic periodic dipole antennas (LPDA) were deployed on a 144 m grid. For the later phases butterfly antennas were installed with spacings of 250 m, 375 m and 750 m. Each radio station consists of two perpendicularly oriented antennas, aligned with magnetic north and east, which are sensitive to the radio emission in the frequency range from 30 to 80 MHz.

3. Analysis of radio emission from inclined air showers

A previous analysis using 561 air showers (1.5 years of AERA phase II data) has shown the potential of a detection of those inclined air showers, even with a sparse antenna grid, at 1.5 km distances like the SD array [6]. Here, we update that analysis including four more years of AERA phase III data. Furthermore, the CoREAS simulation code [7] has been optimized for inclined air showers and now yields more precise results.

For the particle data we use the standard Auger reconstruction of inclined air showers [8]. For the radio detection we require at least three antenna stations that detected a radio pulse with a

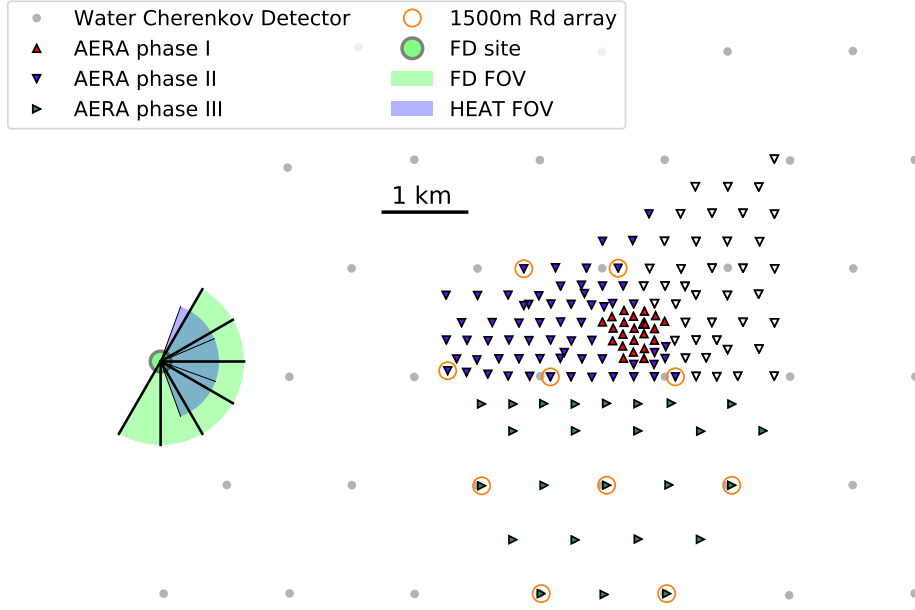


Figure 1: Map of AERA within the Pierre Auger Observatory. The orientation of the triangles indicate the three expansion phases of AERA. The open triangles denote stations that are not capable of receiving an external trigger from the surface detector array and are therefore excluded in this analysis. The orange circles highlight radio stations that will be used for the sparse radio grid in section 3.4.

signal-to-noise ratio¹ above 10. The direction is obtained by a plane-wave fit to the arrival times of the radio pulses. We fit a Gumbel function to the distribution of the opening angle between radio and particle detector reconstruction and only select showers within the 3σ interval around the mean value (cf. Fig. 2). This evaluates to a maximum opening angle of 2.6° . In total we obtain 1972 events in the time period of 26.06.2013 – 8.3.2019 with zenith angles between 60° and 84° . We do not extend the analysis to showers above 84° zenith angle as this requires additional studies of the surface detector reconstruction.

3.1 Characterization of total data set

In the following, we use the arrival direction as reconstructed with the SD. The azimuth distribution (not shown here) shows a clear north-south asymmetry, as showers coming from south have a stronger geomagnetic emission and thus are easier to detect compared to showers coming from the north. The distribution of the \sin^2 of the zenith angle θ increases for more inclined showers (cf. Fig. 2) which indicates an increasing detection efficiency for the coincident observation of air showers with the SD and AERA.

¹Squared maximum of the electric-field amplitude after projection onto the ground plane divided by squared RMS of the background electric-field amplitudes

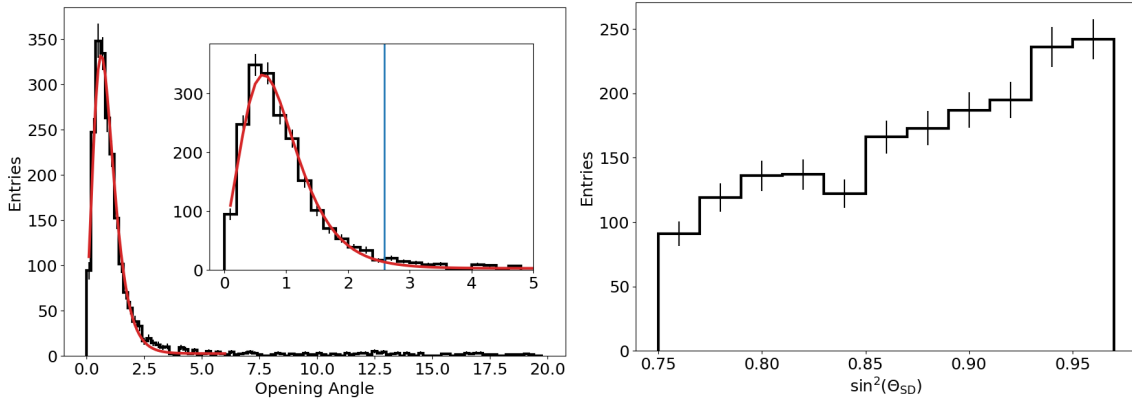


Figure 2: Left: Distribution of the opening angle of particle and radio shower axis. A Gumbel fit is shown in red. The inset figure shows a zoom in on the signal peak, the maximum opening angle used in this analysis, corresponding to a 3σ deviation from the mean, is indicated by the vertical line. Right: Distribution of the \sin^2 of the zenith angles. For each bin, Poissonian errors are shown.

3.2 Size of the radio footprint on ground

To estimate the increase of the radio footprint in the shower plane, excluding projection effects to the ground, we calculate the maximum distance of all antennas with a detected signal from the shower axis reconstructed from particle data. Fig. 3 shows a clear increase of this distance with increasing zenith angle. Qualitatively, this is in agreement with the assumption of forward-beamed radio emission without absorption and scattering in the atmosphere.

A particularly interesting event is shown in Fig. 4. The shower core, as reconstructed by the surface detector, is approximately 12 km away from AERA. In total 14 radio stations have a measured signal clearly above noise. The radio direction reconstruction agrees within 1.2° to the reconstruction of the particle detector. This example shows, that for very inclined air showers, the radio footprint can be significantly larger than the “particle footprint” on the ground.

3.3 Comparison with CoREAS simulations

For this analysis we adapt the standard selection of events with a proper reconstructed energy by the surface detector. Normally the zenith angle is limited to 80° , here we extend the analysis up to 84° and lower the energy threshold to $10^{18.5}$ eV. This results in a degradation in the reconstruction performance that is not relevant for this analysis, as the energy determination remains bias-free and has a resolution better than 25 % [9] (19.3 % for the standard SD event selection of inclined air showers [8], further details in [6]). This subselection yields 170 events. The energy distribution of this subset is shown in Fig. 5, reaching up to $10^{19.8}$ eV.

For each event we perform one full Monte Carlo Simulation with CoREAS using the reconstruction of the surface detector as input. We only simulate proton primaries to obtain maximal shower-to-shower fluctuations, the impact of heavier primary particles is below 10 % and thus smaller than the uncertainty of the energy scale and calibration [6]. We perform a detailed radio detector simulation for each simulated shower, add measured noise and analyse the simulations in the same way as the measured events. A direct comparison of the amplitudes for each antenna

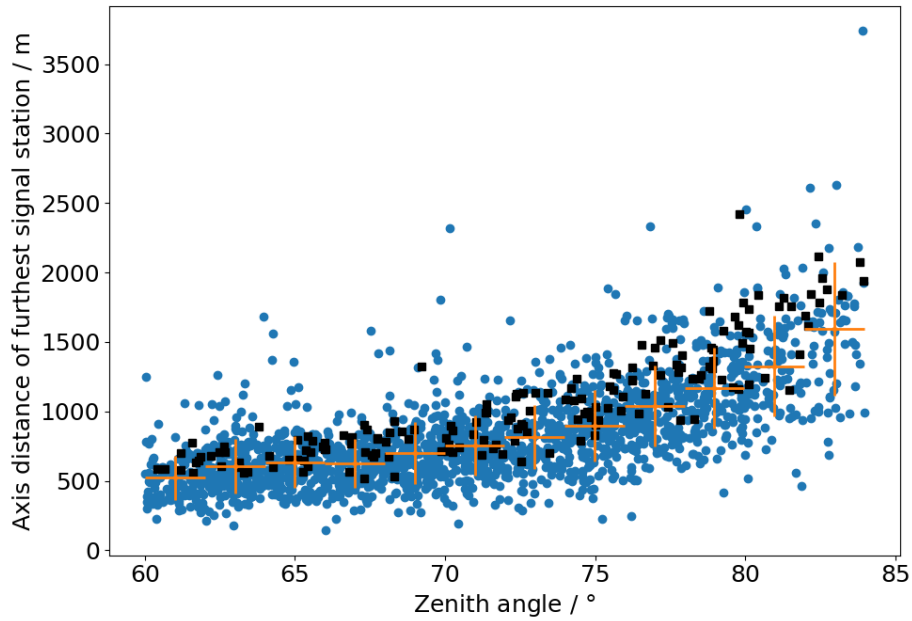


Figure 3: Maximum axis distance of a radio station with a detected signal above noise as a function of zenith angle. Black squares represent the events that have a reconstructed energy from the surface detector (see section 3.3), the remaining events are shown as blue circles. The profile is added in orange, binned in 2° zenith angle.

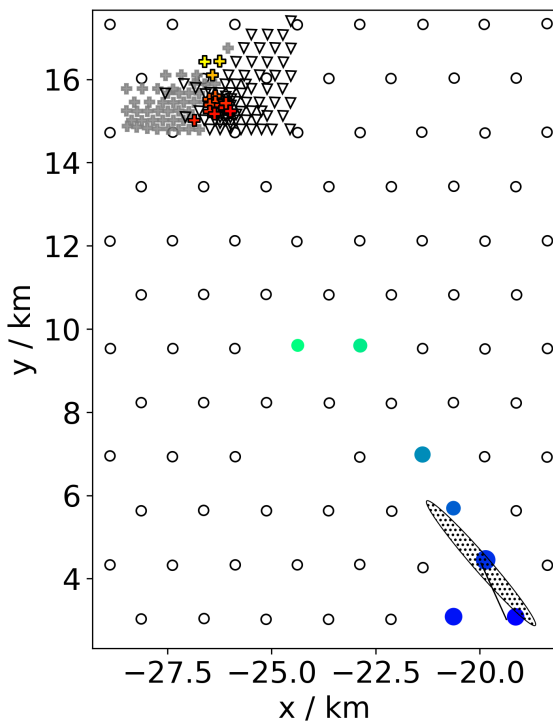


Figure 4: Visualization of the event with the very large radio footprint. The colored circles indicate signals measured with the surface detector, color indicating arrival time and size encoding deposited energy per station. The AERA stations with a detected signal are marked as colored pluses, color and size denote arrival time and energy fluence, respectively. Gray pluses represent stations that did not detect a signal clearly above noise. The open triangles are stations which are not used in this analysis. The impact point reconstructed with the SD is indicated by the one-sigma error ellipse. The line indicates the projection of the shower axis onto the ground.

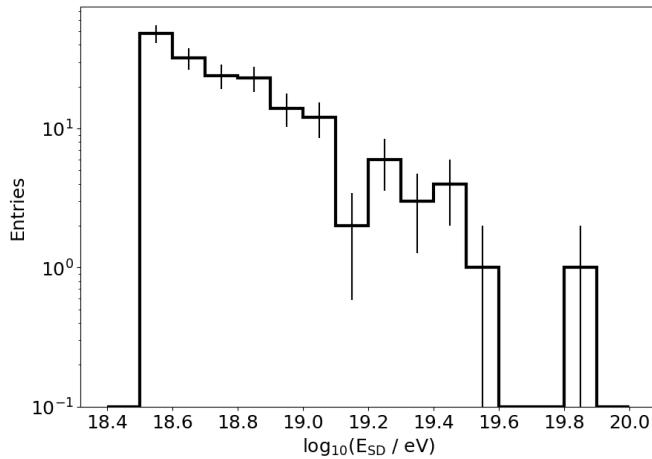


Figure 5: Distribution of the energy reconstructed with the surface detector. For each bin Poissonian errors are shown.

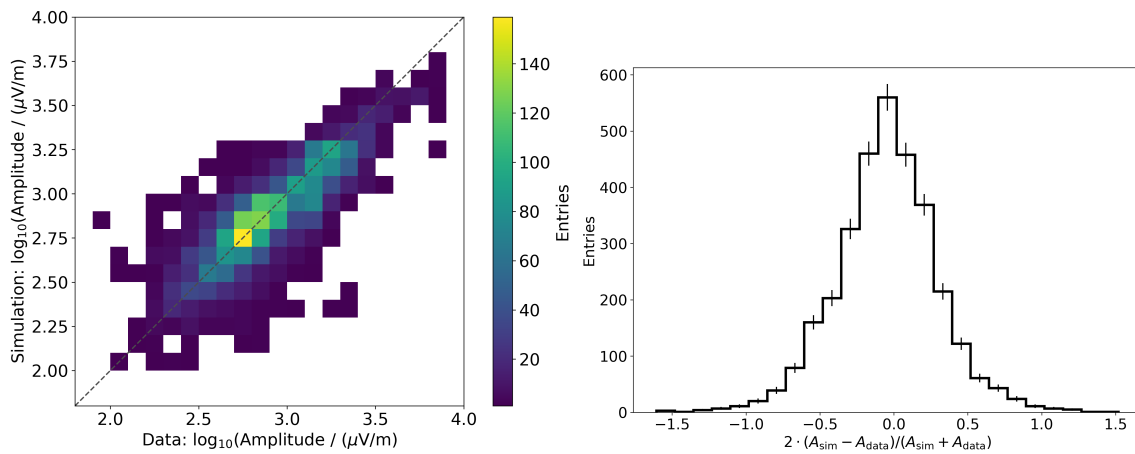


Figure 6: Correlation of the peak amplitudes of measured data and CoREAS simulations for the subset of events with a reconstructed SD energy visualized as the two dimensional histogram and the one dimensional projection.

pulse individually shows a good agreement between data and simulation, see Fig. 6. On average, the simulations underpredict the measured amplitudes by 5% with a spread of 35%. The large spread is caused by the uncertainty of the reconstructed energy and estimated shower core and will likely improve with a radio reconstruction of inclined air showers.

3.4 Prospects of a sparse radio grid

To study the prospects of radio detection using a sparse antenna grid we thin out AERA to an approximate 1.5 km grid. This results in 5 stations for AERA phase II and 10 stations for AERA phase III (cf. Fig. 1). We rerun the analysis on the same raw data and obtain 189 reconstructed radio events. For each event where the opening angle of particle and radio shower axis calculated with the full AERA is smaller than 2.6° we determine the their difference for a sparse AERA grid. On average the opening angle increases by only 0.1° from 0.6° for AERA to 0.7° for the sparse grid.

4. Challenges for radio reconstruction of inclined air showers

The radiation energy, i.e. the integral of the lateral distribution function (LDF) of the energy fluence in the form of radio signals, was shown to be a suitable estimator of the primary cosmic ray energy in the case of vertical air showers [10, 11]. For inclined air showers two new asymmetries have to be taken into account for a precise reconstruction of the radiation energy arising from the propagation of the radio emission through the atmosphere.

The first asymmetry is introduced by early-late effects, i.e. the fact that signals from “early” part of the shower correspond to a narrower beamed emission than signals from the “late” part. The axis distance of each antenna in the shower plane has to be corrected to match a projection along the line of sight from the position in the ground plane to the source, i.e. we describe the LDF in terms of off-axis angle. This can be corrected to first order by assuming that the radio emission originates from a point source located at a known shower maximum X_{\max} [12].

The second observed asymmetry is related to a difference in the effective refractive index seen by close and far antennas. This results in a Cherenkov compression of the radio emission at a different off-axis angle. We simulate antennas on the positive and negative $\mathbf{v} \times (\mathbf{v} \times \mathbf{B})$ axis (\mathbf{v} : shower axis, \mathbf{B} : magnetic field) and project them onto the ground. On this axis the two different components of the radio emission decouple [13]. Thus we do not have to take interference effects into account. The simulated radio stations are then shifted into the shower plane and the early-late corrections are applied. In Fig. 7 we show the difference in the LDF for an air shower coming from south with a zenith angle of 85° . A clear difference in the peak position is shown that disturbs the radial symmetry assumed internally by all current LDF models. This asymmetry vanishes for simulations where the refractive index is fixed to 1 and increases for larger refractive indices.

A radio reconstruction for inclined air showers that include these asymmetries is currently under investigation [14].

5. Conclusion

With AERA, we have measured the radio emission of 1972 air showers with a zenith angle between 60° and 84° . We have shown that the size of the radio emission footprint increases with the zenith angle and illuminates areas of several km^2 on the ground. We have shown that the amplitudes predicted by CoREAS correspond within systematic uncertainties to the measurements. Further work is needed to establish a radio reconstruction of inclined air showers that includes the early late and refractive index asymmetry and to obtain a reliable determination of cosmic ray observables.

Even with a sparse grid of radio antennas with a spacing of 1.5 km we can detect 189 air showers. The accuracy of the reconstructed shower axis decreases only marginally. The successful detection of these events motivated the recent decision to upgrade each station of the surface detector with an additional radio antenna. The upgrade will increase the geometric area equipped with radio antennas from 17 km^2 to 3000 km^2 , thus enabling the detection of radio emission from cosmic rays at the highest energies [15].

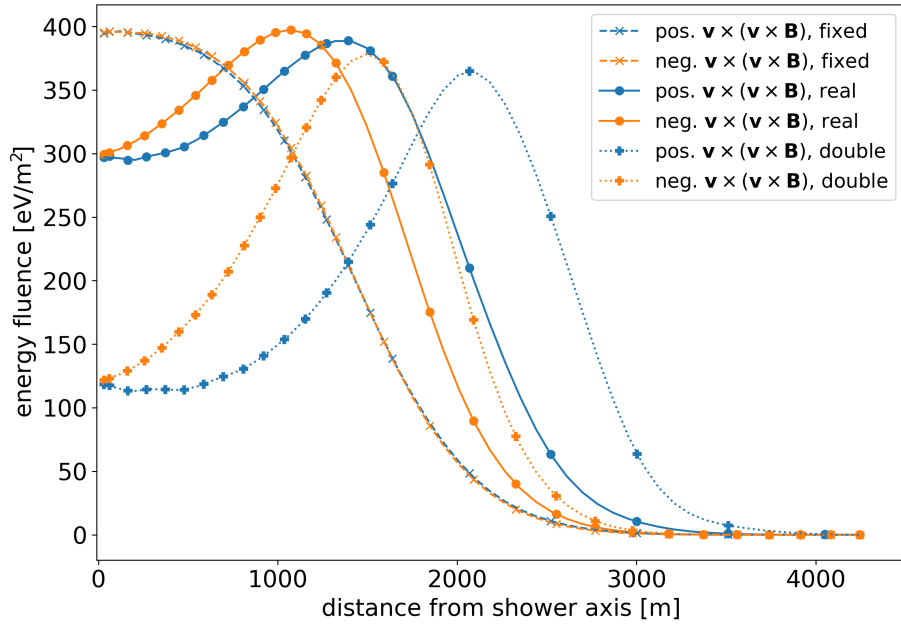


Figure 7: Example of the refractive index asymmetry using different scalings of the refractive index in the CoREAS simulations. We use a constant value of 1 for the whole atmosphere (fixed), a realistic model with a scaling of the refractive index at sea level ($n_0 - 1 = 3.12 \times 10^{-4}$) to higher altitudes (real) and a model where we increased the refractive index at sea level by $1 + 2 \cdot (n_0 - 1)$ (double). The fluence values on the positive and negative $\mathbf{v} \times (\mathbf{v} \times \mathbf{B})$ axis are interpolated for convenience.

References

- [1] T. Huege, Physics Reports **620** (2016) 1 -52
- [2] F. G. Schröder, Progress in Particle and Nuclear Physics **93** (2017) 1 - 68
- [3] T. Huege, A. Haungs, JPS Conf. Proc. **9** (2016) 010018
- [4] A.Aab [Pierre Auger Collaboration], Nucl. Instrum. Meth. A **798** (2015) 172
- [5] E. M. Holt for the Pierre Auger Collaboration, PoS (ICRC2017) 492
- [6] A.Aab [Pierre Auger Collaboration], JCAP **1810** (2018) 026
- [7] T. Huege, M. Ludwig, C. W. James, AIP Conf. Proc. **1535** (2013) 128–132
- [8] A.Aab [Pierre Auger Collaboration], JCAP **1408** (2014) 019
- [9] H. Dembinski, Ph.D. thesis, RWTH Aachen University (2009), https://web.physik.rwth-aachen.de/~hebbeker/theses/dembinski_phd.pdf
- [10] A.Aab [Pierre Auger Collaboration], Phys. Rev. D **93** (2016) 122005
- [11] A.Aab [Pierre Auger Collaboration], Phys. Rev. Lett. **116** (2016) 241101
- [12] T. Huege, L. Brenk, F. Schlüter, 8th ARENA (2018), [arXiv:1808.00729]
- [13] C. Glaser et al., JCAP **1609** (2016) 024
- [14] T. Huege, F. Schlüter, L. Brenk, PoS (ICRC2019) 294
- [15] B. Pont for the Pierre Auger Collaboration, PoS (ICRC2019) 395



The AMIGA underground muon detector of the Pierre Auger Observatory - performance and event reconstruction

Ana Martina Botti*^{a,b} for the Pierre Auger Collaboration^{c†}

^a*Instituto de Tecnologías en Detección y Astropartículas, CNEA-CONICET-UNSAM, Buenos Aires, Argentina*

^b*Karlsruhe Institute of Technology, Karlsruhe, Germany*

^c*Observatorio Pierre Auger, Av. San Martín Norte 304, 5613 Malargüe, Argentina*

E-mail: auger_spokespersons@fnal.gov

Full author list: http://www.auger.org/archive/authors_icrc_2019.html

The Auger Muons and Infill for the Ground Array (AMIGA) aims to both lower the detection threshold of the Pierre Auger Observatory down to energies of $\sim 10^{16.5}$ eV and to directly measure the muon content of extensive air showers. AMIGA consists of an array of coupled water-Cherenkov and buried scintillation detectors deployed in two superimposed triangular grids of 433 m and 750 m spacings. Each underground detector has a total area of 30 m² buried at a depth of 2.3 m, to shield it from the shower electromagnetic component. The scintillation plane is segmented in plastic-scintillator strips with embedded wavelength-shifter optical fibers coupled to a common optical sensor. Before proceeding to the construction of the full-size array, an engineering array was operated until November 2017 to validate and optimize the design, and to evaluate the performance of the detection system. During this phase, scintillation areas of 5 m² and 10 m² and two optical sensors, photomultiplier tubes and silicon photomultipliers, were tested. In this work, we present the status and performance of the array currently equipped with silicon photomultipliers, along with the timing performance and geometry reconstruction of modules equipped with photomultiplier tubes. Analyses and results are based on both laboratory and field measurements. Scintillation areas of 10 m² and silicon photomultipliers as readout have been selected as the baseline design for the full-scale AMIGA array.

36th International Cosmic Ray Conference — ICRC2019

24 July – 1 August, 2019

Madison, Wisconsin, USA

*Speaker.

†for collaboration list see PoS(ICRC2019)1177

1. Introduction

Cosmic rays with energies above $10^{17.5}$ eV are studied at the Pierre Auger Observatory [1] through a hybrid-detection technique, composed of a fluorescence detector (FD) and a surface detector (SD). The FD has 27 fluorescence telescopes distributed at four sites at the edge of the SD. The SD consists of an array of 1660 water-Cherenkov detectors (WCDs) with a 1500 m spacing (SD-1500), covering a total area of 3000 km^2 and a denser array with a 750 m spacing (SD-750) extending over 23.5 km^2 . This smaller array is one of the two components of the Auger Muons and Infill for the Ground Array (AMIGA) enhancement [2]. More recently, an even denser array at a 433 m spacing (SD-433) with an area of 1.9 km^2 is being deployed to extend the SD energy threshold down to $10^{16.5}$ eV.

AMIGA also provides direct measurements of the muon components of the extensive air showers with an underground muon detector (UMD) buried at 2.3 m associated with each AMIGA SD-750 WCD. Each muon detector consists of three 10 m^2 modules segmented into 64 plastic-scintillator strips with wavelength-shifter optical fibers that conduct the light to a photo-detector located at the center of the module [2]. During the prototype phase (finalized in November 2017), an engineering array was deployed for proof of concept, physics validation, and optimization of the detector design. In Fig. 1 the layout of the muon detector engineering array is shown. During this prototype phase, 5 m^2 and 10 m^2 modules were tested, as well as two different photo-detectors: a 64-pixel multi-anode photomultiplier tube (PMT) and an array of 64 silicon photomultipliers (SiPMs). Upon completion of these tests, 10 m^2 modules equipped with SiPMs were chosen for the, currently ongoing, production phase of the UMD, which is also part of AugerPrime, the upgrade of the Pierre Auger Observatory [3]. As a main part of the upgrade, surface scintillator detectors (SSDs) [4], and radio detectors [5], will be installed on top of each WCD in the SD-1500 array. These detectors aim to enhance the separation of the muonic and the electromagnetic component of air showers measured with the WCDs, more specifically, the SSDs for not very inclined showers and the radio detector for horizontal ($>75^\circ$). Each of these instruments will provide complementary information on the air showers composition, which will contribute to an improved estimation of the properties of cosmic-ray primaries. In particular, the UMD will improve the cosmic ray mass identification in the ankle region of the energy spectrum. Furthermore, since it directly measures muons of a sub-sample of showers observed by the upgraded Auger surface detector, the UMD will, in particular, serve as verification and fine-tuning of the methods used to extract shower muon content using SSDs and WCDs.

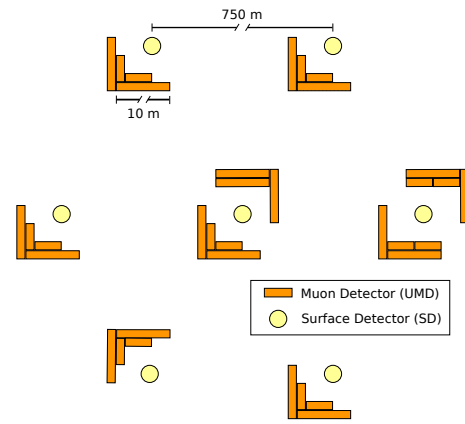


Figure 1: Layout of the AMIGA engineering array. In the prototype phase, each 30 m^2 muon detector was segmented in 5 m^2 and 10 m^2 modules. Also, two positions were equipped with extra *twin* modules to assess the detector uncertainties. Two optical sensors were tested, multipixel photomultiplier tubes and silicon photomultipliers.

2. The AMIGA underground muon detector

To attain a broad dynamic range, the readout electronics of the UMD modules implements both *counter* and *integrator* modes. Schematics of the electronics can be found in Fig. 2. The *counter* mode independently handles the 64 SiPM signals through a pre-amplifier, fast-shaper, and a discriminator, built within each channel of two 32-channel Application-Specific Integrated Circuits (ASICs). The discriminator signal is sampled at 320 MHz (3.125 ns sample time) with a Field-Programmable Gate Array (FPGA) into 64 2048-bit traces. In each trace, a “1”-bit is output if the signal is above the discriminator threshold, set at 2.5 photon-equivalents (PEs) to reject most of the SiPM dark rate [6], and a “0”-bit otherwise. In this working mode, muons can be identified as sequences of “1”s in the binary traces. A simulated single-muon trace is shown in the middle panel of Fig. 2.

On the other hand, with the *integrator* mode the 64 SiPM signals are added up analogically and the result is amplified with low- and high-gain amplifiers. The signals are then sampled at 160 MHz (6.25 ns sample time) with two Analog-to-Digital Converters (ADCs) resulting in two waveforms of 1024 samples. In the right panel of Fig. 2, a simulated trace of a single-muon signal of the *integrator* mode is displayed. The number of muons can then be estimated by dividing the signal charge by the mean charge of a single muon.

Both modes work in a complementary fashion. The *counter* mode is limited by the detector segmentation; two muons arriving at the same strip simultaneously will be counted as a single particle. This effect limits the number of muons that can be detected at the same time. The *integrator* mode improves this limit and extends the detector dynamic range to measure higher muon densities, thus reaching distances closer to the shower core. Furthermore, each working mode has different biases, resolutions, and systematics, and still, they both measure simultaneously the same particles. A combined analysis is foreseen [7] and could be useful to understand these features and to reduce their impact in the detection uncertainties.

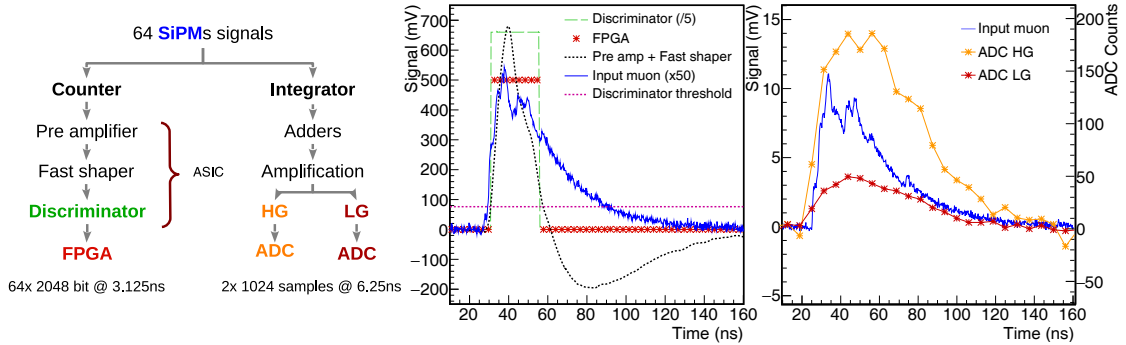


Figure 2: (Left) Schematics of the AMIGA muon detector electronics. The modules implement a *counter* and an *integrator* mode. In the *counter* mode, the output consists of 64 binary traces in which muons can be identified as sequences of “1”. The *integrator* mode outputs two waveforms from which the muon number can be estimated dividing the signal charge by the mean charge of a single muon. (Middle) A simulated single-muon trace in the *counter* mode. The signal from the SiPM and the discriminator pulse are re-scaled for illustration. The FPGA outputs a “1”-bit in the binary trace when the fast-shaper output is above the discriminator threshold. (Right) A simulated single-muon trace in the *integrator* mode. The two ADC outputs (low- and high-gains) are shown.

The main goal of the UMD is to measure the muons of extensive air showers, including their arrival time. As described before, particle counting is performed individually muon-by-muon with the *counter* mode and proportionally to the signal charge with the *integrator* mode. The read-out electronics of the *counter* mode produces binary signals relying on the signal amplitude while for the integrator mode the output signal is based on the total-signal charge. As SiPMs are located at an extreme of each scintillator strip, it is important to characterize the attenuation of the signal along the optical fibers and its impact on the detector efficiency. In the following sections, the optical-fiber attenuation is quantified with laboratory measurements. For this purpose, a dedicated setup was mounted on a test bench and single-muon signals were acquired with the standard UMD electronics. The event trigger was performed by a movable muon telescope and the whole length of the strips was swept in steps of 0.5 m.

3. The *counter* mode muon counting and efficiency

To obtain the number of particles reaching the UMD with the *counter* mode, a counting strategy that optimizes the detector performance needs to be determined. The number of “1”s in the binary trace to identify muons must be selected according to the time span of the muon signal and noise, as well as an inhibition window. The inhibition window consists of a time window in which the searching process for muon identification is stopped after a muon is found. This window is optimized to neither count the same muon twice (over-counting due to a short window) nor to count two muons as one (under-counting due to a long window), and it is the same for all the UMD modules. In Fig. 3 top panel, the signal width at different positions on the scintillator strip is shown, both with laboratory and simulated data. The light-output obtained when a muon impinges the scintillator strip is attenuated by the optical fiber (see Fig. 4). Therefore, the signal width in the muon detector depends on where on the scintillator strip the muon arrived, as it can be seen in Fig. 3 top. If we consider all the signal widths within a 3σ deviation from the mean, most of muon signals last between 12 (37.5 ns) and 4 (12.5 ns) samples. Furthermore, the noise produced by dark rate of the SiPM, which can reach the 2.5 PEs discriminator threshold owing to the inner-cells crosstalk [8], has a typical width of less than 12.5 ns. According to this data, an inhibition window of 37.5 ns, and a minimum width of 12.5 ns maximize the signal-to-noise ratio in the *counter* mode. With this counting strategy, the probability of over-counting per event is reduced by a factor of ~ 2.7 with respect to a strategy in which a minimum width of 3.125 ns (one sample) is requested to count a muon.

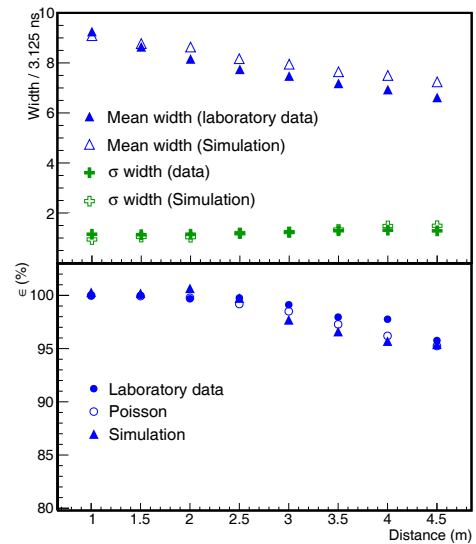


Figure 3: (Top) Width (mean) and width (RMS) over sample time in the *counter* mode as a function of the distance to the SiPM within the detector with both laboratory and simulated data of single muons. (Bottom) Efficiency as a function of the position estimated from laboratory data, simulations, and a Poisson prediction (see text).

The resulting efficiency is shown in Fig. 3 bottom, as a function of the position on the scintillator strip, as measured in data and simulations. The estimation is compared to a simple prediction based on the measured mean number of PEs (see Fig. 4) as a function of the position on the strip. The prediction for the efficiency is obtained by integrating the Poissonian expectations given by that mean value, between the threshold (at 2.5 PEs) and infinity. The Poissonian prediction shows the efficiency loss produced by muon signals with less than 2.5 PEs, which is the *counter* mode threshold. Therefore, the agreement between data and prediction denotes that there is not a significant efficiency loss in the signal processing or in the signal analysis. There is also not significant over-counting due to noise and wide muon signals, which would be seen as efficiencies above 100% (a very small over-counting is then seen for the simulated data at 2 m, resulting in $\epsilon \approx 100.5\%$). By averaging over the distance we obtained a total efficiency of 99.7% and 98.5% for the 5 m² and 10 m² modules, respectively.

4. The *integrator* mode attenuation and calibration

As it was mentioned before, the signal attenuation in the optical fibers has an impact on the muon identification efficiency. In the *integrator* mode, the number of muons is estimated by dividing the total signal charge by the mean charge of a single muon. For this reason, the signal attenuation in the optical fiber has an impact on the detector fluctuations. To understand these fluctuations, measurements of analog SiPM pulses (both muons and dark-rate PEs) were acquired with an oscilloscope at different positions on the scintillator strip. With these measurements, the number of PEs per muon was estimated in charge and amplitude as the ratio between the muon signal and a single PE. The results are shown in Fig. 4 left panel. Due to the time distribution of photons reaching the optical sensor, the curves in charge and amplitude differ significantly from each other (by a factor ≈ 2). Note that the *counter* mode is sensitive to the signal amplitude (as it implements an amplitude threshold) whereas the *integrator* mode is sensitive to the signal charge. In the right panel of Fig. 4 the signal mean charge of single muons in the low- and high-gain ADC channels as a function of the position on the scintillator strip are shown. The attenuation is displayed both for laboratory and simulated data. It is apparent how the PEs attenuation has an important impact on the detector resolution since the total charge of single-muon signals between the beginning and end of the strip differs by a factor of two. Still, this impact significantly diminishes with the arrival of several muons in the whole of the detector module, for which the *integrator* mode is optimized to operate.

To calibrate the ADC channels, the mean charge per muon is needed. A method to obtain this value is to compare the charge in the ADC channels to the number of muons in the *counter* mode using shower events. In Fig. 5 left panel, the signal charge in the *integrator* mode is plotted against the number of muons (N_μ) estimated with the *counter* mode for a 10 m² module deployed in the Observatory. The mean charge for each N_μ is shown along with the individual events, from which the signal dispersion can be seen. The ADC calibration is achieved by fitting the data with a linear fit, where the slope corresponds to the single-muon mean charge.

As illustration, in Fig. 5 right panel, the muon densities measured with the *counter* and *integrator* modes for an example event with a reconstructed energy of $(9.5 \pm 0.4 \pm 0.2) \times 10^{17}$ eV and zenith angle of $(21.8 \pm 0.4)^\circ$ is displayed. The geometry and energy were obtained from the

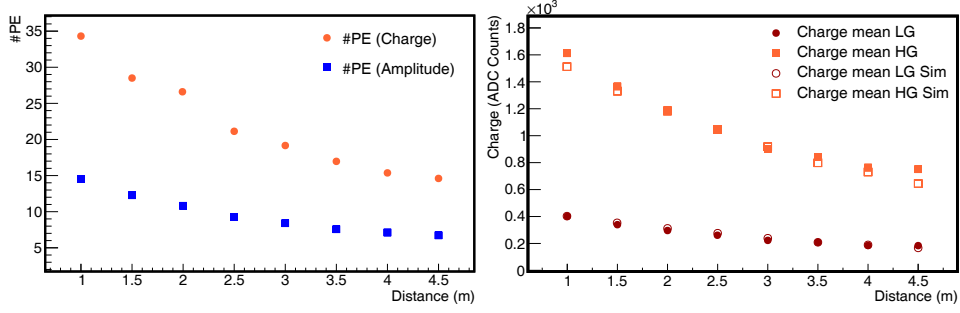


Figure 4: (Left) Number of PEs at the SiPM per muon in charge and amplitude as a function of the position on the scintillator strip. It can be seen how the curves in charge and amplitude differs since the detected photons are time distributed according to the scintillator and optical fiber decays. (Right) Mean charge as a function of the position on the scintillator strip for single-muon signals.

SD-750 reconstruction [10]. The muon lateral distribution function (MLDF) [9] was fitted using only the *counter* mode. Note that the reconstruction of data with the two modes is not expected to entirely agree at this point, as the final corrections for different sources of bias (from clipping corners, noise, etc. [11]) are not yet implemented. Still, it is apparent that both muon-density estimations are quite consistent for this example event.

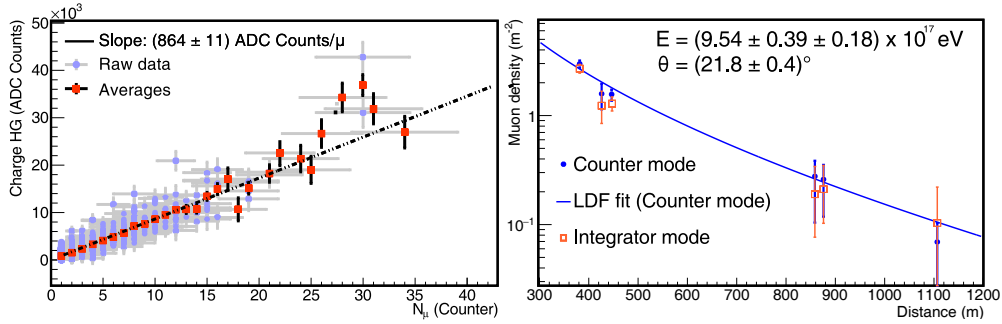


Figure 5: (Left) Signal charge in the *integrator* mode as a function of the number of muons estimated with the *counter* mode for an example UMD module. (Right) Muon lateral distribution function reconstructed with the *counter* mode alone for an example event. The muon densities estimated with the ADC channel are also shown for reference.

5. Timing studies

Before entering into the production phase and selecting SiPMs as optical sensors, multi-anode photomultipliers (PMTs) were tested in the engineering array. During this phase, over one year of calibrated PMT data (October 2015 - October 2016) was acquired [11]. Originally, the AMIGA muon detector was specifically designed to provide direct measurements of muon densities [2]. Results on the muon contents above $10^{17.5}$ eV have been reported using the calibrated PMT data [12]. Nevertheless, the UMD is also suitable to study the muon timing. The measured arrival-time distribution may be used to reconstruct the shower-axis direction of each event.

To reconstruct the shower axis, the arrival time of the muons in GPS coordinates is required. Since the UMD modules do not have an integrated GPS service, the associated WCD timing is exported. The trace of the UMD modules is delayed with respect to the trace of its WCD by a fixed

offset. Each UMD module is synchronized against its associated WCD using the arrival time of the air shower particles.

The timing of the muons observed at different positions is used to determine the arrival direction of the primary particle. The zenith (θ) and azimuth angles (φ) of the shower axis are determined by reconstructing a shower front. To this aim, it is necessary to determine a time observable in each detector. In the SD detectors, the time observable is the start time of the signals (t_0). Since the estimation of t_0 with a low bias requires many particles in a detector, and the UMD modules frequently contain a few muons, the t_0 estimator is not a suitable time observable for the UMD. Instead, an unbiased time estimator is provided by statistics like the median arrival time (t_{50}) observed in a position. The time observable t_{50} , its error model, and the curvature radius (R) are the three ingredients required to reconstruct the geometry of the air showers observed by the UMD.

The shower front is modeled as a bubble expanding at the speed of light from a center (\vec{r}_0) located one curvature radius away from the core position (\vec{r}_c) in the direction of the axis. The arrival time of the front at the UMD module is $t(\vec{r}_i) = \frac{\|\vec{r}_i - \vec{r}_c - \vec{r}_0\| - R}{c} + t_c$, where t_c is the arrival time of the core. The front model depends on the zenith and azimuth angles and on the curvature radius through the position of the shower center \vec{r}_0 . The core position is fixed with the value provided by the SD reconstruction [10]. In the left panel of Fig. 6 the geometrical reconstruction of an event that triggered the whole UMD engineering array is shown. The data corresponds to the t_{50} measured in each position with respect to a plane front oriented with the axis reconstructed by the UMD. To crosscheck the reconstruction results, the distribution of the angle (η) between the axes reconstructed by the SD and UMD is shown in Fig. 6 right panel. The angle that contains 68% of the events ($\eta_{68\%}$) was chosen to be the estimator of the deviation between the UMD and SD axes. For events with energy above $10^{17.5}$ eV, $\eta_{68\%} = 1.8^\circ$.

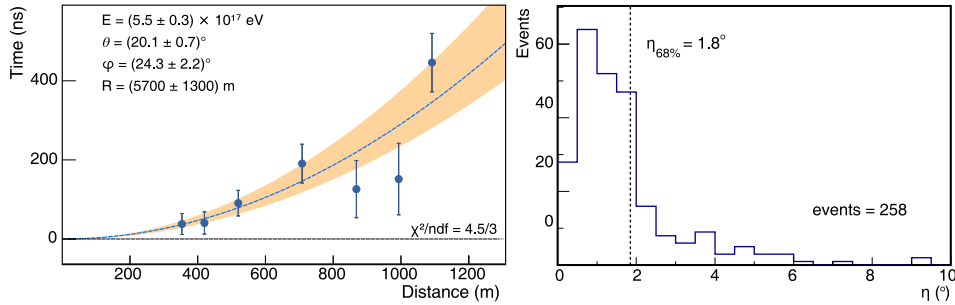


Figure 6: (Left) Delays of t_{50} of an example event measured by the UMD with respect to a plane front oriented with the arrival direction reconstructed by the UMD. (Right) Angle between the axes reconstructed by the UMD and the SD for events with energy above $10^{17.5}$ eV.

As events with high multiplicity in the number of detectors, like the one shown in Fig 6, are rare in the engineering array ($\sim 60\%$ less than the total of events), the radius of curvature has to be fixed in the fit. Therefore, to estimate the curvature radius, the delay of t_{50} with respect to a plane shower front oriented with the SD axis as a function of the distance was measured. For each zenith angle, the median delay (\tilde{t}) was computed in each distance bin (d) and fitted with a spherical front $\tilde{t} = t_0 + \frac{d^2}{2cR}$ as it can be seen in the left panel of Fig. 7. From these fits, the radius of curvature (R) as a function of the zenith angle was obtained as it is displayed in the right panel of Fig 7. The radius of curvature using simulations of iron and proton primaries was also computed, using

QGSJETII-04 as hadronic model. These results are encouraging and prove the potential of the UMD to perform studies on the time distribution of arriving muons in extensive air showers with energies above 1 GeV, which is the muon energy threshold of the UMD.

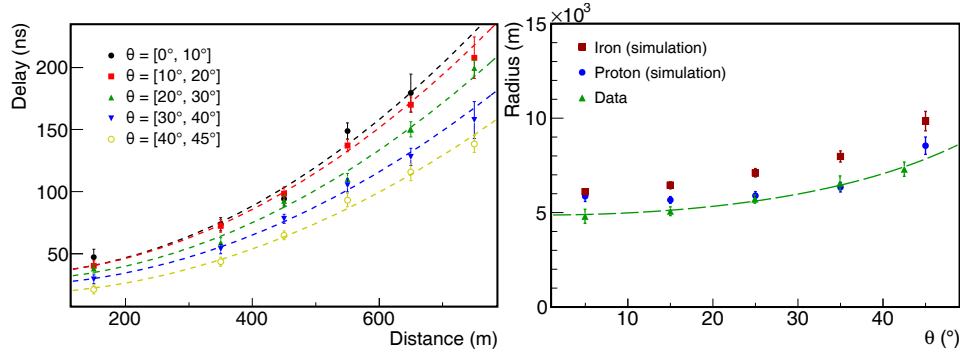


Figure 7: (Left) Residual of the UMD t_{50} with respect to a plane perpendicular to the axis fitted with the SD data for each zenith angle as a function of the distance to the shower core for energies above $10^{17.5}$ eV. From the data, the radius of curvature is obtained. (Right) Radius of curvature as a function of the zenith angle for both data and simulations (QGSJETII-04) with proton and iron primaries.

6. Conclusions

The status of the AMIGA underground muon detector has been presented. The two operation modes (*counter* and *integrator*) have been described, along with their performance in the laboratory. A strategy that optimizes the signal-to-noise ratio in the *counter* mode has been selected based on laboratory data. Furthermore, the *integrator* mode has been calibrated using shower data to obtain the muon densities with both modes. In addition, a new analysis using the arrival time of muons has been presented, showing the capabilities of the UMD to reconstruct the shower geometry and to perform studies on the time distribution of the arriving muons in extensive air showers. These were conducted with modules instrumented with PMTs and will be adapted to SiPMs.

The UMD production phase - with scintillation areas of 10 m^2 and SiPMs as readout - has already started. The full AMIGA array is expected to be completed by 2020.

References

- [1] The Pierre Auger Collaboration. NIM A **798** (2015) 172-213.
- [2] The Pierre Auger Collaboration. JINST **11** (2016) P02012.
- [3] The Pierre Auger Collaboration arXiv:1604.03637 (2016).
- [4] Alvaro Taboada for the Pierre Auger Collaboration. These conference proceedings. PoS (ICRC2019) 434.
- [5] Marvin Gottowik for the Pierre Auger Collaboration. These conference proceedings. PoS (ICRC2019) 274.
- [6] The Pierre Auger Collaboration. JINST **12** (2017) P03002.
- [7] Darko Veberič. Appl. Opt. **51** (2012) 139-147.
- [8] D. Renker, E. Lorenz. JINST **4** (2009) P04004.
- [9] D. Ravnani, et al. Astropart. Phys. **82** (2016) 108-116.
- [10] The Pierre Auger Collaboration. JCAP **08** (2014) 019.
- [11] S. Müller for the Pierre Auger Collaboration. Ultra High Energy Cosmic Rays proceedings (2018) 02013.
- [12] Federico Sánchez for the Pierre Auger Collaboration. These conference proceedings. PoS (ICRC2019) 411.



A Large Radio Detector at the Pierre Auger Observatory – Measuring the Properties of Cosmic Rays up to the Highest Energies

Bjarni Pont^{*a} for the Pierre Auger Collaboration^{†b}

^a*Department of Astrophysics/IMAPP, Radboud University, P.O. Box 9010, NL-6500 GL Nijmegen, The Netherlands*

^b*Observatorio Pierre Auger, Av. San Martín Norte 304, 5613 Malargüe, Argentina*

E-mail: auger_spokespersons@fnal.gov

Full author list: http://www.auger.org/archive/authors_icrc_2019.html

High-energy cosmic rays impinging on the atmosphere of the Earth induce cascades of secondary particles, the extensive air showers. Many particles in the showers are electrons and positrons, which due to interactions with the magnetic field of the Earth emit radiation with frequencies of several tens of MHz. In the last years, huge progress has been made in measuring the characteristics of extensive air showers through their radio signal at these frequencies.

The radio technique is now routinely applied to measure the properties of cosmic rays, such as their arrival direction, their energy, and their particle type/mass. Air showers with zenith angles above 60° have a large footprint of the radio emission on the ground which can be detected with sparse arrays with kilometer-scale spacing. With the Auger Engineering Radio Array (AERA) these "horizontal air showers" are measured, demonstrating the feasibility of the radio technique for highly inclined showers.

At present, the Auger Collaboration is upgrading its detectors. The upgrade includes the installation of radio antennas on each of the 1661 water-Cherenkov detectors of the array. The main objective of the radio upgrade (Radio Detector) is to measure horizontal air showers and to determine the properties of cosmic rays up to the highest energies. The combination of water-Cherenkov detectors and radio antennas will provide muon-electron separation for horizontal air showers at the highest energies.

Details of the technical implementation and the expected performance will be presented.

36th International Cosmic Ray Conference — ICRC2019

24 July – 1 August, 2019

Madison, Wisconsin, USA

^{*}Speaker.

[†]for collaboration list see PoS(ICRC2019)1177

1. Introduction

The Pierre Auger Observatory, located in western Argentina, is the world's largest cosmic-ray Observatory [1]. The objectives of the Observatory are to probe the origin and characteristics of cosmic rays above 10^{17} eV and to study the interactions of these, the most energetic particles observed in Nature. The Auger design features an array of 1600 water-Cherenkov detector stations on a 1500 m grid, spread over 3000 km^2 , and overlooked by 24 air fluorescence telescopes. In addition, three high-elevation fluorescence telescopes overlook a 23.5 km^2 , 61-detector infilled array with 750 m spacing. Radio emission from extensive air showers is measured with the Auger Engineering Radio Array (AERA), comprising more than 150 radio detector stations, covering an area of about 17 km^2 , co-located with the infill array [2, 3].

At present, the Pierre Auger Collaboration is working on an upgrade of the Observatory, Auger Prime [4]. The physics case of the upgrade is outlined in [5]. The *key science questions* to be addressed are: What are the sources and acceleration mechanisms of ultra-high-energy cosmic rays (UHECRs)? Do we understand particle acceleration and physics at energies well beyond the LHC (Large Hadron Collider) scale? What is the fraction of protons, photons, and neutrinos in cosmic rays at the highest energies?

To achieve these objectives, a layer of scintillators is being installed above the water-Cherenkov detectors (the Surface Scintillator Detector), the observation time of the fluorescence detectors is being increased, and underground muon detectors are being installed in a part of the Surface Detector array. In addition, radio antennas will be added to each Surface Detector station — this is the focus of this contribution.

We are going to install a radio antenna on each of the 1661 stations of the Surface Detector array of the Observatory, forming a 3000 km^2 radio array, the largest radio array for cosmic-ray detection in the world. A photograph of a prototype station is shown in Fig. 1. It shows (from bottom to top) the water-Cherenkov detector with a layer of scintillators on top (Surface Scintillator Detector) and a radio antenna (Radio Detector). The concept of radio antennas on top of the Surface Detector stations has been studied earlier at the Auger Observatory on smaller scales [6, 7]. With the combination of water-Cherenkov detector and Surface Scintillator Detector the electron-to-muon ratio (e/μ) is measured for vertical showers. In a similar way the combination of water-Cherenkov detector and Radio Detector will be used to measure the ratio of the electromagnetic energy and the number of muons for horizontal air showers. Thus, the Radio Detector will increase the aperture of the Observatory for mass-sensitive investigations, allowing the e/μ separation for showers with a broad zenith angle range, from zenith with the Surface Scintillator Detector to the horizon with the Radio Detector.

Horizontal air showers have a large footprint of the radio emission on the ground, covering areas of the order of 100 km^2 for very inclined showers. This has been predicted by simulations [8, 9] and also recently been measured with AERA [10, 11, 12]. Thus, the radio emission from such showers can be recorded with a sparse antenna array with 1.5 km spacing.

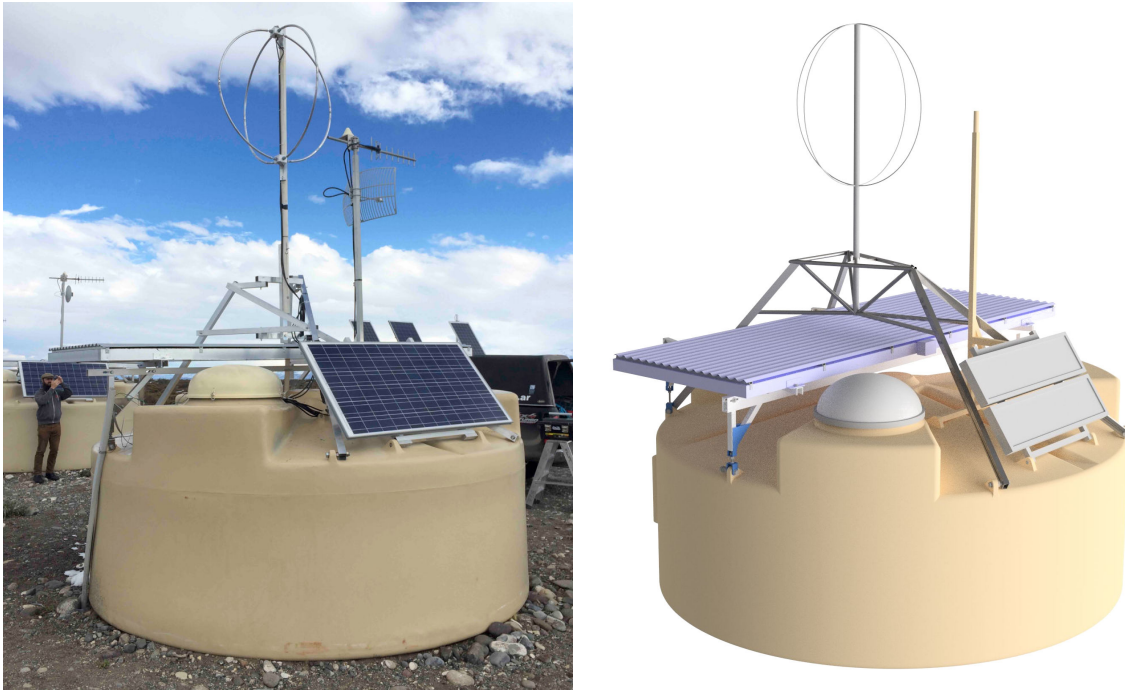


Figure 1: An upgraded station of the Surface Detector array of the Pierre Auger Observatory. On top of the water-Cherenkov detector a layer of scintillators (Surface Scintillator Detector – SSD) and a radio antenna (Radio Detector – RD) are mounted. Left: photograph of a prototype station, right: schematic view.

2. The Radio Detector of the Pierre Auger Observatory

At present we are working on the details of the technical implementation of the Radio Detector. The photograph (Fig. 1) depicts a prototype, which is installed at the observatory since May 2019. The Radio Detector will be fully integrated in the Surface Detector stations, they will form one unit, being comprised of water-Cherenkov detector, Surface Scintillator Detector, and Radio Detector. The different detectors will share the infrastructure such as solar power, battery, communications system, GPS timing, and an integrated data acquisition system. The envisaged system is schematically shown in Fig. 2.

We aim to use a short aperiodic loaded loop antenna (SALLA) to detect the radio emission from air showers in the frequency range 30 to 80 MHz. The SALLA realizes a Beverage antenna as a dipole loop of 1.2 m diameter [13, 14]. The SALLA has been developed to provide a minimal design that fulfills the need for both, ultra-wideband sensitivity, and low costs for production and maintenance of the antenna in a large-scale radio detector. The compact structure of the SALLA makes the antenna robust and easy to manufacture. Beverage antennas include a resistor load within the antenna structure to give a specific shape to the directivity [14]. In the case of the SALLA a resistance of $500\ \Omega$ connects the ends of the dipole arms at the bottom of the antenna. The antenna is read out at the top which is also the position of the Low-Noise Amplifier (LNA). While signals coming from above will induce a current directly at the input of the amplifier, the reception from directions below the antenna is strongly suppressed as the captured power is primarily consumed within the ohmic resistor rather than amplified by the LNA. The resulting strong

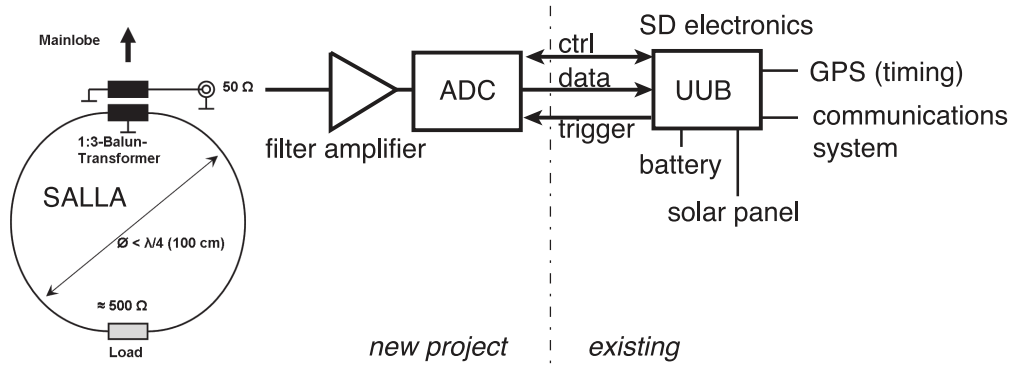


Figure 2: Schematic view of the envisaged read out for the radio antennas. The radio antenna (SALLA) is read out through a filter amplifier and an ADC. The front-end board has an interface to the existing electronics (Upgraded Unified Board - UUB [16]) at each Surface Detector station.

suppression of sensitivity towards the ground reduces the dependence of the antenna on structures below the antenna (like the Surface Scintillator Detector and the water-Cherenkov detector) and on environmental conditions which might vary as a function of time and are thus a source of systematic uncertainty. With the inclusion of an ohmic resistor the SALLA especially challenges its amplifier as only $\sim 10\%$ of the captured signal intensity is available at the input of the LNA. Proper matching between the antenna structure and the LNA is realized with a 3:1 transmission line transformer. The structure of the SALLA creates a sensitivity which is flat as a function of frequency.

The water-Cherenkov detector will issue a trigger signal when energy deposition has been detected. The data from the radio antenna will be passed to the read-out electronics of the Surface Scintillator Detector/water-Cherenkov detector system (UUB) [16] and will be transmitted together with all data from the station to the central data acquisition of the Auger Observatory.

We foresee two polarization directions of the antenna, oriented orthogonal to each other (see also Fig. 1). The signals of the two analogue channels will be pre-amplified in a LNA at the antenna. The signals are transmitted through shielded coaxial cables to the filter amplifier on the front-end board. They will be digitized with a sampling frequency of 200 Msps. A FPGA controls the data flow and the communication with the existing electronics of each Surface Detector station (UUB).

3. Expected performance

We first illustrate the estimated aperture and event statistics achievable with the Radio Detector. These were derived with a Monte Carlo study on the basis of an analytical signal model [15] based on CoREAS simulations [17]. We have expanded the signal model to enable predictions for zenith angles beyond 60° . This expansion entails the continuation of the spline fits relating the parameters R , σ and k to the distance to shower maximum $D_{X_{\max}}$ (cf. Fig. 8 of reference [15]) using CoREAS simulations with zenith angles up to 80° . On the basis of predicted signals for varying energies and event geometries, we determine detection efficiencies, requiring an energy fluence of at least 5 eV/m^2 in at least three antennas on a 1.5 km triangular grid. The estimate of 5 eV/m^2 for the detection threshold was obtained with SALLA prototype stations deployed within AERA

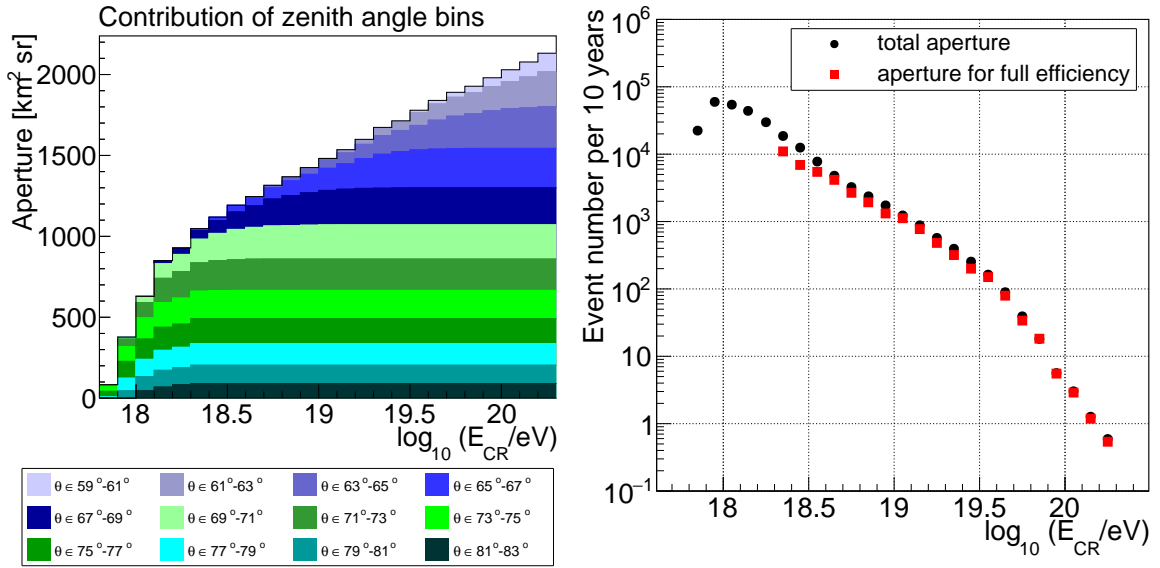


Figure 3: Left: Predicted aperture of the Radio Detector as a function of cosmic-ray energy for different ranges of zenith angles. Detection efficiencies were determined with the requirement of an energy fluence (i.e., energy deposit in the form of radio waves per unit ground area) of at least 5 eV/m^2 in at least three antennas, and with shower cores contained in the geometrical area of the 3000 km^2 array. Right: Number of events measured with the Radio Detector as a function of energy over the course of 10 years, calculated from the aperture using the Auger energy spectrum. Black points correspond to the total aperture as shown in the left panel. Red points correspond to the aperture in regions of parameter space where detection is 100% efficient (for every energy bin only those zenith angles are counted where full efficiency has already been reached).

in 2017. For comparison, the LPDA and butterfly antennas in AERA have a threshold of approximately 2 eV/m^2 . Assuming instrumentation of 3000 km^2 and requiring shower cores to fall within this geometrical area¹, we derive the aperture as displayed in Fig. 3.

It is visible that the energy threshold for coincident detection of showers in at least three antennas decreases with increasing zenith angle. This is due to the growth of the radio-emission footprint with zenith angle. The aperture contribution at the highest zenith angles is, however, limited by the condition that the events need to be contained in the geometric area of the Observatory, which introduces a $\cos \theta$ factor. At lower zenith angles, in particular below 70° zenith angle, the maximum achievable aperture contribution is larger, yet the detection becomes fully efficient only at high energies. A lower detection threshold than the assumed 5 eV/m^2 , possibly achievable using more sophisticated signal cleaning techniques, would thus in particular increase the fully efficient aperture contributed by air showers with low zenith angles. We note that the aperture shown in figure 3 should be considered a “detection aperture” and not a “trigger aperture”, as the trigger will be provided by the Surface Detector. Radio stations with a signal below 5 eV/m^2 will thus also contribute useful information.

Multiplying the aperture with the flux as measured by the Pierre Auger Observatory [19], we

¹We emphasize that this is a conservative scenario, as also air showers without core in the geometrical area of the observatory could be detected; cf. the science case of GRAND [18].

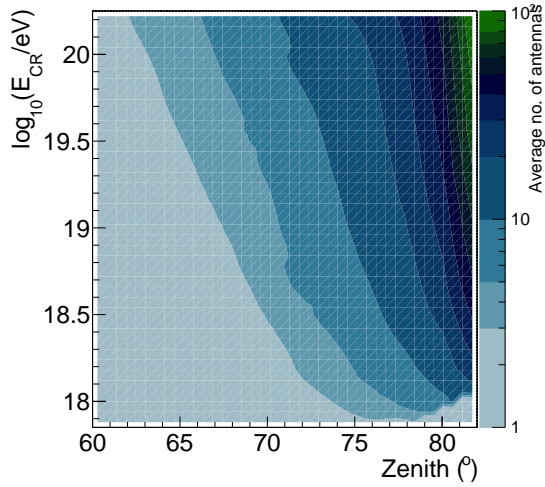


Figure 4: Average number of radio stations with a signal above the detection threshold of 5 eV/m^2 as a function of zenith angle and cosmic-ray energy.

derive the expected number of cosmic rays for the envisaged lifetime of the Radio Detector of 10 years and display it in Fig. 3. Over this period, more than 3000 cosmic rays will be measured at energies exceeding 10^{19} eV, and approximately 300 air showers will exceed an energy of $10^{19.5}$ eV. We note that an increase of the assumed detection threshold mostly affects detection efficiencies and thus event rates at energies below 10^{19} eV. To convey an impression of how well the events will be sampled with the Radio Detector, we have also determined the average number of radio stations with a signal above 5 eV/m^2 as a function of zenith angle and cosmic-ray energy, shown in figure 4.

To illustrate the expected performance, we pick a particular physics case: The Radio Detector will be a powerful tool to study the muon content in inclined air showers. The almost pure separation of the muon content (water-Cherenkov detectors) and electromagnetic energy (radio antennas) of inclined air showers will allow us to determine the energy dependence of the number of muons in inclined air showers, as has previously been done with the combination of water-Cherenkov Detectors and Fluorescence Detectors (FD) [21, 20]. With the Radio Detector, however, we will achieve an order of magnitude higher event statistics: To date, a total of 202 hybrid FD-SD events above $10^{18.8}$ eV have been collected for use in this analysis [20]. Over the lifetime of the Radio Detector, we estimate to collect roughly 6500 air showers in that energy range.

To illustrate the potential, we have performed a simulation study in which we draw events according to the distribution shown in Fig. 3 (red points, i.e., requiring full efficiency). We then smear out the energy, which will be measured by the Radio Detector, by a Gaussian with a σ of 20%, i.e., using a conservative scenario for the energy resolution. We draw muon numbers, taking into account the measured mean number of muons as a function of energy and their measured intrinsic spread above $10^{18.8}$ eV as taken from reference [20]. Furthermore, we smear out the number of muons by the N_{19} measurement resolution as detailed in [22]. Afterwards, we bin the data as a function of (smear) energy and determine the mean number of muons, shown in Fig. 5 (left), as well as the intrinsic spread of the number of muons (after subtracting the N_{19} measurement resolution), shown in Fig. 5 (right).

It becomes obvious that with the vastly increased statistics available through the Radio Detector, a powerful measurement of the mean number of muons as well as their intrinsic spread as a

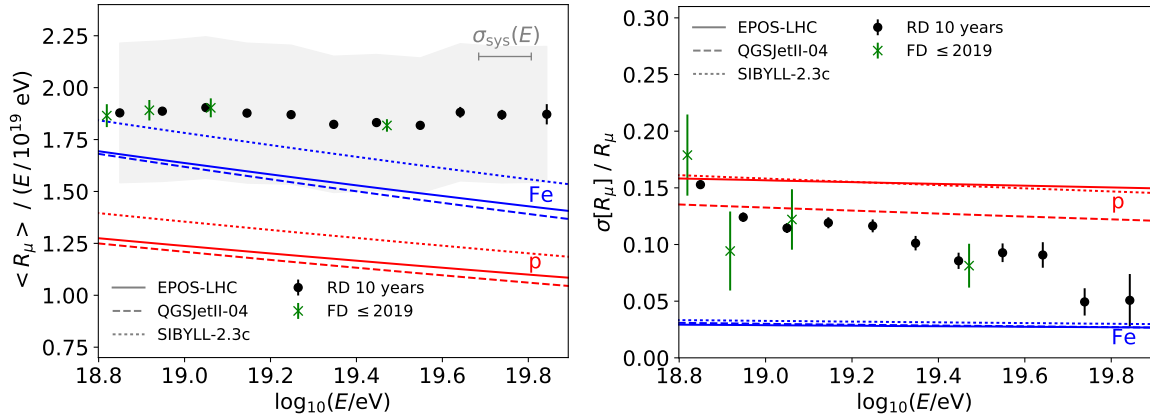


Figure 5: Simulation of a measurement of the mean number of muons (left) and the spread of the number of muons (right) as a function of energy via combined measurements with the water-Cherenkov Detector and the Radio Detector. A conservative energy resolution of 20% has been assumed for the radio measurement. Error bars indicate statistical uncertainties. Green points indicate the currently available data [20]. Black points indicate data as measurable with the Radio Detector over the course of 10 years. The shaded area indicates the systematic uncertainty of the measurement arising from the Auger energy scale and the systematic uncertainty of the muon measurement. Lines indicate model predictions for EPOS-LHC (solid), QGSJETII-04 (dashed), and Sibyll-2.3c (dotted).

function of cosmic-ray energy will be possible. The latter measurement, in particular, will allow in-depth tests of hadronic interactions.

We note that the systematic uncertainty illustrated in the form of a grey band in Fig. 5 (left) is dominated by the 14% uncertainty of the energy scale of the Pierre Auger Observatory. The Radio Detector has potential to validate and improve the energy scale determination up to the highest energies (similar to earlier investigations for vertical air showers [23, 24]), which would help further to perform more stringent comparisons of existing hadronic interaction models with data.

4. Conclusion and outlook

We are at present finalizing the technical design of the Radio Detector of the Auger observatory. First prototypes of all components are installed in the field for an in-situ evaluation of their performance. We aim to start the mass production of the components towards the end of 2019 and to complete the deployment of the almost 1700 units of the 3000 km² Radio Detector before the end of 2021. The Radio Detector will improve the science capabilities of the Auger observatory, by providing electron-muon separation for inclined air showers up to the highest energies. This implies also a larger mass-sensitive set of cosmic rays, measured by the Auger observatory in the overlap region on the sky with the Telescope Array.

The Auger Radio Detector is a natural next step towards future cosmic-ray experiments, applying the radio technique on even larger scales, such as GRAND [18] or a next-generation cosmic ray experiment, applying hybrid detection techniques by combining radio antennas with e.g. segmented water-Cherenkov detectors [25]. The Radio Detector with a 3000 km² array is a logical step

between the presently largest array (AERA, 17 km²) and applications of the technique on a level of tens of thousands of km². The Auger Radio Detector will be the biggest array for the next decade, allowing us to evaluate the detector technology, establish reconstruction methods, and study the physics performance of such large radio arrays.

References

- [1] A. Aab [Pierre Auger Collaboration], Nucl. Instrum. Meth. A 798 (2015) 172–213.
- [2] J. Schulz [Pierre Auger Collaboration], Proceedings of the 34th ICRC Den Haag (2015) [PoS \(ICRC2015\) 615](#).
- [3] T. Huege [Pierre Auger Collaboration], EPJ Web Conf. 210 (2019) 05011.
- [4] A. Castellina [Pierre Auger Collaboration], EPJ Web Conf. 210 (2019) 06002.
- [5] A. Aab [Pierre Auger Collaboration], arXiv (2016) 1604.03637.
- [6] C. Berat [Pierre Auger Collaboration], Nucl. Instr. Meth. A 718 (2013) 471.
- [7] R. Gaior, PhD thesis, <https://hal.archives-ouvertes.fr/tel-01826441>.
- [8] T. Huege, Phys. Rept. 620 (2016) 1–52.
- [9] F. Schröder, Prog.Part.Nucl.Phys. 93 (2017) 1-68.
- [10] A. Aab [Pierre Auger Collaboration], JCAP 1810 (10) (2018) 026.
- [11] M. Gottowik [Pierre Auger Collaboration], Proceedings ARENA 2018 (2018).
- [12] M. Gottowik [Pierre Auger Collaboration], Proceedings of the 36th ICRC, Madison, [PoS \(ICRC2019\) 274](#), 2019.
- [13] O. Krömer, et al., Proceedings of the 31st ICRC, Lodz, Poland, 1232, 2009.
- [14] P. Abreu [Pierre Auger Collaboration], JINST 7 (2012) P10011.
- [15] C. Glaser, S. de Jong, M. Erdmann, J. R. Hörandel, Astropart. Phys. 104 (2019) 64–77.
- [16] D. Nitz [Pierre Auger Collaboration], Proceedings of the 36th ICRC, Madison, [PoS \(ICRC2019\) 370](#), 2019.
- [17] T. Huege, M. Ludwig, C. W. James, AIP Conf. Proc. 1535 (2013) 128.
- [18] J. Alvarez-Muñiz, et al., Science China: Phys., Mech. & Astron., 63, 219501 (2020) <http://arxiv.org/abs/1810.09994>
- [19] F. Fenu [Pierre Auger Collaboration], PoS (ICRC2017),486(2018).
- [20] F. Riehn [Pierre Auger Collaboration], Proceedings of the 36th ICRC, Madison, [PoS \(ICRC2019\) 404](#), 2019.
- [21] A. Aab [Pierre Auger Collaboration], Phys. Rev. D91 (3) (2015) 032003, [Erratum: Phys. Rev.D91,no.5,059901(2015)].
- [22] A. Aab [Pierre Auger Collaboration], JCAP 1408 (08) (2014) 019.
- [23] A. Aab [Pierre Auger Collaboration], Phys. Rev. D 93 (12) (2016) 122005.
- [24] A. Aab [Pierre Auger Collaboration], Phys. Rev. Lett. 116 (24) (2016) 241101.
- [25] J. Hörandel, Proceedings ARENA 2018 (2018).



New Electronics for the Surface Detectors of the Pierre Auger Observatory

Dave Nitz^{*a,b} for the Pierre Auger Collaboration^{c†}

^a*Michigan Technological University, Houghton, Michigan, USA*

^b*Karlsruhe Institute of Technology, Karlsruhe, Germany*

^c*Observatorio Pierre Auger, Av. San Martín Norte 304, 5613 Malargüe, Argentina*

E-mail: auger_spokespersons@fnal.gov

Full author list: http://www.auger.org/archive/authors_icrc_2019.html

The surface detector array of the Pierre Auger Observatory consists of 1660 water-Cherenkov detector stations (WCDs) that sample the charged particles and photons of air showers initiated by energetic cosmic rays. Each station continuously samples signals from photomultiplier tubes (PMTs) viewing the water volume, and records a $\approx 20 \mu\text{s}$ trace whenever a local trigger condition is satisfied. Absolute timing is provided by a GPS receiver on each station, and power is provided by a solar power system. The Observatory is currently implementing an upgrade, “AugerPrime”. AugerPrime includes the addition of a small PMT to increase dynamic range, a plastic scintillator above each WCD to enhance the separation of electromagnetic and muon shower components, a radio detector to measure the radio emission of inclined air showers, and an infill of buried muon counters to provide additional cross checks. Consequently, new electronics to support these additional detectors is also being implemented. In addition to more measurement channels, the new electronics includes improved GPS receivers, higher sampling frequency, increased dynamic range, increased processing capability, and improved calibration and monitoring systems. This paper presents the design of the new electronics and discusses performance characteristics observed in laboratory measurements and engineering array data.

36th International Cosmic Ray Conference — ICRC2019

24 July – 1 August, 2019

Madison, Wisconsin, USA

^{*}Speaker.

[†]for collaboration list see PoS(ICRC2019)1177

1. Introduction

The Pierre Auger Observatory [1] consists of 1600 water Cherenkov detectors (WCDs) on a 1500 m triangular grid covering 3000 km² near Malargüe, Argentina. Another 60 WCDs form an infill region. The array is overlooked by four fluorescence detector sites that each contain 6 telescopes viewing a 180° azimuth by 30° elevation field of view. Three additional telescopes at one of the sites can be tilted 30° higher to view lower energy showers at their maximum and overlook a 30 km² infilled surface array with a 750 m spacing. Extensive air showers (EAS) induced by ultra-high energy cosmic rays (UHECRs) are sampled at ground level by the Surface Detector (SD). The Fluorescence Detector (FD) measures the EAS development by detecting the nitrogen UV light produced by the shower's particles along their passage in the atmosphere. Additional instrumentation for R&D on muon and radio-based detection is also located on the site.

In its first two decades, the Pierre Auger Observatory has made significant contributions to the study of UHECRs. In order to make further progress and more fully harness the power of statistics, the Auger Collaboration decided to improve the sensitivity to composition of the SD. The Pierre Auger Observatory is therefore undergoing a significant upgrade of its experimental capabilities called AugerPrime. The AugerPrime upgrade will allow us to disentangle the muonic and electromagnetic components of extensive air showers [2, 3, 4], thereby enhancing the ability of the Observatory to study UHECR composition, composition-assisted anisotropies and hadronic interaction effects at the highest energies.

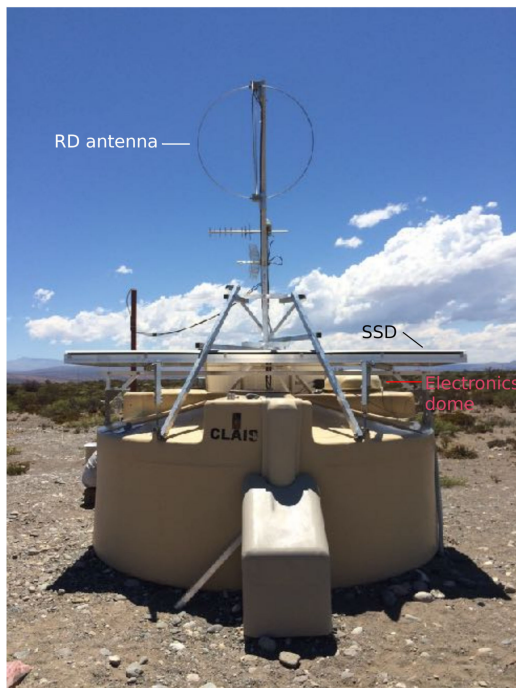


Figure 1: Photo of a prototype AugerPrime detector. Shown are the SSD (black annotation) atop the WCD along with a radio detector antenna (large circular antenna at highest point with white annotation). The UUB is hidden underneath the dome (red annotation) visible between the top of the WCD and bottom of the SSD on the right side of the top of the tank.

AugerPrime consists of a 3.8m × 1.3m scintillator-based surface detector (SSD) and a radio detector (RD) [5] added atop each water Cherenkov detector. A full prototype station is shown in Fig. 1. This allows separation of the muonic and electromagnetic (EM) parts of the shower by exploiting the different responses of the various detector types to each component and therefore

enhancing the composition sensitivity. The WCD has good sensitivity to both muonic and EM components while the SSD and RD are predominantly sensitive to the EM component. Shower universality and matrix methods are used to correct for differences in the response for each detector type. The SSD and RD are complementary in their solid angle coverage, with the SSD being optimized for more vertical showers, and the RD optimized for inclined showers with higher zenith angles [6]. A small PMT is added to the WCD to increase the dynamic range [7]. Improved support for the buried muon counters (AMIGA) [8] is also incorporated.

The surface detector electronics is being upgraded to support the detector enhancement. This involves replacing the main electronics board, the so-called Unified Board (UB) with an Upgraded Unified Board (UUB) [9]. In addition to providing support for the SSD, the RD, AMIGA, and the small PMT, the UUB includes faster and more precise ADCs and a faster central processor.

Backwards-compatibility with the current dataset is maintained by keeping the time-span of the PMT traces similar to that in the current electronics and by providing 20 MHz cutoff digital filtering of the recorded traces in order to emulate the current triggers. Additional full bandwidth triggers are also implemented to enhance the triggering.

An AugerPrime engineering array (EA) of 12 stations has been operating at the Auger Observatory site since October, 2016 [10]. The EA is integrated in the standard Observatory's operation, with signal traces recorded by the SSD detectors and read out through the Auger communications network [11], packaged into events by the Central Data Acquisition system and sent to the data repository in Lyon, France, for analysis by the collaboration.

The low level firmware code, UUB operating system code, UUB DAQ code, and code for the control micro-processor are all stored in appropriate software repositories that provide access for the collaboration. For example, the firmware source code, along with example test programs, documentation, and the compiled "bitstream" files are made available to the collaboration via a GitHub repository¹, while for historical reasons the DAQ code is stored in an SVN repository.

2. Digital functionality of the UUB

The major portion of the AugerPrime electronics upgrade is to replace the original UB with the UUB, which is designed to fit the existing RF enclosure, and accept the existing PMT, GPS antenna, and communications cables. The new electronics employs faster ADCs (120 MHz instead of 40 MHz) with larger dynamic range (12 bits each instead of 10 bits) and a significantly more powerful FPGA. Specifically, it employs a Xilinx Zynq-7020 All Programmable SoC (Artix-7 FPGA and associated Cortex A9 Dual 333 MHz ARM co-processor) instead of the older Altera Cyclone series FPGAs used in the original electronics. Whereas the logic code of the current FPGAs is written in an Altera specific variant of VHDL called AHDL, the logic code of AugerPrime version is primarily written in IEEE standard synthesizable Verilog. Xilinx Vivado is used for the overall framework, and for standard modules such as memories, UARTs, and processor bus interfaces. Xilinx PetaLinux runs on the embedded ARM processor.

The UUB integrates various functions (analog signal processing, triggering, calibration, GPS time tagging, slow control, and data acquisition) on a single board. The FPGA is connected to a 4

¹<https://github.com/auger-prime-sde/uub-firmware>

Gbit LP-DDR2 memory and 2 Gbit flash memory. The FPGA implements in programmable logic basic digital functions like the readout of the ADCs, the generation of triggers, and the interfaces to the LED flasher, GPS receiver, and memories. High-level functions like the data handling and the communications with the communications radio transmitter are implemented under LINUX. The current local station software originally written in OS-9 has been ported to LINUX which expands the possible pool of experts for DAQ code development and maintenance. The speed of the upgraded CPU is more than 10 times faster than that of the current one, with a similar increase in memory. This allows more sophisticated processing in the local station. The addition of accessible trigger IN/OUT signals and high-speed USB facilitates tests both in the lab and in the field.

The current local triggers [11, 12, 13] (threshold trigger, time-over-threshold trigger (ToT), multiplicity of positive steps (MoPS) trigger, etc) are implemented using digitally filtered waveforms to reproduce the current trigger characteristics. This allows detectors with the new electronics to behave identically to the existing detectors at the trigger level and allows deployment of new electronics during the maintenance of the current system without disturbance to the data taking. The increased local processing capabilities allow new triggers to be implemented such as asymmetry-based triggers, and combined SSD and WCD triggers. The current muon memories and scalers are retained. The form factor of the UUB printed circuit board is the same as that of the UB, which allows UUB to be installed in the current enclosure, only requiring a new front panel.

Synchronization of the detectors is provided by tracking variations of the local 120 MHz clock with respect to the GPS 1 PPS signal. For the upgraded electronics we have selected the Synergy SSR-6TF timing GPS receivers. This receiver is functionally compatible with the Motorola Oncore UT+ GPS one that is used with the current electronics. The fundamental architecture of the time-tagging firmware module parallels the time-tagging design concept used in the current electronics and is implemented in the UUB board FPGA. The on-board software for initialization of the time-tagging modules, GPS hardware control, and timing data is similar to the current one, with minor modifications needed for the new UUB hardware. The intrinsic GPS device accuracy after the applied granularity correction (the so-called negative sawtooth) is ≈ 2 nanoseconds, and thus makes a negligible contribution to the overall timing accuracy.

Two digital connectors are provided for additional detectors. These connectors provide 8 differential LVDS lines, each of which can be individually defined as input or output in the FPGA. One of these is use for the radio detector, and the other is used for AMIGA. This connector also provides unregulated +24 V, switched and limited, with a current monitor.

3. Analog functionality of the UUB

A design goal of AugerPrime is to measure shower properties at energies above 6×10^{19} eV as close as 250 m from the shower core. For this purpose the WCD is equipped with an additional small photomultiplier tube (SPMT), a 1 inch Hamamatsu R8619 PMT, dedicated to the measurement of large signals. The SPMT signal is also digitized with 12 bits at 120 MHz in a separate channel. The SPMT gain and the amplification are set such that the dynamic range is extended by a factor of 30 to 20,000 VEM (vertical equivalent muon). This is shown in Fig. 2. The dynamic range for the SSD is 20,000 MIP (minimum-ionizing particle).

Even before PMT saturation, the dynamic range of the signals from the large XP1805 PMTs (LPMTs) and the SSD PMT is larger than can be measured by a single ADC on the UB or UUB. In the current electronics (UB) the anode channel of each PMT is fed to one input (low gain), while the signal from the last dynode is amplified on the PMT base to before being provided to a 2nd input (high gain) for each PMT. The ratio between the low and high gain signals is ≈ 32 , and is calibrated using background muons in the field.

The amplified dynode signal currently used, however, is too noisy for the increased dynamic range of the UUB. Therefore the high and low gain signals are both derived from the anode signal using 2 parallel amplifiers with different gains. This has a further advantage that the low/high gain ratio is determined solely by the electronics and no longer needs to be determined from online calibrations. The signals of the 3 large PMTs are split with a gain ratio of 32 into 2 ADC channels each. The SSD PMT signal is also split, but with a gain ratio of 128 into 2 ADC channels. Fig. 3 displays a check of the ratio of the high gain to low gain channels in one station. The gain ratio is within 0.3% of the nominal ratio of 32, as expected with the use of 0.1% gain setting resistors.

The pulse response of the XP1805, when expressed in terms of bandwidth, is ≈ 70 MHz. This is well matched to a 120 MHz ADC and associated 60 MHz Nyquist filter. We have chosen to use commercial 12 bit 120 MHz AD9628 ADCs, which achieve this performance with minimal power consumption, an important consideration due to the nominal 10 W station power budget. The 7-pole differential Bessel filter is implemented using passive components to minimize noise contribution.

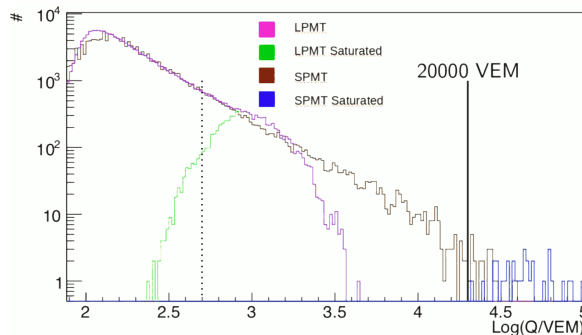


Figure 2: Extension of the dynamic range to 20,000 VEM using the small PMT. Here LPMT refers to the XP1805 PMTs, SPMT to the R8619 PMT, and “saturated” to signals which saturate the respective ADCs.

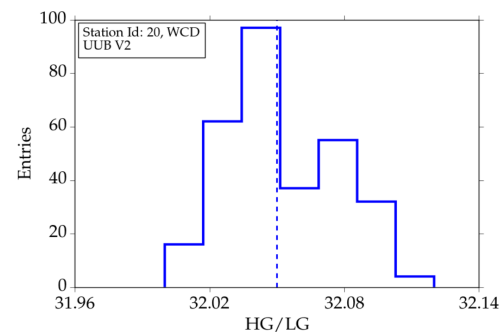


Figure 3: Example of check of the ratio of high gain to low gain channels.

4. UUB slow control functionality

The UUB is equipped with a micro-controller (MSP430) for the control and monitoring of the PMT’s high voltage, the supervision of the various supply voltages and reset functionality. The power-on sequence of the several supplies for the FPGA is quite complex, and this is controlled by the micro-controller. It controls 16 logic I/O lines, steers a DAC (digital-to-analog converter) with eight analog outputs and senses through multiplexers up to 64 analog signals with its internal ADC. The MSP430 also provides a USB interface which can be used to monitor and control the various

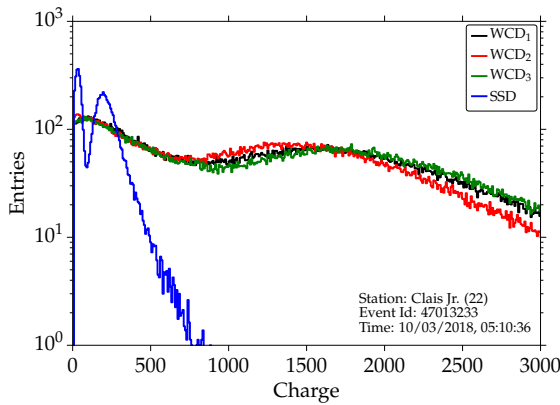


Figure 4: Example of calibration histogram of an EA detector. Calibration histograms for the previous minute are provided for each event that is read out.

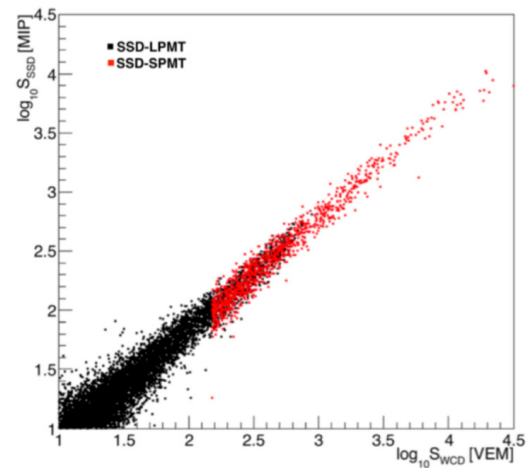


Figure 5: Correlation of signals in the SSD vs the WCD. The LPMTs are used up to saturation (black dots). The measurements are extended by means of the SPMT (red dots).

power supplies through a command line interface. More than 90 monitoring variables - including currents and voltages of the power supply and the PMTs are managed by the slow-control software. This information is then packaged by the DAQ system running on the FPGA's ARM processor and sent through CDAS to the Auger monitoring database.

5. Calibration

The VEM signal is the reference unit of the WCD high-gain calibrations, and was previously determined on a test tank with an external trigger hodoscope to give on average 95 photoelectrons at the cathode of the XP1805 PMTs. This corresponds to ≈ 1500 integrated ADC counts above pedestal after signal digitization on the UUB. Due to its small area, the SPMT cannot be calibrated using atmospheric muons. A selection of small showers allows us to cross-calibrate it with the VEM signals of the LPMTs. The SSD calibration is based on the signal of a minimum-ionizing particle going through the detector. About 40% of the calibration triggers of the WCD produce a MIP in the SSD. An example of the VEM and MIP calibration histograms is shown in Fig. 4. The very good correlation between the calibrated signals of the WCD and SSD is shown in Fig. 5.

In addition to routine calibrations with physics events, each WCD is equipped with two LEDs. While these are not stable sources of calibrated light, they are useful for monitoring and linearity tests. These LEDs are also used for the SSD prototypes, but are not planned for all SSD stations.

6. Current status and performance

Two prototype iterations (+ retrofits) have been produced and extensively exercised in the AugerPrime EA [14]. Fig. 6 displays the RMS noise performance of a V2 UUB measured in the EA. The measured noise has already reached the level estimated using PSpice calculations.

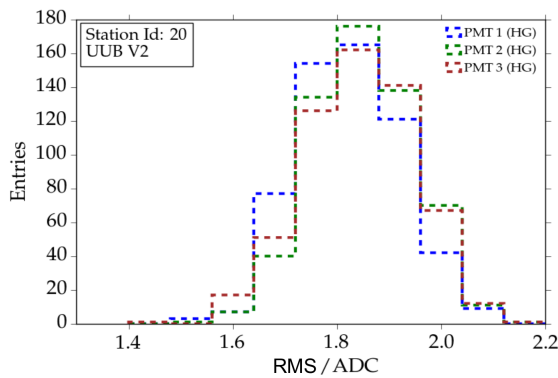


Figure 6: Measured RMS noise of a V2 UUB in the field. The performance is consistent with PSpice simulations of the noise.

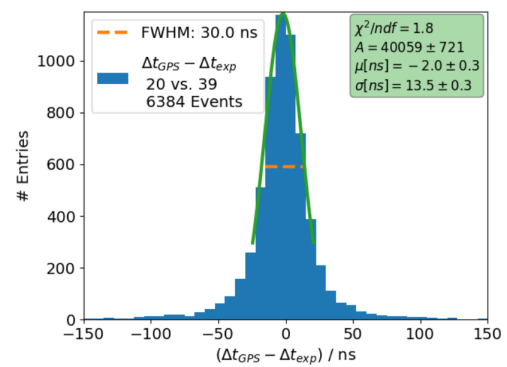


Figure 7: Measured timing resolution on showers using 2 nearby stations in the AugerPrime EA. Single station resolution is $13.5/\sqrt{2} = 9.5$ ns.

The timing resolution has been measured using showers triggering 2 nearby stations in the AugerPrime EA. This is shown in Fig. 7. The end-to-end single station timing accuracy in real showers, including the effects of shower front fluctuations and quantization due to the 120 MHz system clock, has been measured by comparing nearby stations to be better than 10 ns, a significant improvement over the current 13 ns.

For additional information please see Ref. [14].

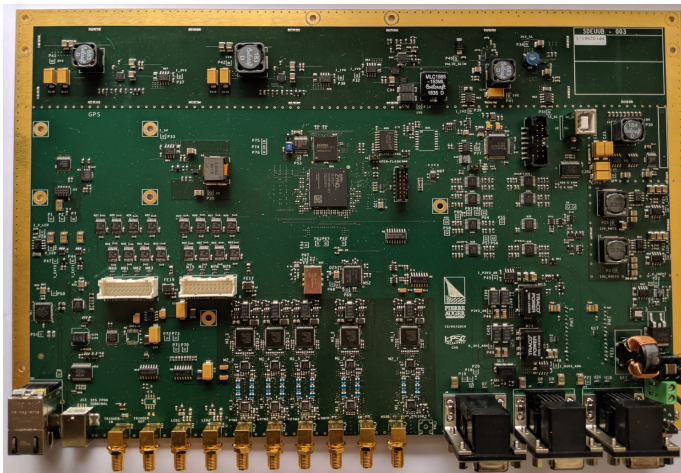


Figure 8: Photo of a V3 UUB. Shielding cans which will be installed over the DC-DC converters are not shown in this photo.

The power consumption of the UUB was targeted to be 10 W. The actual power consumption is 12 W. However, this turns out to not be an issue as the addition of the RD, which was not included in the original AugerPrime design, necessitates in any case an associated upgrade of the solar power system, which has sufficient capacity for both the UUB and the RD.

Based upon the experience with the V1 and V2 prototypes a V3 UUB design, incorporating small improvements, and especially improved shielding of emitted RFI, has been implemented. A photo of a V3 UUB is shown in Fig. 8. Production of the full batch (enough pre-production + production units to instrument the full array + spares) of UUBs has been initiated.

References

- [1] **Pierre Auger** Collaboration, P. A. Collaboration, “The Pierre Auger Cosmic Ray Observatory,” *Nucl. Instrum. Meth.* **A798** (2015) 172–213.
- [2] **Pierre Auger** Collaboration, D. Martello, “The Pierre Auger Observatory Upgrade,” in *The Pierre Auger Observatory: Contributions to the 35th International Cosmic Ray Conference (ICRC 2017)*, pp. 147–154. 2017.
https://inspirehep.net/record/1618430/files/1617990_147-154.pdf.
- [3] **Pierre Auger** Collaboration, A. Castellina, “AugerPrime: the Pierre Auger Observatory Upgrade,” *EPJ Web Conf.* **210** (2019) 06002, [arXiv:1905.04472](https://arxiv.org/abs/1905.04472) [astro-ph.HE].
- [4] **Pierre Auger** Collaboration, A. Aab *et al.*, “The Pierre Auger Observatory Upgrade - Preliminary Design Report,” [arXiv:1604.03637](https://arxiv.org/abs/1604.03637) [astro-ph.IM].
- [5] **Pierre Auger** Collaboration, B. Pont, “A large radio detector at the Pierre Auger Observatory - measuring the properties of cosmic rays up to the highest energies,” in *PoS(ICRC2019)395, these proceedings*. 2019.
- [6] **Pierre Auger** Collaboration, A. Aab *et al.*, “Observation of inclined EeV air showers with the radio detector of the Pierre Auger Observatory,” *JCAP* **1810** no.~10, (2018) 026, [arXiv:1806.05386](https://arxiv.org/abs/1806.05386) [astro-ph.IM].
- [7] **Pierre Auger** Collaboration, A. Castellina, “The dynamic range of the AugerPrime Surface Detector: technical solution and physics reach,” in *The Pierre Auger Observatory: Contributions to the 35th International Cosmic Ray Conference (ICRC 2017)*, pp. 161–168. 2017.
https://inspirehep.net/record/1618432/files/1617990_161-168.pdf.
- [8] **Pierre Auger Collaboration** Collaboration, A. Aab *et al.*, “The Pierre Auger Observatory: Contributions to the 33rd International Cosmic Ray Conference - The AMIGA muon detectors of the Pierre Auger Observatory: overview and status (ICRC 2013),” [arXiv:1307.5059](https://arxiv.org/abs/1307.5059) [astro-ph.HE].
- [9] **Pierre Auger** Collaboration, T. Suomijarvi, “New electronics for the surface detectors of the Pierre Auger Observatory,” in *The Pierre Auger Observatory: Contributions to the 35th International Cosmic Ray Conference (ICRC 2017)*, pp. 155–160. 2017.
https://inspirehep.net/record/1618431/files/1617990_155-160.pdf.
- [10] **Pierre Auger** Collaboration, Z. Zong, “First results from the AugerPrime engineering array,” in *The Pierre Auger Observatory: Contributions to the 35th International Cosmic Ray Conference (ICRC 2017)*, pp. 177–184. 2017.
https://inspirehep.net/record/1618434/files/1617990_177-184.pdf.
- [11] D. Nitz, “Triggering and data acquisition systems for the Auger observatory,” *IEEE Trans.Nucl.Sci.* **45** (1998) 1824–1829.
- [12] **Pierre Auger** Collaboration, D. Nitz, “The front-end electronics for the Pierre Auger Observatory surface array,” *IEEE Trans.Nucl.Sci.* **51** (2004) 413–419.
- [13] **Pierre Auger** Collaboration, J. Abraham *et al.*, “Trigger and aperture of the surface detector array of the Pierre Auger Observatory,” *Nucl.Instrum.Meth.* **A613** (2010) 29–39, [arXiv:1111.6764](https://arxiv.org/abs/1111.6764) [astro-ph.IM].
- [14] **Pierre Auger** Collaboration, A. Taboada, “Analysis of Data from Surface Detector Stations of the AugerPrime Upgrade,” in *PoS(ICRC2019)434, these proceedings*. 2019.



Test benches for the upgrade of the Pierre Auger Observatory electronics

Martina Boháčová^{*a} for the Pierre Auger Collaboration^{b†}

^a*Institute of Physics, Prague, Czech Republic*

^b*Observatorio Pierre Auger, Av. San Martín Norte 304, 5613 Malargüe, Argentina*

E-mail: auger_spokespersons@fnal.gov

Full author list: http://www.auger.org/archive/authors_icrc_2019.html

The Pierre Auger Observatory, the largest cosmic ray detector ever built, has been collecting scientific data since 2004. As part of the AugerPrime upgrade, the Observatory is currently undergoing a modification of the surface detector stations, which involves a replacement of their electronics with a faster and a more powerful system that provides channels for additional detectors as well as increased dynamic range and processing capability, higher sampling frequency, and improved timing, calibration and monitoring systems. The testing of the new electronics boards will be conducted in three stages: the production test performed at the manufacturer site, the climate tests including accelerated ageing executed in a laboratory and finally the full functionality tests effectuated before the deployment at the Observatory in Argentina. A description of the test benches and the testing procedures is given together with some examples of the performance of the prototype.

36th International Cosmic Ray Conference — ICRC2019

24 July – 1 August, 2019

Madison, Wisconsin, USA

^{*}Speaker.

[†]for collaboration list see PoS(ICRC2019)1177

1. Introduction

The Pierre Auger Observatory design features a large detection area collecting unprecedented event statistics, a combination of several detection techniques allowing one to lower the systematic uncertainties of the results obtained, and constitutes a continuous effort of more than 450 scientist from 17 countries. The amount of gathered scientific results largely surpasses the original expectations. The Surface detector (SD) array is formed by 1660 water-Cherenkov detectors (WCD) placed in a triangular grid with 1500 m spacing on the area of around 3000 km². The array is fully efficient above 3×10^{18} eV and continuously samples both the electromagnetic and muonic parts of the extensive air showers (EAS) with nearly 100 % duty cycle. The WCDs are overseen by 27 fluorescence telescopes located on the boundary of the array, observing the longitudinal profile of the electromagnetic component of the air shower. Fluorescence detector (FD) can only be operated during clear moonless nights. A thorough description of the Observatory is given in [1].

After fifteen years of operation the Observatory is being upgraded. The main scientific aspects motivating the upgrade are the following: lack of primary mass composition information at the highest energies, the observation of the composition getting heavier with higher energy hampering anisotropy searches, and the discrepancies between hadronic interaction models and the measured shower parameters. The upgrade, currently underway, aims at resolving these issues. Each WCD will be equipped with a 4 m² plastic scintillator mounted on the top (Surface Scintillator Detector or SSD). The two detectors will provide complementary information about the electromagnetic and muonic components of the shower. An additional Radio Detector (RD) will be mounted on top of each WCD for the observation of radio signal in 30 – 80 MHz band from inclined showers to add yet another measurement of the electromagnetic component. Adding a small, less sensitive PMT to the three already in place inside the WCDs will enlarge the dynamic range and permit one to study signals closer to the shower core. Finally, buried scintillators will accompany 61 SD stations to provide a pure muon signal on a small sample of showers (AMIGA - Auger Muons and Infill for the Ground Array). A more powerful, modernized electronics will allow one to interface the additional detectors as well as the current ones. Faster FADCs with higher resolution will resolve a finer temporal structure of the signals. A comprehensive description of the Observatory upgrade can be found in the Preliminary Design Report [2].

2. Upgraded Surface Detector electronics

To accommodate the baseline design detectors as well as the additional detectors of Auger-Prime, the current Unified Board (UB) will be replaced by an Upgraded Unified Board (UUB), providing four additional channels. It has to fit into the same RF enclosure with only the front panel replaced and has to accept the existing PMT, GPS antenna and communications cables. The new UUB integrates data acquisition, analog signal processing, triggering, calibration and Slow-Control (SC) functionality on a single board. The new electronics design features more powerful FPGA (Xilinx Zynq-7020) together with 512 MB RAM, a 256 MB Flash memory, and faster ADCs (120 MHz instead of 40 MHz) with larger dynamic range (12 bits instead of 10 bits). New triggers are implemented using digital filtering, which permits one to reproduce the current trigger characteristics so that data taking can continue during the deployment period.

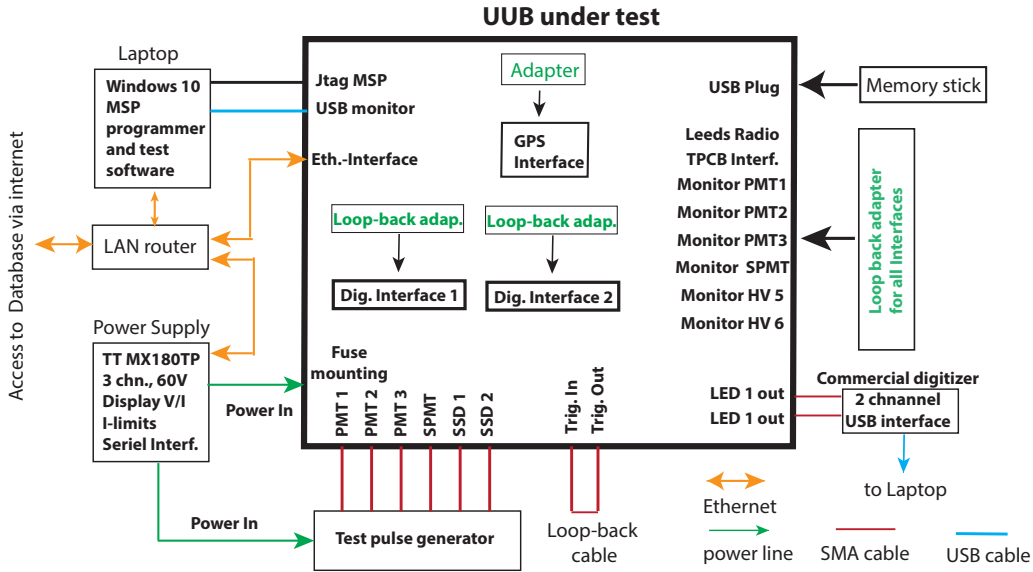


Figure 1: Scheme of the production test setup.

All analog inputs accept signals up to 2 V except the SSD channel, which accepts up to 8 V. Each PMT signal is split into two branches with different amplification gain, high gain (HG) and low gain (LG), and passed through an anti-aliasing filter with the cut-off frequency of 60 MHz. Therefore the HG/LG ratio is designed to be 32 (or 128 for the ratio of the SSD channels) and is set purely by resistor values in the analog front-end. The SlowControl part of the UUB is responsible for controlling the power supplies and PMT voltages, watchdog and reset functions. In addition, the SC monitors currents, voltages, temperature and humidity. It is implemented by micro-controller MSP430. Detailed description of the new SD electronics can be found in [3].

3. Production test

The purpose of the Production test is to verify that all functional blocks of the UUB were assembled correctly and to program the MSP430. All tested UUB interfaces are connected: the power supply connector to a programmable power supply (TT MX180TP), the SMA front-end inputs to a test pulse generator, the GPS interface to an adapter, both digital interfaces to loop-back adapters, the D-Sub type connectors for controlling and monitoring of PMT high-voltages to loop-back adapters. Further, the LED outputs are connected to a commercial digitizer, the Ethernet interface to a LAN router, the SMA connectors trigger out to the trigger in, the USB host connector to a memory stick, the USB device connector to the test computer, and MSP JTAG connector to a JTAG programmer.

The test proceeds in the following eight steps: 1) the UUB supply voltage is varied over the allowed range ($19\text{ V} < U_{\text{in}} < 32\text{ V}$) and the system checks that UUB's voltage limiter switches the UUB off in case of under or over-voltage; 2) SlowControl MSP is programmed via JTAG, the UUB is powered off/on - the MSP is expected to start and the UUB to boot PetaLinux on Zynq cores; 3) UUB internal voltages and currents drawn are read out of SC and compared with the prescribed values; 4) electrical connections to the GPS interface, to the radio connector and the digital interfaces

are verified by generation of appropriate signals and read out via loop-back adapters; 5) a ramp signal is generated at both LED outputs and acquired by a two-channel commercial USB digitizer to verify the signal shape; 6) PMT-like signals are sent to the six SMA front-end inputs by a custom made test pulse generator, recorded by the UUB, transferred to the test system (via Ethernet) and analyzed. Parameters as baseline, RMS noise, pulse amplitude are determined and verified to be within prescribed margins; 7) access the memory stick in the UUB host connector is verified; 8) finally, a reset command is issued via the radio interface to verify that the UUB restarts. All tests are evaluated and the test results are uploaded into a dedicated database.

4. Environmental stress screening

Environmental stress screening (ESS) is performed to characterize the behaviour of the new electronics under changing environmental condition and to provoke early failures. Climate tests are conducted in three stages: the pre-test, burn-in and temperature cycling. The purpose of the pre-test, which is performed on individual boards, is to diversify the MAC addresses, to measure the noise of the analog chain with open connectors and to acquire a thermal image of the powered UUB in order to discover thermal irregularities. After the pre-test the burn-in and thermal cycling is performed with a batch of ten boards at the same time. The scheme of the test bench for temperature cycling is shown in Fig. 2. The test bench consists of a climate chamber (MKFT 115, Binder), test function generator (AFG3252C, Tektronix), a power supply (HMP 4040, Rohde&Schwarz) and custom devices: a signal distribution board, a power control board and a trigger fan-out. The temperature inside the chamber is monitored by the chamber itself as well as by two sensors BME280 (Bosch).

The signal distribution board is designed to fan-out the signal from the function generator to the 60 channels on ten UUBs ($50\ \Omega$ impedance). It operates in three modes: a) the attenuated mode, where the input signal is attenuated by a factor 32 (for testing HG UUB channels), b) the frequency mode, where the input signal is propagated to all 60 outputs with unmodified amplitude (bandwidth 70 MHz, maximum output amplitude $2\ V_{pp}$), and c) the amplified mode, where the input signal is propagated to 50 UUB inputs (5 per UUB) with the same amplitude and amplified by a factor of 4 to the 10 SSD inputs (bandwidth 10 MHz, maximum output amplitude $8\ V_{pp}$). The power control board monitors the current drawn by individual UUBs and allows to switch individual UUBs off in case of a failure. The trigger board distributes the trigger signal to the UUBs with a programmable delay.

4.1 Temperature cycling and burn-in

During the temperature cycling 10 UUBs are placed inside the climate chamber at a minimum distance 5 cm from each other. During the burn-in process the temperature in the chamber will change rapidly in the range $-20\ ^\circ\text{C}$ and up to $70\ ^\circ\text{C}$ to provide a maximum thermal stress. The temperature range is slightly larger than the range the UUBs have to face in the pampas. Only an Ethernet connection for read out and control, a power supply and an external trigger will be attached to allow monitoring of the noise, ADC bits functioning and SC values.

The burn-in is followed by 10 cycles with intermediate measurement points. Additional 6 SMA connectors have to be mounted on each UUB in order to provide analog test signals. The

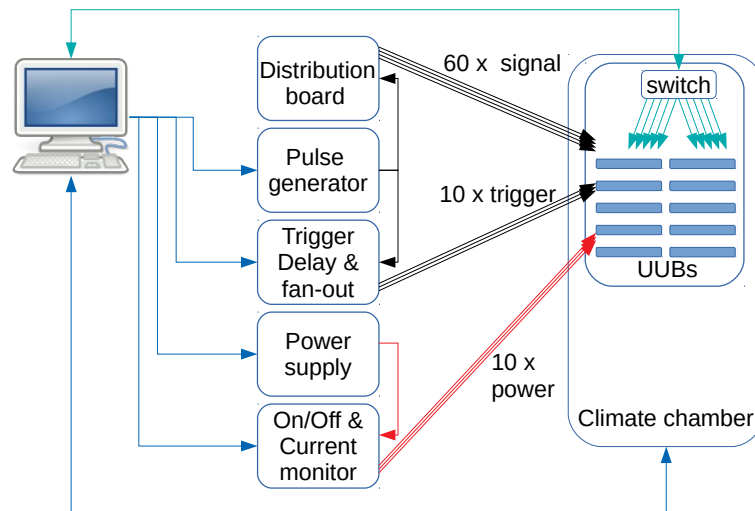


Figure 2: Scheme of the experimental setup for climate tests.

cycling starts at 20°C going down to -20°C and up to 70°C - the same range as the burn-in but this time with a temperature change of $\sim 3^\circ\text{C}/\text{min}$). Every 20 – 25°C a 1-minute interval for measurements and readout follows after 5 minutes of temperature stabilization (14 + 1 minute at the extreme temperatures). Thus, the measurement points are: 20, 0, -20, 0, 20, 45, 70 degrees Celsius. In the last cycle a power ON/OFF test is performed at extreme temperatures. During the whole cycling process, the current drawn by each UUB, temperature readings from the chamber, BME280 sensor, Zynq as well as SC values are monitored. In case of a critical quantity outside of limits the operator is notified.

The duration of both testing parts is approximately equal (~ 21 h). Thus, 20 UUBs will be tested in 48 hours with sufficient time allowed for manipulation and maintenance.

4.2 Measurement point - performed tests

- **Noise test:** The pedestal and noise RMS for each channel is derived from the whole ADC trace, when no input signal is present.
- **Linearity test:** The test pulse consists of five half-sine pulses connected with a baseline. The test pulse is issued with twelve amplitudes covering the whole dynamic range of the ADCs. The recorded trace is fitted by a model function and its amplitude is calculated. The gain is derived from a linear regression of input and output amplitudes.
- **Frequency test:** The test pulse is a burst of sine waves, 22 μs in length. The external trigger is adjusted such, that the recorded sine wave spans the full UUB acquisition window (17 μs). Voltage amplitudes of 1.6 V_{pp} for LG and 50 mV_{pp} for HG channels are used at seven frequencies (10 MHz, 20 MHz, 30 MHz, 40 MHz, 50 MHz, 59 MHz and 70 MHz). The measured signal is fitted by a sum of a sine and a linear function. The cut-off frequency (i.e. 3 dB drop) is calculated from the fit parameters for each channel.

- **Ramp test:** Analog inputs are disabled during this test and ADCs are switched to a mode, where they generate an internal ramp signal. Sequential ADC values are required to increase by one ADC count.
- **Hot/cold start:** In cycle 9 high temperature, the UUB power supply voltage will be gradually increased until all the UUBs shutdown. Then the voltage will be gradually decreased below 32.4 V – all UUBs are expected to restart. The point of shutdown and startup of each UUB will be recorded. Next, the temperature cycle will continue down to -20°C , where an analogical procedure will be conducted. The required low voltage limit there is 19.1 V.

4.3 Automation of data acquisition and storage

The test run is controlled by a computer with devices connected via USB (the climate chamber, the function generator, the power supply, the power control, the trigger delay, the environmental sensors), UUBs under test are connected via a Gigabit Ethernet router. The controlling software is implemented in Python and functions interfacing particular devices are run in separate threads in order to avoid I/O limitations. To read *slow* quantities out of the UUB an embedded HTTP server is used and commands are sent to the UUB via a dedicated HTTP request. The UUB FPGA features four buffers for ADC traces. As the test function parameters (the function type, amplitude, frequency, the distribution board mode) vary, it is necessary to match an acquired ADC trace with these parameters unambiguously. For this purpose, a dedicated C-based code running on the UUB periodically checks if a new ADC trace is available, reads the ADC trace out, splits raw data into parts and sends them as a bunch of UDP packets with a simple header to the control PC. On the control PC side, a dedicated Python thread listens for these UDP packets, assembles them, converts them into a NumPy array, bundles them with the test function parameters and passes them to a data processing thread. If all UDP packets for a particular ADC trace are not received within a predefined timeout interval, the ADC trace is discarded, thus allowing a reliable recording of hundreds of ADC traces per second. Measured data together with monitoring values are stored in the database.

5. SD station simulator

The SD station simulator is designed as a standalone portable test system, which can be used for the final functional test reproducible later in other laboratories. Functional blocks of the system are depicted in Fig. 3. The system is governed by an industrial single-board computer (SBC) running Scientific Linux, a LabVIEW based graphical user interface, test control software, and a ROOT/C++ data analysis software for evaluation of recorded pulses. The SBC communicates via USB with other components: a custom developed DAC card featuring 6 analog outputs, a power card providing all internal supply voltages as well as power supply for UUB, a Labjack U12 DAQ card, and an extension amplifier card.

The DAQ card serves for monitoring voltages generated by the the UUB to set the PMT high voltage (HV). For testing of the UUB SSD channels featuring an -8 V range, an extension amplifier card providing the required range with $50\ \Omega$ output impedance is integrated into the system. A Landau-shape pulse is generated by a custom made DAC card based on Zynq 7020 (the same

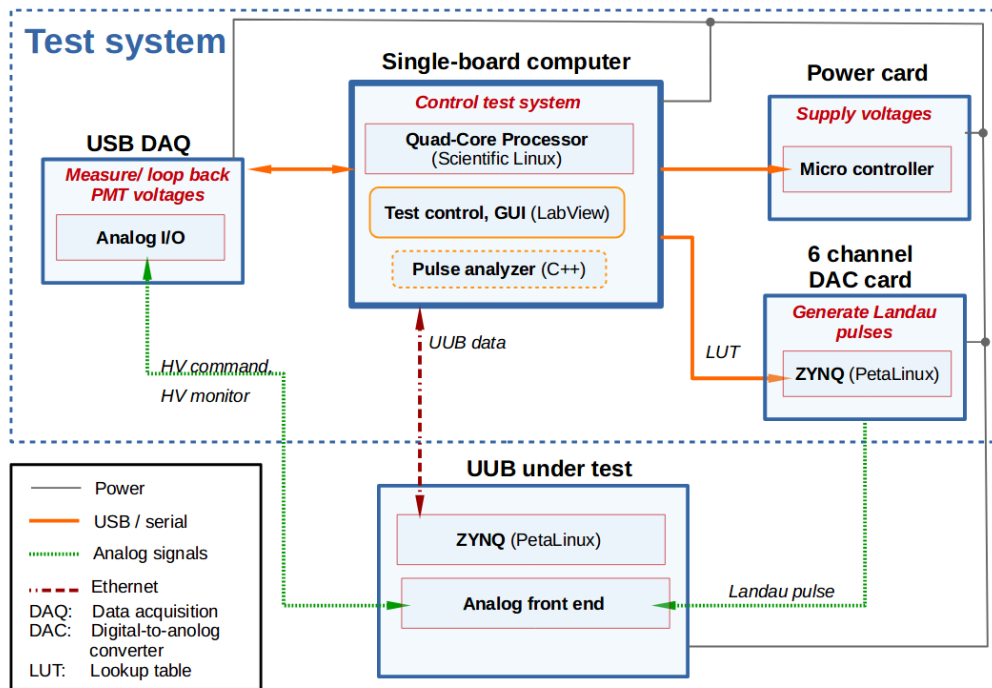


Figure 3: Block scheme of the portable test system setup.

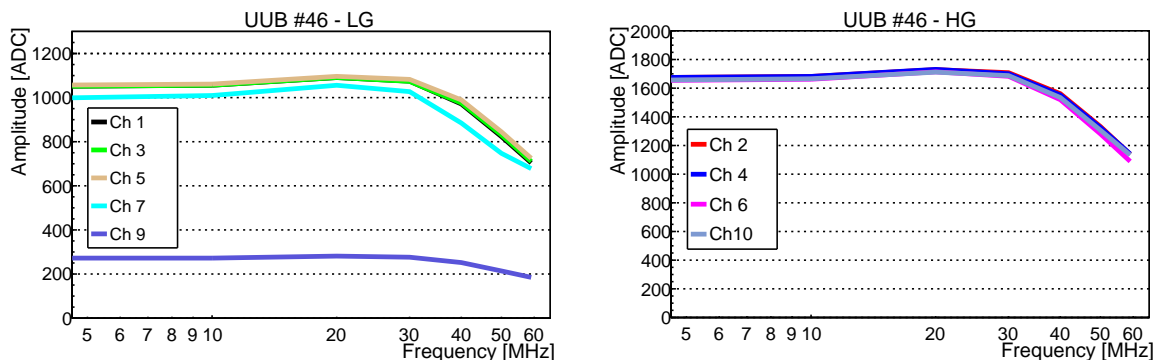


Figure 4: Performance of the UUB V1 prototype under frequency test.

as used in UUB) and three dual-channel 12-bit digital-to-analog converters (DAC) with 500 MSPS rate.

The system performs two tests: *Single pulse test* (SPT) and *PMT voltage test* (PVT). In the *Single pulse test* the system generates a Landau pulse shape (of two amplitudes: 50 mV and 800 mV; and of two FWHM 40 ns and 200 ns) and sends it to analog inputs of the UUB. The pulses are sampled and the ADC traces analyzed. 100 pulses are issued per each configuration, out of which mean values of measured amplitude, FWHM, pulse rising and falling edges, and pedestal position and noise are calculated. In the *PMT voltage test* the system instructs the SC to set the control voltage for the PMT HV (range 0 – 2.5 V) via DAC and outputs it on a dedicated pin on the D-Sub interface. The system reads out this voltage via DAQ card and compares it with the expected value.

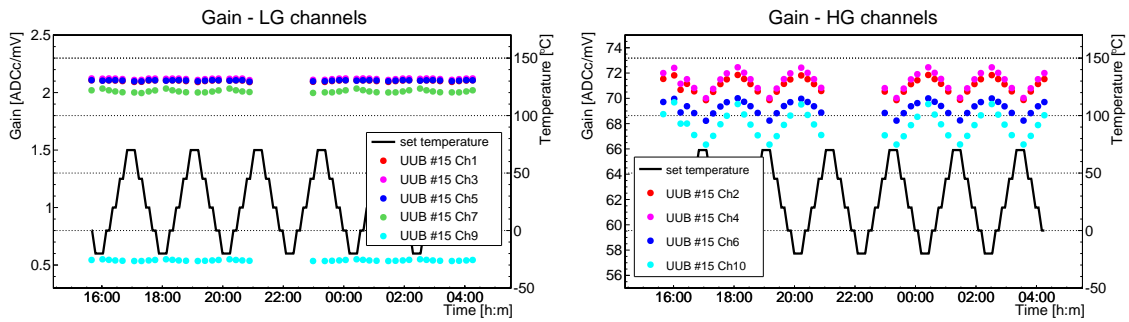


Figure 5: Temperature dependence of the gain of the analog chain.

6. Performance of the prototype UUB

Three UUBprototype versions have been developed and tested in the preparatory period. Two examples of the version 1 UUB performance are shown in Fig. 4 and 5. The scan in frequency described in Section 4.2 was performed using a sine wave with amplitude 500 mV for LG and 25 mV for HG channels. The results presented in Fig. 4 show a good performance of the anti-aliasing filter. The gain of each channel is derived from the linearity test and plotted as a function of temperature in Fig. 5. The temperature dependence of the gains observed in version 1 is expected to decrease in the final version of the UUB. However, the calibration in the field is done every minute so any remaining fluctuation will be taken into account. Further examples of the performance of the new electronics are presented in [4].

7. Conclusions

Three types of test benches were prepared to cover essential tests and characterization of the new surface detector electronics before being transported to the Pierre Auger Observatory site - the production test bench, the ESS test bench and a portable test system.

Acknowledgments

The successful installation, commissioning, and operation of the Pierre Auger Observatory would not have been possible without the strong commitment and effort from the technical and administrative staff in Malargüe, and the financial support from a number of funding agencies in the participating countries, listed at <https://www.auger.org/index.php/about-us/funding-agencies>. The presenter was supported by EU Operation Fund project CZ.02.1.01/0.0/0.0/16013/0001402.

References

- [1] A.Aab et al. [Pierre Auger Collaboration], Nucl. Instrum. Meth. A **798** (2015) 172.
- [2] A.Aab et al. [Pierre Auger Collaboration], AugerPrime - Preliminary Design Report, arXiv:1604.03637, 2016.
- [3] D. Nitz [Pierre Auger Collaboration], “New Electronics for the Surface Detectors of the Pierre Auger Observatory”, PoS(ICRC2019)370, these proceedings.
- [4] A. Taboada et al. [Pierre Auger Collaboration], “Analysis of Data from Surface Detector Stations of the AugerPrime Upgrade”, PoS(ICRC2019)434, these proceedings.



Production and Quality Control of the Scintillator Surface Detector for the AugerPrime Upgrade of the Pierre Auger Observatory

Jan Pękala^{*a} for the Pierre Auger Collaboration^{b†}

^a*Institute of Nuclear Physics PAS, Radzikowskiego 152, 31-342 Kraków, Poland*

^b*Observatorio Pierre Auger, Av. San Martín Norte 304, 5613 Malargüe, Argentina*

E-mail: auger_spokespersons@fnal.gov

Full author list: http://www.auger.org/archive/authors_icrc_2019.html

The Pierre Auger Observatory is undergoing a major upgrade, called AugerPrime. One of the goals of this upgrade is to improve the capabilities of the existing stations of the surface detector. The main modification consists in the addition of a new scintillator surface detector (SSD) to each water-Cherenkov detector station. The large-scale production of the SSDs started in 2017. The detector assembly is done in six laboratories with the collaboration of many other institutions providing components. Each institution involved follows common procedures, making sure that all the high standards set by the design are being met. We describe these procedures, which include quality checks of all components and a final certification of each detector with cosmic-ray muons. The deployment of the SSDs at the Observatory is already under way.

36th International Cosmic Ray Conference — ICRC2019

24 July – 1 August, 2019

Madison, Wisconsin, USA

^{*}Speaker.

[†]for collaboration list see PoS(ICRC2019)1177

1. Introduction

The Pierre Auger Observatory [1] is currently undergoing a major upgrade, called AugerPrime [2, 3]. The main goal of this upgrade is to better determine the cosmic-ray composition at the highest energies. The composition has already been studied using the hybrid method of air shower observation, i.e., simultaneously by the surface detector (SD) and the fluorescence detector (FD) [4]. However, the limited duty cycle of the FD translates into low event statistics above $\sim 10^{19.5}$ eV. The new AugerPrime detector arrangement will result in composition-sensitive data in this interesting region of flux suppression.

The main element of the AugerPrime upgrade is the addition of new scintillator surface detectors (SSDs) on top of the existing water-Cherenkov detectors (WCDs) of the SD. The SSDs will provide complementary measurements of air-shower particles arriving at the ground. Scintillator detectors have responses to muons and electromagnetic particles that are different from those of the WCDs, which means that this additional information will enable a reliable disentangling of these components of air showers.

Further elements of the upgrade include: the addition of a fourth small (1" diameter) photomultiplier tube (PMT) to the WCDs; equipping the SD stations with new electronics [5]; augmenting the duty cycle of the FD by about 50%; an extension of the AMIGA (Auger Muons and Infill for the Ground Array) project by an additional array of 61 scintillator detectors buried 2.3 m underground [6]; and adding radio detectors to every SD station [7].

2. Design of the SSD

The SSD was designed to be large enough to measure the density of air-shower particles with statistical uncertainties comparable to those of the WCDs. On the other hand, the requirement that the SSD be mounted on top of the WCD tank placed upper limits on the size and the weight of the SSD. The detector must be resistant and durable, to withstand several years of exposure to different weather conditions at the Pierre Auger Observatory, at locations where maintenance is very difficult. The cost of the SSDs was also an important factor.

The active part of the SSD is comprised of scintillator bars of dimensions $160\text{ cm} \times 5\text{ cm} \times 1\text{ cm}$, produced on the FNAL/NICADD Extrusion Line [8]. Each scintillator has two co-extruded channels through which wavelength-shifting optical fibers are routed, and an outer protective/reflective layer of TiO_2 . There are 48 scintillators in each SSD, placed symmetrically on both sides of the detector (fig. 1 left).

Plastic wavelength-shifting fibers are used to collect the light emitted inside the scintillators. A Kuraray Y11(300)M S-type fiber, of 1 mm diameter, was chosen, as its absorption spectrum matches well that of the light produced in the scintillators. Each fiber runs inside two scintillator bars through channels separated by a distance of 10 cm, with both ends meeting in the central part of the SSD. Outside the scintillators the fibers are guided in styrofoam routers.

All 96 fiber ends are bundled into a "cookie" - a poly(methyl methacrylate) (PMMA) cylinder that provides optical coupling to a single PMT. The cookie is fixed to an aluminum tube placed in the middle of one of the long sides of the SSD frame. The tube serves as a housing for a

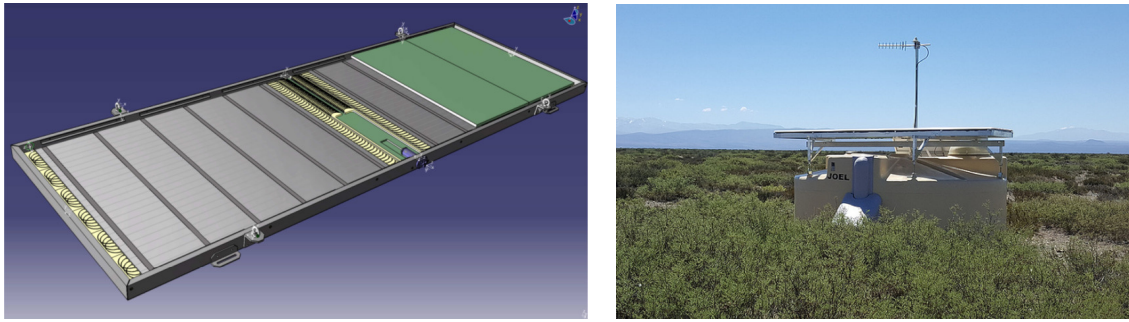


Figure 1: Drawing of an open SSD, showing the layout of the components (left), and photo of one of the deployed SSDs (right).

Hamamatsu R9420 PMT (1.5" diameter). The PMT can be installed in a completed SSD at any later time, during the deployment of the detectors.

The main mechanical element of the SSD is its enclosure box [9]. The sides of the rectangular box (3.8 m × 1.3 m) are made of aluminum profiles. A composite panel, made of two sheets of aluminum glued to a block of extruded polystyrene, serves as the bottom of the box; it strengthens the structure, and also serves as a support for all of the inner components of the detector. On top the box is closed with an aluminum sheet. All elements of the enclosure box are glued together using Ottocoll S610 silicone sealant, which ensures that the box is light-tight. To allow for equalization of pressure, several small holes are drilled into the frame; to keep the enclosure light-tight the inner hole is covered (glued and riveted) with a disk of sintered metal.

Additionally on top of the box a sunroof is installed: corrugated sheets reflecting sunlight and allowing for air flow, which prevents excessive heating. The completed detector is mounted on top of the WCD tank using a rigid support frame, built of aluminum beams.

The design of the SSD was tested and validated in the Pierre Auger Observatory. Twelve prototype detectors were deployed in late 2016, and since then the upgraded stations have been continuously in operation [10].

3. Organization of the production

The AugerPrime upgrade is a joint effort of all institutions of the Pierre Auger Collaboration. Numerous institutions take part in working on different elements of the upgrade. This joint work is especially prominent in the building of the SSDs, where all institutions involved collaborate closely. Many of the components were purchased or manufactured by one institution, and then distributed among partners according to demand. The remaining components and materials were procured locally by each institution - aluminum profiles for the frames were ordered from commercial manufacturers, and small mechanical parts were bought or produced in local workshops. The assembly of the detectors has been distributed among six sites: RWTH Aachen University, Laboratory of Subatomic Physics and Cosmology Grenoble, Karlsruhe Institute of Technology, Institute of Nuclear Physics Kraków, INFN Lecce and NIKHEF Nijmegen, with two more institutions working on PMT preparations: Bergische Universität Wuppertal and INFN Napoli.



Figure 2: Workshops dedicated to SSD assembly in Grenoble (left) and Karlsruhe (right).

Each of the institutions has been able to assemble the SSDs thanks to the resources already available there, e.g., technical departments experienced in building scientific instruments. Some adaptations were necessary, like isolation of any particular SSD assembly area, to protect the fibers and scintillators from UV light exposure (fig. 2). Dedicated equipment had to be prepared prior to the assembly process, like tiltable tables, at which gluing of fibers into cookies takes place. Also test measurement stations had to be prepared. Having built the SSD prototypes, the Karlsruhe group hosted staff from other sites to share their experience, and also visited them at their institutions when the SSD assembly was starting.

During the preparations and early stages of production, all problems encountered, as well as any minor non-conformities were reported and discussed, and solutions to deal with them formulated. As a result of this process, a detailed assembly procedure was developed. All separate fabrication and assembly sites follow this common procedure, which ensures that all of the SSD design standards are met.

4. Assembly procedure

The assembly of a SSD starts with preparation of the frame of the enclosure box. Four pieces of aluminum profile, with ends cut at a 45° angle, are glued into a rectangular frame using insert corner pieces and Ottocoll S610 sealant. Alternatively, frames welded by a commercial provider were used in Krakow and Grenoble. Next a composite panel is glued into the frame, using the same sealant that ensures light-tightness. After each step the glue is allowed to cure for a day. Before assembling the detector, a number of holes are cut in the frame to accommodate the aluminum tube of the PMT housing (fig. 3 right - bottom part), to allow for equalization of pressure, and for rivets used to attach support brackets on the outside and U-beams fixing the scintillators on the inside.

Prior to assembly, the ends of the channels in the scintillators are graded, to remove any rough edges, and compressed air is blown through the channels, to make sure they are clean. Outer routers are placed at both ends of the SSD frame, and then the scintillators are positioned, 24 bars on each side. Finally, inner routers are placed and fixed at the inner ends of the scintillators. Next, the fibers are inserted - usually directly from the spools on which they are delivered (fig. 3 left). Each fiber is inserted into one scintillator bar, then at the other end it is guided following a groove in the router



Figure 3: Inserting fibers into scintillators (left) and the inner part of an assembled SSD (right).

to be inserted into another bar. The remaining parts of the fiber are fixed in the proper grooves of the inner routers, making sure that both ends are of the same length.

The next steps in the assembly process are carried out at tiltable tables raised to the upright position (fig. 2 right), which allows for easier access and facilitates greatly the optical gluing of the 96 fiber ends inside the cookie. Fiber ends require finishing after cutting, to prevent inefficiency in light collection. As an alternative to more difficult polishing, the plastic fiber ends are melted. A borosilicate glass plate heated to $150\pm 30^{\circ}\text{C}$ is used. Each fiber end is delicately placed on this plate for about one second, which is sufficient to melt and flatten the cut surface of the fiber (fig. 4 left). The improvement of the light transmission is directly visible in a reflection off the heated plate. In case the fiber gets melted for too long, a bead may appear, which can be easily corrected by cutting off this small piece of fiber and repeated melting.

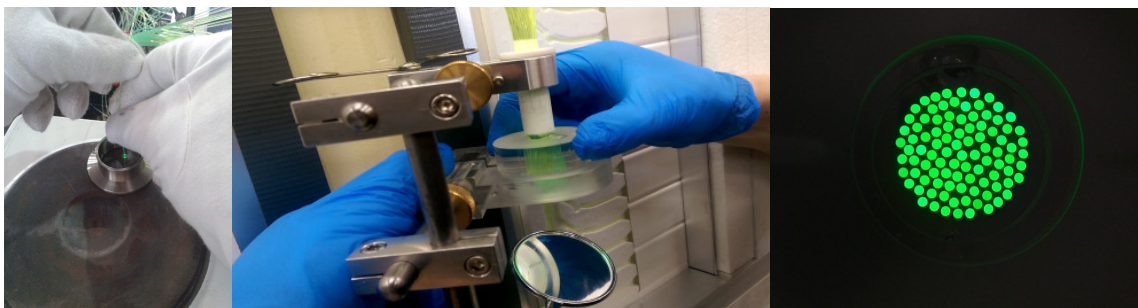


Figure 4: Fiber ends are melted in order to get a flat, smooth surface (left) and are glued inside the cookie (center). A photograph of a ready cookie (right).

All 96 fiber ends are bundled and placed in the opening of the PMMA cookie. The front surfaces of the fibers are aligned on the surface of the cookie window, which is then moved away by about 1 mm, to leave some space for the optical glue. Eljen EJ-500 is used as the optical cement. As a two-component glue, it requires mixing, after which it needs to be set aside or dessicated to get rid of air bubbles trapped during the mixing. The glue is poured slowly, to allow all air to escape through the hole designed for this purpose. In case an air bubble gets caught in front of the fiber ends, it is still possible to force it out by twisting or tapping the cookie (fig. 4 center). After

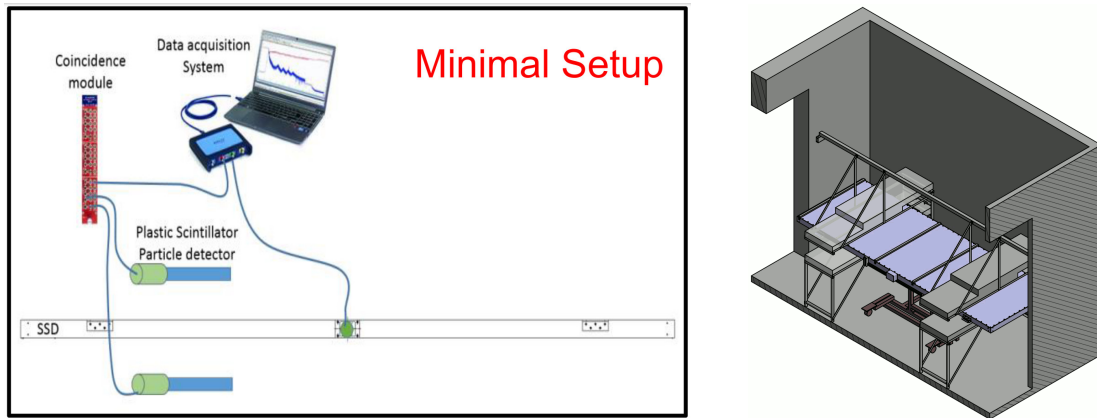


Figure 5: Scheme of a minimal setup for local tests of SSDs (left) and drawing of the test stand in Nijmegen (right).

allowing sufficient time for the glue to cure (usually overnight), the cookie is fixed to the inner end of the aluminum tube (fig. 3 right and fig. 4 right).

To minimize the enclosed volume of air inside the SSD and to additionally fix the components, the remaining volume of the frame is filled with lightweight styrofoam blocks. Next, the detector is closed by gluing and riveting the top cover. Finally, the roof support bars are attached. The sunroof itself is mounted later, prior to deployment at the Observatory.

The procedure for assembling all SSD units includes quality checks at each step. All components are inspected before they are used. Especially important is ensuring the quality of those components of the SSD that produce and guide light: scintillators, fibers and cookie. The greatest risk of damage occurs during the insertion of the fibers into the scintillators. The fiber can occasionally but rarely get scratched or bent too much, even with trained and experienced personnel. In such a case it gets replaced with a new piece. Finishing the fiber ends and gluing the cookie is done by the most experienced staff members. Every step is controlled and documented, and the information about all components used to build all detectors is recorded and stored in a database especially developed for this purpose (e.g. SSD serial number, date of production, individual bar-codes of the scintillators, batch numbers of fibers and glues, picture of the fiber ends glued in the cookie).

5. Validation of the detectors

In addition to the controls at each step of the assembly, all SSDs undergo additional tests at each site upon completion. These tests provide an opportunity to detect any deficiencies that could not be identified earlier, as well as enabling a baselining of the quality of data each detector can provide. Each of the SSD production sites has at least one PMT at its disposal, with which it is possible to test the SSDs.

The tests are done with cosmic-ray muons. This enables us to determine the detector response to a reference minimum-ionizing particle (MIP). To identify these particles it is necessary to have an external trigger system. At two SSD production sites (Karlsruhe and Lecce) it was possible to use already existing muon detectors, that provide a trigger over the whole area of the SSD, and a high-resolution (~ 1 cm) measurement of the muon track. At other sites dedicated test stations were

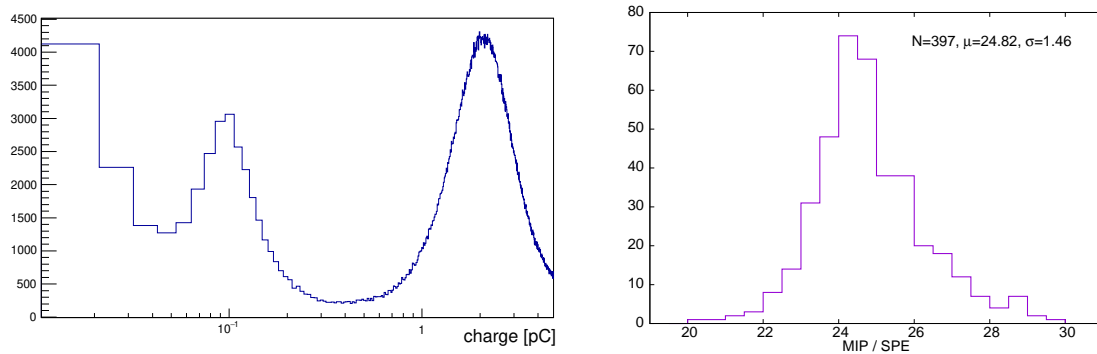


Figure 6: Histogram of signals recorded in a test measurement, with peaks corresponding to electronics noise, SPEs and MIPs (left). Distribution of test results for SSDs made in Karlsruhe (right).

prepared, using components available locally. A minimum requirement was to have two particle detectors working in coincidence, that would provide a trigger over a fraction of the SSD active area (fig. 5 left). The measurement should cover as large and as representative a part of the SSD area as possible. This was done by building the external detectors so they cover a fraction of all scintillators, on both sides of the SSD, during a measurement (fig. 5 right), or alternatively by moving smaller detectors over different parts of the SSD in the course of a test run. Each test measurement takes at least a few hours, to collect a sufficient number of MIP events.

The test measurements allow us to identify not only signals of MIPs, but also those of single photoelectrons (SPE). Fits of the peaks in the histograms are used to determine the mean charge of the MIP and SPE (fig. 6 left). The ratio of these values can be used as an estimate of the quality of the tested SSD - it reflects the efficiency of the key detector components at generating (scintillators), collecting (fibers) and transmitting (cookie) the light. An example of test results from one institution is shown in fig. 6 (right). Results from different institutions are obtained using different test setups (including different PMTs). To enable some comparison, 2 or 3 detectors from each production site were sent for test measurements to Karlsruhe. These cross-tests are used to rescale the results obtained in other institutions, which show that they are in good agreement, with mean values of $\text{MIP/SPE} \sim 24 \pm 2$, i.e. exceeding the design requirements by a factor of ~ 2 .

The total efficiency of SSDs is measured in testing, as well as the uniformity of response over the active area of the detector. Institutions that had the advantage of high-resolution detectors performed detailed studies of some detectors. These showed that signals from individual scintillator bars deviate typically by no more than 10% from the average. Signals from opposing ends of a scintillator bar differ by $\sim 5\%$, as follows from the light attenuation in the fiber. For routine measurements at all sites the shape of the MIP peak in the histogram of all recorded signals can be used as an estimate of detector uniformity. If a significant part of the detector were deficient, it would cause a deformation of this peak. A Gaussian fit sigma of the order of 30% of the mean value is a sign of a satisfactory uniformity of the tested SSDs.

Another test is done by measuring the trigger rate of each SSD. Any significant deviation from expected trigger rates (which should be stable for a fixed electronics setup) would be an indication of some problem with a given SSD. An increase of trigger frequency is an indication that the

enclosure box is not light-tight. Even careful visual inspection during and after gluing might not be enough to ensure complete light-tightness, and this test helps to verify this - to make any light leaks more prominent, a high intensity light is directed in the course of the test at all glued interfaces. A trigger rate smaller than expected could be caused by some damage in a part of the active area of the SSD or a light loss in the cookie. All test measurements are also stored in the SSD database, including e.g. values of MIP and SPE, histograms of measured signals, dark count rate.

6. Status of the production and deployment

The large-scale production of the SSDs started in 2017. As of the middle of 2019 the production of the SSDs is nearing its end, with some of the sites having already finished their share. The completed detectors are being shipped in batches to Argentina. The SSDs have been undergoing continuous deployment since October 2018. The local Argentinean team has a challenging task of transporting the SSDs to different WCD stations located in hard to reach areas, but has still been able to install ~ 6 detectors per working day. As of July 2019, over 350 detectors have been deployed, of which 77 are operational. The SSDs will be equipped with PMTs, and also new electronics will be installed, as soon as these components become available. The deployment of the SSDs should be completed in 2020.

References

- [1] Pierre Auger Collaboration, *The Pierre Auger Cosmic Ray Observatory*, *Nucl. Instrum. Meth. A* **798** (2015) 172.
- [2] Pierre Auger Collaboration, *The Pierre Auger Observatory Upgrade - Preliminary Design Report*, arXiv:1604.03637.
- [3] D. Martello for the Pierre Auger Collaboration, *The Pierre Auger Observatory Upgrade*, in proceedings of *ICRC2017*, PoS (ICRC2017) 383 (2017).
- [4] Pierre Auger Collaboration, *Combined fit of spectrum and composition data as measured by the Pierre Auger Observatory*, *JCAP* **04** (2017) 038.
- [5] D. Nitz for the Pierre Auger Collaboration, *New Electronics for the Surface Detectors of the Pierre Auger Observatory*, in proceedings of *ICRC2019*, PoS (ICRC2019) 370 (2019).
- [6] A. M. Botti for the Pierre Auger Collaboration, *The AMIGA underground muon detector – performance and event reconstruction*, in proceedings of *ICRC2019*, PoS (ICRC2019) 202 (2019).
- [7] B. Pont for the Pierre Auger Collaboration, *A large radio detector at the Pierre Auger Observatory - measuring the properties of cosmic rays up to the highest energies*, in proceedings of *ICRC2019*, PoS (ICRC2019) 395 (2019).
- [8] D. Beznosko, A. Bross, A. Dyshkant, A. Pla-Dalmau, and V. Rykalin, *FNAL-NICADD Extruded Scintillator*, IEEE Nuclear Science Symposium (2004), FERMILAB-PUB-05-344.
- [9] R. Šmída for the Pierre Auger Collaboration, *Scintillator detectors of AugerPrime*, in proceedings of *ICRC2017*, PoS (ICRC2017) 390 (2017).
- [10] A. Taboada for the Pierre Auger Collaboration, *Analysis of Data from Surface Detector Stations of the AugerPrime Upgrade*, in proceedings of *ICRC2019*, PoS (ICRC2019) 434 (2019).

7

Outreach



PIERRE
AUGER
OBSERVATORY



Social Impact of Outreach at the Pierre Auger Observatory

Beatriz García^{*a} for the Pierre Auger Collaboration^{†b}

^a*Instituto de Tecnologías en Detección y Astropartículas, Figueroa Alcorta 122, 5501 Godoy Cruz, Mendoza, Argentina*

^b*Observatorio Pierre Auger, Av. San Martín Norte 304, 5613 Malargüe, Argentina*

E-mail: auger_spokespersons@fnal.gov

Full author list: http://www.auger.org/archive/authors_icrc_2019.html

The Pierre Auger Observatory in Argentina started its construction in 1999 and is operating at full capacity since 2008. From its initiation, scientists and staff of the Observatory are focused on working at the frontiers of scientific knowledge and on serving as a reference on education and outreach. The impact of the interactive new approach on science communication for the general public and the connections with other institutions in the region such as the Planetarium of Malargüe and the University of Cuyo produce great synergy with the community. The year 2019, the year of the centenary of the International Astronomical Union, provides an opportunity to develop new activities in the framework of continuous innovation in education and outreach. In this presentation, we propose a virtual trip through the 20 years that the Auger Observatory transmits scientific knowledge in Malargüe and beyond.

*36th International Cosmic Ray Conference — ICRC2019
24 July – 1 August, 2019
Madison, Wisconsin, USA*

*Speaker.

†For collaboration list see PoS(ICRC2019)1177

1. Introduction

The year 2019 marks the 20th anniversary of the formal inauguration of the Pierre Auger Observatory [1]. At this anniversary the scientists and staff of the Observatory are not only working with the well-known surface and fluorescence detectors, but they are also installing new detectors and instruments to complete AugerPrime, the upgrade of the Observatory. During this period of upgrading the Observatory, the challenges of education and communication with the public become more and more important and the methods by which this task can be fulfilled demand ever more creativity. During this new stage of the Observatory, it is appropriate to look at its achievements as a guideline to face the challenges for the future.

2. Pierre Auger Observatory and the Community

Since the first meeting of the incipient Pierre Auger Collaboration in Valle Grande, San Rafael in 1996, where the project leaders Jim Cronin, Alan Watson, and Paul Mantsch were present (Figure 1, left), the Observatory meetings became opportunities to share various projects with the community, to establish lasting relationships and to participate in local activities. Examples of such actions are the organization of Science Fairs, participation in the parade celebrating the anniversary of Malargüe and the activities at the Visitor Center, which includes visits from schools originating from the whole country, and of tourists from all over the world. This important task was led from the beginning by Greg Snow (Figure 1, right), who passed away on May 4, 2019, and to whom we dedicate this work.

An example of a positive effect of the Observatory on the local community is the contribution of several members of the Auger collaboration as professors in the Faculty of Exact and Natural Sciences of the Universidad Nacional de Cuyo in the Malargüe Annex. Many university students have performed internships at the Observatory, including students of local secondary technical schools, which resulted in the hiring of three electromechanical technicians who were incorporated into two new Auger projects. Members of the Observatory participated in global actions, such as GalileoMobile [2], which included the installation of a small telescope at the school in the town of Carapacho in 2015 (see Figure 2).

The Observatory staff is in continuous contact with both the city and the countryside due to the travel of technicians maintaining the detectors. Families that have detectors in their fields and the schools in the site consider the loan of batteries for power storage very important. The laying of power lines in very remote areas, required to feed the fluorescence telescopes, had resulting benefits for the local inhabitants near those facilities. In 2005, a study on the social impact of the Observatory was carried out. The study was based on new concepts on organizational management through Corporate Social Responsibility criteria. Social Impact is defined as the "change or set of lasting changes that occur in society, economy, science, technology and the environment, improving their indicators as a result of the execution of research, development, innovation, that introduce added value to products, services, processes and technologies". The social impact is not only about the result, but it relates to its effect, the impact on people, the economy, and the environment. The full set of results at that moment exceeds the scope of this article, but from the study it was concluded that the relationship between the Observatory and the government was present since the genesis of



Figure 1: First directors and manager of the Observatory. From left to right: Alan Watson, Jim Cronin and Paul Mantsch (left); Greg Snow happily explaining data to the crowd at a balloon launch site. Red data points are from a test flight from the previous day on the 90th anniversary of the discovery of Cosmic Rays (right).

the project, as it was largely the decision and vision of the local authorities that finally managed to get the Observatory installed there. When analyzing the actions carried out by the Observatory staff in Malargüe, it was noticed that the Observatory staff work in a network with local companies and government. Examples of this network are concrete actions for the community, such as:

- The Michigan scholarships, whose purpose is the stay of a high-school student at Michigan University during a year. This is made possible thanks to the coordinated work of the Municipal government, the Municipal Academy of English, schools in the area, the National Technological University and the Observatory.
- The construction of the High School "Cronin" using funds from the Granger Foundation.
- The construction of the Malargüe Planetarium, financed by the Municipality, with the advice from scientists from the Observatory.
- The dissemination of free guided visits to the Observatory, working together with the local government, the Malargüe Tourism office, and tourist agencies.

2.1 The Visitor Center

The Visitor Center (VC) of the Observatory was conceived as part of the complete design of the central building of the Observatory (see Figure 3), which is a landmark in the city. It was installed thanks to a contribution of the University of Chicago, and designed by the architects



Figure 2: GalileoMobile Project. Telescope at the office of the Site Manager Gualberto Ávila (left); assembling the telescope at the school in Carapacho (right).



Figure 3: The Pierre Auger Observatory headquarters in Malargüe.

Boccanegra and Paoletti. During the first years, visitors were received at the main area of the VC where an explanatory talk on the Observatory and its objectives were given by trained guides, ready to answer questions related to the nature of the cosmic rays: what are they? from where do they come from? how do they arrive with such energy?.

Several special presentations were designed to explain the scientific and engineering issues related to the Observatory. Throughout the years, the contact with the public has evolved. Hand in hand with the International Year of Physics (2005), the International Year of Astronomy (2009), the International Year of Light (2015) and having passed the centenary year of the discovery of cosmic rays by Victor Hess in 1912, we decided to address the public in a more creative way, appealing to interactivity and new applications to make the VC more attractive. By applying the principles of Design Thinking [3], the VC was completely remodeled in 2017. This change also meant a revitalization of resources and led to an increase in the number of visitors and the possibility of reaching a wider audience, taking into account methods of inclusive science, based on adaptations for blind and visually impaired, deaf and disabled persons and also through new tools, as virtual

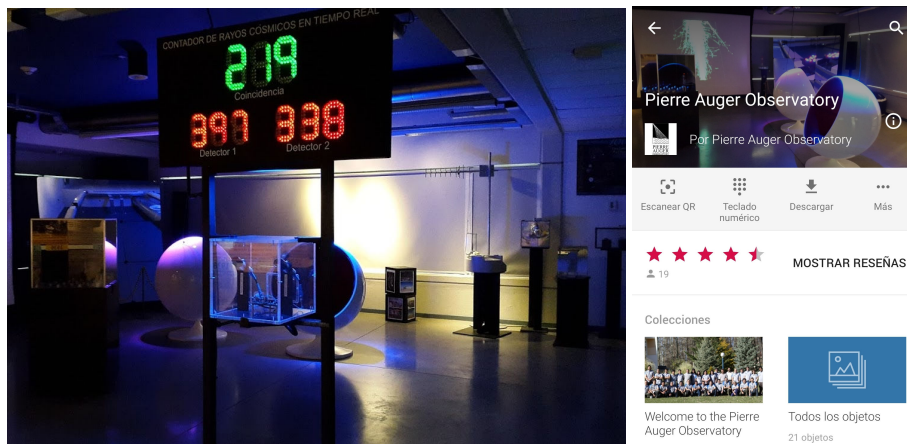


Figure 4: Visitor Center: general view (left), virtual tour (right).



Figure 5: Auger in: Tecnópolis 2011 [4] (left) , Tecnópolis 2012 (right).

guides (see Figure 4).

Since 2002, the Pierre Auger Observatory has received more than 123,000 visitors, and at the public exhibitions as Tecnópolis [4], the mega-exhibition of science, technology, industry and art in Argentina supported by the Ministry of Science, Technology and Productive Innovation between 2011 and 2016 (see Figure 5), the Auger space received more than 3 million visitors.

2.2 The Science Fair

Since 2005, the Observatory organizes bi-annual Science Fairs aiming to provide a space for students to promote research skills. The main objective of this activity is to guide and stimulate young people in the use of the scientific method by promoting a scientific exchange between the exhibitors, and establish communication between the students and the researchers of the Pierre Auger Observatory.

In the last editions, the Fairs received visitors from all over the country. With the possibility to show projects developed in the schools to observatory scientists, a special bond is created between participants and jury (made up of members of the collaboration). Over the years, a significant improvement in the quality of the proposals has encouraged us to continue with the initiative [5].

In 2019, a new approach to this activity was proposed to the Collaboration Board of the Observatory, that takes into account a series of anniversaries and events taking place in 2019: the 20th anniversary of the Observatory, the 100 years of the International Astronomical Union (www.iau-100.org), the 50 years of the first moon landing, the International Year of the Periodic Table of the Chemical Elements and a Total Solar Eclipse, that crosses the Argentinean territory on July 2nd. Taking these events as flagships, we aim for the Auger 2019 Science Fair to address specific issues and to create a stronger appeal to the community.

2.3 The Parade

Since the year 2001, the Pierre Auger Collaboration participates in the parade celebrating the anniversary of the department of Malargüe [5]. Along with children from schools, non-profit organizations, dance groups and musicians, the scientists working at the Observatory parade and participate in the joy and being part of the community. Without a doubt, they have contributed to the changes of the Malargüe community throughout the 20 years of existence of the Observatory.

2.4 Public access to the scientific data

The Pierre Auger Collaboration agreed to make 10% of their data available to the public. The website of the *Comisión Nacional de Energía Atómica* (CNEA) allows browsing the events compiled since 2004, and it is updated daily [6]. This resource permits to enter a selection for events in an "event search window", search for an event with the selection menu or show an event that is already in cache. It is also possible to download ASCII files with all events for further analysis. In some cases, the available data have been used for the development of university-level degree projects and projects of middle-level students.

3. Pierre Auger and the Scientific Tourism

Malargüe is an attractive city for scientific tourism. The nearby presence of the Andes mountain range contains ski slopes and other activities linked to mountaineering. The existence of caverns (*Caverna de las Brujas* in Bardas Blancas), wetlands (Llancanelo lagoon, the largest bird reserve in the country), paleontological records and unique volcanic areas (Payunia), as well as the possibility of dark skies, contribute to the intrinsic value of the department in a remarkable way. In this context, the installation of the Malargüe Planetarium, founded in 2008 and dependent on the Municipality [7], was one of the many contributions by the Observatory in science communication. The cooperation between the Observatory and the Planetarium led to the production of two of the first Argentinean shows for digital planetaria, "Cosmic Rays"(for the centenary of their discovery) and *Travelers of the Light* (on the occasion of the International Year of Light, IYL2015). In the latter case, the show was conceived as part of a trans-media production, which includes educational material for teachers, short videos designed for use in schools, exclusive interviews, among other special products. The cooperation with the Planetarium has also ensured the installation of interactive modules in the Planetarium Museum (Figure 6).



Figure 6: Interactive Museum at Planetario Malargüe, IYL2015 space.

4. Conclusions and next steps

The Pierre Auger Observatory is strong in the community, in terms of education and the dissemination of the physical and astronomical sciences. After 20 years of existence in the Department of Malargüe, it is time to update the impact studies, analyze the efficiency of the knowledge transfer to the community and to improve the synergy between the different actors in the local society. It is possible, on the other hand, to observe how Malargüe as a result of Auger is integrated into the world by adhering to scientific activities that care for and preserve the environment and at the same time educate the local community, for example in very important and actual topics for astronomical observations such as the control of the Light Pollution. It should be noted that this activity has great adhesion in the community that benefits from the high level of visibility and acceptance that the observatory generates. The new forms of communication allow us to establish a direct relationship with the public through social networks. It is imperative that the Observatory improves the use of these new trends as they generate a large visibility and impact. The collaboration moves forward with a strategic campaign using social networks, the preparation of a package of released data plus the procedure to manage them to be disseminated massively, and the production of contents for interactive screens. A fluid contact with the press and the institutions interested in the subject of astroparticle physics is essential and, in the particular case of the Pierre Auger Observatory itself, an inter-institutional network between those scientific centers that are part of the International Collaboration will be part of the outreach effort for the next decade. This network enables the extensive use of different resources in education and dissemination in a coordinated manner, with a broad spectrum of ideas, proposals and projects and interaction between scientists and interested people, throughout the world.

References

- [1] Pierre Auger Observatory, <http://www.auger.org>
- [2] GalileoMobile, <http://www.constellationproject.org/>
- [3] Pérez, S. Maya, J. Mancilla, A., De la Vega, G., Yelos, D., Cancio, A. García, B., Think on Science and innovate with design, Proceedings of CAP Conference, Fukuoka, Japan, pp 204-205, 2018.
<https://drive.google.com/file/d/1JqGgsFvxZIATxvoCZ-kGo4xVjTxBQS7Q/view?usp=sharing>

- [4] Tecnópolis 2011, <http://www.tecnopolis.mincyt.gob.ar/categoria/2011/page/2/>
- [5] Timmermans, C. for the Pierre Auger Collaboration, Education and public outreach of the Pierre Auger Observatory, Proceedings of the ICRC2017, Busan, Korea, PoS(ICRC2017)392, <https://pos.sissa.it/301/392/pdf>
- [6] Public Event Display at Pierre Auger Observatory, <https://www.auger.org/index.php/edu-outreach/event-display>
- [7] Planetario Malargüe, <https://planetario.malargue.gov.ar/institucional/>